BERICHTE
aus dem
INSTITUT FÜR MEERESKUNDE
an der
CHRISTIAN-ALBRECHTS-UNIVERSITÄT KIEL

Nr. 320

A Model Study of Arctic Sea Ice Variability

von

Michael Hilmer

Kiel 2001

Kopien dieser Arbeit können bezogen werden vom:
Institut für Meereskunde Kiel
Fachbereich Ozeanzirkulation und Klima
Düsternbrooker Weg 20
24105 Kiel, Germany

ISSN 0341-8561

Diese Arbeit wurde von der Mathematisch-
Naturwissenschaftlichen Fakultät der
Christian-Albrechts-Universität zu Kiel
als Dissertation angenommen.

Contents

Zusammenfassung

Das Ziel dieser Studie ist die Untersuchung der Variabilität des arktischen Meereises auf interannualen bis multi-dekadischen Zeitskalen. Aufgrund der eher geringen Anzahl direkter Beobachtungen basiert diese Untersuchung auf simulierten Daten. Unter Verwendung von realistischen, täglichen Antriebsfeldern des Oberflächenwindes und der Oberflächentemperatur, abgeleited aus den NCEP/NCAR Reanalysedaten, wurde die arktische Meereisdecke mit einem dynamisch-thermodynamische Meereismodell über den Zeitraum 1951–1999 simuliert. Um die relativen Einflüsse von Wind und Lufttemperatur auf die interannuale Variabilität des simulierten Meereises zu untersuchen, wurden zusätzlich idealisierte Simulationen durchgeführt, bei denen entweder nur die interannuale Variabilität des Windes oder die der Lufttemperatur vorgeschrieben wurde. Vergleiche mit verfügbaren Beobachtungen von Satelliten, Driftbojen, U-Booten und ozeanographischen Verankerungen zeigen eine gute Übereinstimmung mit den langzeitlich gemittelten Simulationsergebnissen der Eiskonzentration, der Eisdrift, der Eisdicke und des Eisvolumenexports in den Nordatlantik. Darüberhinaus wird gezeigt, daß das Meereismodell in der Lage ist, die beobachteten interannualen Schwankungen der Eisausdehnung zu reproduzieren.

Die Simulationsergebnisse weisen eine ausgeprägte interannuale Variabilität von wichtigen Eigenschaften der arktischen Eisdecke wie zum Beispiel seiner Dicke, seiner räumlichen Ausdehnung oder des Eisvolumenexports in den Nordatlantik auf. Diese Schwankungen werden bezüglich ihrer Ursachen in den atmosphärischen Antriebsfeldern und ihres Einflusses auf den Süßwassereintrag in den Nordatlantik untersucht. Darüberhinaus werden durch statistische Analysen dominante Moden der interannualen Variabilität der simulierten Eisdecke identifiziert und teilweise in Beziehung zu den dominanten Moden atmosphärischer Variabilität gesetzt. Diese sind in den hohen nördlichen Breiten die Arktische Oszillation (AO) und die Nordatlantische Oszillation (NAO). Es wird gezeigt, daß die AO zu zyklonalen und antizykonalen Schwankungen der Eisdrift führt, welche wiederum mit Änderungen der Eisadvektion zwischen der Beaufort- und Ostsibirischen See einhergehen und somit zu erhöhter Variabilität der Eisdicke in diesen Regionen führen. Die NAO ist für die außer-Phase Variabilität der winterlichen Eisausdehnung zwischen den Regionen östlich und westlich von Grönland verantwortlich. Weiterhin zeigt die NAO seit Mitte der siebziger Jahre kohärente Variationen mit dem winterlichen Eisvolumenexport durch die Fram Straße, wärend im Zeitraum davor kein Zusammenhang zwischen beiden Prozessen existierte. Die zeitliche Änderung der Kohärenz zwischen der NAO und dem Eisvolumenexport wird auf eine Ostwärtsverschiebung der Zentren interannualer NAO-Variabilität in den siebziger Jahren zurückgeführt. Diese Verschiebung führte dazu, daß positive und negative NAO-Winter von verstärkten meridionalen Windanomalien im Bereich der Fram Straße begleitet waren und somit kohärente Variationen beider Prozesse auf interannualen Zeitskalen ermöglicht wurden.

Neben interannualen Variationen weisen die Simulationsergebnisse auch signifikante langzeitliche Änderungen der arktischen Meereisdecke auf. Durch den Anstieg der Lufttemperaturen hat das gesamte Meereisvolumen der Arktis seit Mitte der sechziger Jahre um ca. 16% abgenommen. In Übereinstimmung mit Beobachtungen treten die stärksten Abnahmen des Packeises in der Ostsibirischen See und in der Nähe des Nordpols auf,

wogegen die Eiskonzentration und die Eisdicke nördlich des Kanadischen Archipels und in der Baffin Bucht zugenommen haben. Die Abnahme des Oberflächenluftdrucks in der Arktis führt zu einer Abschwächung der großskaligen antizyklonalen Zirkulation des Meereises. Während die Effekte der langzeitlichen Änderungen des Windfeldes insgesamt zu einer Dämpfung der thermisch bedingten Abschmelzens des Packeises führen, sind dynamische Effekte während der letzen 15 Jahre für eine Beschleunigung des Abnahme des Eisvolumens verantwortlich.

Abstract

The focus of the present study is the investigation of the variability of the Arctic sea ice cover on interannual to multi-decadal time scales. Because there is only a rather small number of direct observations, this investigation is based on simulated data. Using realistic daily fields of near surface wind and air temperature derived from the NCEP/NCAR reanalysis, the Arctic sea ice cover is simulated with a dynamic-thermodynamic sea ice model integrated over the time period 1951–1999. Additionally, sensitivity experiments with prescribed interannual variability of either only winds or only air temperatures are performed in order to identify their relative contributions to the simulated variability of the ice pack. A comparison of available observations from satellites, drifting buoys, submarines, and oceanographic moorings reveals a good correspondence of the long-term averaged quantities of the simulated ice concentration, ice drift, and ice thickness, respectively. Moreover, it is shown that the simulation is able to reproduce the observed interannual variations of the sea ice extent.

The simulation results reveal pronounced interannual variability of the main quantities of the Arctic sea ice cover as, for instance, its thickness, its areal extent, and the ice volume export into the North Atlantic. These variations are investigated with respect to their main causes in the atmospheric forcing fields and to its possible impacts on the freshwater input into the North Atlantic Ocean. Moreover, from statistical analyses of the model output dominant modes of interannual variability are identified and partly related to the dominant modes of atmospheric variability of the northen high latitudes, that are the Arctic Oscillation (AO) and the North Atlantic Oscillation (NAO). It is found that the AO leads to cyclonic and anticyclonic ice drift variations which are associated with changes of the ice mass advection between the Beaufort and East Siberian Seas leading to enhanced ice thickness variability in those regions. The NAO is responsible for the out-of-phase variability of the wintertime ice extent between the regions east and west of Greenland. Moreover, since the mid-1970s the NAO exhibits coherence with variations of the wintertime ice volume export through Fram Strait which is missing in the time period before. The temporal change of the link between both processes is explained by an eastward shift of the NAO's centers of interannual variability around the mid-1970s. This eastward shift was associated with increased anomalous meridional wind components near Fram Strait during high and low NAO winters and, hence, with increased coherence between the NAO and sea ice exports through Fram Strait on interannual time scales.

On the background of interannual variability the simulation also reveals significant long-term trends of the Arctic ice pack. Because of a rise of surface air temperatures, the total ice volume of the Arctic has linearly decreased by about 16% since the mid 1960s. In agreement with observational estimates, largest thinnings occur in the Eastern Arctic and near the North Pole whereas the ice concentration and thickness north of the Canadian Archipelago and in the Baffin Bay have slightly increased. The deepening of Arctic surface air pressures led to a weakened anticyclonic large-scale flow of the ice pack. Whereas the effects of long-term changes of the wind field generally tend to damp the thermally induced thinning of the ice cover, the dynamic effects during the last 15 years of the simulation led to an acceleration of the decrease of the Arctic ice pack.

Chapter 1

Overall Introduction

The Arctic is the vast northern polar region of land and sea embracing the Arctic Ocean and the northern parts of Europe, Asia, and North America (Fig. 1.1). Astronomically, the Arctic is defined as the region north of the Arctic Circle (66°33' N) where the sun does not set during summer solstice and where darkness dominates the winter months. During most of the year the air temperatures are below freezing but rise up to about 10°C during summer over the land areas. The Arctic has economically gained attention due to the occurrence of minerals and because of its rich fishing grounds. However, primarily due the mostly perennial ice cover of the Arctic Ocean, it represents a key region for global climate.

As an interface between atmosphere and ocean the rather thin sea ice cover controls most of the transfers of heat, momentum, and matter between the two much larger media. Due to its low thermal conductivity it prevents the underlying, relatively warm ocean of losing heat to the much colder atmosphere during the non-summer seasons. During day time, ice and snow efficiently reflect the short-wave solar radiation, but act as a nearly perfect black body radiator for the long-wave terrestrial radiation during night. Therefore, during summer the sea ice cover reduces the energy absorbed at the surface because of its high albedo compared to seawater. The strong cooling of the atmosphere at the surface stabilises its stratification and, therefore, contributes to a colder local climate by reducing atmospheric convection. The rejection of salt by growing sea ice increases the density of the underlying seawater and, thus, constitutes the initial step for the deep water formation during wintertime. Melting sea ice, however, represents a freshwater input for the ocean and leads to a stabilisation of its surface layers. Averaged over a seasonal cycle, the net freezing rate is different from zero at most locations due to divergence and convergence of the sea ice flow. Therefore, the sea ice drift in combination with freezing and melting processes represents a buoyancy flux for seawater which in turn affects the density structure and the baroclinic flow in the ocean. Because of its impacts on the freshwater flux, its reflecting properties, and the release of latent heat associated with thermodynamic growth, the effects of sea ice for the ocean are similar to those of clouds for the atmosphere.

However, the large sensitivity to climate perturbations is the cause that the sea ice cover plays a dominant role in climate variability and climate change. This large sensitivity can primarily be attributed to the temperature-albedo feedback. That is, an initial surface warming of the polar atmosphere would be enhanced by less reflection of solar radiation due a reduced ice cover. Therefore, and due to the large atmospheric stability in high latitudes, climate models predict under increased greenhouse gas forcing scenarios the

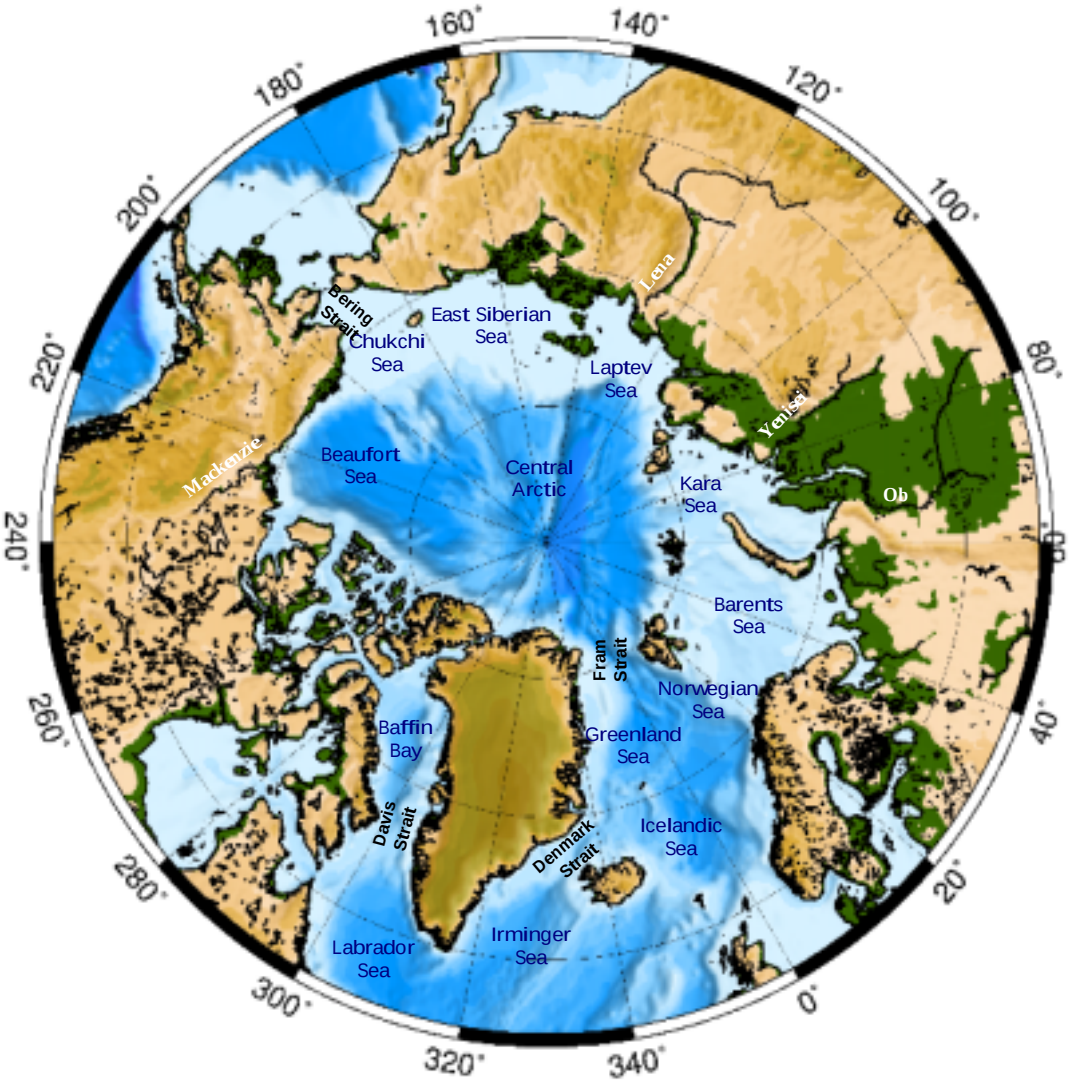

Figure 1.1: The Arctic and its periphery.

largest surface warming in polar regions. A global warming would thus be detectable at an early stage by changes of the sea ice cover.

A global warming is expected because human activities like, for example, the burning of fossil fuels, changing of land-use, and agriculture, have been led to an increase of the major greenhouse gases Carbon dioxide, Methane, and Nitrous oxide by 30%, 145%, and 15%, respectively, compared to their pre-industrial values (prior to 1750). These increases correspond to a direct radiate forcing of the climate system of $2.45\,Wm^{-2}$ [*Houghton*, 1996]. From measurements there is evidence that global mean temperatures have risen by 0.3 to 0.6°C since the late 19th century and that recent years have been among the warmest since instrumental records despite the cooling effect of the Mt. Pinatubo volcanic eruption in 1991. However, at present it is not possible to make very confident statements about the

relative contributions of specific natural and anthropogenic effects on the observed climate change although the changes in global near-surface atmospheric temperatures cannot be readily explained by natural climate variability [*Barnett et al.*, 1999].

Contrary to its importance for climate variability and climate change, the Arctic and its sea ice cover has been one of the worst observed regions on earth (the same holds also for Antarctica). It is only since the last two decades that considerable efforts in observation techniques, i.e. the use of satellites and automatic drifting buoys, have allowed an area-wide monitoring of the ice pack's extent and flow. Whereas the 1995-report of the Intergovernmental Panel on Climate Change (IPCC) [*Houghton*, 1996] has assessed no significant trend of the high latitude sea ice cover, there has been an increased number of studies during the late 1990s indicating a reduction of the Arctic ice pack. During the last year, these reports have also received considerable attention in the newspapers. Satellite based observations have revealed that the overall sea ice area of the Arctic has decreased by about 5% [*Parkinson et al.*, 1999] and its perennial fraction by roughly 14% [*Johanessen et al.*, 1999] since the late 1970s. However, due to the seasonal cycle of ice thickness and the land-locking of the Arctic Ocean, from physical reasoning and from climate model simulations [e.g. *Voss and Mikolajewicz*, 2001] it is expected that in the case of an atmospheric warming first the Arctic ice pack becomes thinner and then its ice covered area decreases. Accordingly, *Rothrock et al.* [1999b] report that the comparison of submarine based ice thickness estimates from the 1960s and 1970s with those of the 1990s revealed a decline by about $1.3\,m$ in some regions of the Arctic Ocean.

However, little is known about the variability of the ice pack and about its long-term averaged properties. Moreover, despite recent observational efforts, very little is known about the spatio-temporal behaviour of the ice volume and the freshwater transports associated with freezing and melting of sea ice. Therefore, the objective of this study is the investigation of the interannual to longer-term variability of the Arctic sea ice cover which helps to determine the variability of these 'non-observables' and to assess the significance of recent observational evidences for a retreat of the Arctic sea ice cover.

The strategy for achieving this goal is as follows: A hind-cast experiment with a state-of-the-art dynamic-thermodynamic sea ice model forced with realistic atmospheric data over the last five decades is performed to produce a dataset of the Arctic ice pack. A comparison with observed sea ice quantities assesses the confidence in the simulation results, whereas the analysis of the model output focuses primarily on the variability of the 'non-observables'. Moreover, by performing idealised simulations the relative contributions of wind and air temperatures to variations of the ice pack on interannual and longer time scales will be assessed. On the basis of the interannual variations revealed by the model, the significance of long-term trends of the simulation will be evaluated.

According to this strategy the thesis is organised as follows: Chapter 2 gives a short description of the applied sea ice model and of the forcing data used for the model integrations. Primarily as a basis for further analyses, Chapter 3 presents the long-term mean state of the major simulated sea ice variables. Chapter 4 describes the interannual variability of ice extent, ice thickness, and sea ice transports and investigates possible links to dominant modes of atmospheric variability, such as the Arctic/North Atlantic Oscillations. In Chapter 5, long-term trends of individual sea ice quantities are analysed and related to long-term changes of surface air temperature and the wind field. Chapter 6 completes the thesis with a final discussion. For a better readability of this thesis, each chapter, and also each section of Chapter 4, includes a separate introduction as well as a

conclusion and discussion of its main results.

Chapter 2

Model Description and Analysis Methods

2.1 Introduction

The aim of this chapter is to introduce the basic features of the numerical and statistical methods used throughout this study. In particular, the sea ice model which was applied to generate the data basis for this study as well as details of the model integrations are introduced. Furthermore, some statistical methods applied for the analysis of the model data are outlined.

2.2 The Sea Ice Model

In order to simulate the sea ice cover of the Arctic Ocean a dynamic-thermodynamic sea ice model forced with realistic atmospheric data is used. The sea ice model is based on the fundamental work of *Hibler* [1979] regarding the dynamics and that of *Parkinson and Washington* [1979] regarding the thermodynamics. In particular, the model used in the present study is that of *Harder* [1996] and represents an optimised version of the viscous-plastic approach proposed by *Hibler* [1979]. It was developed by the Sea Ice Model Intercomparison Project of the Sea Ice - Ocean Modeling Panel of the Arctic Climate System Study under the World Climate Research Programme [*Harder*, 1997; *Kreyscher et al.*, 1997, 2000; *Lemke et al.*, 1997]. In this section the main features of the model are introduced and details of the experimental design of the model integrations are given.

2.2.1 Model Physics

As the fundamental assumption of the model the sea ice cover is considered as a two-dimensional continuum described by the main properties mean ice thickness h describing the ice mass per unit area, ice concentration A describing its areal coverage, and ice drift $\mathbf{u}$. Thus, the temporal evolution of the ice cover can be described by balance equations of the following type:

$$\frac{\partial E}{\partial t} + \nabla \cdot (\mathbf{u}\, E) = S_E \tag{2.1}$$

where E represents the prognostic quantities h or A. That is, the local changes of these quantities depend on the convergence of their mass fluxes $-\nabla \cdot (\mathbf{u}\, E)$ as well as on a thermodynamic source and sink term S_E.

The thermodynamic evolution of sea ice is in general described by an energy balance of the oceanic mixed layer following *Parkinson and Washington* [1979]. That is, in the absence of sea ice (initial state) the net heat flux $Q_n = Q_a + Q_o$ into the mixed layer leads to a change of its temperature depending on the atmospheric heat flux Q_a and the heat flux from the deep ocean Q_o. The evolution of the mixed layer temperature is described by an implemented one-dimensional mixed layer model [*Lemke*, 1987] with a fixed mixed layer depth. If the mixed layer cools down to the freezing point of sea water its temperature remains fixed at this value and the energy budget is balanced by the release of latent heat due to freezing of sea ice. In general, in the presence of sea ice the energy budget is balanced by freezing or melting of sea ice according to $Q_a + Q_o + \rho_i L_i S_h = 0$, where ρ_i is the density of sea ice, L_i is the specific heat of fusion for sea ice, and $S_h = \partial h/\partial t$ represents the change of the mean ice thickness of the grid cells (ice volume per grid cell area). The atmospheric heat flux at the top of the ice surface or of the mixed layer (if sea ice is absent)

$$Q_a = Q_h + Q_l + R_{s,\downarrow} + R_{s,\uparrow} + R_{l,\downarrow} + R_{l,\uparrow} \tag{2.2}$$

consists of the turbulent fluxes of sensible and latent heat (Q_h and Q_l respectively), the incoming and outgoing short-wave radiative fluxes ($R_{s,\downarrow}$ and $R_{s,\uparrow}$ respectively), and the incoming and outgoing long-wave radiative fluxes ($R_{l,\downarrow}$ and $R_{l,\uparrow}$ respectively). The conductive heat flux through the ice is described by the zero-layer approach of *Semtner* [1976]. That is, heat storage within the ice is neglected and the heat conduction depends on the actual ice thickness within a grid box $D = h/A$ as well as on the temperature difference between bottom and top of the ice according to

$$Q_c = A\, \kappa_i\, \frac{(T_b - T_t)}{h} \qquad . \tag{2.3}$$

Here, T_b and T_t denote the temperatures at the bottom and the top of the ice and κ_i is its thermal conductivity. To account for different thicknesses of individual ice floes within a grid cell, the thermodynamic calculations are performed separately for open water and seven ice thickness categories following *Hibler* [1984], assuming a uniform distribution of ice thickness D between zero and twice the mean ice thickness h of the individual grid cells.

To account for its reflective and isolating effects a prognostic snow layer according to *Owens and Lemke* [1990] is also included. The evolution of the snow layer is determined from an additional balance equation like Eq. 2.1 with the mean snow thickness h_s as the prognostic quantity. The source of snow is the prescribed precipitation rate. However, only precipitation over ice and snow covered grid cells with surface air temperatures below freezing is assumed to add to the snow layer. Snow melt depends on the same energy balance as described for the ice surface (Eq. 2.2). Note, that the effects of snow for the energy balance are represented by different albedo values affecting $R_{s,\uparrow}$ and a different thermal conductivity which modifies Q_c (see, e.g., *Semtner* [1976]). It is assumed, that the snow cover has to be melted totally before the ice is melting. Besides its effects on the thermal conductivity, this assumption has profound effects on the albedo of the surface

(see Tab. 2.1). Because the albedo strongly depends on the properties of the surface the model also distinguishes between melting and freezing snow and ice, respectively.

The source and sink term of the areal coverage of sea ice S_A depends, besides the thermodynamic ice growth (G_h) or ice melt (M_h), on the actual ice concentration and on the mean ice thickness of the individual grid cells as well as on a dynamically contribution due to shear. After *Hibler* [1979] these processes are empirically parameterised by

$$S_A = \frac{1-A}{h_0} G_h + \frac{A}{2h} M_h + Q_A \tag{2.4}$$

with the open water fraction $(1-A)$, the lead closing parameter h_0 and the shear contribution term Q_A. The physical interpretation of Eq. 2.4 is that under freezing conditions ($G_h = max(S_h, 0) \geq 0$) the ice concentration increases depending only on the open water fraction. Note that h_0 is a constant, empirically derived parameter. Under melting conditions ($M_h = min(S_h, 0) \leq 0$) the rate of decrease of A is controlled by both the actual ice covered portion of the grid cell and its mean ice thickness. That is, the areal fraction of thin ice decreases more rapidly under melting conditions than that of thick ice whereas the thermodynamic increase is only controlled by the open water area. The Q_A term of Eq. 2.4 represents a change of the areal ice coverage due to shear strength which primarily simulates winter openings of the ice pack. See *Harder* [1994, 1996] for a detailed description of this term.

The evolution of the sea ice drift $\mathbf{u}$ is in general determined from the momentum balance

$$m \frac{D\mathbf{u}}{Dt} = \tau_\mathbf{a} + \tau_\mathbf{w} - mf\mathbf{k} \times \mathbf{u} + \mathbf{F_i} - mg\nabla H \tag{2.5}$$

with the atmospheric and oceanic drags $\tau_\mathbf{a}$ and $\tau_\mathbf{w}$ respectively, the Coriolis force $-mf\mathbf{k}\times\mathbf{u}$ ($\mathbf{k}$ is the unit vector normal to the surface) depending on ice mass per unit area m and on the Coriolis parameter f, the internal forces $\mathbf{F_i}$, and the force due to the sea surface tilt $-mg\nabla H$ where g denotes the gravitational constant and H the sea surface dynamic height. *Harder* [1996] has shown that for time scales not shorter than one day the inertial term $m\,D\,\mathbf{u}/D\,t$ on the left hand side of Eq. 2.5 is 2 to 3 orders of magnitude smaller than the other forces acting on the ice pack [see also *Steele et al.*, 1997]. Therefore, the inertial term is neglected and $\mathbf{u}$ can be solved diagnostically. The atmospheric and oceanic drags are described according to boundary layer theory [*McPhee*, 1979] and the sea surface tilt is derived from the ocean current via geostrophy. The internal forces $\mathbf{F_i}$

Table 2.1: Albedo values for different surface types after *Perovich et al.* [1986]. Surface types are classified as melting snow or melting ice if snow or ice are present and the surface temperature is 0°C.

	Open Water	Melting Ice	Dry Ice	Melting Snow	Dry Snow
Albedo	0.10	0.68	0.70	0.77	0.81

are calculated as the divergence of the stress tensor which in turn is related to the ice velocity field by a viscous-plastic rheology according to *Hibler* [1979]. That is, the sea ice model accounts for shear and compressive deformation, but shows no resistance against divergent ice drift. Moreover, the bulk and shear viscosities as well as the ice pressure are non-linear functions of the ice thickness and ice concentration. For normal strain rates the ice behaves as a plastic material whereas it shows viscous behaviour for very small strain rates. A detailed description of the rheology scheme is given in *Harder* [1996], *Kreyscher* [1998], and *Kreyscher et al.* [2000]. Moreover, *Kreyscher et al.* [2000] gives a comparison of the viscous-plastic rheology with other constitutive laws used in dynamic sea ice models.

2.2.2 Model Grid

For numerically solving of the model equations these are discretised in space and time. That is, derivatives are represented by finite differences. Details of the numerical implementation of the sea ice model equations are given in *Hibler* [1979] and *Zhang and Hibler* [1997].

Using a daily time step the model equations are solved on a staggered Arakawa B-grid [see e.g. *Mesinger and Arakawa*, 1976] with a horizontal resolution of $1^\circ \times 1^\circ$. The model domain (Fig. 2.1) covers the entire Arctic and extents southward to about 55°N on the Atlantic side. Thus, it includes the Greenland/Irminger/Norwegian (GIN) Seas as well as the Baffin Bay and the northern part of the Labrador Sea (see also Fig. 1.1). To avoid a singularity at the North Pole and to minimise the distortion of the shape of the grid cells from ideal squares the model grid was rotated with regard to the geographical coordinate system. The model's north pole is rotated into the Indian Ocean at 0°N and 60°E in geographical coordinates such that the model equator runs through the geographical North Pole and matches the geographical meridians 30°W and 150°E. At this configuration the horizontal resolution corresponds to roughly $110\,km$. Outflow cells with natural outflow condition are defined at the Bering Strait and along the Atlantic border of the model domain.

2.2.3 Forcing Data

The forcing of the model consists of explicitly prescribed atmospheric and oceanic quantities which affected the fluxes of energy, momentum, and matter. The fluxes themselves are not explicitly prescribed, because they are also significantly affected by the evolving sea ice cover. According to the time step of the model, the forcing quantities are prescribed daily at each grid point of the model domain.

The atmospheric forcing variables wind, temperature, humidity, cloud cover, and precipitation rate are derived from reanalysis products of both the European Centre for Medium-Range Weather Forecasts (ECMWF) [*Gibson et al.*, 1997] and the collaborative effort of the National Center for Environmental Prediction (NCEP) and the National Center for Atmospheric Research (NCAR) [*Kalnay et al.*, 1996]. Especially for the investigation of variability these data products have the advantage of being gridded data sets not affected by artificial changes due to changes of the analysis schemes. That is, the reanalysis data are temporally consistent with regard to analysis techniques. The effects of changes of the analysis system as apparent in operational products are shown by, e.g. [*Harder et al.*, 1998, their Fig. 1]. There, the time series of the 2-m air temperature of the North Pole derived from ECMWF operational analyses for the period 1986–92 is

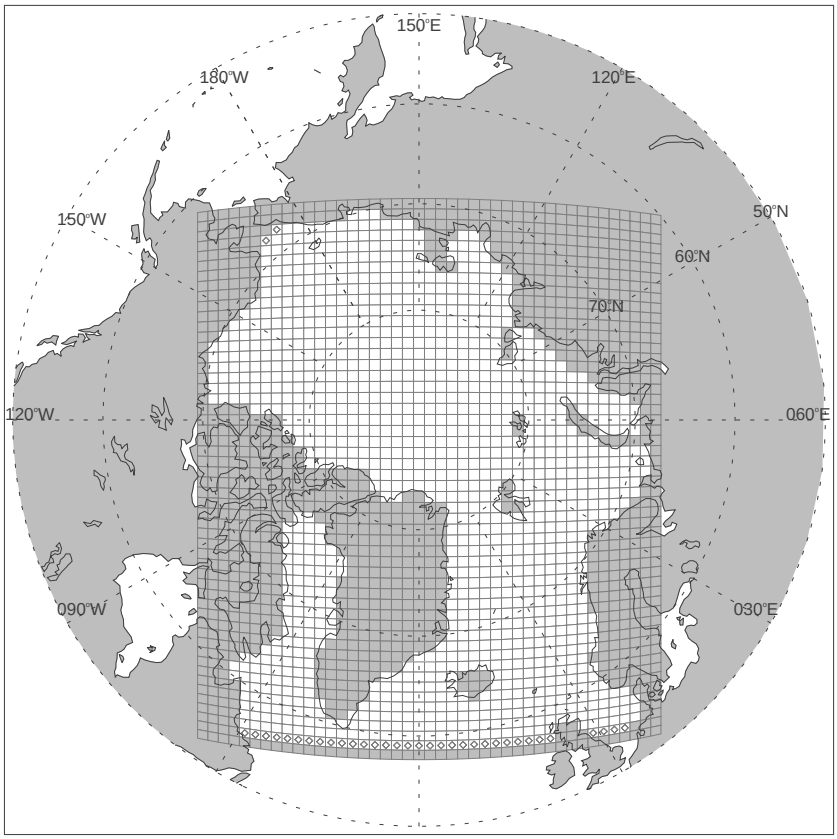

Figure 2.1: Model grid for scalar variables. The squares denote the grid cells which are represented by the scalar variables. The scalar variables themselves are defined at the centre of each grid cell. The non-shaded cells mark those of open water in which sea ice can be formed. The rhombuses denote outflow cells.

shown. Because climatological monthly mean temperatures were prescribed over sea ice surfaces, the daily 2-m temperatures in those regions are basically constant within each month, with artifical steps up to 10°C at the beginning of the each new month [see also *Martin and Munoz*, 1997]. Moreover, the mean summer temperatures during the melting period decreased from about 0°C in 1986 to unrealistic −2°C in 1992 in this data set. Although such problems are not apparent in the reanalysis products, the reanalysis data are still affected by temporal differences in both the number and quality of the available observations included in the data assimilation systems. In comparison to gridded data sets derived from direct observations, an important advantage of reanalysis data is, that in regions lacking measurements, data are 'dynamically' interpolated due to the incorporation of numerical weather prediction models into the analysis schemes. However, the magnitude of this advantage in turn depends on the quality of those models.

The NCEP reanalysis is an intermittent data assimilation system performed with a

T62 model with 28 vertical sigma levels whereas for the ECMWF reanalysis a T106 model with 31 vertical levels was used. Moreover, the assimilation systems consist of a statistical interpolation procedure which is also different in both reanalyses (see *Kalnay et al.* [1996] and *Gibson et al.* [1997] respectively). The output of both data sets is 6-hourly and covers for the NCEP data the period 1948–present (for this study data from 1948–99 are used) and for the ECMWF data the 15-year time interval from 1979 to 1993 (ERA-15 hereafter).

a) Interannual Atmospheric Forcing

As interannual forcing of the model the 10-m winds and 2-m air temperatures (SAT) derived from the NCEP/NCAR reanalysis are used. That is, only winds and temperatures are prescribed daily over the entire period of 1948–99. The main reason for choosing the NCEP/NCAR data is the considerably longer time period covered by this data set (51 years) compared to that of the ERA-15 (15 years). However, a second but not unimportant reason is that the ERA-15 SATs still show a summer mean temperature not exceeding $-1.8°C$ which is the freezing temperature of seawater rather than the melt temperature of desalinated sea ice [*Rigor et al.*, 2000]. Therefore, without any corrections, the ERA-15 temperatures are not suitable to force sea ice models. From a comparison with temperature observations of Soviet North Pole Drifting stations *Martin and Munoz* [1997] found a good agreement between the NCEP/NCAR SATs and the available direct observations within the Arctic. Only during the summer months there is less agreement because the NCEP/NCAR SATs do not show the observed variance during that time and are rather constant. From a comparison of statistical parameters like, e.g., variance, mean, and amplitude of the seasonal cycle, *Hilmer* [1997] found also a good agreement between the NCEP/NCAR data and observations of North Pole drifting stations reported by *Colony et al.* [1992].

The wind field data, which affect both the momentum balance and the turbulent heat fluxes in the model, have not yet been focus to a systematic validation. However, no major errors are expected in the Arctic because there is a sufficient coverage with direct surface pressure observations from coastal land stations and automatic drifting buoys within the ice pack. However, problems have been reported for the Antarctic [*Windmüller*, 1997] regarding the lack of topography induced southerly winds in the western Weddell Sea. This has been attributed to a poor representation of the topography of the Antarctic Peninsula in the reanalysis due to the rather coarse resolution of the incorporated numerical weather prediction model. Therefore, uncertainties of the surface winds near Greenland are also possible.

b) Climatological Atmospheric Forcing

In contrast to the modelling studies of *Harder et al.* [1998], *Hilmer et al.* [1998], and *Kreyscher et al.* [2000] atmospheric forcing data for total cloud coverage, near surface atmospheric humidity, and precipitation rate are derived from the ERA-15 and are prescribed as spatially varying, climatological seasonal cycles. That is, for each grid point and every day of the year the long-term mean value of the corresponding ERA-15 data is prescribed to the model. These quantities are derived from the ERA-15 instead of the NCEP/NCAR reanalysis because of significant deficiencies of these parameters in the NCEP/NCAR data set.

Due to a moisture diffusion parameterisation derived for the mid-latitudes, the NCEP/-NCAR reanalysis exhibits a spurious wave pattern in the fields of precipitation (P) and evaporation/sublimation (E) [*Cullather et al.*, 2000]. That is why the specific humidities derived from the NCEP/NCAR reanalysis data show partly unrealistic values in high latitudes which significantly affect the magnitude and direction of the long-term averaged latent heat flux at the ice surface when used as forcing of the sea ice model [*Hilmer*, 1997]. Because of these problems, *Hilmer et al.* [1998], *Kreyscher* [1998], and *Kreyscher et al.* [2000] used mean annual cycles of relative humidity derived from the ECMWF operational analyses for the period 1986–92 as forcing of their model integrations. Here, from the 2-m air temperatures and 2-m dew point temperatures of the ERA-15 an averaged seasonal cycle of relative humidity was derived and prescribed to the model. Using the current air temperatures the relative humidity is subsequently transformed by the model into specific humidity for the parameterisation of the latent heat flux [*Smith*, 1998] and into water vapour pressure for that of the incoming short-wave radiation [*Zillmann*, 1972].

The precipitation rates, which are needed for the evolution of the prognostic snow layer, are also derived from the ERA-15. From a comparison of the reanalysis products with climatologies based on North Pole drifting station data *Serreze and Hurst* [2000] found that both reanalysis products capture the major spatial features of the annual mean precipitation of the Arctic but that the ERA precipitation field looks decidedly better.

For the parameterisations of the incoming solar [*Zillmann*, 1972; *Laevastu*, 1960] and the downward long-wave [*König-Langlo and Augstein*, 1994] radiative fluxes total cloud fractions are needed. These were also derived from the ERA-15 data because they show a much closer correspondence with the observations than those from the NCEP/NCAR data [*Walsh and Chapman*, 1998]. In particular, the latter do not show the observed seasonality. The cloud coverage, however, is important for the high latitude surface energy balance because it reduces the long-wave radiative heat loss during the winter seasons when nearly no solar insulation is apparent. *Walsh and Chapman* [1998] estimated that during September-March the cloud-radiative forcing is positive with magnitudes of 20-30 Wm^{-2}.

c) Oceanic Forcing

The oceanic forcing of the model consists of the heat fluxes from the deep ocean into the mixed layer and of the ocean current speeds. In particular, spatially varying patterns of annual mean ocean currents and a mean annual cycle of the oceanic heat fluxes derived from a coupled sea ice-ocean model integration [*C. Köberle*, AWI Bremerhaven, pers. Comm.] is used. The oceanic heat fluxes in the central Arctic Ocean exhibit magnitudes of about $2\,Wm^{-2}$ in all seasons, but can become significantly larger in the adjacent Atlantic areas with largest magnitudes of about $400\,Wm^{-2}$ in the Norwegian Sea during winter. It is important to note for the further analysis, that due to this forcing oceanic effects cannot directly influence the variability of the simulated the ice cover but do significantly affect its long-term mean properties. However, because observed fields of weekly Sea Surface Temperature (SST) and sea ice extent are prescribed to the NCEP/NCAR reanalysis they would have affected their SATs. Therefore, oceanic variations are implicitly included into the present sea ice model integration via the prescribed NCEP/NCAR SATs.

2.2.4 Experimental Design

In order to get an initial condition for the model integrations discussed in the remainder of this study a spin-up integration was performed first. For this spin-up integration the model starts with an ice-free ocean and a prescribed spatially constant mixed-layer temperature near the freezing point of seawater. As atmospheric forcing the fields of wind and SAT of the first year of the NCEP/NCAR data set, that is 1948, were used. In order to reach a near equilibrium state this forcing was repeatedly prescribed for 500 years and the results of this integration were stored as initial fields for the subsequent model runs. However, the ice pack in real nature would have been different from the equilibrium field obtained after the spin-up integration because it was also affected by the atmospheric conditions prior to 1948. In order to account for these effects, the first 2 years (1949/50) of the subsequent integrations were excluded from the analyses carried out in the remainder of this study which, therefore, focus on the period 1951–99.

Starting from the initial condition obtained by the spin-up procedure three different model integrations were performed differing only in the forcing of winds and SATs. That is, besides a standard simulation, two additional integrations with idealised forcings were carried out in order to investigate the separate effects of interannual variability of either winds or SATs only. The first integration, considered as the standard run, used both wind and temperature forcing over the entire NCEP/NCAR reanalysis period 1949–99. The the second integration (TEMP hereafter) was forced with SATs over the period 1949–99 as in the standard run, but with the daily wind fields of 1949 only which were repeatedly prescribed (periodic forcing). The third integration (WIND hereafter) used the wind fields of 1949–99 as in the standard run, but the repeatedly prescribed daily SAT fields of 1949 as atmospheric forcing of the model.

The advantage of using periodic forcing with daily fields of a single year for the idealised simulations instead of a climatological mean annual cycle is primarily the prevention of problems which arise when using averaged wind vectors. That is, by averaging of the wind field the associated wind speeds are reduced, thus affecting both the turbulent heat fluxes and the dynamics. The disadvantage, on the other hand, is that the atmospheric conditions of an individual year does not represent its long-term averaged properties. To test whether the choice of the individual year used as periodic forcing significantly affect the simulated interannual variability six additional idealised integrations using wind or SAT fields from 1958, 1986, and 1970 were carried out similar to WIND and TEMP. Subsequently, the statistical properties of the annual mean time series of quantities which are considered as important for the analyses of the remainder of this study, that is total sea ice volume, ice area, and ice volume export through Fram Strait, were compared. Although there are differences between the corresponding long-term averages and variances the interannual variability of those integrations is very similar. That is, the correlations between the time series of the specific simulations are large with lowest values for the total sea ice volume of $r = 0.95$, for the sea ice area of $r = 0.89$, and for the ice export of $r = 0.94$. Summarising it can be stated that the choice of the year for the periodic forcing is not important for the interannual variability.

2.3 Analysis Methods

Although the time step of the model is one day and the model output is stored at this temporal resolution the subsequent analyses deal primarily with monthly and annual averages. For the analyses of the, at least monthly averaged, model output and for the determination of relations between the simulated sea ice quantities and the atmospheric forcing data statistical analysis methods are applied. Among rather common methods like, e.g. correlation analysis, some more advanced techniques are used and will shortly be sketched below.

2.3.1 Associated Regression Patterns

The purpose of this method is finding a typical pattern $\mathbf{p}$ of a vector time series $\mathbf{y_t}$ (time depending spatial patterns, e.g. patterns of annual mean SATs or SLPs) which are associated with anomalies of a specified index time series x_t (e.g. annual mean ice exports). The basic assumption of this method is a linear relation between x_t and elements of $\mathbf{y_t}$ according to

$$\mathbf{y_t} = \mathbf{p}\,\tilde{x}_t + noise \tag{2.6}$$

with $\tilde{x}_t$ being the normalised anomaly time series of x_t according to $\tilde{x}_t = (x_t - \mu_x)/\sigma_x$, where μ_x denotes its mean value and σ_x its standard deviation. The normalisation of x_t ensures that $\mathbf{p}$ has the same magnitudes as the vector time series $\mathbf{y_t}$. Therefore, the pattern $\mathbf{p}$ can be considered as the typical anomaly pattern of the quantity $\mathbf{y_t}$ which is linearly associated with a positive anomaly of x_t of one standard deviation in magnitude. In particular, $\mathbf{p}$ consists of slopes of the linear regressions between the normalised index time series $\tilde{x}_t$ and the individual time series of $\mathbf{y_t}$. The statistical significance of $\mathbf{p}$ can be assed by testing the individual regression slopes using standard procedures. For a more detailed description of associated regression patterns see, e.g., *von Storch and Zwiers* [1999].

2.3.2 EOF Analysis

Empirical Orthogonal Function (EOF) analysis aims to identify a set of anomaly patterns $\mathbf{e}^i$ which explain most of the variance structure of a vector time series $\mathbf{y}_t$ (for a detailed description see, e.g. *von Storch and Zwiers* [1999]). In particular, the $\mathbf{e}^i$ represent the Eigenvalues of the covariance matrix of $\mathbf{y}_t$. The $\mathbf{e}^i$ form an orthonormal set of vectors with $\mathbf{e}^1$ explaining most of the variance of $\mathbf{y}_t$, $\mathbf{e}^2$ explaining most of the remaining variance, and so forth. By projecting the $\mathbf{e}^i$'s onto the original anomalous vector time series $\mathbf{y_t}$ a so-called Principal Component (PC) time series $\alpha_t^i = \langle \mathbf{y}_t, \mathbf{e}^i \rangle$ is obtained which can be considered as weights of the $\mathbf{e}^i$. In other words, the i-th PC time series describes the strength at which the associated anomaly pattern $\mathbf{e}^i$ is present in the original anomalous vector time series at a given time.

Throughout the remainder of this study, the first EOF will be called the 'first mode' of the variability (first EOF mode) of $\mathbf{y}_t$ consisting of a pattern E1[$\mathbf{y}_t$] and an associated expansion time series PC1[$\mathbf{y}_t$]. Moreover, both the patterns and the PCs of the EOFs are normalised in such a way that the magnitudes of the $\mathbf{e}^i$'s are comparable to those of $\mathbf{y}_t$.

Note that EOFs are designed to explain variance rather than to describe 'coherent structures'. If the latter is desired, as, for instance, for the analysis of dominant modes of

drift patterns, then the correlation matrix has to be used instead of the covariance matrix [*von Storch*, 1995]. Moreover, for the EOF analysis of ice drift variability a so-called 'combined EOF' method will be applied. That is in general, two vector time series $\mathbf{x}_t$ and $\mathbf{y}_t$ of the size M and N respectively (but of the same length in the time domain) are added together to form a vector time series $\mathbf{z}_t$ of the size $M + N$ which is then subject to the same analysis as described above but using the correlation matrix. The resulting $\mathbf{e}^i$'s are decomposed in the same way as both vector time series were added together. In the particular case of sea ice drift, the vector time series (or, in other words, time depending patterns) of both drift components are added together.

2.3.3 SVD Analysis

The Singular Value Decomposition (SVD) analysis is a statistical tool aimed to define dominant anomaly patterns of two different vector time series $\mathbf{x}_t$ and $\mathbf{y}_t$ which explain maximum covariability between both datasets (for a detailed description see *Bretherton et al.* [1992]). In practice, this method contains a SVD decomposition (in the sense of the fundamental matrix operation) of the temporal cross-covariance matrix defined by the two vector time series. It results in orthogonal pairs of patterns $\mathbf{p}^i$ and $\mathbf{q}^i$ that explain as much as possible of the mean-squared temporal covariance between the two fields. In particular, the first pair explains most of the covariance between $\mathbf{x}_t$ and $\mathbf{y}_t$, the second pair most of the remaining covariance, and so forth. As for the EOFs, the projection of these patterns onto their corresponding anomalous vector time series yields associated expansion time series $\beta_t^i = \langle \mathbf{x}_t, \mathbf{p}^i \rangle$ and $\gamma_t^i = \langle \mathbf{y}_t, \mathbf{q}^i \rangle$ which, similar to the PCs of the EOFs, can be considered as time dependent weights of the $\mathbf{p}^i$ and $\mathbf{q}^i$.

Also similar to the EOF analysis, the first pair of singular vectors together with their associated expansion time series will be called the 'first mode' of covariability between $\mathbf{x}_t$ and $\mathbf{y}_t$ (first SVD mode) and are denoted in the remainder of this study as S1[x,y]. In contrast to *Bretherton et al.* [1992], in the present study the singular vectors themselves will be considered instead of correlation maps (see *Bretherton et al.* [1992]). Moreover, the associated expansion time series β_t^i and γ_t^i are normalised by their standard deviations. The singular vectors $\mathbf{p}^i$ and $\mathbf{q}^i$, on the other hand, are multiplied by the standard deviations of their associated expansion time series in order to obtain magnitudes which are comparable with those of the original vector time series.

Chapter 3

Simulated Mean State

3.1 Introduction

Until the end of the 19th century the myth of an unfrozen "Open Polar Sea" has been alive. For example, in 1878 the German geographer *A. Peterman* stated, "the central area of the polar regions is more or less free from ice" [*Guttridge*, 1988]. One year later, in 1879, the JEANETTE expedition had finally destroyed this myth when the ship was captured by pack ice in the vicinity of Wrangel Island. This expedition was also the first pointing to the drifting nature of the Arctic ice pack. Locked in the ice the JEANETTE drifted within two years from Wrangel Island to the New Siberian Islands where it was crushed by the ice and sank in 1881. Three years later, some items of one of JEANETTE'S crew members were found on an drifting floe at the shore of south-west Greenland [*Vaughan*, 1994]. With the North Pole in his mind, it was the JEANETTE expedition which inspired *F. Nansen* to undertake a drift voyage within the ice pack with his research vessel FRAM. Starting from the New Siberian Islands in 1893 the FRAM arrived north of Spitsbergen in 1896 (Fig. 3.1) and provided the first detailed view of Arctic ice pack.

Today, our knowledge about the large-scale characteristics of the Arctic ice pack has significantly increased but is still far from complete. The scientific investigation of Arctic sea ice began in May 1937 when the first drifting ice station NP-1, headed by *I.D. Papanin*, was set up by the Soviets near the North Pole. From 1950 onward it was followed by a number of manned research stations established on various floes within the ice pack. Figure 3.1 shows the trajectories of some of these early drift stations. Since 1979, the spatial pattern of Arctic sea ice motion is determined by a number of automatic data buoys deployed under the patronage of the International Arctic Buoy Programme (IABP). By interpolating all available data beginning with the FRAM drift *Colony and Thorndike* [1984] derived the mean field of sea ice motion (Fig. 3.2). The major features of this pattern are the anticyclonic motion in the western Arctic known as the Beaufort Gyre and the linear drift of ice from the Eurasian coast to Fram Strait which is called the Transpolar Drift Stream (TPDS). A back-trajectory analysis of the buoy data [*Pfirman et al.*, 1997] has revealed that it takes about three years for an ice floe originating in the Beaufort Sea to drift into the Laptev Sea, and that it takes a further three years to exit the Arctic through Fram Strait. Today, the most advanced technique for observing the field of sea ice motion is the tracking of brightness temperature patterns obtained by satellite based passive microwave sensors [e.g., *Agnew et al.*, 1997; *Kwok et al.*, 1998; *Martin and Augstein*, 2000]. At a temporal resolution of about 3 days this technique provides nearly

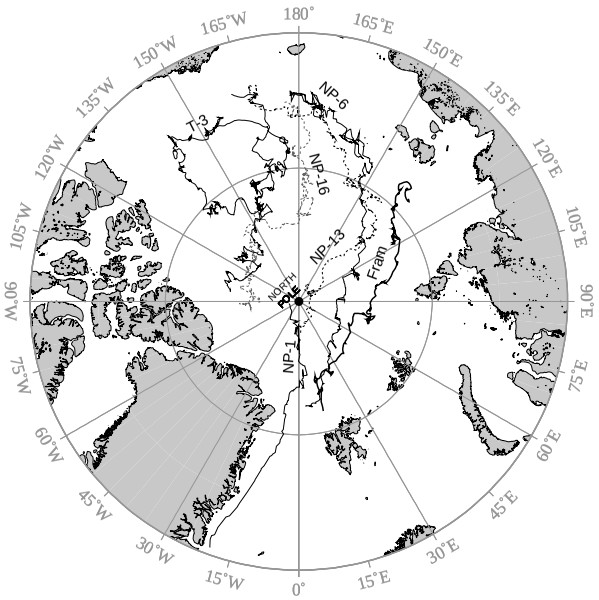

Figure 3.1: Early explorations of the Arctic sea ice motion. Shown are the drift trajectories of the Fram (1893–1896), the soviet drift stations NP-1 (1937-1938), NP-6 (1956-1959), NP-13 (1964-1967), NP-16 (1968-1972), as well as the drift track of the US Ice Island T-3 (1961-1971). (Courtesy, *T. Martin*, IfM, Kiel)

complete fields of ice drift vectors at a resolution of about $100\,km \times 100\,km$.

Prior to the application of remote sensing to the ice drift the passive microwave imagery has already proved to be an excellent tool in continuously observing the sea ice concentration, and, thus, in monitoring the sea ice extent [e.g., *Parkinson et al.*, 1987; *Comiso et al.*, 1997; *Cavalieri et al.*, 1999]. Before the era of satellite remote sensing, information about sea ice concentration was recorded in ice charts by various national agencies. A collection of these ice charts forms an ice concentration data set for the period 1953–1977 [*Walsh and Johnson*, 1979a]. Thus, as for the sea ice drift, there is good information about the areal coverage of sea ice to define the present-day mean state as well as the mean annual cycle of the Arctic sea ice extent and its interannual variability.

Unfortunately, far less is known about the ice thickness. First measurements of Arctic basin sea ice thickness carried out by *F. Nansen* and, later, by Soviet expeditions revealed magnitudes of 3.1 to $3.8\,m$ within the TPDS and maximum values for non-ridged sea ice between 3.0 and $5.0\,m$ [*McLaren et al.*, 1990, and references therein]. However, there exist only a limited number of observations to define its large-scale spatial pattern. Beginning in 1958 with the voyage of USS Nautilus, sea ice draft[1] measurements of some under-ice submarine cruises have been published [e.g., *LeSchack*, 1980; *McLaren*, 1989; *McLaren et al.*, 1992; *Bourke and McLaren*, 1992; *Wadhams*, 1997]. Analysing submarine sonar data from four of these cruises during 1960–1977, *LeSchack* [1980] made the first attempt to construct a map of Arctic sea ice thickness (Fig. 3.3). This map shows increasing thick-

[1]The ice draft denotes the submerged portion of ice below sea level. Given the physical properties of snow, sea ice and sea water it can be converted into the entire thickness of the ice sheet. Ice drafts are provided by under-ice sonar technique mounted on submarines or oceanographic moorings.

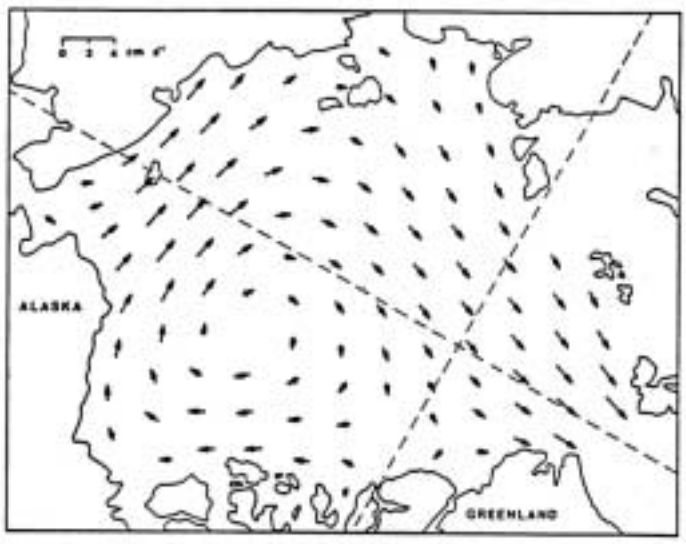

Figure 3.2: Climatological mean pattern of observed Arctic sea ice motion. The arrows show the interpolated motion field based on data from manned drift stations and automatic data buoys for the period 1893–1982 (research stations: 1893–1972; automatic buoys: 1979–1982). (From *Colony and Thorndike* [1984]).

ness from the Eurasian shelves towards the Canadian coast with the thickest ice located north of Greenland and the Canadian Archipelago. Using an extended data set containing 12 cruises between 1958 and 1978 *Bourke and McLaren* [1992] calculated seasonal maps of mean ice thickness and ice roughness which confirmed these findings. Other attempts to measure the large-scale characteristics of ice thickness like, for instance, acoustic tomography [*Jin et al.*, 1993], the analysis of wave propagation in the ice pack, or satellite altimetry, are still under development [*S. Laxon*, pers. comm.; *Wingham*, 1999].

Although there has been a large increase of the knowledge about the Arctic ice pack there are still some of its properties which cannot, at least sufficiently, be deduced from the present-day observational basis. That is, among others, the total sea ice volume, the net freezing rate, or the sea ice volume transports through the major straits connecting the Arctic with the adjacent seas. Using the available observations for validation, numerical sea ice models can provide further information about the nature of the Arctic ice pack. One of the first large-scale numerical sea ice models was presented by *Parkinson and Washington* [1979]. With simplified dynamics and using annual mean forcing data their simulation produced a reasonable ice extent but an unrealistically, nearly zonal symmetric ice thickness pattern for the Arctic. *Hibler* [1979, 1980] investigated the effects of ice dynamics and thermodynamics on ice thickness by coupling both in a dynamic-thermodynamic sea ice model. Integrated over a seasonal cycle for the period 1962–1963 the model produced a realistic drift pattern showing the features which are known from the analysis of buoys and drift station data (see Fig. 3.2). In agreement with submarine data (see Fig. 3.3) but in contrast to the results of *Parkinson and Washington* [1979] his model integration showed a pronounced ice buildup along the Canadian Archipelago with ice exceeding $6\,m$. From a 39-year integration with realistic daily wind forcing *Flato* [1995]

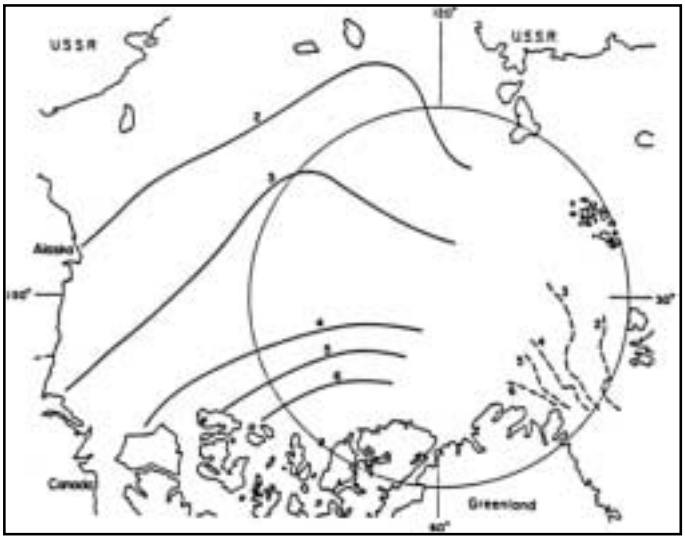

Figure 3.3: Climatological mean pattern of observed Arctic sea ice thickness. The contours are based on submarine sonar data [*LeSchack*, 1980] for the period 1960–1977 (solid contours: summer 1960, summer 1962, and winter 1960; dashed contours: April 1977). (From *Hibler* [1980]).

has shown that this ice buildup is a persistent feature of the ice thickness pattern in a long-term context. Moreover he found substantial decadal scale changes of ice thickness in other regions of the Arctic, especially in the East Siberian Sea. An important and less verifiable result of these numerical simulations is that the annual net production of sea ice is dominated by the North Slope and Siberian near-shore regions. There, on average, offshore ice advection creates open water and thinner ice. This feature has been confirmed by a number of recent modelling studies. Using more advanced forcing data *Harder et al.* [1998] and *Hilmer et al.* [1998] have shown that maximum annual mean growth rates reach magnitudes of about $1.5\,m/year$ off the Siberian coast. Maximum melting of sea ice occurs in the Greenland and Irminger Seas at annual mean melt rates, which locally exceed $3\,m/year$. Thus, numerical models have shown, that there is a net transport of sea ice from the Eastern Arctic to the North Atlantic on a route which was already indicated by the early expeditions of Jeanette and Fram.

This chapter is aimed to present the mean state of the sea ice model integration at $1^\circ \times 1^\circ$ horizontal resolution forced with roughly half a century of realistic atmospheric data. Mean values as well as mean annual cycles of some of the major quantities of the model are discussed. On the one hand this chapter can be considered as a further contribution to enhancing the knowledge about the mean features of the Arctic ice cover. Since this study primarily deals with the variability of the ice pack, this chapter gives a reference to most of the anomalies considered later on. Not attempting a comprehensive validation, some of the results will be compared with observational data to give an impression of the model's quality. A detailed validation of the model used in this study is already given by *Kreyscher* [1998] and *Kreyscher et al.* [2000].

3.2 Sea Ice Concentration

Since nearly three decades, the ice concentration has been routinely observed by satellite based passive microwave imagery. Analysing sea ice concentrations for the period 1973–1987 using data from both, the Nimbus-5 Electrically Scanning Microwave Radiometer (ESMR) and Nimbus-7 Scanning Multichannel Microwave Radiometer (SMMR), *Parkinson and Cavalieri* [1989] have shown that within the mean annual cycle the ice extent of the Arctic has a minimum of $8.5 \cdot 10^6\, km^2$ in September and reaches a maximum of $15 \cdot 10^6\, km^2$ in March.

The ability of passive microwave sensors to retrieve sea ice concentrations derives from the sharp contrast in microwave emissivities and from polarisation differences between open water and sea ice. Because the atmospheric contributions to the radiation signal received by the satellite sensors are much smaller in the microwave spectral range than at other frequencies, microwave remote sensing of sea ice is nearly independent from weather effects like clouds. Thus, the temporal resolution of the microwave retrievals is actually at the order of days and is only limited by orbital parameters of the satellites. A detailed overview about algorithms for deriving sea ice properties from passive microwave remote sensing is given by, e.g., *Steffen et al.* [1992].

An advanced, coherent satellite data set[2] for the period 1979–1997 is used for the comparison of the model results with observations. It consists of sea ice concentration

[2]The data set of satellite based sea ice concentrations were derived as monthly mean data from the National Snow and Ice Data Center (NSIDC) via ftp from: ("http://nsidc.org").

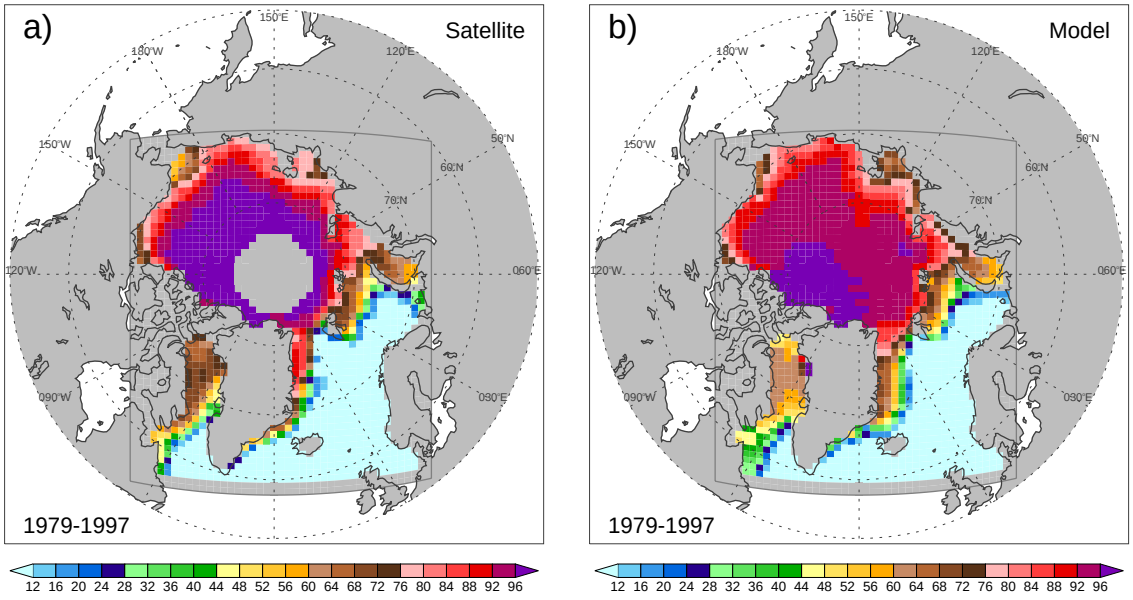

Figure 3.4: Comparison of long-term averaged sea ice concentrations (%) for the Arctic model domain. a) Satellite derived sea ice concentrations merged onto the model grid. The gray shaded circle near the North Pole depicts a data gap of the satellite instruments due their orbits. b) Sea ice concentrations from the simulation. The mean values are based on data for the period 1979–1997.

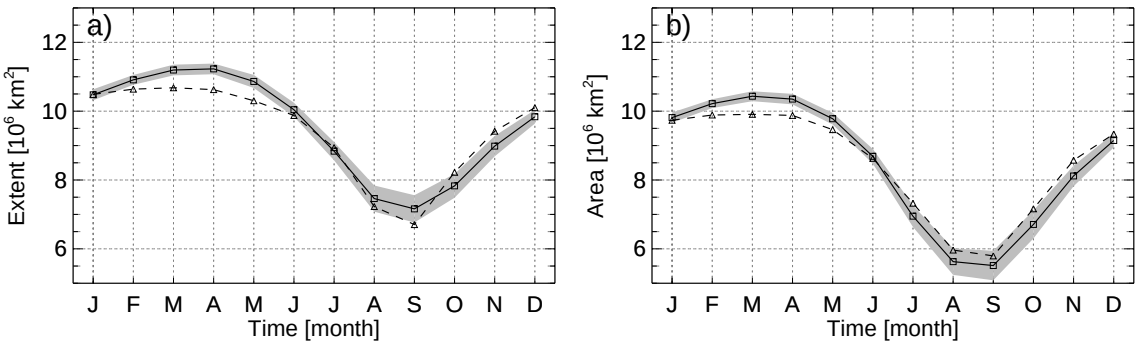

Figure 3.5: Mean annual cycle of the extention of the Arctic ice pack. a) Mean annual march of sea ice extent ($10^6\,km^2$), which is the accumulated area of grid cells covered with sea ice with concentrations of at least 15%. b) Mean annual cycle of sea ice area ($10^6\,km^2$), which is the accumulated area of grid cells covered with sea ice multiplied by their ice concentrations. Model data (solid lines with squares) are plotted together with satellite observations (dashed lines with triangles). The long-term monthly mean values are based on data for the period 1979–1997. For the model data the associated standard deviations for each of the twelve months based on the entire simulation period 1951–1999 are plotted as the grey shaded areas.

data derived from the Nimbus-7 SMMR and the Defense Meteorological Satellite Program's (DMSP) DMSP-F8, -F-11 and -F13 Special Sensor Microwave/Imager (SSM/I) data and was generated using the Goddard Space Flight Center (GSFC) Bootstrap algorithm [*Comiso*, 1995]. To ensure improved temporal consistency between the different sensors as well as an enhanced removal of weather and land contamination the GSFC Bootstrap Algorithm was updated [*Cavalieri et al.*, 1999] before processing the data. For the comparison in this study the satellite data, originally available at $25\,km \times 25\,km$ resolution on a polar stereographic grid, were merged onto the grid boxes of the model.

In general, the comparison of the long-term mean values of ice concentration (Fig. 3.4) reveals a good agreement between the simulation and the satellite observations. For the sea ice extent the difference between the mean values (simulation minus observation) amounts to $0.15 \cdot 10^6\,km^2$, which is 1.6% relative the observed mean of $9.44 \cdot 10^6\,km^2$. There is nearly no difference between the mean values of sea ice area (for the definition of 'ice extent' and 'ice area' see caption of Fig. 3.5). In particular, a slight overestimation of the ice extent by the model is evident in the Greenland Sea and in the Labrador Sea whereas in the central Arctic and in the Baffin Bay the ice concentrations are slightly underestimated. However, the magnitudes of these differences are of the order of 8–10% and, thus, they are within the range of accuracy of the satellite retrievals. During the summer period, when the sea ice surface becomes wet by melting snow and ice, the accuracy of the satellite derived ice concentrations is between 10% and 20% and during the rest of the year between 5% and 10% [e.g. *Steffen et al.*, 1992]. Figure 3.5a shows that the ice extent of the model (satellite) data varies within the mean annual cycle from a maximum in April of $11.2 \cdot 10^6\,km^2$ (in March of $10.7 \cdot 10^6\,km^2$) to a minimum in September of $7.2 \cdot 10^6\,km^2$ ($6.7 \cdot 10^6\,km^2$). The maximum values are smaller than in other publications [e.g., *Parkinson and Cavalieri*, 1989; *Parkinson et al.*, 1999] because the model domain considered in this study does not include the Sea of Okhotsk and the Hudson Bay. Within the annual cycle, the largest

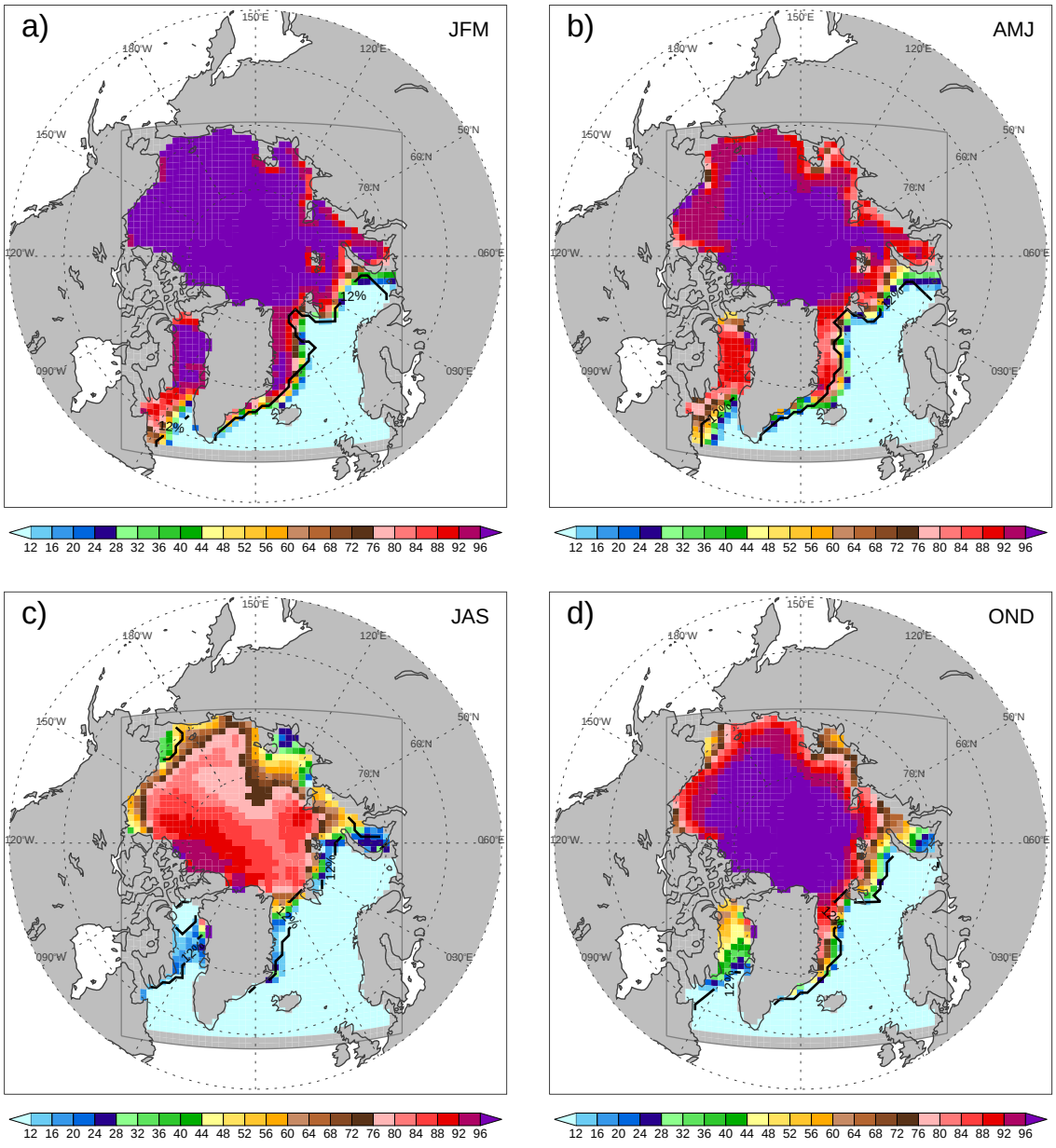

Figure 3.6: Long-term seasonal averages of ice concentration. a)–d) show the averaged seasonal ice concentrations for winter–autumn, relating to the period 1979–1997. Additionally, the ice edge derived from the satellite observations is added to each panel (solid line).

difference between model data and observations occur during the winter months for both, ice extent and ice area (Fig. 3.5). The Root Mean Square Differences (RMSD) throughout the mean seasonal cycle amount to $0.35 \cdot 10^6\, km^2$ (3.7% relative to the satellite mean) and to $0.34 \cdot 10^6\, km^2$ (4.0% relative to the satellite mean) for the ice extent and the ice area respectively.

The averaged seasonal evolution of the ice concentration field is shown in Figure 3.6.

In the winter season (Fig. 3.6a), nearly the entire Arctic is covered with very compact ($> 96\%$) sea ice. In comparison with the satellite data, the model overestimates the ice extent in the Greenland Sea region, especially north of Iceland. During spring (Fig. 3.6b), the most compact ice retreats to the centre of the Arctic, north of $80°N$. In the coastal areas, except north of Greenland and the Canadian Archipelago, the compactness of the ice pack is reduced to concentrations between 80% and 90%. During summer (Fig. 3.6c), the ice compactness in these areas further decreases to values of less than 50 % or can even become zero in several years (Fig. 4.5). In the central Arctic the summer ice concentration decreases to about 80% with a positive gradient towards the Canadian Archipelago. An interesting feature of the summer ice pack occurs in the Baffin Bay region. In both, the simulation and the observations, there remains an isolated ice tongue extending from Baffin Island to the western coast of Greenland. Finally, freezing starts nearly everywhere in the model domain during autumn (see Fig. 3.16d) and leads to a recovery of the ice pack (Fig. 3.6d). During this season the differences between both data sets are smallest (Fig. 3.5 and 3.6).

3.3 Sea Ice Drift

After *Colony and Thorndike* [1984] the general circulation of the ice pack is mainly a function of the mean annual atmospheric surface pressure and the geometry of the basin. On time scales from days to months, more than 70% of the variance of the ice motion is explained by the winds, whereas the long-term drift pattern equally reflects the effects of winds and ocean currents [*Thorndike and Colony*, 1982]. Moreover, within a distance of $400\,km$ to the coast contributions from internal forces become important.

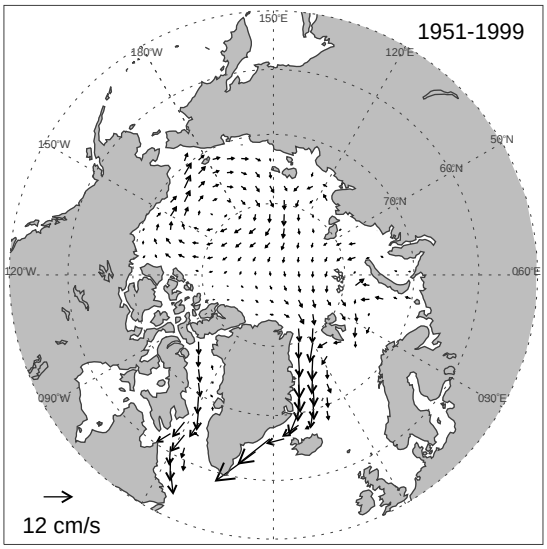

Figure 3.7: Long-term mean pattern of modelled ice drift based on data for the period 1951–1999. For clarity only every fourth vector is shown.

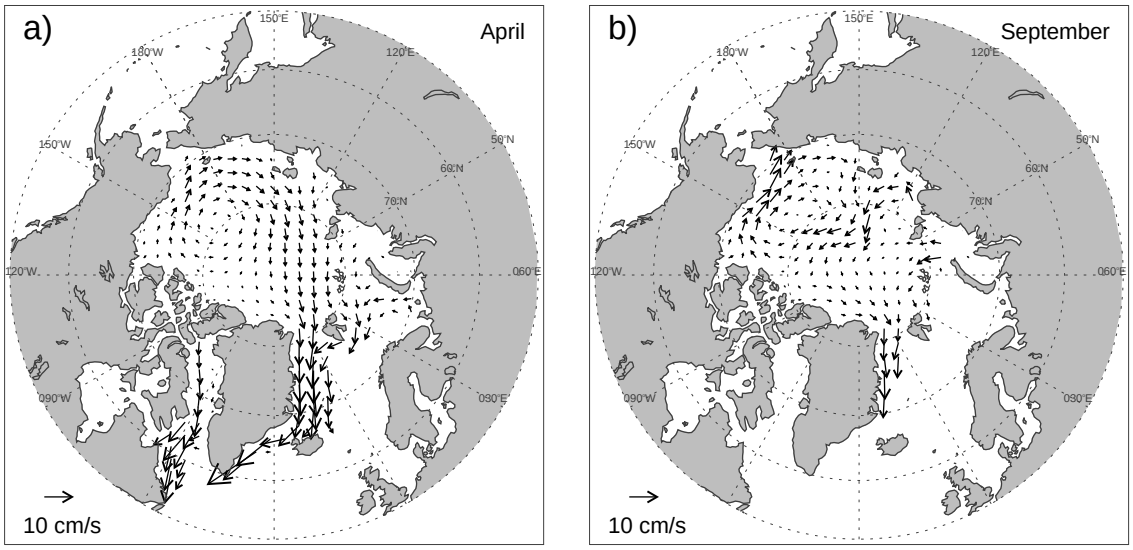

Figure 3.8: Long-term monthly means of ice drift for a) April and b) September. The averages are based on monthly mean data for the period 1951–1999.

These characteristics of the ice motion field are clearly evident in the simulation results. The long-term mean pattern of the modelled ice drift (Fig. 3.7) shows the main features which are well known from observations. It consists of a pronounced anticyclonic gyre in the Beaufort Sea and of a TPDS which is directed from the Laptev Sea to Fram Strait. Due to the ice buildup north of Greenland and the Canadian Archipelago the internal forces of the ice pack increase in this area. This leads to a resistance against the usually convergent ice drift and results in small drift velocities. The largest drift speeds with magnitudes of about $10\,cm/s$ are simulated in the Greenland and Irminger Seas where the forcing by the surface winds is strongest.

In wintertime, the drift pattern (see Fig. 3.8a as an example) is dominated by the strong anticyclonic circulation of the wind field in the Beaufort and East Siberian Seas region. In the Greenland and Irminger Seas the strong southward drift is caused by both, cyclonic winds connected to the Icelandic Low and anticyclonic, katabatic winds due to the persistent high pressure zone over Greenland. In summer, the averaged field of ice motion (see Fig. 3.8b as an example) reflects primarily the circulation of the prescribed oceanic currents because changing directions of the wind forcing, which is dominated by transient cyclones entering the Arctic Basin, are averaging out their impact. North of Greenland slightly reduced internal forces due to a looser ice pack of less thickness lead to enhanced drift velocities in this area.

In Fram Strait, where most of the ice leaving the Arctic passes through, a pronounced seasonal cycle of the drift speed is evident (Fig. 3.9). Compared to the long-term mean of the cross-strait averaged southward drift speed of $4.3\,cm/s$, largest velocities occur during the winter months with magnitudes of about $6\,cm/s$. From June to October, the southward drift speeds are below the long-term average with a minimum of $0.5\,cm/s$ in

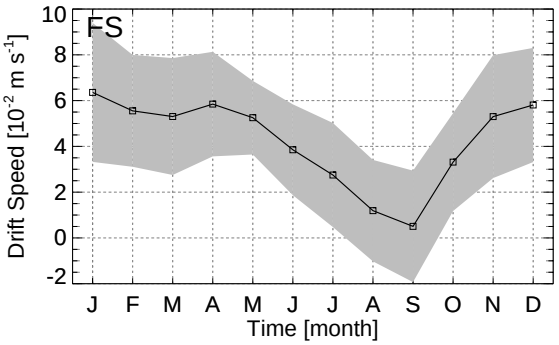

Figure 3.9: Mean annual cycle of the cross-strait averaged southward ice drift component in Fram Strait. The grey shaded area marks the standard deviations of the individual monthly means.

September. The standard deviations of the long-term monthly means are generally larger than $2\,cm/s$. Thus, the September ice drift in Fram Strait can be directed northward in several years.

Using buoy data from 1979–1994 as well as satellite derived ice drift data for the winters 1978/1988 and 1994/1995 *Kreyscher* [1998] and *Kreyscher et al.* [2000] present a detailed validation of the simulated ice drift of four different sea ice models including the model used in this study. Apart from a generally good correspondence on various time scales, the viscous-plastic model which is used in the present study shows some deficiencies in the southern Beaufort Sea, the Laptev Sea, and north of the Canadian Archipelago. The drift stoppage north of the Canadian Archipelago is slightly overestimated by the model in summer and underestimated in winter. *Kreyscher* [1998] attributes these deficiencies to a lack of a variable ice strength parameter accounting for density variations within the ice floes due to melting.

3.4 Sea Ice Thickness

Knowledge about the ice thickness is essential because it controls the rate of energy transfer between the ocean and atmosphere when sea ice is present. Moreover, the motion and the deformation of sea ice depends on the ice strength which in turn is determined by the ice thickness. From observations there is only little known about its large-scale characteristics. Most of the present knowledge about the mean state and the variability of the ice thickness was gained by theoretical studies using numerical sea ice models [e.g., *Hibler*, 1979, 1980; *Flato*, 1995; *Harder et al.*, 1998] using various forcing data over a broad range of time periods. The results of these models were partly tested against available observational data which where mostly gathered by military submarines. On the other hand, data from numerical simulations of ice thickness were used to assimilate observations. For instance, *Rothrock et al.* [1999b] used the mean seasonal cycle of simulated ice thickness to adjust submarine measurements taken in different seasons to make them comparable.

Apart from differences arising from the physics and numerics implemented into the particular models and from the quality of the forcing data used, the mean field of ice thickness depends largely on the length of the integration period due to decadal scale

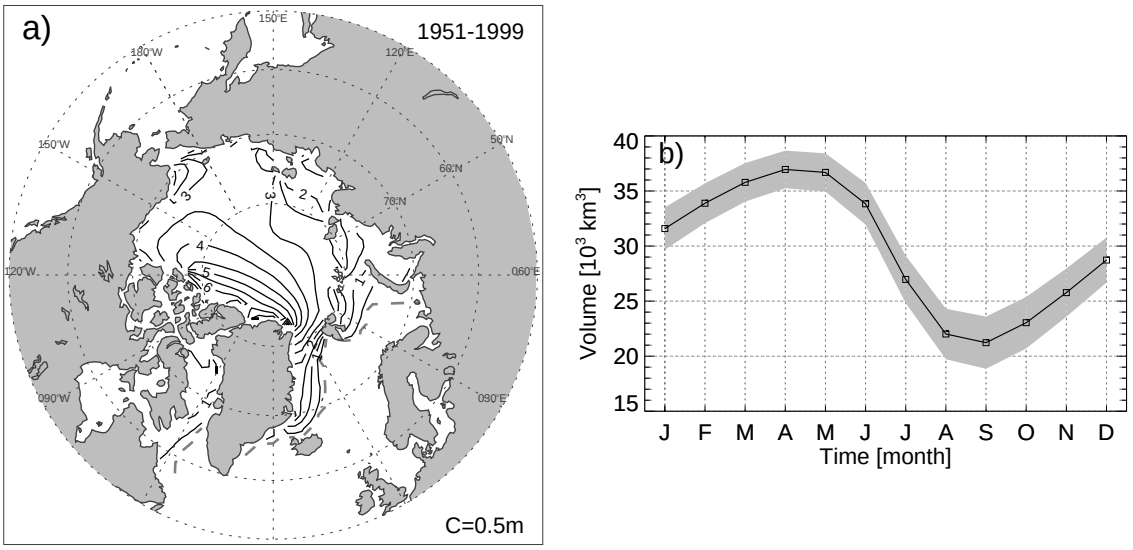

Figure 3.10: Long-term mean state of modelled ice thickness. a) shows the spatial pattern of long-term mean ice thickness (m). The ice edge, based on the 12% contour of ice concentrations, is indicated by the gray dashed line. b) shows the mean seasonal cycle of the total sea ice volume ($10^3\,km^3$). The sea ice volume represents the integral of ice thickness times the grid cell area over all grid cells of the model domain. Averages are based on data for the period 1951–1999.

variations [*Flato*, 1995]. Using a ∼50 years long set of atmospheric reanalysis data this study represents one of the longest sea ice model integrations with prescribed realistic forcing. The simulated mean pattern of ice thickness (Fig. 3.10a) is in general similar to previous modelling results. It shows an increase of ice thickness from about $2\,m$ at the Siberian coast towards more than $6\,m$ north of Greenland and the Canadian Archipelago. At the North Pole the long-term averaged ice thickness amounts to $4.0\,m$ (see Table 3.1). A tongue of rather thick ice between $3.0\,m$ and $3.5\,m$ extends from the Beaufort Sea to the East Siberian Sea. This feature is neither apparent in contour maps based on observations [*LeSchack*, 1980; *Bourke and McLaren*, 1992], nor in most of the previous modelling results. Only those studies which use a rather long forcing data set [*Flato*, 1995; *Arfeuille et al.*, 2000] show large ice thicknesses in the East Siberian Sea too, because of pronounced interannual variability in this region (see Fig. 4.8). The total sea ice volume (SIV) is defined as the sum over the ice thickness at each grid point of the model domain multiplied by their grid cell area. Its long-term mean amounts to $29.7{\cdot}10^3\,km^3$ and it shows a pronounced seasonal evolution (Fig. 3.10b). The maximum volume of $37.0 \cdot 10^3\,km^3$ is simulated in April whereas the minimum occurs in September with $21.2 \cdot 10^3\,km^3$. Thus, the amplitude of the seasonal cycle is roughly half as large as the long-term average.

During the wintertime the thickest ice occurs in the American and Asian parts of the Arctic (Fig. 3.11a) with maximum values exceeding $7\,m$ north of Ellesmere Island. In the Beaufort and East Siberian Seas the ice thickness is about $4\,m$.

In September, largest differences to the winter situation appear in the Siberian Arctic. In the European part of the Siberian coast (Barents, Kara, and Laptev Seas) the ice thickness is reduced to less than $1\,m$, whereas in the East Siberian Sea the ice pack is

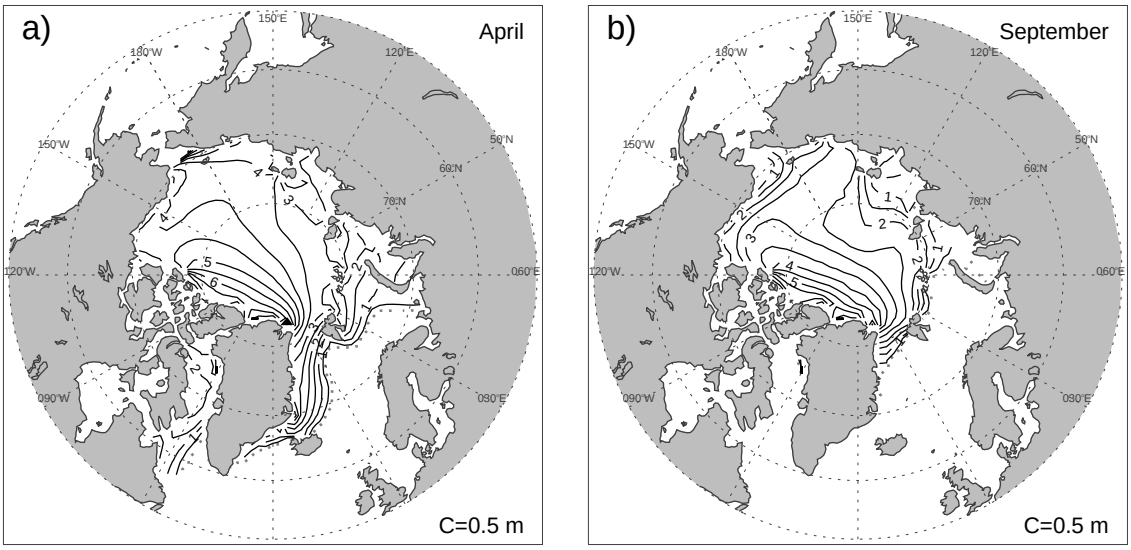

Figure 3.11: Long-term monthly means of ice thickness (m) for a) April and b) September. The averages are based on monthly mean data for the period 1951–1999.

still 2.5 m thick. As indicated by the summer average of ice concentration (Fig. 3.6c), the Baffin Bay is nearly ice-free. The same holds true for most parts of the Greenland Sea, except the region north of about 76° N. In Fram Strait the ice cover is still very compact with an average thickness of about 2.5 m (Fig. 3.13). This is confirmed by Upward Looking Sonar (ULS) measurements for the period 1990–96 [*Vinje et al.*, 1998] which reveal a mean September thickness of 2.25 m in Fram Strait.

Figure 3.13 shows the mean seasonal cycles of ice thickness for eight individual points of the model domain representing sub-areas of the ice pack with different properties (see Fig. 3.12). Some characteristic numbers of these curves, like e.g. the mean value and the amplitude of the seasonal cycle, are summarised in Table 3.1. One feature which is common to all regions except the Canadian Archipelago is that the summer minimum of ice thickness always occurs at the end of the melt season. For the North Pole the onset of freeze occurs, on average, on August 16 whereas at the marginal seas the end of the melt season is achieved one month later, on September 21 [*Rigor et al.*, 2000]. The seasonal maximum is, in addition to freezing processes, largely determined by the ice dynamics. This is most pronounced in Fram Strait, where the thickest ice occurs in July. During this time cyclonic ice motion in the region north of Greenland causes advection of very thick ice from this area to Fram Strait and, thus, predominates the thermodynamic effect of summertime melting. Similar arguments hold for the Canadian Archipelago, where the amplitude of the seasonal cycle is the smallest among the selected locations. There, changes of the drift direction can significantly alter the ice thickness. Moreover, only in this region interannual variations are comparable to the amplitude of the mean annual cycle (see Tab. 3.1).

A comprehensive validation of the simulated large-scale sea ice thickness is presently

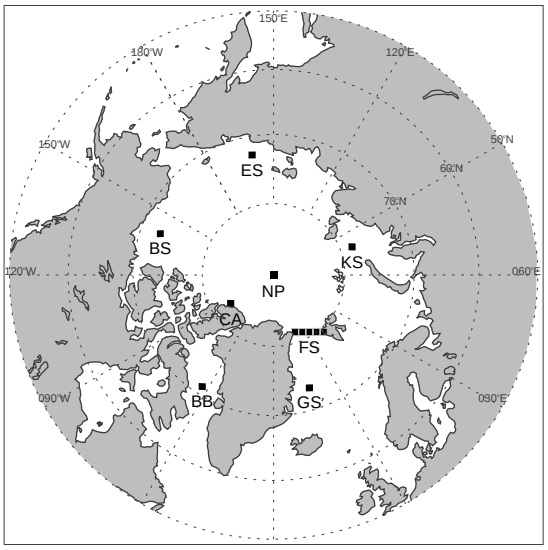

Figure 3.12: Location of grid cells which were selected for the comparison of the seasonal cycles of ice thickness shown in Figure 3.11 and Table 3.1.

not possible due to the lack of a sufficiently large number of adequate observations. However, at least an impression of the model's quality can be achieved by comparing the available measurements with the simulation results. With the beginning of the era of nuclear powered submarines in the late 1950's it was possible to move under the ice pack for several weeks. The USS Nautilus was the first vessel to cross the Arctic Basin via the North Pole in August 1958 [*McLaren*, 1989]. Since that time, the U.S. Navy has conducted many cruises under the Arctic ice pack but only comparatively little of their collected data has been released for public use due to national security restrictions. Moreover, the available U.S. Navy data include restrictions stating that positions of the data must be rounded to the nearest 5 minutes of latitude and longitude, and that the date is to be rounded to the nearest third of a month. In the 1990's the U.S. Navy conducted purely scientific cruises under the patronage of the Scientific Ice Expeditions (SCICEX) program and released the collected data completely unclassified. Because the submarines measure the ice draft on a rather narrow strip of a few meters width and covering time periods from days to weeks, these submarine data represent only snapshots of the spatial structure of the ice thickness field for a certain month of a certain year.

For this study, data of 10 submarine cruises[3] carried out in different regions of the Arctic during the period 1976–1997 are used for comparison with the simulation results. They consist of four sets of U.S. Navy data (under restrictions regarding date and position), three sets of SCICEX data, and data from three cruises conducted by the U.K. Royal Navy. In general the submarines were equipped with a narrow-beam sonar which measures the

[3]These data, Submarine Upward Looking Sonar Ice Draft Profile Data and Statistics, were obtained from the National Snow and Ice Data Center, University of Colorado at Boulder. For a description of the data set see: "http:\\nsidc.org\NOAA\ULS_Drafts\index.html"

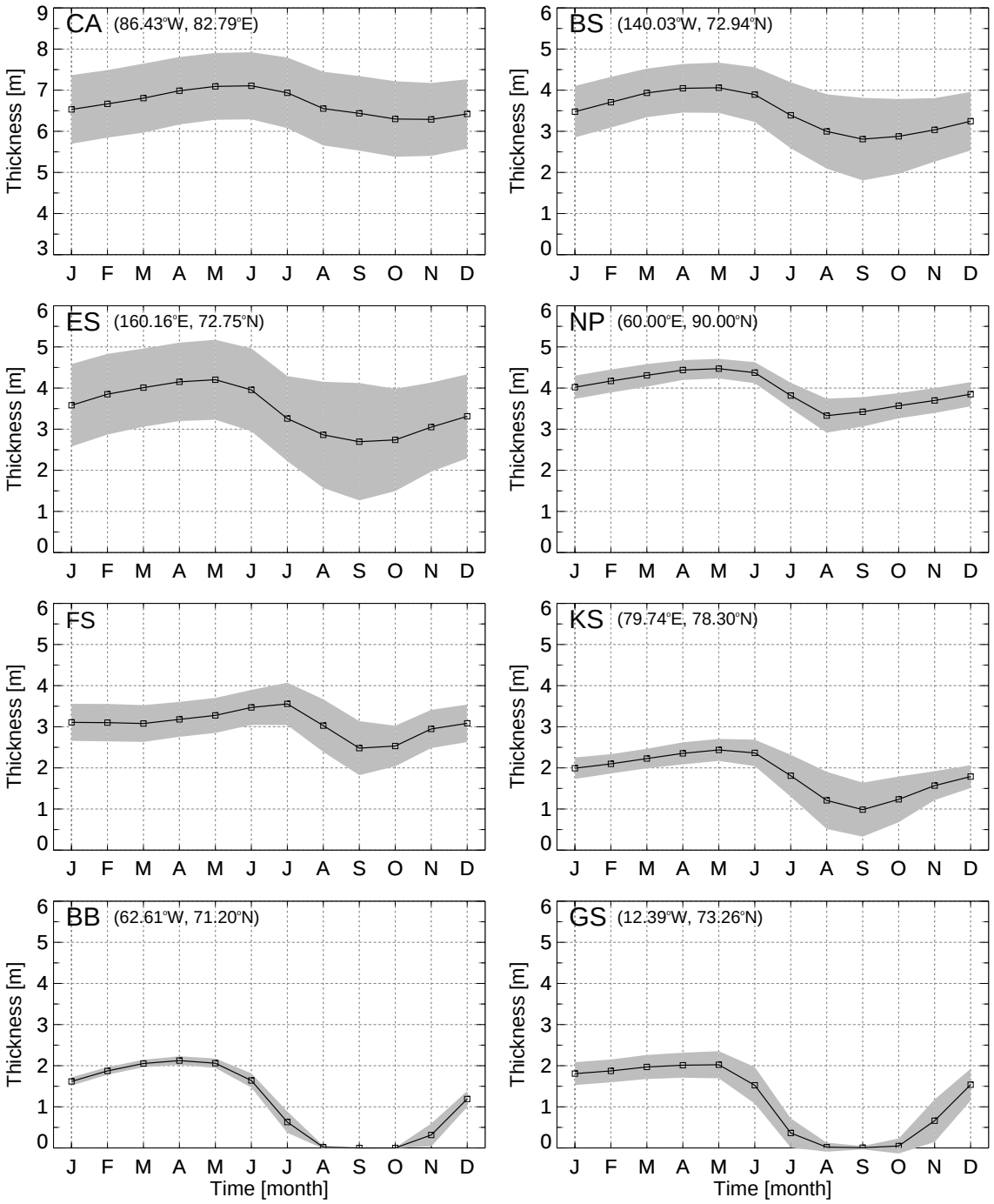

Figure 3.13: Mean seasonal cycles of thickness (m) for selected grid cells (CA = Canadian Archipelago, BS = Beaufort Sea, ES = East Siberian Sea, NP = North Pole, FS = Fram Strait, KS = Kara Sea, BB = Baffin Bay, and GS = Greenland Sea) of the model domain. Note the differing offset for the CA. The grey shaded area marks the standard deviations of the individual monthly means. For the location of the grid cells see Figure 3.12.

travel time between a transmitted and received sonar pulse between the location of the sonar and the bottom of the ice. Depth variations of the submarines were corrected by measuring a smoothed profile of leads and tracks and subtracting it from the under ice profile. Additionally, the resulting ice draft profile was interpolated to equally spaced $1\,m$ intervals.

Ice draft measurements taken on a straight line without gaps larger than $250\,m$ were summarised into so-called tracks. Due to instrumental problems and sampling variability standard errors for the mean ice draft of these tracks are in the range between 8% and 15% for a $50\,km$ track, depending on the instrument and on the region [*Wadhams*, 1997]. *Rothrock et al.* [1999b] stated that the overall errors for a 50-km segment are probably less than $0.3\,m$.

For the comparison with the model results the ice draft observations have to be multiplied by a factor which relates the ice draft to ice thickness. This factor depends on the densities of the ice slab as well as of the thickness and the density of an eventually overlying snow layer. Due to the lack of information about the individual densities as well as the thickness of the snow cover, an empirically derived constant factor of 1.136 is used in the present study [*Vinje et al.*, 1998]. To account for the horizontal resolution of the sea ice model of $110\,km \times 110\,km$ mean drafts from tracks shorter than $50\,km$ were excluded from the analysis. For each date, the associated grid box of the model was determined from the mean position of the particular track and the model value of this grid box was extracted. In the case of the restricted U.S. Navy data, the associated model values were averaged over the given third of the month. Values of tracks located within the same grid box at the same day were averaged. Finally, for each cruise the observed and the modelled thickness values are plotted as time series along the submarine course.

Table 3.1: Characteristics of modelled ice thickness for different regions (see Fig. 3.12) of the Arctic. The values are based on simulated data for the period 1951–1999. Given are the long-term averages (m), the standard deviations of the annual mean time series (m) and their percentages relative to the long-term averages (%), and the amplitudes of the seasonal cycles (m) and their percentages relative to the long-term averages (%).

Region	Long-Term Mean Value	Standard Deviation		Amplitude of Seasonal Cycle	
	[m]	[m]	[%]	[m]	[%]
Canadian Archipel.	6.68	0.75	11	0.82	4
Beaufort Sea	3.46	0.67	19	1.25	36
East Siberian Sea	3.47	0.99	29	1.51	44
North Pole	3.96	0.26	7	1.14	29
Fram Strait	3.07	0.38	12	1.08	35
Kara Sea	1.84	0.32	17	1.45	79
Baffin Bay	1.13	0.09	8	2.12	187
Greenland Sea	1.15	0.22	19	2.02	176

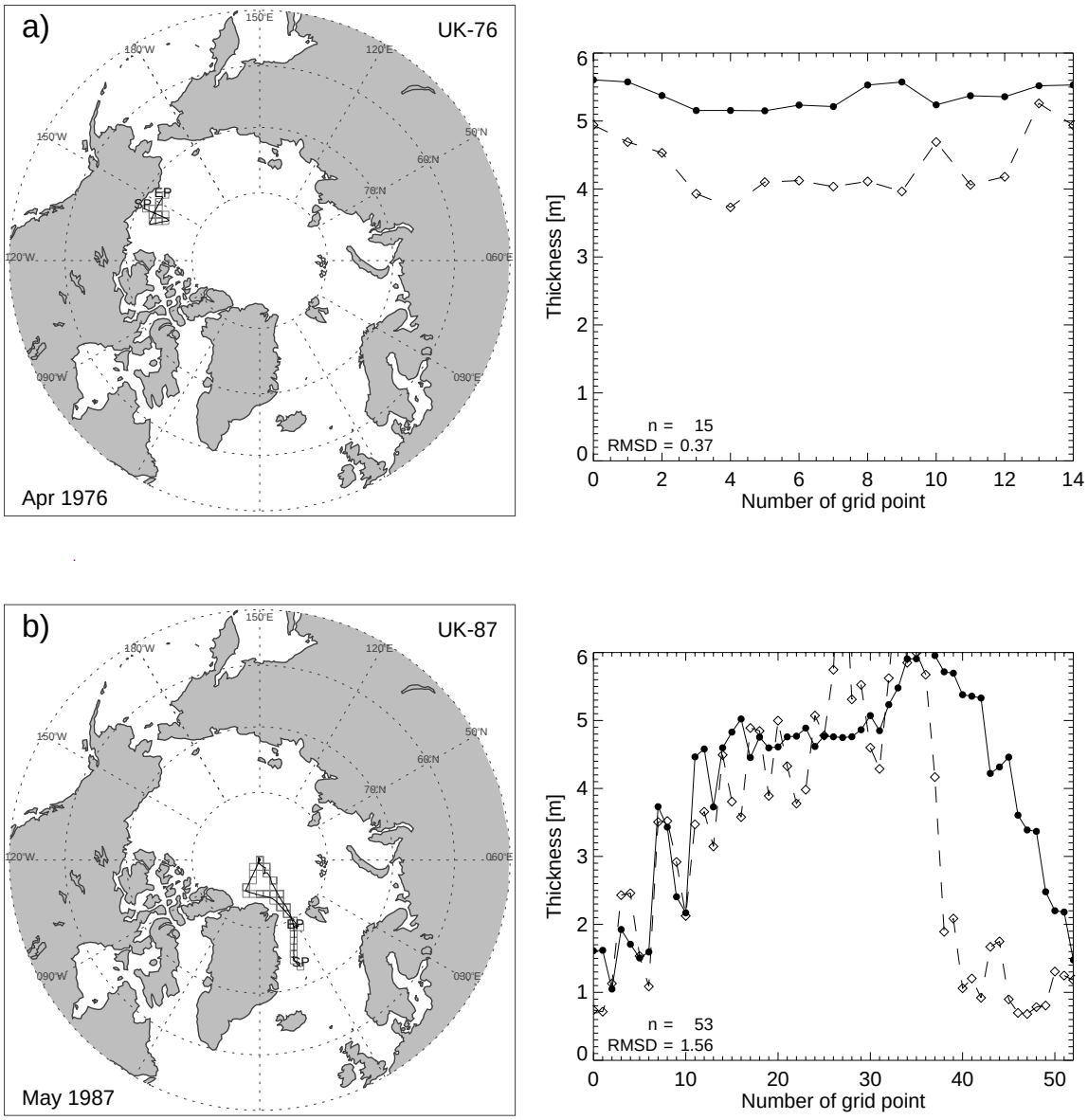

Figure 3.14: Comparison of submarine based ice thickness observations with model results. The left figure of each panel shows the submarine course together with the corresponding grid cells of the model which where used for the comparison. The name of each cruise according to the NSIDC data base is stated in the upper right corner of each plot whereas the date of the cruise is stated in the lower left. The names of the British cruises begin with "UK", those of the SCICEX cruises begin with "SCICEX", and the rest of the names belong to cruises conducted by the U.S. Navy. The thickness values (m) along the submarine course beginning at the starting point of the cruise are shown in the right figure of each panel. Model data are plotted as solid lines with circles whereas submarine observations are marked by the dashed lines with diamonds. To assign the thickness values to its location within the course, the starting points (SP) as well as the ending points (EP) of each cruise are marked.

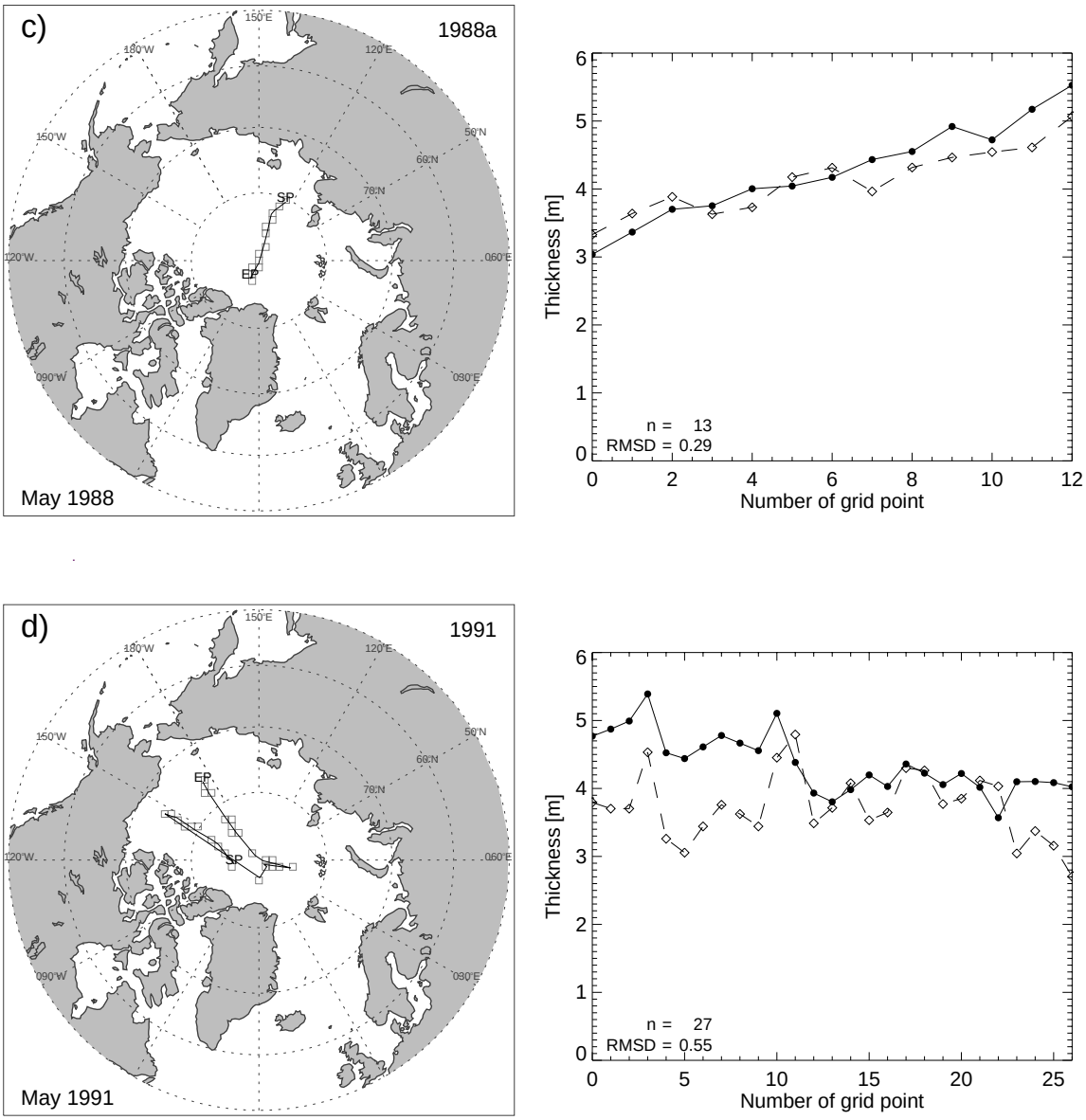

Figure 3.14: (continued)

The results of the comparison are summarised in Figure 3.14. For each of the cruises the number of tracks used for the comparison is stated together with the RMSD between both data sets. This number excludes differences of the mean values (bias) and serves as a rough estimate of the spatial agreement or disagreement, respectively. However, rather than evaluating pure numbers, this comparison is more focused on finding out, from a qualitative point of view, which of the general features of the ice thickness pattern are successfully simulated by the model.

The *UK-87* cruise (Fig. 3.14b), also discussed earlier by *Wadhams* [1997], investigated the ice pack in an triangular region bounded by Fram Strait, the northern coast of Green-

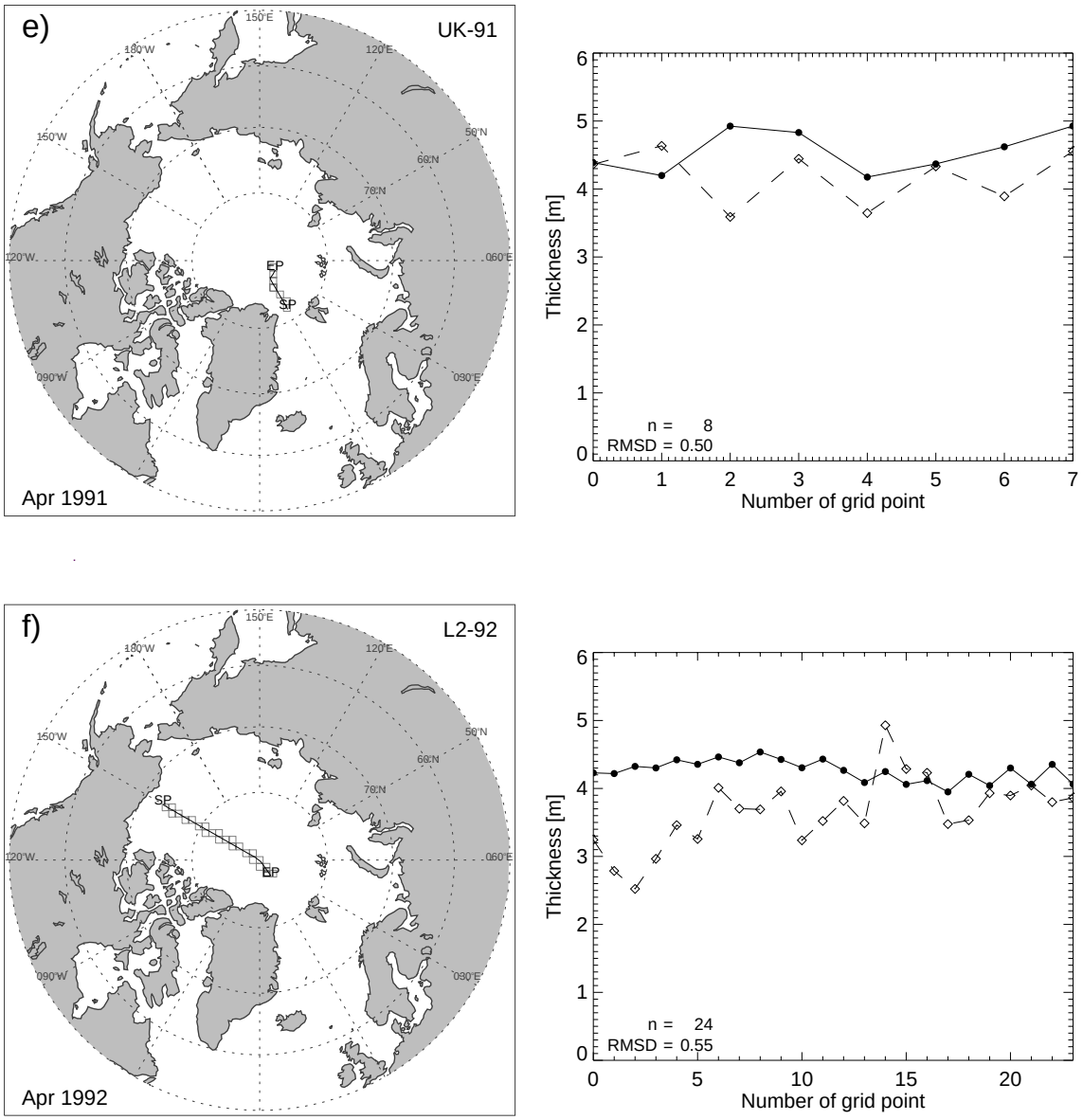

Figure 3.14: (continued)

land, and the North Pole. The comparison reveals, that the model successfully simulates the South-North gradient of ice thickness within the East Greenland Current. Moreover, there is an agreement in the magnitude of the ice buildup off the northern coast of Greenland with values exceeding 6 m in both datasets. For the region upstream of Fram Strait the *UK-91* data also show accordance with the model. The U.S. Navy cruise *1988a* in May 1988 (Fig. 3.14c) provides data of a cross-basin section directed from the Laptev Sea to north of Greenland. In both, the submarine data and in the model results, the ice thickness increases from 3 m in the Eastern Arctic to values of about 5 m at the opposite coast. Within the centre of the Arctic Basin data from the U.S. Navy cruises *1991* and

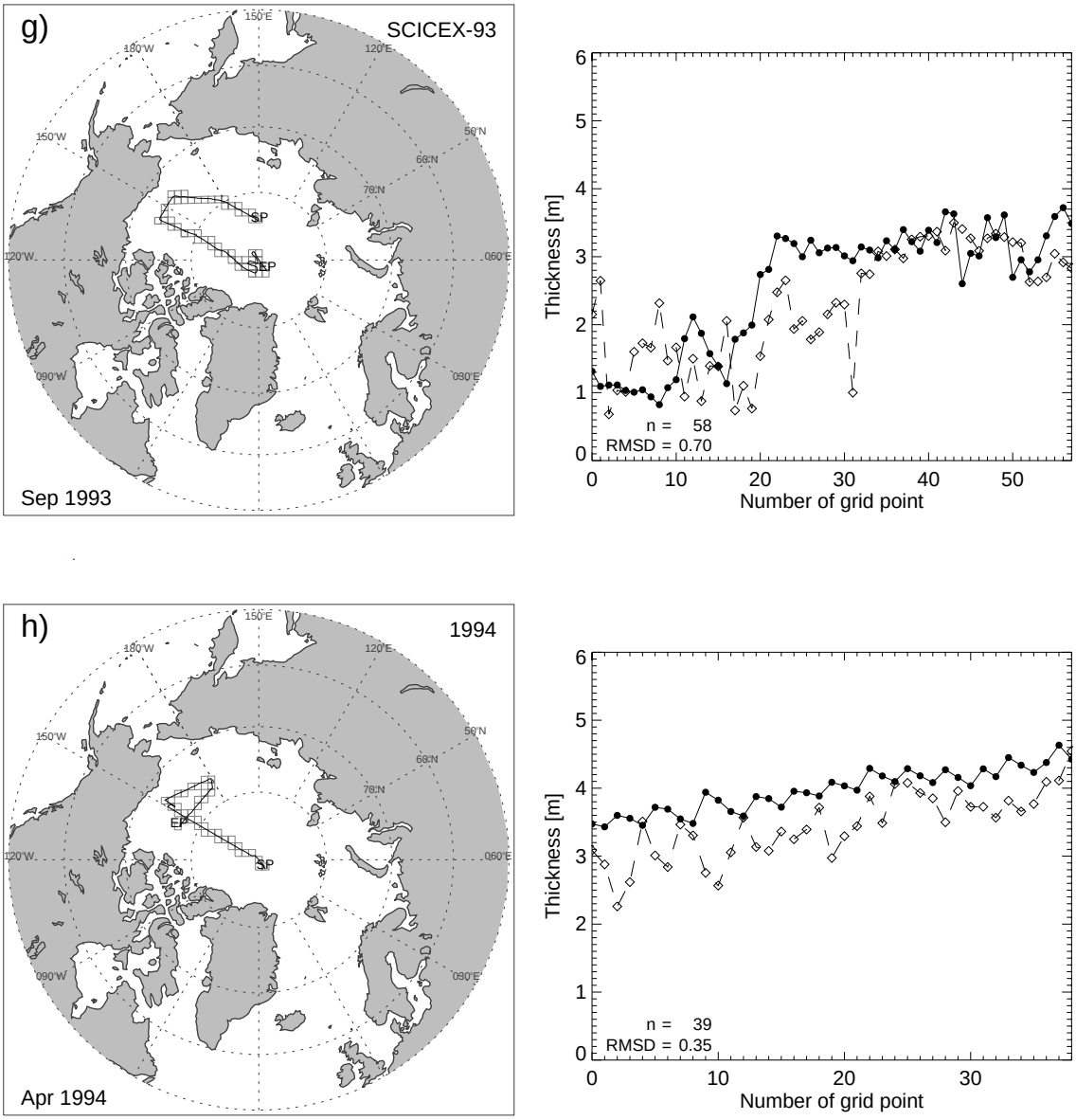

Figure 3.14: (continued)

SCICEX-96 also indicate agreement of the sea ice model with observations (Figs. 3.14g,i). Most of the submarine data cover the section between the Beaufort Sea and the North Pole (Figs. 3.14a,d,f,g,h,j). In general the model simulates the ice thickness along this section reasonably well, except in the Beaufort Sea. In this region the model overestimates the ice thickness by 1–2 m, which points towards a systematic deficiency of the model. Another marked discrepancy between simulation and observations emerges in the East Greenland Sea (Fig. 3.14b) where the model overestimates the ice thickness by several meters. However, this part of the ice pack is characterised by a sharp East-West gradient

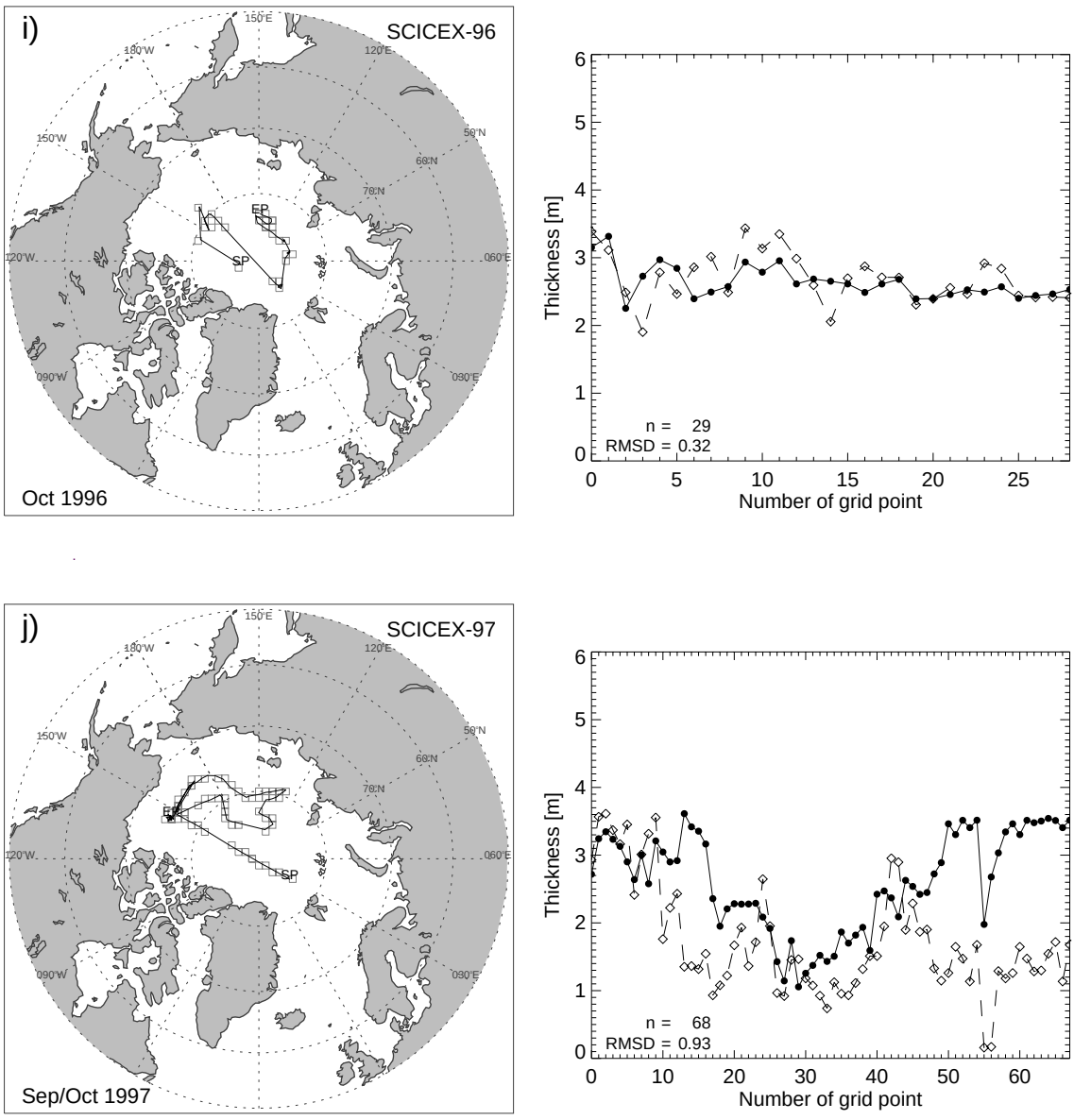

Figure 3.14: (continued)

of ice thickness. Thus, a small displacement along this gradient, perhaps within the range of the size of a model grid box, can lead to large differences. In regions with smaller gradients, the comparison of two different spatial scales — $50\,km$ tracks of some meters width against grid boxes of $110\,km \times 110\,km$ — can lead to additional, smaller differences.

Overall, from the available data sets of submarine ice draft observations it can be deduced that the sea ice model forced with realistic atmospheric data is well capable of reproducing the gross features of the spatial distribution of Arctic ice thickness. As stated by the SCICEX 2000 Workshop Organizing Commitee [*Rothrock et al.*, 1999a] the release

of more, presently unpublished ice draft data, collected during the last 40 years by military submarines, as well as ongoing scientific under ice cruises will improve our knowledge about Arctic ice thickness significantly. At the Applied Physics Laboratory of the University of Washington, Seattle, USA there are ongoing efforts in digitising about 1800 roll charts from submarine cruises prior to 1986. Therefore, from an optimistic point of view, the increasing number of available observations could make possible a comprehensive validation of sea ice models in the near future.

3.5 Net Freezing Rate

The rate of melting and freezing of sea ice integrated over a seasonal cycle — the net freezing rate — is one of the most important parameters of sea ice affecting the ocean. The freezing of sea ice increases the salinity of the underlying oceanic layer due to the release of brine. This release occurs because brine can only partly be integrated into the crystal structure of sea ice. Moreover, other processes like, e.g. brine expulsion and gravity drainage cause a further desalination of sea ice with increasing age [*Weeks*, 1998]. When sea ice melts it acts as a freshwater source of the ocean because its salinity is only about 10% of that of sea water. Owing to the mean motion of the ice pack, melting and freezing processes do not necessarily balance each other on a regional scale. Thus, they become the oceanic equivalent of the hydrological cycle in the atmosphere consisting of precipitation and evaporation [*Aagaard and Carmack*, 1989].

The longterm average of the simulated net freezing rate (Fig. 3.15) shows a net ice

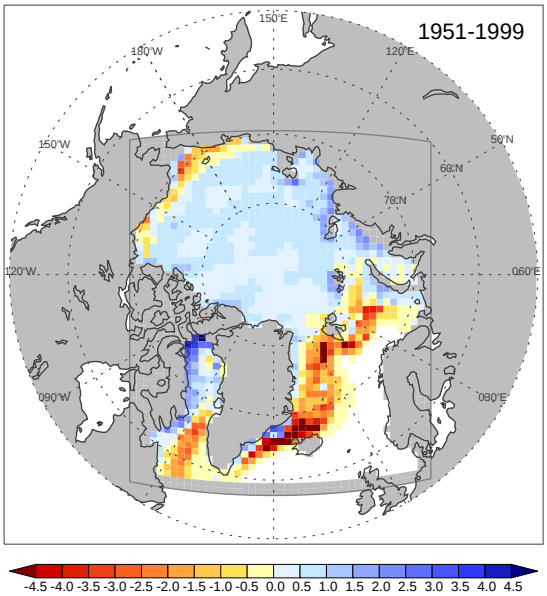

Figure 3.15: Long-term average of simulated net freezing rates ($m/year$) for the period 1951–1999. Blue shaded areas mark net freezing (positive growth) whereas the red shadings identify regions of net melting (negative growth).

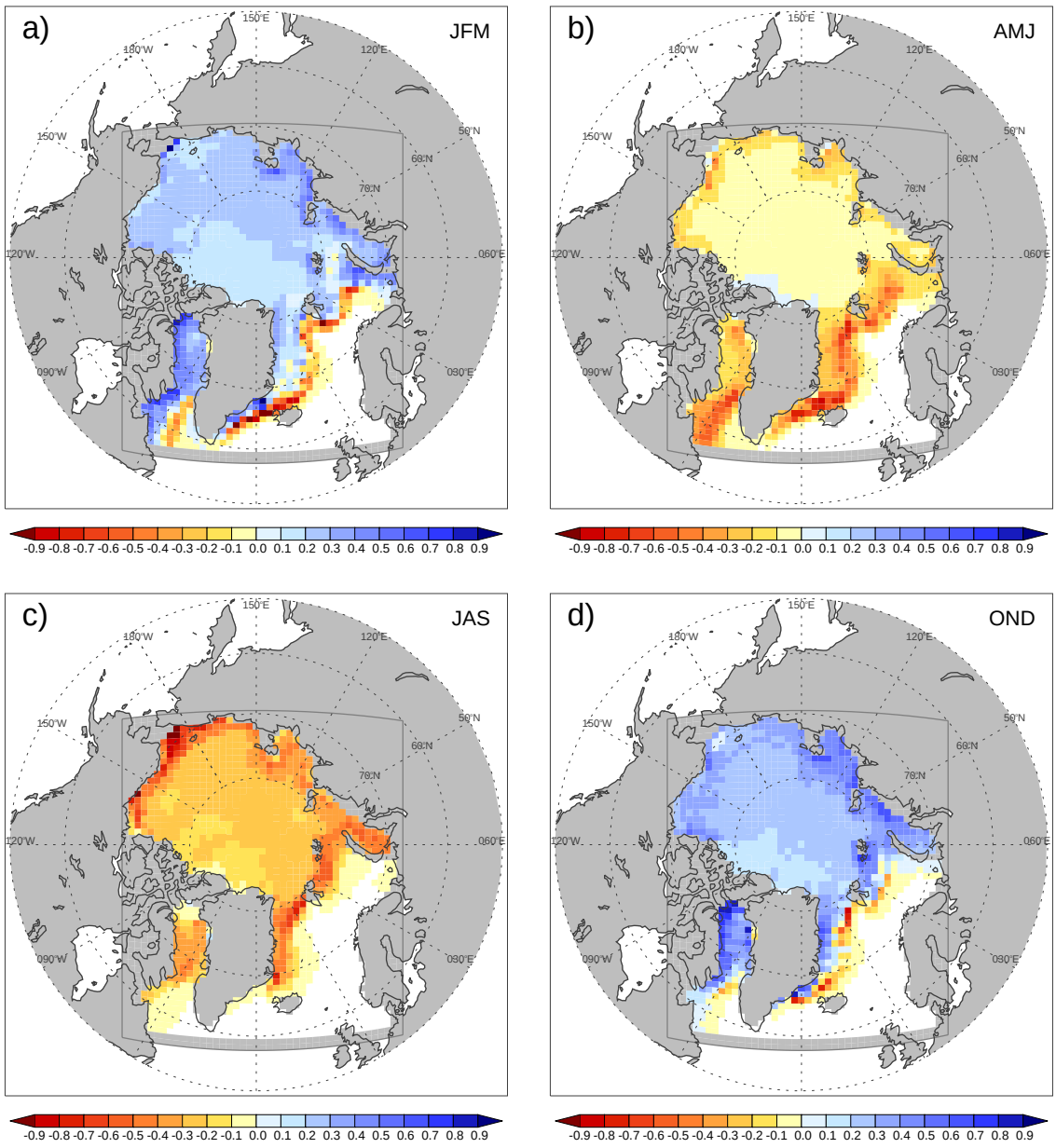

Figure 3.16: Seasonal means of simulated net freezing rates ($m/year$) for the four seasons (JFM = January–March, AMJ = April–June, JAS = July–September, and OND = October–December). The averages are based on data for the period 1951–1999.

growth of about 0.5 $m/year$ in the central Arctic Basin. Since evaporation rates are usually small over the ice pack, freezing of sea ice is the only effective negative freshwater flux in the Arctic Ocean with magnitudes comparable to those in highly evaporative seas [*Aagaard and Carmack*, 1989]. Although there are essentially no direct observations of this quantity, the simulated net freezing rate agrees with observational estimates. From measurements along

an Arctic transect *Koerner* [1973] estimated an overall net growth of about $0.5\,m/year$, partitioned into $1.1\,m/year$ of growth and $0.6\,m/year$ of melt. Additionally, *Steele and Flato* [1999] estimated the same net freezing rate based on indirect data from a study of chemical tracers in the Arctic Ocean. Moreover, a comparison of simulated net freezing rate from a couple of numerical sea ice models [*Steele and Flato*, 1999] reveals, that this value is in good agreement with previous theoretical studies.

The largest net growth rates are simulated at the Siberian coast reaching magnitudes of up to $2\,m/year$. In this region generally offshore winds create divergence of the ice pack which leads to low ice thicknesses and increased areas of open water. The same situation prevails in the northern Baffin Bay but with larger magnitudes due to the very low temperatures of the wintertime northwesterly winds. Regions of net melting are the GIN Seas, the Labrador Sea and the coastal areas of the Beaufort and Chukchi Seas. Note that the positive net freezing rates in Bering Strait are purely artificial as a consequence of the model's outflow condition. As a result of the large ice volume export from the Arctic via Fram Strait maximum melting occurs in the Greenland Sea and especially in the Denmark Strait region with net growth rates of about $-4\,m/year$. Note that positive net freezing rates occurring in grid cells directly adjacent to the coast of Greenland are due to cold katabatic winds which are apparent in the reanalysis data. Taking into account the lower density and salinity of sea ice compared to sea water, the freshwater input into the ocean associated with the negative growth rates in the southern Greenland Sea is at least as large as the annual atmospheric freshwater input for this area. *Serreze and Hurst* [2000] give an annual mean precipitation for the region at the southeastern coast of Greenland of about $1.4\,m$. Subtracting evaporation from precipitation *Cullather et al.* [2000] estimated a net atmospheric freshwater flux of $0.3 - 1.0\,m/year$ for this area.

Considering seasonal averages (Fig. 3.16) reveals that the ice edge at the Atlantic side of the model domain is the only region which exhibits permanent melting throughout all seasons. This is caused by the southward transport of sea ice into a warmer environment. In all other regions there is a distinct annual cycle of growth and melt. Because the magnitude of the heat transfer between bottom and top of an ice slab depends on the ice thickness (see Eq. 2.3), during freezing the strength of the ice growth rate also depends on this quantity. Apart from the influence of the oceanic and atmospheric forcing, largest growth rates hence occur where ice thicknesses are smallest and vice versa. Therefore, the maximum growth rates are simulated in Autumn (Fig. 3.16c), when the ice thickness starts to increase from its minimum values reached in August and September (Fig. 3.13). On the other hand, due to its larger thickness, the ice buildup region north of Greenland and the Canadian Archipelago exhibit the smallest growth rates within the model domain.

Integrated over the central Arctic, that is the model domain excluding the Baffin Bay/ Labrador Sea region and the GIN Seas, the total annual ice growth amounts to roughly $3400\,km^3/year$. This amount corresponds to about 14% of the mean sea ice volume of this area. In other words, 1/7 of the central Arctic's ice volume is renewed every year.

3.6 Sea Ice Exports

The spatial pattern of the net freezing rate (Fig. 3.15) in combination with the mean field of ice motion (Fig. 3.7) implies a net export of sea ice from the Arctic to lower latitudes.

Due to its lower density and its much lower salinity compared to sea water about 80%[4] of the exported sea ice volume can be considered as fresh water. Therefore, sea ice exports can affect the density structure of the upper oceanic layers in the melting regions and, furthermore, can become crucial for the global thermohaline circulation [e.g. *Marotzke and Willebrand*, 1991; *Rahmstorf*, 1995]. *Aagaard and Carmack* [1989] have estimated that the sea ice export through Fram Strait is the largest freshwater contribution to the GIN Seas. Recently, the deployment of moored ULS's in Fram Strait since the 1990s enables an observationally based estimation of this export [*Vinje et al.*, 1998]. However, long-term estimates can only be achieved by applying statistical regression models based on the available observations of sea ice drift and sea ice thickness in Fram Strait [*Dickson et al.*, 2000], or, as done in the present study, by integrating numerical sea ice models. A summary of both estimates and modelling results is given in *Kreyscher* [1998].

The sea ice volume flux IVF across a given section S is calculated as:

$$IVF = \int_S u_\perp(x,t)\, h(x,t)\, dx \tag{3.1}$$

where x is the position along the section, $u_\perp$ is the southward drift speed (SDS) perpendicular to the section, and h is the mean ice thickness of the grid cell. The volume fluxes are usually given in units of Sv ($Sverdrup = 10^6\, m^3 s^{-1}$) or $km^3/year$. In the present study transports across four sections are considered. Two of them, Fram Strait and Barents Sea, representing sections, which are connecting the Arctic Ocean to the adjacent seas. The the other two sections, Denmark Strait and Davis Strait, are located farther south outside the Arctic. The representation of the sections by the model grid is shown by Fig. 2.1.

The long-term averages of the volume exports together with other characteristic numbers are summarised in Table 3.2. The major part of the ice leaving the Arctic Ocean passes through Fram Strait at an average rate of $\sim 2600\, km^3/year$. This value is somewhat smaller than the observational estimate of $\sim 2850\, km^3/year$ by *Vinje et al.* [1998].

[4] Multiyear sea ice has an averaged salinity of $\sim 4\, psu$ [*Weeks*, 1998] whereas the salinity of high latitude sea water is $\sim 35\, psu$. Moreover, the density of sea ice corresponds to roughly 90% of that of sea water. Conservation of mass thus reveals that roughly 80% of the volume of sea ice represents fresh water.

Table 3.2: Characteristics of simulated sea ice exports out of the Arctic. The values are based on simulated data for the period 1951–1999.

Region	Long-Term Mean Value	Long-Term Mean Value	Standard Deviation	Amplitude of Seasonal Cycle
	(km^3/yr)	(Sv)	(Sv)	(Sv)
Fram Strait	2632	0.083	0.017	0.099
Davis Strait	832	0.026	0.005	0.060
Denmark Strait	601	0.019	0.007	0.055
Barents Sea	440	0.014	0.006	0.028

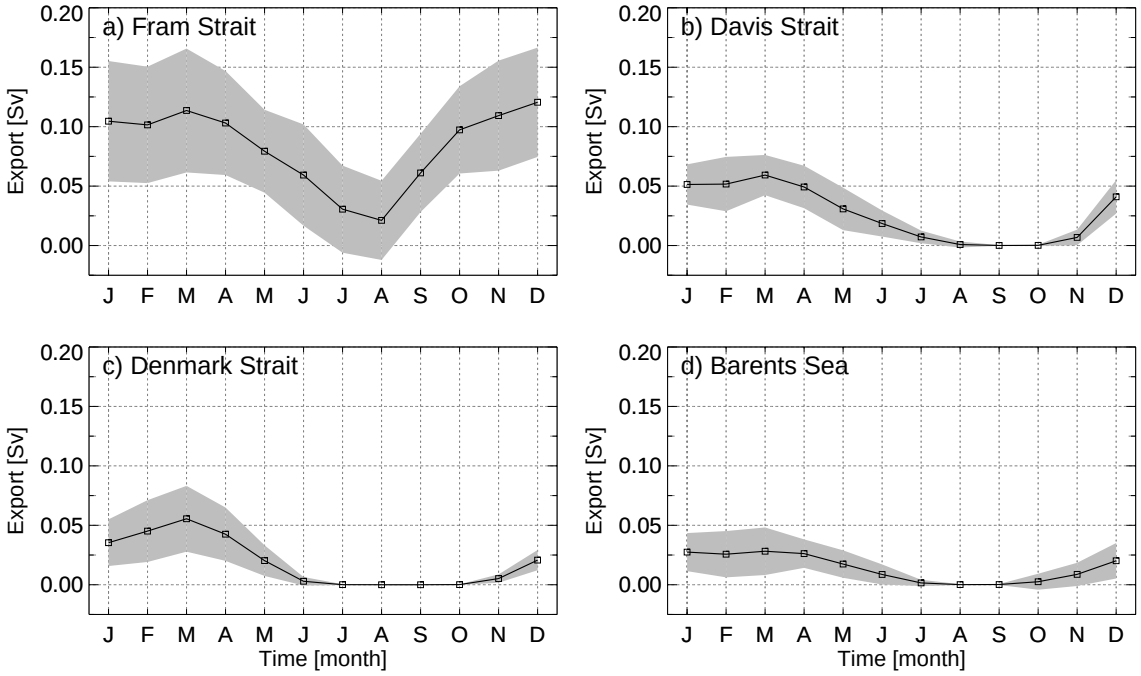

Figure 3.17: Mean seasonal cycles of sea ice exports through Fram Strait, Denmark Strait, Davis Strait, and the Barents Sea.

However, the comparison of both numbers is not fully appropriate because the observations cover the period 1990–1996 whereas the mean value of the simulation is based on 49 years integration. When considering exactly the same period the model reveals an export of $\sim 2870\,km^3/year$ which is in agreement with the observations. Moreover, as will be discussed in the next chapter, this export exhibits pronounced interannual variability as indicated by the standard deviation of the longterm mean of 20% (relative to its mean value).

Table 3.3: Mean river discharges of some of the world's largest rivers. The left side of the table shows values for the world's largest three rivers whereas on the right side the three largest rivers of the Arctic Basin are listed. The values are taken from *Milliman and Meade* [1983].

River	Long-Term Mean Value (km^3/yr)	Long-Term Mean Value (Sv)	River	Long-Term Mean Value (km^3/yr)	Long-Term Mean Value (Sv)
Amazon	6300	0.200	Yenisei	560	0.018
Zaire	1250	0.040	Lena	514	0.016
Orinoco	1100	0.035	Ob	385	0.012

Comparing with an additional southward export of $\sim 450\,km^3/year$ through the Barents Sea, the transport through Fram Strait represents roughly 80 % of total outflow from the Arctic. Adding both numbers yield it that every year about 10% of the Arctic Ocean's sea ice volume is exported into the North Atlantic. Compared to the discharges of the worlds largest rivers (see Tab. 3.3) the sea ice export through Fram Strait is the second largest freshwater flux on earth, corresponding to about one third of the Amazon's discharge. In the model the major part of the exported volume melts within the Greenland Sea (Fig. 3.15), whereas 23% of it passes Denmark Strait farther south. On the western side of Greenland about $800\,km^3/year$ of sea ice are transported southward from the Baffin Bay into the Labrador Sea.

The largest export rates occur during wintertime in the months December, January, February, and March (DJFM). Due to the retreat of the ice edge, except for Fram Strait, there is no ice export at all during the summer months. In Fram Strait, as indicated by the corresponding standard deviations, there can even be a northward transport during summer in some special years. Considering the annual cycles of the components determining the volume export (see Eq. 3.1) reveals that the seasonal march of the Fram Strait ice export is mainly determined by the southward drift speed (Fig. 3.9). Due to its advective nature the ice entering Fram Strait does not show distinct thickness changes during the seasonal cycle (Fig. 3.13).

3.7 Conclusions

In this chapter the mean state of a hind-cast simulation of the Arctic sea ice cover of the second half of the past century was presented. The purpose of the chapter was threefold. First, a comparison with observations showed the ability of the simulation to reproduce known features of the Arctic ice pack. In particular, it was shown that:

- There is a good agreement between satellite based ice concentration data with the simulation results. In particular, differences between the long-term averages of both data sets are within the range of accuracy of the satellite retrievals. Moreover, RMSDs of the mean seasonal cycles of sea ice extent and the sea ice area are only $\sim$ 4% relative to the observed long-term average. Deviations from the satellite observations occur mainly in wintertime when the model overestimates the extent of the sea cover.

- The simulated mean drift pattern shows the large scale features which are known from drifting buoys and satellite observations.

- The gross features of the spatial distribution of ice thickness are well reproduced by the model, as revealed by a comparison with ice draft measurements carried out during 10 military submarine cruises. However, the model overestimates systematically the ice thickness in the Beaufort Sea.

- At least for the time period of 1990–1996 the simulated mean ice volume export through Fram Strait matches perfectly the observational estimate.

Second, having about 50 years of simulated data, the analysis of the long-term characteristics of the Arctic ice pack revealed the following insights:

- The long-term average of Arctic ice thickness shows, additional to the widely accepted spatial distribution, a tongue of thicker ice with values of $3 - 3.5\,m$ which extends from the Beaufort into the East Siberian Sea.
- The timing of the wintertime maximum of ice thickness within the mean seasonal cycle depends strongly on ice dynamics, whereas the occurrence of the minimum coincides with the end of the melt season.
- In the Greenland and Irminger Seas the mean annual amount of melting sea ice exceeds precipitation minus evaporation. Therefore, sea ice represents the largest contributor to the freshwater input into the ocean in this area.
- Every year, roughly 10% of the total sea ice volume is exported into the North Atlantic. The most part of this export, about 80%, passes through Fram Strait, whereas the remainder leaves the Arctic east of Spitsbergen. With a long-term average of $2600\,km^3/year$ of exported sea ice and an associated fresh water discharge of about $2000\,km^3/year$ the Fram Strait sea ice export represents the second largest fresh water flux on earth, only exceeded by the threefold larger discharge of the Amazon river.

Third, because the remainder of this study primarily deals with deviations from the long-term averages, the above presented results serve as a reference for the following analyses.

3.8 Discussion

During the course of the 20th century, both observational and modelling efforts have significantly increased our knowledge about the Arctic ice pack. Primarily remote sensing techniques for deriving ice concentration and ice drift have contributed to a comprehensive monitoring of major properties of the ice cover. Together with ice drift observations from automatic data buoys these observations furthermore enable a validation of numerical sea ice models [*Kreyscher et al.*, 2000]. However, the data base for the ice thickness, which is primarily formed by sporadic submarine observations, is still very sparse and allows only a rather qualitative comparison with the model results. Therefore, the results of sea ice models have presently to be considered as the best guess for the long-term and large scale pattern of the Arctic ice thickness. This will probably change in the near future by both the release of additional presently classified submarine data and by the forthcoming efforts of the CryoSat mission[5] [*Wingham*, 1999] of the European Space Agency (ESA). Cryosat will be launched in 2003 and is aimed to detect climate variability and trends of the cryosphere. This goal will be achieved by RADAR altimetry of the thickness of the continental ice sheets and of sea ice.

Besides presenting the sea ice model's view of the long-term properties of the Arctic sea ice cover, the primary aim of the above analysis is to give a reference for the analysis of interannual to long-term variability of Arctic sea ice which will be investigated in the remainder of this study.

[5]Further informations about the ESA's CryoSat programme can be obtained from the following internet address:"http://www.estec.esa.nl/explorer/cryosat/".

Chapter 4

Interannual Variability

4.1 Introduction

The major factors determining the dynamic and thermodynamic variability of sea ice are the atmospheric fields of near surface winds and temperature [*Walsh et al.*, 1985; *Deser et al.*, 2000]. Therefore, it is expected that a sea ice model forced by those quantities should be able to reproduce major features of the interannual to decadal variability of the Arctic ice cover. Although this is interesting in its own, knowledge about Arctic sea ice variability bears far-reaching importance for the adjacent media ocean and atmosphere. As suggested by several authors [*Mysak et al.*, 1990; *Deser and Blackmon*, 1993; *Wohlleben and Weaver*, 1995; *Mysak and Venegas*, 1998], sea ice variability could be a key issue in either triggering variability in ocean and atmosphere or in transferring variability between both fluids.

By far the most prominent example of interannual to decadal variability of the northern high latitudes being associated with Arctic sea ice was the occurrence of the "Great Salinity Anomaly" (GSA) of the northern North Atlantic in the 1970s (Fig. 4.1). Whereas *Pollard and Pu* [1985] explained the formation of the initial salinity minimum in the Greenland Sea in 1968 by differences between evaporation and precipitation, *Dickson et al.* [1988] suggested more localised wind anomalies as its possible cause. The third hypothesis, suggested by *Aagaard and Carmack* [1989], was that excessive sea ice exports into the Greenland Sea caused the initial salinity minimum. Following the analysis of *Walsh and Chapman* [1990] and the modelling efforts of *Häkkinen* [1993] the latter hypothesis turned out to be the most probable.

Another example of how sea ice variability could affect the Atlantic ocean was suggested by *Deser and Blackmon* [1993]. By investigating dominant modes of SST variability of the North Atlantic they found a close link between decadal sea ice variations in the Labrador Sea with SSTs east of Newfoundland. Using sea ice extent observations, the early studies of *Walsh and Johnson* [1979a, 1979b] and *Lemke et al.* [1980] identified out of phase variations of the sea ice cover east and west of Greenland. Having a longer data set, [*Slonosky et al.*, 1997] and *Deser et al.* [2000] identified those variations to be dominant during wintertime and being associated with and driven by the North Atlantic Oscillation (NAO). The NAO, on the other hand, represents the dominant mode of wintertime atmospheric variability in the North Atlantic region and describes the strengthening or weakening of the Azores High and Icelandic Low [e.g. *Hurrell*, 1995]. Recent studies [*Kwok and Rothrock*, 1999; *Dickson et al.*, 2000] indicate that the NAO has, furthermore, impact onto the sea ice

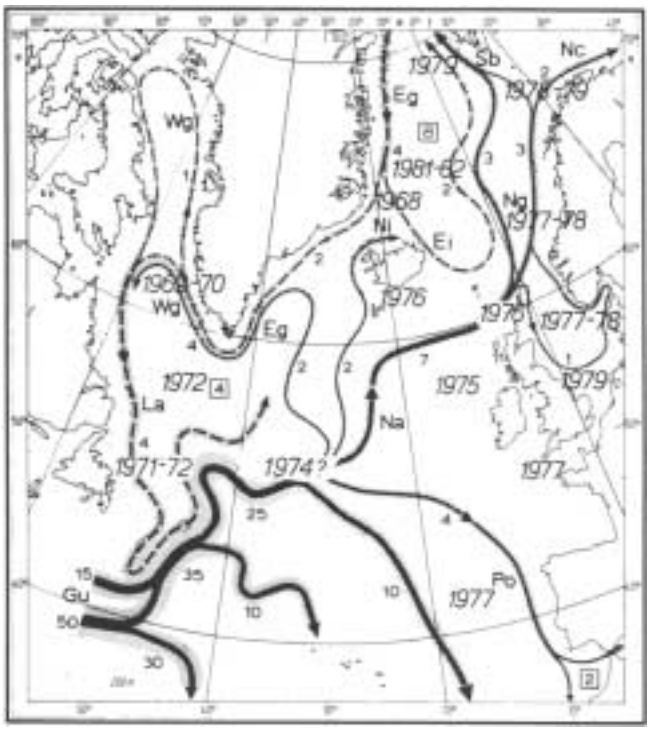

Figure 4.1: Timing of the North Atlantic Salinity minimum of the 1970's superimposed by *Dickson et al.* [1988] on the transport scheme for the North Atlantic from *Dietrich et al.* [1975]. (From *Dickson et al.* [1988]).

export through Fram Strait.

The NAO, however, can be considered to a certain degree as part of a larger scale SLP variation, the Arctic Oscillation (AO) [*Thompson and Wallace*, 1998; *Deser*, 2000]. SLP anomalies associated with the AO cover the entire Arctic ocean and were brought into context with cyclonic or anticyclonic sea ice drift variations [*Johnson et al.*, 1999] as described by *Gudkovich* [1961] and *Proshutinsky and Johnson* [1997]. Moreover, recent decreases of Arctic SLP where found be associated with pronounced summer opening of the sea ice cover in the East Siberian and Laptev Seas [*Serreze et al.*, 1995; *Maslanik et al.*, 1996, 1999].

Although there has much been found about Arctic sea ice variability from observational studies there is still a large potential for modelling efforts. This is primarily because recently developed reanalysis data sets enable realistically hind-cast simulations of sea ice models over a rather long time period. As a result, besides the observed quantities, also the 'non-observable' of the Arctic ice pack, such as ice export, ice thickness, or net freezing rate, can be analysed and related to the variability of the forcing data. Moreover, idealised simulations can be performed to asses the relative contributions of individual forcing parameters.

The following chapter is organised as follows. The analyses of the interannual variability of ice coverage, ice thickness, and ice exports as well as the investigation of a possible link between the Fram Strait ice export and the NAO are presented in separate

sections. Due to their somewhat different scopes, the individual sections contain separate introductions as well as separate conclusions and discussions.

4.2 Variability of Ice Extent

4.2.1 Introduction

By far the largest database about the Arctic ice pack has been collected for the parameters ice extent and ice concentration. Based on ice charts collected from various national agencies and on recent satellite observations there exists a monthly database for the sea ice extent of the Arctic which covers the period from 1953 to present [e.q. *Chapman and Walsh*, 1993; *Parkinson et al.*, 1999]. On the basis of this half-a-century long data set much has been found about interannual variations of the Arctic sea ice extension. As an example, *Walsh and Johnson* [1979a] have shown that both the summer and winter ice coverage of the Arctic can substantially vary between individual years. Overall, the largest variations of the sea ice extent occur within the annual cycle but interannual variations are generally of the order of 1/3 of the seasonal excursions [*Lemke et al.*, 1980].

The relevance of the interannual variations is highlighted when considering the debate about trends of the Arctic ice extent as an indicator of a possible climate warming. *Walsh and Johnson* [1979a] reported from a 25-yr dataset (1953–1977) of gridded sea ice concentrations that the extent of the Arctic's ice pack increased from the mid-1960s whereas it decreased during the early 1970s. From sea ice charts of the United Kingdom Meteorological Office for the period 1966–1976 *Lemke et al.* [1980] found a mean retreat of the total sea ice cover of 0.4% per year. However, this overall negative trend was partitioned into a large increase in the Davis Strait area and a large decrease in the eastern Atlantic region. From satellite observations *Parkinson and Cavalieri* [1989] found a small decrease during 1973–1976 (0.6% per year) which was followed by a small increase (0.2% per year) in the period 1979–1986. They also found concurring variations of ice coverage in the seas east and west of Greenland. On the background of these interannual variations *Parkinson and Cavalieri* [1989] concluded that no definitive identification of an overall trend for the entire period was possible. About the same conclusion was obtained by *Johanessen et al.* [1995] who investigated satellite based ice extent time series of the SMMR and SSM/I sensors separately. Although they found a decrease of ice extent ($-2.5\%/dec$ and $-4.3\%/dec$ for the periods 1978–87 and 1987-94 respectively) and ice area of the Arctic they stated that due to the shortness of the separate time series even a single unusual year can substantially influence the estimated trends. Using the same satellite observations but arranged into a combined, matched data set *Cavalieri et al.* [1997] found a statistically significant decrease of the Arctic ice extent ($-2.5\%/dec$) but found also interannual variations of about the same magnitude ($2.3\%/dec$). Statistically significant trends were also estimated by *Chapman and Walsh* [1993] who analysed a combined data set consisting of both ice charts and satellite observations for the period 1953–1990. Moreover they found that the time scale of sea ice anomalies ranges from months to years and that some larger anomalies can be tracked through several years.

As a prominent example of this persistence *Mysak and Manak* [1988] have shown that the large positive ice extent anomaly of the Greenland Sea in 1968, which was associated with the GSA [*Dickson et al.*, 1988], was presumably advected by the subpolar gyre into the Labrador Sea where it re-emerged in 1972. They further suggested that the time scale of the subpolar gyre is responsible for decadal scale anomalies in the Baffin Bay/Labrador Sea region and in the Greenland, Barents, and Kara Seas. Moreover they found out-of-phase variations of the ice extents in the Beaufort and Chukchi Seas compared to those of

the Greenland Sea. Given the latter relation *Mysak et al.* [1990] suggested a feedback loop in which anomalous river runoff from the Mackenzie river leads to increased ice coverage of the Beaufort Sea and, by advection, to enhanced ice extents of the Greenland Sea 3 years later. Subsequently, positive ice extent anomalies cause enhanced cyclogeneses over the Greenland Sea region which in turn are believed to increase the precipitation over the Mackenzie's drainage area. However, from a model study *Tremblay and Mysak* [1998] found runoff anomalies of the Mackenzie to be not sufficient in creating noticeable sea ice variations in the Beaufort and Chukchi Seas. Thus, questioning an important link of the feedback-chain of *Mysak et al.* [1990] reduces the overall confidence in their decadal loop.

A more objective approach in analysing ice extent variations was presented by *Walsh and Johnson* [1979a] and *Walsh and Johnson* [1979b]. From EOF analyses of monthly anomalies they extracted dominant modes of ice extent variations. One of these modes shows opposite anomalies between Atlantic and Pacific regions of the Arctic which is consistent with the above described findings of *Mysak et al.* [1990]. Another mode, which was also indicated by other studies, shows opposite anomalies between the western and eastern sides of Greenland, i.e., between the Baffin Bay/Labrador Sea region and the Greenland and Barents seas. From additional EOF analyses of meteorological parameters they concluded that the surface air temperatures show the strongest relation to sea ice fluctuations. Moreover, they found that the coupling between sea ice and atmospheric anomalies is considerably stronger if spatial modes are considered than it is for area averaged quantities. From asymmetries of the ice-atmosphere cross-correlation functions they further found a dominance of atmospheric forcing of sea ice anomalies [see also *Lemke et al.*, 1980], that is, there are more indications that the atmospheric variability causes sea ice variations than vice versa. Similar analyses were presented in a recent paper of *Deser et al.* [2000] but considering summer and winter season variability separately and using a significantly longer data set (1953–1997) which is based on an updated version of that of *Chapman and Walsh* [1993]. As previously identified by *Slonosky et al.* [1997], the dominant mode of wintertime variability was found to be a pattern of concurrent anomalies at the western and eastern coasts of Greenland which is temporally correlated with the North Atlantic Oscillation (NAO). In summertime largest interannual variability was found at the Siberian coasts, that is, in the Kara, Laptev, and East Siberian seas.

During the summer season, when the ice is not restricted by land, the ice cover of the Arctic generally exhibits larger interannual variability than during the other seasons [e.g. *Parkinson et al.*, 1999]. *Chapman and Walsh* [1993] found the record summer minimum within their dataset (1953-1990) in 1990 as well as other pronounced minima in 1977 and 1981. Considering the satellite record only, the most extreme minima occured since 1990 [*Serreze et al.*, 1995; *Maslanik et al.*, 1996] and were concentrated in the Laptev and East Siberian seas. *Maslanik et al.* [1996] found that in the summers of 1990, 1993, and 1995 the sea ice extents were 13%, 9%, and 12% less than the average respectively. Moreover, *Maslanik et al.* [1999] reported about a recent negative anomaly in 1998 which this time occurred in the Beaufort Sea and represents the record minimum ice coverage of this area.

Although most information about sea ice extent variability have been extracted from observations, there are still some open questions which can be answered by numerical models. One of these question is, e.g., about the relative importance of thermodynamic versus dynamic processes for the formation of the extreme summertime anomalies of the 1990s [*Maslanik et al.*, 1996]. By comparing idealised simulations with a sea ice-only model *Kreyscher* [1998] found that the record minimum of the ice extent in 1990 was

primarily attributable to dynamical effects caused by interannual variability of the wind forcing. Moreover he found that the summertime ice extent can largely be explained by anomalies of the circulation of the wind field. A comparison of four sea ice models with different rheologies but the same thermodynamics and the same forcing [*Kreyscher et al.*, 2000] revealed also an importance of the implemented dynamical scheme. Only two of the analysed models, one of them is the model used in the present study, were able to reproduce the observed summer minima.

The main purpose of the following section is the comparison of the model results with observations. This will not only be limited to the comparison of zero and first order moments but will also show that the sea ice model is able to reproduce some important features of the observed interannual ice extent variability. Moreover, according to *Kreyscher* [1998], the relative contributions of SAT and wind forcing of large sea ice anomalies will be investigated.

4.2.2 Temporal Evolution of Sea Ice Extent and Ice Area

The temporal evolution of simulated ice extent and ice area for the period 1951–1999 is shown in Fig. 4.2. Overall, both quantities show pronounced variability on time scales from years to decades. That is, among short-term year-to-year variability there are longer period of persistent negative (1990s) or positive (1960s) anomalies. The latter period was subject to early trend estimates which coincide with the model results and can now be considered from a longer-term perspective. Within the period 1953–77 there is an increase of ice extent during the 1960s and a decrease in the early 1970s as was analysed by *Walsh and Johnson* [1979a]. *Lemke et al.* [1980] found a slight decrease within the period 1966-76 which now appears as the downward slope of a longer-term positive anomaly. Over the entire simulation period there appears a slight downward trend in both the ice extent and ice area which will be considered in more detail in Chapter 5. The record winter maximum of the simulated ice coverage appeared in 1983, whereas the summer minimum was reached in 1990.

Compared to the satellite estimates, which are available since 1979, the sea ice model generally overestimates the ice extent throughout all seasons but autumn (Fig. 4.3a). The root mean square differences (RMSD) between model and observations increases from spring to summer and decreases thereafter (Fig. 4.3a). This is due to the fact that during summer the ice pack is less bounded by the coasts and, thus, deviations of the model from the observational "truth" are more likely to occur. Similar differences to the satellite data are found for the ice area (Fig. 4.3b) but with a general underestimation by the model during the second half of the seasonal cycle. However, in relation to their overall mean values the errors of ice extent and ice area are generally in the range of 2–10%. Regionally, the smallest RMS differences between observed and modelled ice concentrations are found in the central Arctic with values smaller than 10% for both annual and monthly means (not shown). The largest RMS differences are found near the ice edges with values of up to 15% for annual mean data and up to 25% if monthly means are considered (not shown). Note, however, that the accuracy of the satellite estimates ranges from 10-20% during the melting season to 5-10% during the remainder of the year [e.g. *Steffen et al.*, 1992]. The maximum interannual differences with values of about 30% ice concentration are found within the East Greenland Current (EGC). This can at least partly be explained by the occurrence of the Greenland Sea "Odden" feature which obviously cannot be resolved by

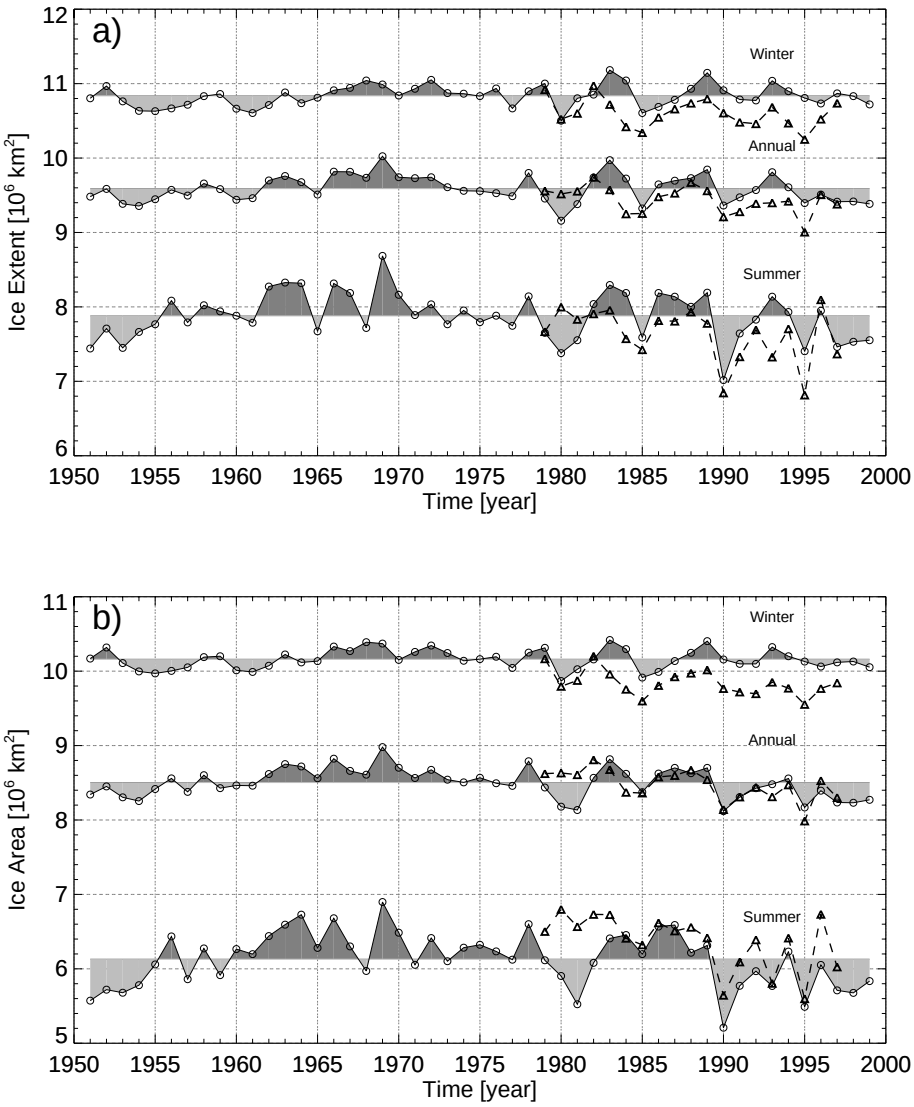

Figure 4.2: Annual time series of Arctic ice extent and ice area. Shown are simulated (solid lines with circles) together with observed (dashed line with triangles) time series for winter (JFM), annual, and summer (JAS) averages of a) sea ice extent and b) sea ice area. The observations are derived from satellite retrievals of ice concentration merged onto the model grid.

the model. The "Odden" is an ice tongue within the Greenland Sea between 73°N and 77°N which can protrude eastward to about 5°E. It usually forms at the beginning of the winter season and can cover about $300\,000\,km^2$ [*Shuchman et al.*, 1998]. Although the impact of oceanographic parameters has not yet been quantified, from the analysis of meteorological conditions only *Shuchman et al.* [1998] concluded that oceanic processes within the Greenland Sea must play a key role in the formation and maintenence of this interannual feature.

During roughly the last two decades the temporal evolution of simulated ice extent and ice area anomalies is generally in good agreement with the satellite observations except for the first 2–3 years of the observational record (Fig. 4.2). The correlation coefficients

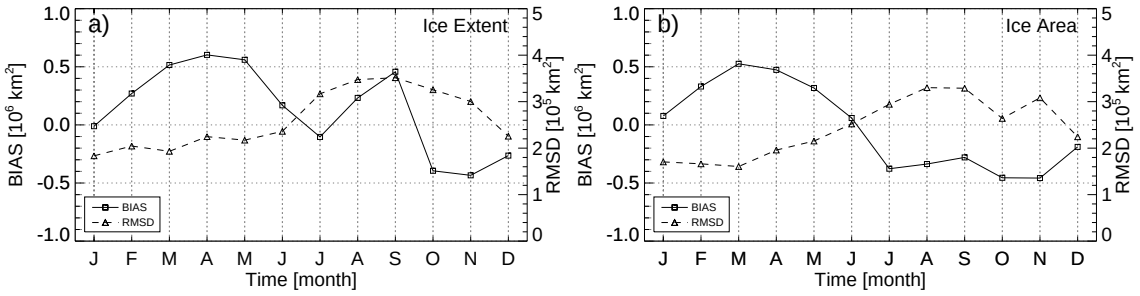

Figure 4.3: Mean seasonal cycles of BIAS (solid) and RMSD (dashed) between simulated and satellite derived ice extent (a) and ice area (b) in km^2 of the time period 1979–1997. Note the different scales for BIAS and RMSD. The left ordinate is for the BIAS whereas the right ordinate shows the scale for the RMSD.

between the annual mean time series over the period 1982–97 are $r = 0.67$ for the ice extent and $r = 0.81$ for the ice area. Taking the entire satellite period into account the correlations are smaller ($r = 0.41$ and $r = 0.54$ for extent and area respectively) because the model significantly underestimates the ice coverage in 1980/81. This period coincides with a record maximum of the SATs of the extra-tropical Northern Hemisphere [*Walsh*, 1991; *Serreze et al.*, 2000] within the last 50 years which is also evident in the NCEP/NCAR data. The possible reasons for this discrepancy between the satellite retrievals and the model results are manifold. Among them are inaccuracies of the satellite estimates, the forcing data, and the model physics, or interannual effects of other forcing quantities which are not included the present integration (e.g. oceanic or hydrological effects). Deficiencies of the model physics are not very likely because other sea ice integrations using different types of sea ice models show similar differences compared to the satellite data. In the comparison of four different rheology schemes *Kreyscher et al.* [2000] showed that all of the investigated models underestimate the ice extent during 1979–81. Moreover, an integration of the global coupled sea ice-ocean model CLIO [*Goosse et al.*, 1999] forced with NCEP/NCAR SATs (as in the model integrations of *Kreyscher et al.* [2000]) and winds does also underestimate the ice extent during this time [*Fichefet and Goosse, pers. comm.*]. The same holds for the coupled sea ice-ocean model integration of *Zhang et al.* [2000] although this was forced by winds and temperatures not derived from the NCEP/NCAR data. When considering the differences to the satellite data in more detail it emerges that the most pronounced underestimations occur during summer (Fig. 4.2) and autumn and are most pronounced in the Laptev Sea, the outermost Beaufort Sea, and in the Baffin Bay (not shown). During autumn variations of the oceanic mixed layer depth can have significant impact onto the refreezing process due to differences of its heat storage. That is why variations of river runoff into the Arctic Ocean could have been important (note that none of the above cited model integrations used interannually varying river runoff data). Enhanced freshwater discharge from Arctic rivers can stabilise the oceanic stratification and lead to a shallower mixed layer which faster cools down in autumn. However, non of the four major rivers entering the Arctic Ocean shows significantly enhanced discharges in the early 1980s (Fig. 4.4). It is only the Ob-river entering the Kara Sea which exhibits a pronounced positive anomaly in 1979 (roughly 50% above average; see also Tab. 3.3) that could have freshened the waters at the Siberian coast.

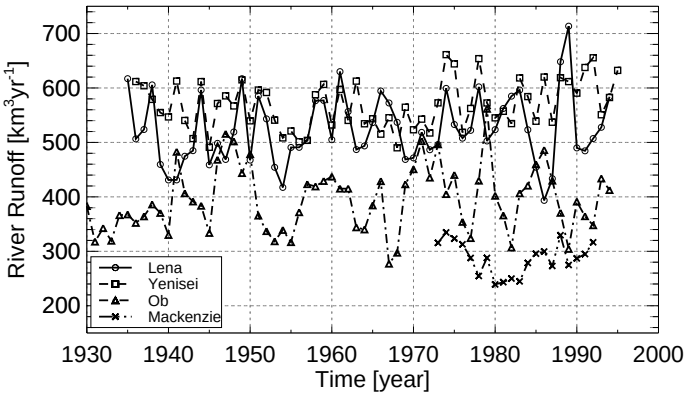

Figure 4.4: Annual runoff time series ($km^3\,yr^{-1}$) of the four major Arctic rivers Lena (solid with bullets), Yenisei (dashed with squares), Ob (dash-dotted with triangle), and Mackenzie (dash-dot-dotted with crosses). The runoff data were obtained from the Global Runoff Data Centre (GRDC), Bundesanstalt für Gewässerkunde, Kaiserin-Augusta-Anlagen 15–17, D-56068 Koblenz, Germany.

Summarising, the underestimation of the modelled ice extent and ice area during the early 1980s cannot satisfactorily be explained. Assuming the correctness of the satellite retrievals it is unlikely that this difference is due to deficiencies of the physics implemented in the sea ice model. However, apart from this discrepancy, it can be stated that the sea ice model forced by interannual varying SATs and winds is able to reproduce the gross features of the observed temporal evolution of the Arctic ice extent.

4.2.3 Analysis of the Recent Summer Minima

Observational data show that the most extreme minima of the Arctic ice coverage have all occured since 1990. The same holds also for the model results although there are additional minima of the sea ice area of comparable magnitude in 1951 and 1981 (see Fig. 4.2). The large summer reductions during the 1990s primarily occured in the Laptev and East Siberian Seas and were accompanied by increasing cyclone activity north of Siberia [*Maslanik et al.*, 1996] and rising air temperatures [e.g. *Serreze et al.*, 2000]. Moreover, during the 1990s there was also a record minimum of sea ice extent in the western Arctic. Although these recent minima have been well observed using passive microwave imagery and analysed by considering meteorological parameters [*Serreze et al.*, 1995; *Maslanik et al.*, 1996, 1999] the relative contributions of winds and temperatures to the formation of these anomalies could not be assessed. This point will be addressed in the following by comparing the observed summer ice concentrations of 1990, 1995, and 1998 with the results of the standard sea ice model integrations and, additionally, with the output of the two idealised simulations using either winds (WIND) or surface air temperatures (TEMP) as the only interannual varying forcing quantity.

Based on the observational record of *Chapman and Walsh* [1993] and on recent satellite retrievals the Arctic sea ice area exhibited its record minimum during 1990 which was characterised by extensive ice-free conditions along the Siberian coast [*Serreze et al.*, 1995] (Fig. 4.5a). It corresponds to a reduction of 30% of the ice covered area in the Siberian sector from 140°E to 160° north of 80°N [*Serreze et al.*, 1995]. From IABP temperature data (consisting of data from coastal stations and buoys) *Serreze et al.* [1995] found that

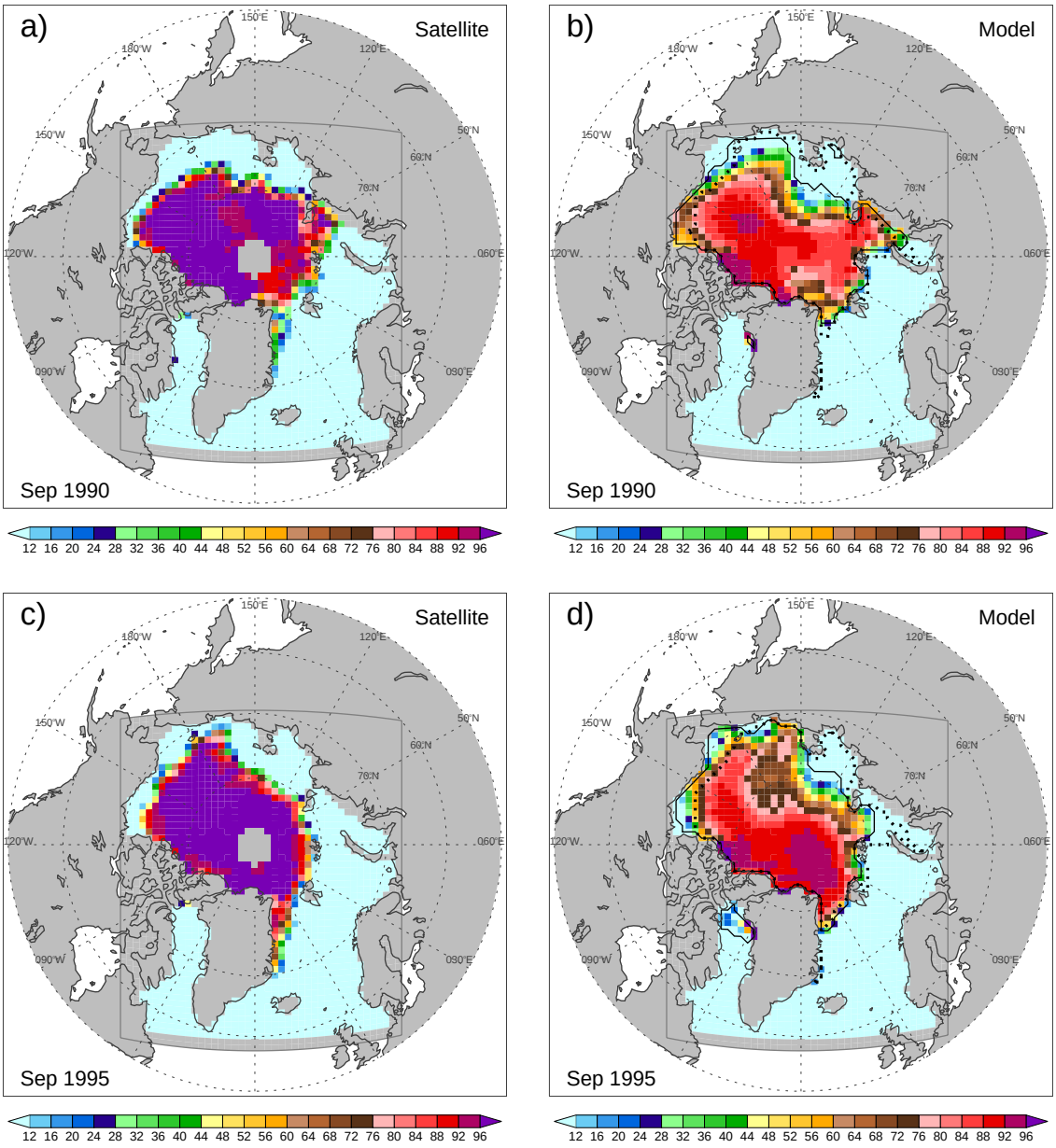

Figure 4.5: Observed and simulated summer minima of the Arctic sea ice extent. Shown are the September ice concentrations for both satellite (left panel) and simulation (right panel) for 1990 (a and b), 1995 (c and d), and 1998 (e and f). Additionally to the standard simulation the ice edges (15% contour) of the idealised simulations WIND (solid line) and TEMP (dotted line) are shown.

from May to June 1990 all of the Arctic Ocean experienced positive temperature anomalies with largest values of ~ 2.5–$3.0\,^{\circ}$C in the Laptev, the East Siberian, and the Chukchi seas. In July SATs were below average along the Siberian coast but they were above average again in August. Moreover, melt onset occured this time at least 10 days earlier along the coast from the Laptev Sea to Alaska. The SLP field was also highly unusual during this year [*Serreze et al.*, 1995]. It was characterised by an anomalously low centred north of

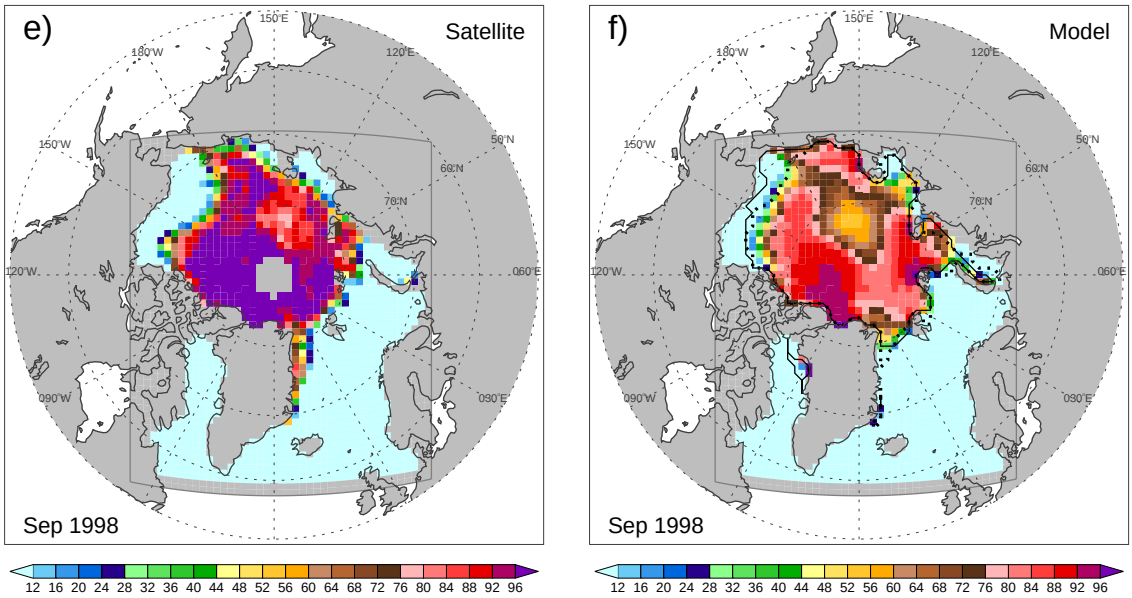

Figure 4.5: (continued)

Severnaya Zemlya ($\sim$ 80°N, 100°E) and higher than normal pressures over the southern Beaufort Sea which lead to strong southerly winds along the coasts from the Laptev Sea to north of Alaska. The September ice concentration field simulated by the sea ice model (Fig. 4.5b) shows a rather good correspondence to the observations. Having in mind the reduced accuracy of the satellite retrievals during summer (10–20%) the model slightly overestimates the ice extent in the East Siberian, the Chukchi, and the Beaufort seas. On the other hand, simulated ice concentrations are lower in the northern Laptev Sea and within in the East Greenland Current. However, the overall character of the anomaly is well captured by the model. Considering the ice edges of the idealised simulations it turns out that primarily anomalous winds were responsible for the ice free conditions in the Laptev and East Siberian seas. That is, the ice edge of the WIND integration in September 1990 is very close to that of the standard simulation. On the other hand, having only anomalous SATs in 1990 the ice edge would still extend to the coasts. This points towards the dominance of northward ice advection supported by enhanced melting due to the ice-albedo feedback in creating the large summer minimum of 1990. The ice-albedo feedback is important because the anomalous offshore winds not only lead to enhanced northward advection of ice but lead also to an enhanced breakup of the ice pack by divergence which in turn decreases its albedo. From the idealised simulations it can further be deduced that in the Beaufort Sea the anomalous winds tend to increase the ice coverage whereas positive temperature anomalies would lead to larger ice free areas in this region as was observed. This can be explained by advection of very thick ice from north of the Canadian Archipelago. In 1989 and 1990 the ice thickness in this region was the largest within the entire simulation period (Fig. 4.8). The latter explains why the SAT anomalies in the Beaufort Sea region in 1990 were not sufficient to melt enough ice to effectively reduce the ice extent as was questioned by *Serreze et al.* [1995].

In general the same conclusions as for 1990 hold also for the summer minimum of 1995.

However, ice thicknesses in both the Beaufort Sea and north of the Canadian Archipelago were on average this time (Fig. 4.8). This is probably the reason for the comparatively large open water area in the southern Beaufort Sea in both the observation and the model (Fig. 4.5c and d). Although the sea ice minimum of 1995 is not as pronounced as that of 1990 the open water areas in the Laptev Sea are again primarily due to the anomalous wind forcing.

The most recent summer reduction of Arctic ice extent occured in 1998 and was this time concentrated in the Beaufort and Chukchi seas (Fig. 4.5e and f). With an ice extent of 39% below average this anomaly represents the record minimum of the western Arctic based on observations from 1953–present [*Maslanik et al.*, 1999]. The atmospheric conditions of 1998 were characterised by above average SLPs over the Beaufort Sea. This leads to enhanced south-easterly winds in this area which are associated with the advection of anomalously warm air [*Maslanik et al.*, 1999]. Moreover, in 1998 the offshore blowing winds were stronger and the associated temperature anomalies greater over the southern Beaufort Sea than is typical for years with light ice coverage in this region. The latter might be the reason for the roughly equal contributions of winds and SATs to the sea ice minimum as can be concluded from the idealised simulations (Fig. 4.5f). In contrast to the above discussed anomalies the dynamical effects of the wind field in 1998 are sufficient to create the observed open water area. This is further emphasised by the fact that the opening of the southern Beaufort Sea already started in April (not shown) which cannot be attributed to melting. As a consequence of this early opening the annual averaged ice thickness in this region exhibits its record minimum in 1998 with an anomaly of about $2\,m$ below the long-term average (Fig. 4.8).

4.2.4 Dominant Modes of Ice Coverage Variability

A further validation of the models ability to reproduce observed features of Arctic sea ice variability is the analysis of preferred modes as was done for observational data [*Walsh and Johnson*, 1979a,b; *Lemke et al.*, 1980; *Deser et al.*, 2000]. Whereas the earlier of these studies focused on ice extent variations of longitudinal sectors without consideration of the season the recent study of *Deser et al.* [2000] investigated anomalous fields of ice concentration separately for winter and summer. The subsequent analysis will follow the methodology of *Deser et al.* [2000] that is, the leading modes of both winter and summer ice concentration variations will be extracted by EOF decomposition. To focus on interannual variability only linear trends were subtracted from the seasonal mean anomalies prior to the EOF analyses.

Fig. 4.6a shows the leading EOF of simulated winter sea ice concentration anomalies which is very similar to that found from the observations [*Deser et al.*, 2000, their Fig. 3]. It primarily projects onto the Atlantic sectors of the ice cover, that is the Baffin Bay/Labrador Sea region as well as Greenland and Barents seas. This is not surprising because these are the only regions during the wintertime where the ice cover is not bounded by land and, thus, the ice edge is free to vary. Note, that the same holds for the Northern Pacific which is not included into the model domain. In more detail, the pattern of the EOF exhibits opposite anomalies in the Greenland/Barents Seas and in the Baffin Bay/Labrador Sea region and explains 35% of the overall variability during wintertime (the second and third modes explain 21% and 11%, respectively). The associated expansion time series (Fig. 4.6c) shows the temporal evolution of this mode which

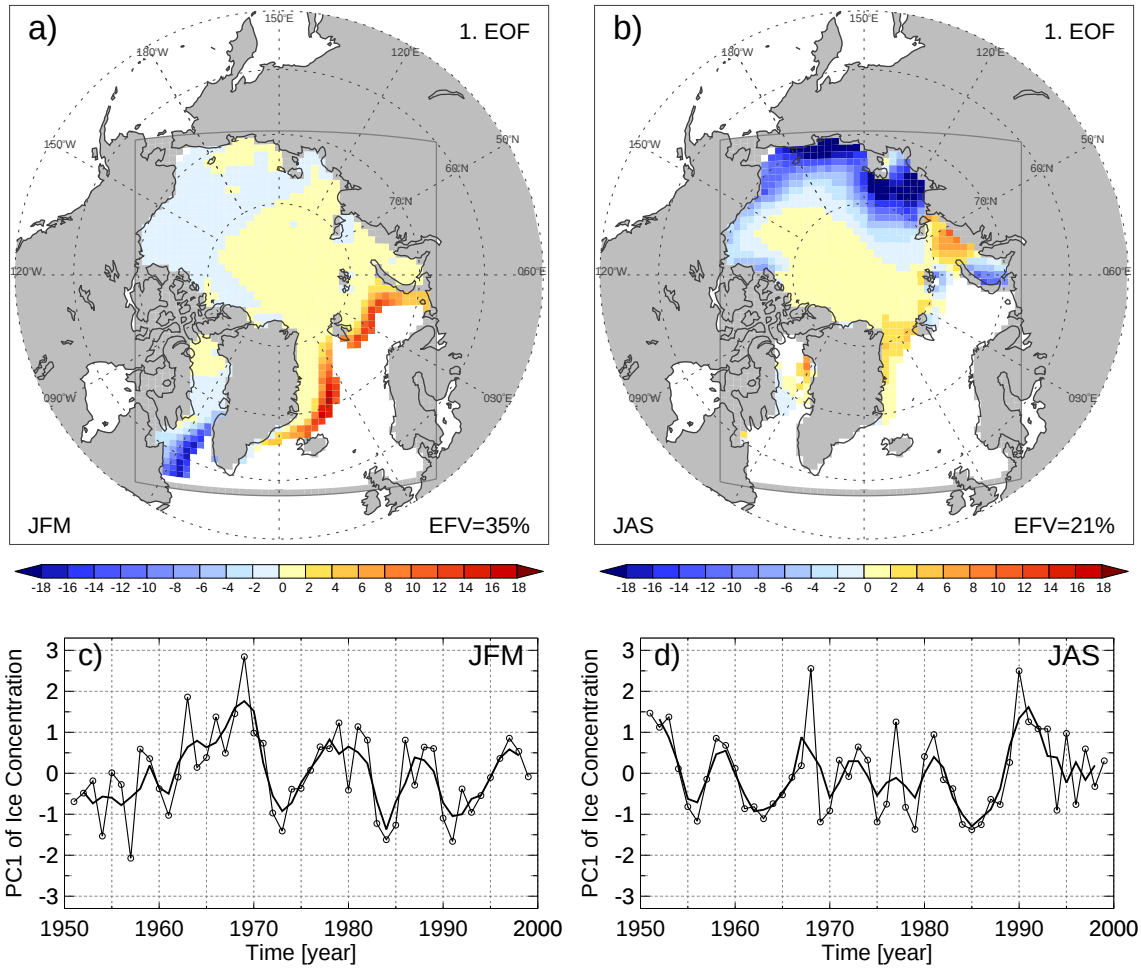

Figure 4.6: Leading modes of ice concentration variability for winter and summer. Shown are the patterns and associated expansion time series (PCs) of the first EOFs for both wintertime (a and c) and summertime (b and d) sea ice concentration variability. The portion of explained field variance (EFV) is stated in the lower right panel of a and b respectively. The thick lines in c and d represent 3-yr running averages of the corresponding PCs. After the criterion of *North et al.* [1982] the EOFs are well separated from their corresponding subsequent modes.

closely corresponds, depart from the linear trend, to that found from the observations [*Slonosky et al.*, 1997; *Deser et al.*, 2000] (note that linear trends were subtracted prior to the analysis). That is, in the 1960s, the late 1970s and early 1980s, and in the late 1990s ice concentrations were above average in the eastern North Atlantic whereas they were anomalously low west of Greenland. On the other hand, the opposite holds true for the early 1970s, the mid 1980s, and during the early 1990s. As was pointed out by *Deser et al.* [2000] the atmospheric pattern associated to this mode is that of the NAO which is the dominant mode of atmospheric variability during wintertime. It is associated with enhanced north-westerlies and below average temperatures over the Baffin Bay/Labrador Sea region and with enhanced south-westerlies and positive temperature anomalies over the eastern portion of the North Atlantic and Europe [e.g. *Hurrell*, 1995]. Indeed, the NAO index explains about one third of the variability of the expansion time series (PC) of

the ice mode, as was also found from the observations [*Deser et al.*, 2000]. The correlation coefficient of $r = -0.56$ between the NAO index (note, that the linear trend of the NAO index was subtracted to be consistent with the EOF analysis) and the PC time series of the ice concentration EOF means that the anomaly pattern of Fig. 4.6a is typical for low NAO winters and that the opposite holds for high NAO winters. From the observations it could not be deduced whether the thermodynamic effect through advection of SAT anomalies or the dynamic effect through wind-driven ice drift anomalies [*Deser et al.*, 2000] dominates the observed sea ice variations. This question, however, can be investigated by comparing EOFs of the idealised simulations WIND and TEMP with the first mode of the standard simulation. The pattern of the first EOF of the WIND simulation (not shown) strongly projects onto ice concentration anomalies in the East Greenland Current north of Iceland but exhibits nearly no anomalies in the Baffin Bay/Labrador Sea region. This is primarily due to the dominance of wind-driven variations of the ice export through Fram Strait which result in ice edge variations further south. Correspondingly, no significant correlations between both the patterns and the time series of the dominant EOFs of the WIND and the standard simulation are apparent (there is also no correspondence with lower order EOFs of WIND). On the other hand, the dominant EOF of the TEMP simulation exhibits a very close correspondence to that of the standard run. That is, the spatial patterns of the EOFs are very similar (spatial correlation of $r = 0.97$) and so are the associated time series (serial correlation $r = 0.96$). Thus, from the simulation results it can be concluded that the thermodynamic effects of enhanced (reduced) ice growth by advection of anomalously cold (warm) air associated with the NAO are more important for the out-of-phase variations of the ice concentration at the eastern and western coasts of Greenland than the purely dynamic effects.

As was indicated in the previous subsection variations of the summertime ice coverage are more concentrated on the ice edges at the Siberian and Alaskan coasts. Accordingly, the pattern of the dominant EOF of ice concentration variability during the summer season (Fig. 4.6b) projects most strongly onto these regions. It shows opposite anomalies between the Laptev, East Siberian, Chukchi, and Beaufort Seas and the remainder of the ice pack. From the associated PCs (Fig. 4.6d) it can be concluded that summer reductions of the ice coverage due to this mode occured in the early 1950s, in 1968, and in the early 1990s. However, the first EOF only explains 21% of the overall summertime variability of ice concentration but explains half ($r = 0.70$) of the summer ice area and roughly one third ($r = 0.55$) of the summer ice extent variability (Fig. 4.2). As was mentioned in the previous subsection primarily the effects of anomalous winds were responsible for the pronounced openings of the summer ice cover. This conclusion is further supported by the analysis of the dominant summertime EOFs of the idealised simulations. That is, the first EOF of the WIND simulation exhibits most similarity to that of the standard case in both the spatial ($r = 0.94$) and the temporal ($r = 0.90$) domain. However, also the leading mode of TEMP integration shows some correspondence to that of the standard integration with the spatial and temporal correlation coefficients of $r = 0.48$ and $r = 0.49$ respectively.

4.2.5 Conclusions

The interannual variability of the modelled sea ice extent and ice area was investigated. Because much about this topic has already been found from observations the above inves-

tigations can primarily be considered as a validation of the model. From the comparison of the simulation results with the observations it can be stated that:

- In comparison to satellite estimates of the sea ice extent and ice area the model slightly overestimates (underestimates) the extent of the Arctic ice pack during wintertime (summertime) and shows largest interannual root mean square deviations from the satellite retrievals during summertime. However, the overall errors of ice extent and ice area are in the range of 2–10% relative to their corresponding mean values.

- Apart from a discrepancy in 1980/81 the temporal evolution of interannual anomalies of ice area and ice extent is well reproduced. Especially the recent summer openings of the Arctic ice cover are captured well by the model.

- EOF analyses of ice concentration variability during both winter and summer revealed dominant modes which are close to the one found from observations. That is, a pronounced seesaw between the Baffin Bay/Labrador Sea and the Greenland/Barents Seas during winter and in-phase variations along the Siberian and Alaskan coasts during summer.

Complementary to observational studies, the relative impacts of interannual anomalies of winds and surface air temperatures on sea ice variations were investigated. From the analysis of the idealised simulations WIND and TEMP the following conclusions can be drawn:

- Anomalous winds were most important for the evolution of the summertime minima in the Siberian sectors. In the Beaufort Sea, on the other hand, the recent openings depend on both, the advection of ice thickness from the region north of the Canadian Archipelago and the temperature anomalies.

- Accordingly, the leading mode of summertime variability is also primarily related to anomalous winds as the similarity of the first EOFs of the standard integration and the WIND simulation reveals.

- The leading mode of wintertime variability, that is the seesaw between the regions west and east of Greenland, is primarily attributable to the thermodynamic effects of the advection of anomalously cold or warm air masses.

4.2.6 Discussion

Interannual variability of the simulated Arctic ice extent is investigated and compared to results from observational studies. Given the capability of the sea ice model to reproduce the major sea ice properties [*Kreyscher et al.*, 2000] the comparison presented above can be considered as a sensitivity study to assess the degree to which observed sea ice variations can be explained by surface winds and surface air temperatures. On the other hand, ice coverage variations which occured in nature and were probably caused by processes not captured by the present simulation (e.g. interannual variations of clouds, precipitation, ocean currents, oceanic heat budget) could have affected the prescribed forcing fields and, thus, are reflected by the model. However, because the remainder of this chapter concentrates on sea ice parameters which have not been sufficiently observed (e.g. ice

thickness and ice volume transports) the above shown rather good agreement between the model results and observed sea ice extent variations are necessary to have confidence in the findings of the remainder of this study.

Another great advantage of modelling studies, besides the possibility to investigate "non-observables" of the sea ice cover, is their possibility of performing specific sensitivity studies. In particular, the relative importance of interannual variations of winds and temperatures on recent summer minima of the ice coverage is assessed. After *Maslanik et al.* [1996] these recent openings of the ice cover are related to cyclone activity in the Arctic which sharply increased since 1989. This is important because the position of the increased cyclone activity north of Siberia [*Maslanik et al.*, 1996, their Fig. 4] typically places the East Siberian Sea in the warm sector of the cyclones leading to stronger and more frequent warm, southerly winds. From the idealised simulations it is found, that the circulation anomalies without anomalous advection of warm air are sufficient to create the observed sea ice reductions of the eastern Arctic. This agrees with the findings of *Deser et al.* [2000] who found rather large temporal correlations ($r = 0.73$) between eastern summer sea ice indices with indices of their associated spring SLP patterns. *Kreyscher* [1998] came to the same conclusion by analysing a sea ice model integration without interannual variability of SATs over the period of 1979–1995. He found that the summer ice extent of this integration explains a large portion of the observed variations. Furthermore, he found a close relation between the circulation of the wind field and the summer ice extent. As suggested from *Maslanik et al.* [1996] and *Deser et al.* [2000], atmospheric circulation anomalies during spring initiate the sea ice anomalies by early breakup of the ice cover due to northward advection away from the coast which is, furthermore, accelerated by the positive ice-albedo feedback. *Zhang et al.* [2000] found from a modelling study an enhanced ice-albedo feedback in the eastern Arctic during 1989–96 relative to 1979–88 forced by changes in ice advection. In the present study, the close correspondence between the dominant modes of summertime variability of the standard and the WIND integrations reveals a general dominance of atmospheric circulation anomalies in determining summer ice area fluctuations.

A separate consideration of winter and summertime modes of variability, as done by *Deser et al.* [2000], is sensible because there exist large seasonal differences of the areal ice coverage and because the ice-albedo feedback only acts during summertime. This is highlighted by the fact that the dominant mode of wintertime variability is concentrated to the subarctic seas west and east of Greenland. Moreover, from the comparison with the leading modes of the idealised simulations it is found that during wintertime primarily SAT variations dominate the sea ice fluctuations. In particular, the temperature seesaw associated with the NAO is the primary reason for the out-of-phase variations of the ice coverage in the Baffin Bay/Labrador Sea and Greenland/Barents seas. This was previously identified by *Walsh and Johnson* [1979b] although they did not separate between summer and winter season and analysed a considerably shorter data set. On the other hand, *Yi et al.* [1999] found from SVD analyses of sea ice and atmospheric variations that this mode is primarily forced by NAO-related wind fluctuations.

A possible consequence of the decadal-scale variability of sea ice in the Baffin Bay/ Labrador Sea region is the creation of SST anomalies in the North Atlantic as suggested by *Deser and Blackmon* [1993]. They found pronounced negative correlations between the sea ice anomalies (leading by 1–2 years) and the temporal evolution of the second mode of wintertime SST and SAT variability which is characterised by opposite anomalies in

the regions east of Newfoundland and off the southeast coast of the United States. The strong correlations indicate that heavy sea ice in the Labrador Sea precede winters of colder-than-normal SSTs east of Newfoundland. Thus, there are not only indications that SAT variations force sea ice variability (as shown above) but there are also hints that sea ice variations lead to anomalies in SAT and SST. However, this direction of influence cannot be investigated with a sea ice model forced by SATs and winds and should be the focus of coupled models.

Summarising, apart from the rather good correspondence between the model results and the satellite observations, it is the close agreement of the dominant modes of simulated ice concentration variability with that found from observations [*Slonosky et al.*, 1997; *Deser et al.*, 2000] which enhances the confidence in the results of the remainder of this study.

4.3 Variability of Ice Thickness

4.3.1 Introduction

The problem of the poor availability of ice thickness observations in the Arctic was already mentioned in Chapter 3.4 where the mean state of the simulated ice thickness was compared to observational estimates. The case is much worse if variations about this mean state are considered. In contrast to the ice concentration, where satellites supply sufficiently large-scale informations for most of the last three decades, there are essentially no observational products allowing the large-scale estimation of the interannual variability of ice thickness. However, knowledge about natural ice thickness variations is essential in the context of assessing the significance of possible long-term trends of this parameter. For example, *Wadhams* [1990] presented evidence for a thinning of sea ice north of Greenland which was based on a comparison of submarine data from 1976 and 1987. Using an extended, multi-year data set *McLaren et al.* [1992] have shown that the interannual variations of ice thickness in the central Arctic were too large to assess the statistical significance of this decrease.

The present knowledge about interannual and longer-term variability of large scale sea ice thickness was entirely gained by numerical models. *Walsh et al.* [1985] showed from a nearly 30-yr integration of a sea ice-only model, that the total mass of Arctic sea ice exhibits strong seasonal and interannual variability. From a 39-yr integration of a primarily wind-driven sea ice model (interannually varying air temperatures were only prescribed near the coasts) *Flato* [1995] found substantial, concurring ice thickness variations in the Beaufort and in the East Siberian Seas. This was also found by *Arfeuille et al.* [2000] who analysed a purely wind-driven sea ice model integration which roughly covers the last four decades. From an analysis of several regional ice thickness anomalies they concluded that both advection and local effects contributed to these ice thickness variations. Moreover, they related ice thickness anomalies to SLP changes which alter the sea ice circulation regime. The existence of two different circulation regimes in the Arctic, an anticyclonic regime with a pronounced and a cyclonic regime with a weakened Beaufort Gyre, was first reported by *Gudkovich* [1961] from a comparison of SLP patterns with ice drift observations. Using a barotropic ice-ocean model with a prescribed ice thickness pattern *Proshutinsky and Johnson* [1997] have shown the alternation between these both regimes on a time scale of 10–15 years. *Johnson et al.* [1999] found that the circulation regimes modelled by *Proshutinsky and Johnson* [1997] were driven by pressure anomalies over the North Pole being very similar to the Arctic Oscillation (AO) pattern. However, they did not find much temporal correspondence with the AO index. *Polyakov and Johnson* [2000] suggested from a 50-yr integration of a coupled sea ice-ocean model that ice thickness variations are primarily driven by two oscillatory atmospheric modes acting in the Arctic domain. First, the decadal-scale AO drives the two circulation regimes and, second, a so-called low-frequency oscillation contributes to longer-term variability at periods of about 50-years. They argue that the superposition of both modes in the 1990s may explain the strong decrease of ice thickness during this time which is apparent in their model as well as in the observations *Rothrock et al.* [1999b]. However, for the definition of the low-frequency oscillation they refer to multi-decadal spectral peaks in individual geophysical time series of the North Atlantic region but they do not give a physical description nor an explanation of this mode.

The Arctic Oscillation, however, is a well defined oscillatory mode of the Arctic Atmosphere. It is described by the leading EOF of wintertime SLP variability of the northern hemisphere poleward of about 20°N which is characterised by a near annular structure with one centre of action located over the North Pole and two opposite centres located over the Azores and the Aleutians respectively. It is a robust pattern that dominates month-to-month and interannual variability. *Thompson and Wallace* [1998] have shown that this SLP mode is coupled to upper stratosphere variability. By statistical analysis they described the existence of a deep vertical coupling in the wintertime polar vortex. The AO resembles the NAO (see section 4.5) in many respects, but its centre of action covers more of the Arctic and giving it a more zonally symmetric appearance. Moreover, the AO accounts for a substantially larger fraction of northern hemisphere SAT variance than the NAO [*Thompson and Wallace*, 1998]. However, its annual character was partly questioned by *Deser* [2000]. She has shown that the Pacific and the Atlantic centres of the AO share less than 3% of their variance and, therefore, there is no coordinated behaviour of the SLP in these regions.

The aim of the following section is the description of the interannual variability of the present sea ice integration. After a short comparison with observational data long-term interannual time series from selected grid points are discussed. Furthermore, by using both EOF and SVD analyses preferred modes of variability as well as their relation to the atmospheric forcing data are identified. As for the ice extent this section is a necessary prerequisite for the analysis of long-term changes which will be discussed in Chapter 5. Moreover, results of this section can be used for supporting observational strategies as, for example, the planning of possible future scientific submarine missions [*Rothrock et al.*, 1999a].

4.3.2 Observational Estimates

For the comparison of the mean spatial pattern of simulated ice thickness with observations in Section 3.4 data from under-ice submarine cruises were used. However, for the assessment of the models ability to reproduce the observed interannual variability it is necessary to have annual time series of observed ice thickness at individual locations. In contrast to the ice concentration, remote sensing techniques for the derivation of ice thickness are still at an early state of development and reliable products are not yet available. Therefore, ice draft measurements from ULS moorings are presently the only source for multi-year time series of ice thickness.

Table 4.1: Data gaps for the ULS-based ice thickness time series shown in Fig. 4.7.

Year	Beaufort Sea	Fram Strait
1991	Jan, Feb, Mar	
1993	Aug, Sep, Oct	
1995	Jul, Aug	Aug
1997	Mar, Aug, Sep	

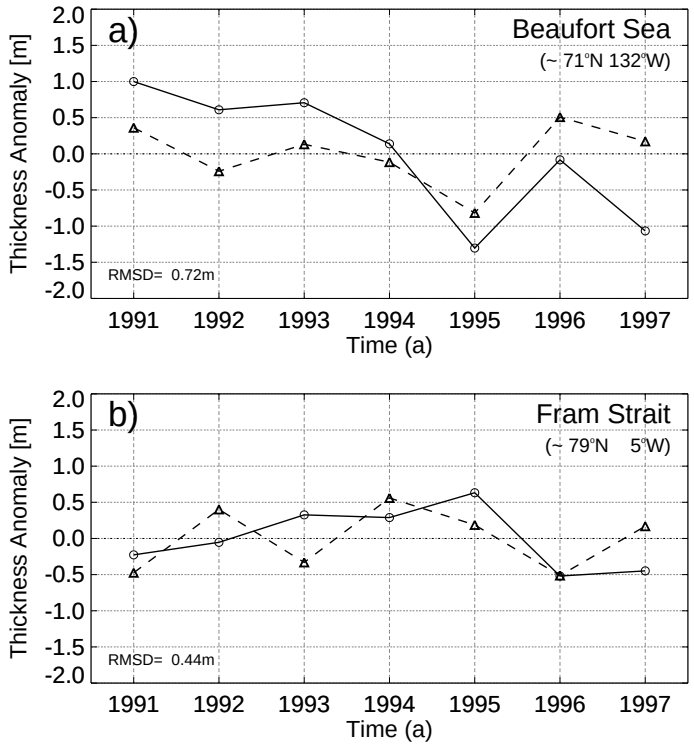

Figure 4.7: Comparison of simulated (solid) with observed (dashed) annual mean anomalies of ice thickness at sites in a) the Beaufort Sea and b) Fram Strait. The observations for the Beaufort Sea were derived from an updated version of the moored ULS data set of *Melling and Riedel* [1996]. The ice thickness time series for Fram Strait is based on moored ULS data obtained from the Norwegian Polar Institute ("http://www.npolar.no/adacit/"). A constant factor of 1.136 was applied for the conversion from ice draft to ice thickness [*Vinje et al.*, 1998]. Note, that individual annual mean values are influenced by missing data in the observational time series (see Tab. 4.1). For comparison simulated data were averaged over the same specific months as was done for the observations. Similar figures are presented by *Kreyscher et al.* [2000] (their Fig. 9) but for a shorter time period and for additional sea ice models.

Moored ULSs have been deployed in the Arctic since 1987 [e.g. *Melling and Riedel*, 1996; *Vinje et al.*, 1998]. But it is only since 1991 when near-continuous monthly mean time series of ice draft measurements have been available. Multi-year time series are available from Fram Strait and from the near-shore Beaufort Sea for the period 1991–1997 (see Fig. 4.7 for geogr. locations). Due to technical problems there are some gaps in these time series (see Tab. 4.1) which make an estimation of interannual variability rather difficult. That is, annual averages calculated without data for some specific months are biased towards lower or higher annual mean values depending on the season when the data are missing. For example, the annual mean thickness for the Beaufort Sea site in 1993 will be overestimated because there are no data for the summer season (Aug, Sep, Oct; see Tab. 4.1).

However, the observational time series are well suitable for a comparison with the simulated data. Fig. 4.7 shows the time series of ice thickness anomalies for both the ULS data and the simulation results. For comparison, annual mean values of the modelled

data were calculated by averaging over the same specific months as were done for the ULS data. Overall, there is a fairly good agreement between simulated and observed annual mean anomalies with RMSDs of $0.72\,m$ for the Beaufort Sea and $0.44\,m$ for Fram Strait. Especially the temporal evolution of the ice thickness anomalies are well reproduced by the sea ice model. Even when taking the data gaps into account, there is a tendency in the Beaufort Sea of decreasing ice thicknesses which is also evident in the model data. Furthermore, both the observations and the model indicate a relative minimum in 1995 which cannot be attributed to missing data in July and August. In contrast to the Beaufort Sea site there are rather constant ice thickness values in Fram Strait with only small annual deviations from the 7-yr mean value.

On the other hand, there are marked systematic differences between both data sets which amount to biases of $1.73\,m$ and $-0.91\,m$ for the Beaufort Sea and Fram Strait respectively. That is, the model overestimates the ice thickness in the Beaufort Sea (as was also evident in the submarine data; see Fig. 3.14). This overestimation, which is also typical for other sea ice models [*Kreyscher et al.*, 2000], may be partly attributed to topography and coastline effects which are not well resolved by large scale models [*Kreyscher et al.*, 2000]. In Fram Strait there is an underestimation of the ice thickness by the model which can be explained by the coarse resolution of the cross-strait thickness profile by the model. Note that an ULS beam has a typical footprint of the order of meters whereas the sea ice model provides ice thickness values representing an average over a $100\,km \times 100\,km$ grid box.

Summarising, the above comparison cannot be considered as a validation of the modelled interannual variations. This is mainly because the observational time series are only available from two locations in the Arctic representing very small spatial areas which cannot be resolved by the model. However, the comparison has shown that, at least for those two locations, the modelled ice thickness variations roughly reproduce those of the observations and, thus, confidence in the modelled interannual variability is enhanced.

4.3.3 Simulated Ice Thickness Anomalies

Fig. 4.8 shows the annual mean time series of ice thickness anomalies for the eight grid points for which the annual mean characteristics were discussed in Section 3.4 (Fig. 3.12). The corresponding long-term averages are presented in Tab. 3.1 and their corresponding annual mean seasonal cycles are depicted in Fig. 3.11. In agreement with other modelling studies [*Flato*, 1995; *Arfeuille et al.*, 2000] largest interannual variability was simulated in the Beaufort Sea, the East Siberian Sea, and in the Canadian Archipelago (see also Tab. 3.1). In these regions, annual mean anomalies exhibits magnitudes of up to $2\,m$.

In the Beaufort Sea pronounced positive deviations from the long-term average (larger than $0.5\,m$) occured in the years 1965–1967, 1974–1976, and 1990–1993. The timing of these local maxima nearly perfectly agrees with those found by *Arfeuille et al.* [2000] (note that they considered regional averages instead of single grid points). The fact, that *Arfeuille et al.* [2000] used NCEP/NCAR wind fields as the only interannually varying forcing quantity of their model points towards the hypothesis that primarily circulation changes are responsible for these anomalies. Discrepancies to the model results of *Arfeuille et al.* [2000] appear when the timing and the magnitudes of the minima are considered. In the Beaufort Sea large negative anomalies occured in 1981-1982 and in 1998. The latter minimum is the largest within the 49-yr time series with a magnitude of nearly $2\,m$ below

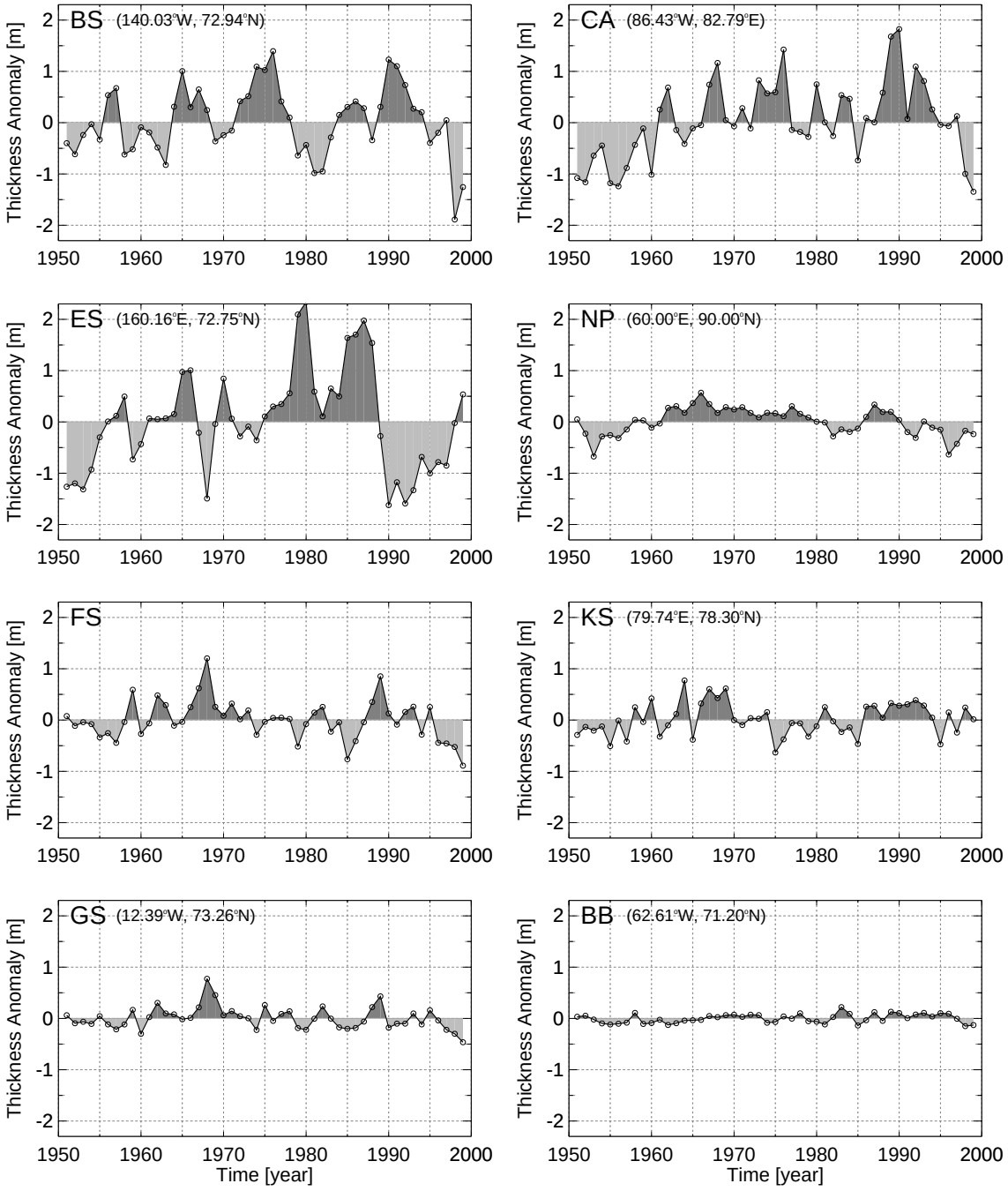

Figure 4.8: Annual mean time series of ice thickness anomalies (m) for selected grid cells (CA = Canadian Archipelago, BS = Beaufort Sea, ES = East Siberian Sea, NP = North Pole, FS = Fram Strait, KS = Kara Sea, BB = Baffin Bay, and GS = Greenland Sea) of the model domain. For the location of the grid cells see Figure 3.12.

the long-term average. It coincides with an observed record minimum of the ice coverage in Beaufort and Chukchi Seas as reported by *Maslanik et al.* [1999]. The decrease from large positive anomalies in 1990 to slight negative anomalies in 1995-1997 is also evident in the ULS time series from the Beaufort Sea site (Fig. 4.7a).

Similar anomalies as in the Beaufort Sea are evident north of the Canadian Archipelago. Both time series share about 20% of their variance ($r = 0.48$, significant at $p = 95\%$). From submarine data in the same region *Wadhams* [1990] found that the ice thickness north of Greenland decreased by about 15% from 1976 to 1987. This estimate roughly agrees with the model results. The ice thickness time series of the Canadian Archipelago exhibits a difference between 1976 and 1987 of $\sim 1.3\,m$ which corresponds to a decrease of 19% (relative to the mean value of $6.68\,m$). Without information about the interannual variability *Wadhams* [1990] interpreted his findings as observational evidence for a significant thinning of the ice cover north of Greenland. However, as the simulation results show, only two years after the observed minimum the ice thickness anomaly north of the Canadian Archipelago was well above the value of 1976. Furthermore, the time series exhibit its record largest value in 1990 with a positive anomaly of $1.9\,m$ which corresponds to the 2.5-fold of the standard deviation.

The largest annual mean anomalies within the entire model domain are simulated in the East Siberian Sea with a standard deviation of $0.99\,m$ and individual anomalies of up to $2\,m$ in magnitude. Pronounced positive deviations occured in 1965–1966, 1979–1980 and in 1985–1988. Negative anomalies were strongest in 1951-1953, 1968, and 1990-1995. Again, the latter anomaly coincides with observed large reductions of ice coverage in this region. *Maslanik et al.* [1996] reported that greatest decreases in ice extent in the Laptev and East Siberian Seas occured in 1990, 1993, and 1995. Comparing the anomalies in the East Siberian Sea with those of the Beaufort Sea it seems that they are out of phase after 1970. However, the correlation between both time series is only small ($r = -0.14$ for the entire period and $r = -0.32$ after 1970) and not statistically significant.

Ice thickness variations at the North Pole were often the focus of scientific discussions about a possible thinning of the Arctic ice pack [*Bourke and Garret*, 1987; *McLaren*, 1989; *McLaren et al.*, 1990; *Wadhams*, 1990]. However, these studies were based on measurements from only a few submarine cruises. *McLaren et al.* [1990] concluded that too little is known about the natural variability of Arctic sea ice thickness to draw any conclusions about climate induced changes of the ice thickness. From six submarine cruises in late April/early May *McLaren et al.* [1992] estimated a standard deviation of the North Pole ice thickness of about $1\,m$. This estimate is about 3–4 times larger than the standard deviation of the 49-yr time series of modelled April ice thicknesses (Fig. 3.11). For annual mean data the simulation reveals an interannual variability of $0.26\,m$ for the North Pole (Tab. 3.1). In contrast to the above discussed time series the ice thicknesses at the North Pole does not exhibit very large anomalies. It rather reflects the inverse of the Northern Hemisphere SAT time series (Fig. 5.1a) with an increase from the 1950s to the mid-1960s and a slight decrease thereafter. This dependence is confirmed by the fact that the area-averaged SAT of the NCEP/NCAR data (lower panel of Fig. 4.11) explains about 40% of the ice thickness variability in the following year ($r = -0.63$ when SAT leads by one year) and 30% of its instantaneous variability ($r = -0.52$ at lag 0).

Downstream of the North Pole, in Fram Strait, the interannual variability increases and individual anomalies become larger. This can be explained by ice thickness changes due to altering drift directions. Such variations result in the advection of ice from different

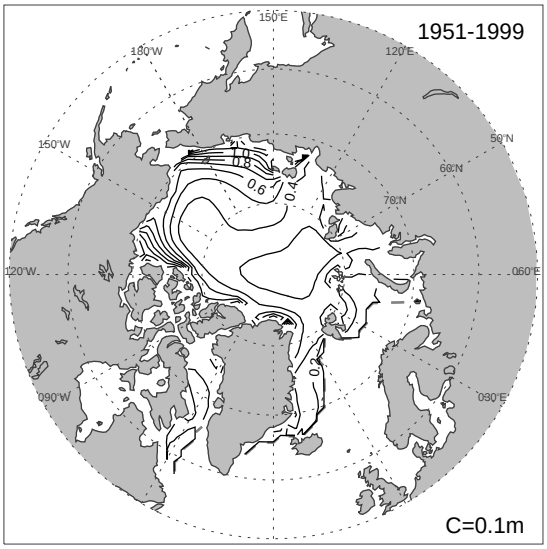

Figure 4.9: Interannual variability of simulated ice thickness. Shown are the standard deviations of ice thickness (m) for each grid point. The values are based on annual mean time series for the period 1951–1999.

regions such as the Canadian Archipelago or the Kara Sea. A more detailed analysis of ice thickness variations in Fram Strait will be presented later in Section 4.4. Due to the advection by the East Greenland Current, the ice thickness variability in the Greenland Sea is very similar to that in Fram Strait but with smaller magnitudes of the anomalies.

Fig. 4.9 shows the overall pattern of ice thickness variability. As described above largest standard deviations are present in the East Siberian and in the Beaufort Seas with magnitudes exceeding $1\,m$. Besides the ice edges a local minimum with magnitudes of about $0.3\,m$ appears around the North Pole. In the following subsection this pattern will be decomposed into preferred modes of variability by means of statistical analysis methods.

4.3.4 Modes of Ice Thickness Variability

In the previous subsection ice thickness variations at subjectively selected grid points of the model domain were analysed. In the following the simulated ice thickness variability will be discussed from an objective point of view considering the ice pack as a whole. Additionally, the following analysis will identify the impact of the atmospheric forcing onto ice thickness variations. Thereby, a strategy similar to that used by *Venegas et al.* [1997] for analysing of atmosphere-ocean variability in the South Atlantic will be applied. That is, the determination of dominant modes of ice thickness variability from EOF analyses and, subsequently, the relation of the identified modes to the forcing quantities by comparing with coupled modes of SVD analyses.

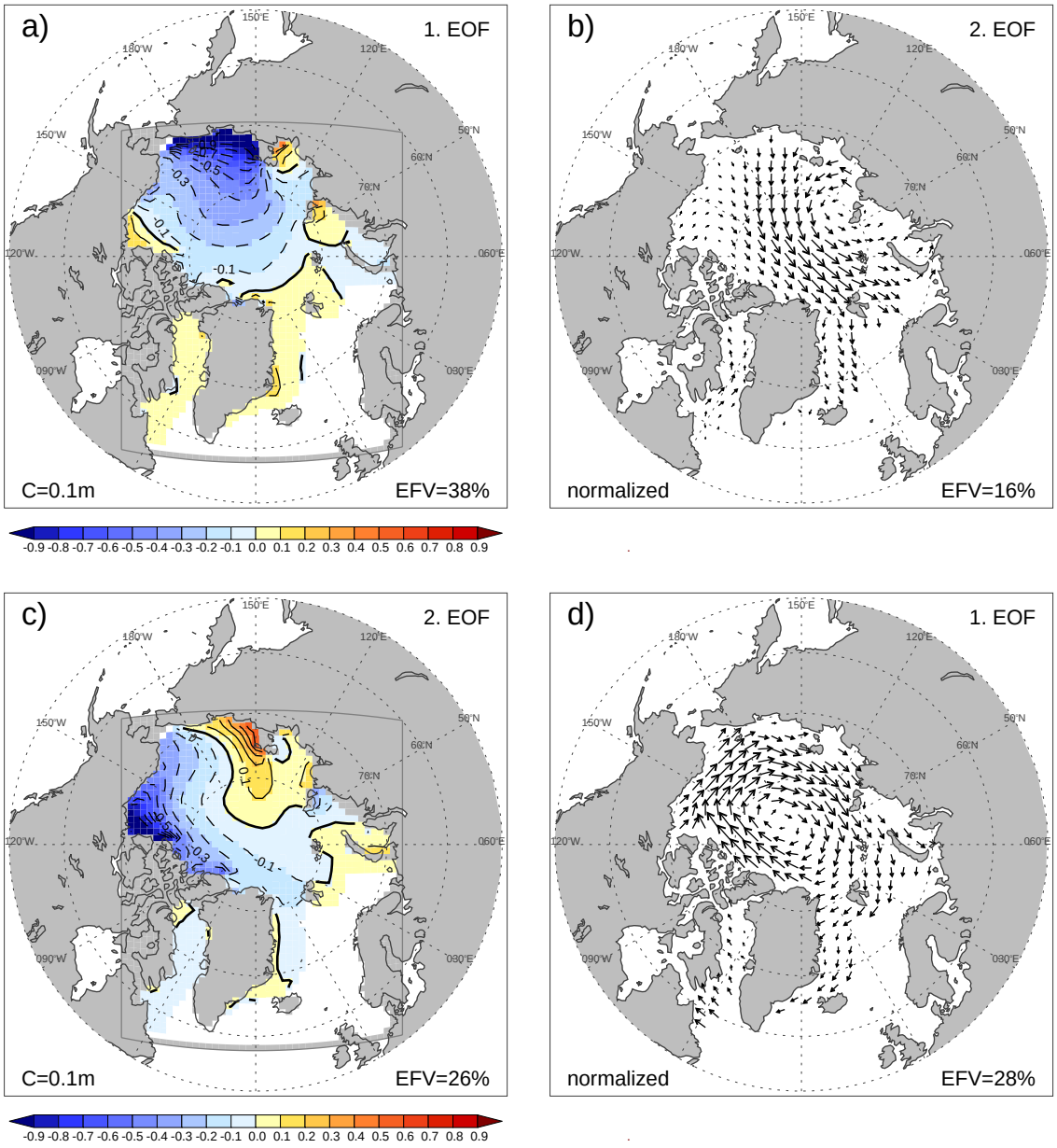

Figure 4.10: First two dominant modes of ice thickness (left panel) and ice drift (right panel) variability based on separate EOF analyses. The portion of explained field variance (EFV) is stated in the lower right of each panel. The EOFs of the ice thickness anomalies (a and c) were estimated by classical EOF decomposition whereas those for sea ice drift variability (b and d) are based on a combined EOF analysis. That is, the time series of both vector components form the covariance matrix (for details see Chapter 2). The first and second EOFs are well separated from their corresponding subsequent modes after the criterion of *North et al.* [1982]. All estimates are based on simulated annual mean anomalies for the period 1951–1999. Linear trends were removed beforehand.

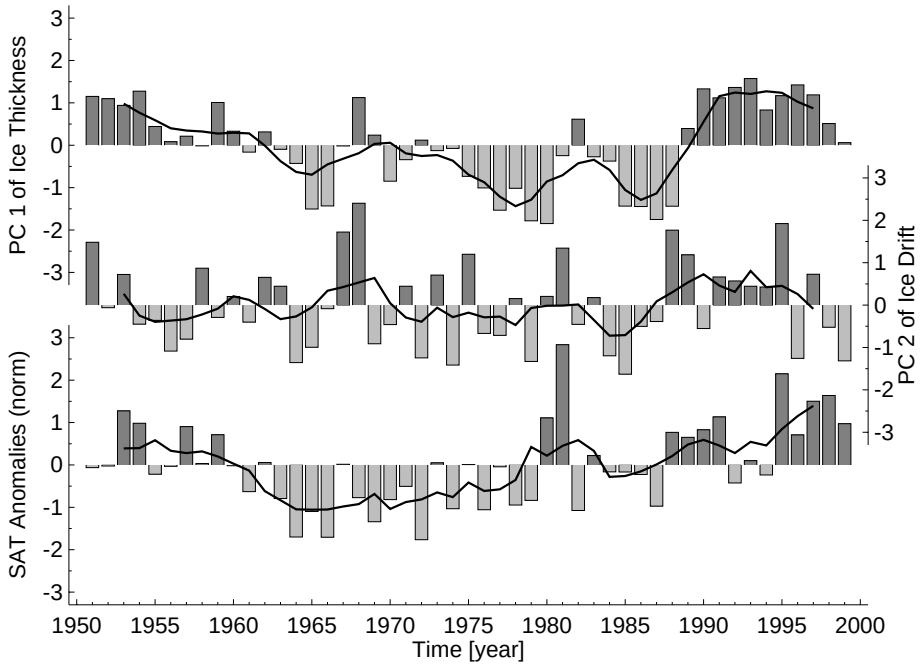

Figure 4.11: Time series associated with the first mode of ice thickness variability. Top) Principal component time series of first EOF of ice thickness anomalies (Fig. 4.10a). Middle) Principal component time series of the second EOF of ice drift anomalies (Fig. 4.10b). Bottom) Normalised anomalies of area averaged northern hemisphere (50°N–90°N) SAT derived from NCEP/NCAR reanalysis data. The correlation statistics between those time series are given in Table 4.2.

a) EOF Analysis of Ice Thickness and Ice Drift

In order to identify possible preferred modes of variability an EOF analysis of the annual mean anomalies of the simulated ice thickness was performed. Moreover, for the investigation of possible mechanisms creating ice thickness anomalies, also ice drift variations were analysed by EOF decomposition. To consider interannual variability only, linear trends were removed from the data prior to the analyses.

Overall, the first five EOFs of ice thickness explain together 85% of the total variance whereas about 75% are explained by only the first three EOFs. However, only the first two modes of ice thickness variability will be discussed in the following. The portion of variance explained by EOF1[h] and EOF2[h] is 38% and 26% respectively. Their corresponding Eigenvectors (E1[h] and E2[h]) are shown in Fig. 4.10a and c and their corresponding expansion time series (PC1[h] and PC2[h]) are depicted in the top panels of Fig. 4.11 and Fig. 4.12 respectively.

E1[h] is characterised by a more or less overall thinning (or thickening, depending on the sign of the corresponding PC time series) of the ice pack. Largest magnitudes are apparent at the East Siberian coast with anomalies of up to $1\,m$. Amplitudes decrease towards the Beaufort Sea and Fram Strait. Anomalies of opposite sign, which are apparent in the Atlantic sector of the model domain and at the lee sides of the East Siberian Islands and Severnaya Zemlya, are negligibly small. As indicated by the portion of explained

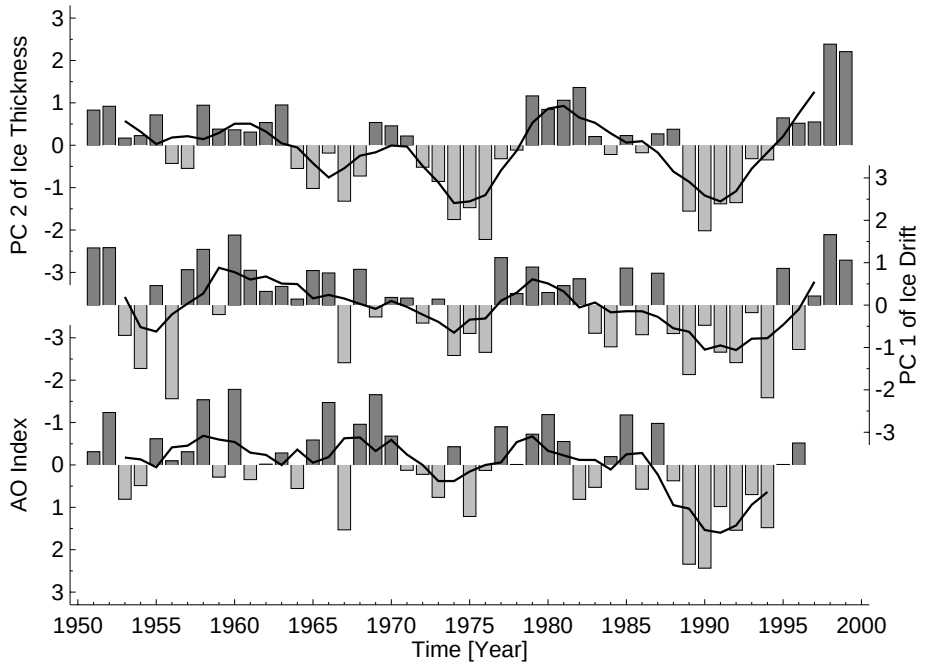

Figure 4.12: Time series associated with the second mode of ice thickness variability. Top) Principal component time series of the second EOF of ice thickness anomalies (Fig. 4.10c). Middle) Principal component time series of the first EOF of ice drift anomalies (Fig. 4.10d). Bottom) Normalised anomalies of the Arctic Oscillation index [*Thompson and Wallace*, 1998]. Note that for comparison the scale of the AO index is inverted. The correlation statistics between those time series are given in Table 4.2.

variance and by its near-uniform spatial structure the expansion time series of this first mode of ice thickness variability strongly resembles much of the variations of the total sea ice volume (Fig. 5.3). Due to the large auto-correlation time scale of the total sea ice volume (SIV) the instantaneous correlation with PC1[h] of $r = -0.59$ is statistically significant only at the 90%-confidence level. However, if the SIV time series lags the PC1[h] by one year the magnitude of the negative correlation is much larger and amounts to $r = -0.79$ (statistically significant at the 99%-confidence level). This lag can be explained by the advection and subsequent spreading of ice thickness anomalies originated in the East Siberian Sea region to the centre of the ice pack and , thus, affecting a larger areal fraction.

From considering the spatial structure of E1[h] it is obvious to suggest that SAT variations might be involved in forcing this mode. In fact, there is a significant correlation between the time series of area averaged extra-tropical northern hemisphere SAT variations (Fig. 4.11) with PC1[h] if the SAT leads by one year ($r = 0.52$, see Tab. 4.2). In particular, this relation is mainly based on the correlation with SAT anomalies during spring (May and June) of the previous year.

Another possible mechanism for creating ice thickness anomalies as shown be E1[h] is the advection of ice towards or away from the East Siberian coast by changes of the strength of the TPDS. Such ice drift variations are apparent in the pattern of the second mode of ice

drift variability (E2[u]) as shown in Fig. 4.10b. Moreover, its corresponding expansion time series (PC2[u]) is significantly correlated with the principal components of E1[h] in the following year ($r = 0.53$). Moreover, ice motion variability as described by E2[u] emerges downstream of the TPDS. That is, changes of the strength of the TPDS affect both the ice thickness and ice drift speed at Fram Strait (Fig. 4.21) and, hence, the ice volume export through this passage (Fig. 4.17a). This is highlighted by the fact that the annual mean time series of the volume export through Fram Strait shares about 60% of its variance with that of the expansion time series of E2[u] ($r = 0.77$). This coherence is based on roughly equal correlations of PC2[u] with both ice thickness variations ($r = 0.62$) and southward drift speed anomalies ($r = 0.55$) at Fram Strait. The anomalous SLP field associated with surface wind anomalies forcing such ice drift variations must be characterised by anomalous low pressure over the Kara and Laptev Seas and an anomalous high centred over the Canadian Archipelago. Such a pattern, similar to that shown in Fig. 4.14d, emerges as the second EOF of extra-tropical northern hemisphere SLP variability as was shown by, e.g., *Fyfe et al.* [1999] and *Skeie* [2000]. Associated with these SLP variations are anomalous offshore winds blowing from Siberia polewards and, thus, advecting warm air masses from lower latitudes onto the ice pack (or advecting cold polar winds towards the Siberian coast at the opposite phase of EOF2[SLP]). Hence, the combined effects of divergence by offshore ice motion together with positive SAT anomalies contribute to ice thickness variations as shown by E1[h], as was the case in creating the large summer opening of the 1990s shown in Sec. 4.2.

The second mode of ice thickness variability, E2[h], exhibits a dipole structure with opposite anomalies in the Beaufort and East Siberian Seas and with magnitudes of up to $0.7\,m$. From its spatial structure it can be hypothesised that the second mode of ice thickness variability primarily represents a redistribution of ice between both centres of action. Accordingly, the temporal correlation of this mode with the total ice volume is only moderate ($r = -0.49$, statistically significant only at the 90%-confidence level). The hypothesis of a redistribution of mass is confirmed by the existence of a corresponding pattern of ice drift variability. That is, the first mode of ice drift variability (Fig. 4.10d) shows alternating cyclonic or anticyclonic ice motion anomalies which can be associated

Table 4.2: Correlation statistics for the time series associated with the first two dominant modes of ice thickness variability. 1-year lagged correlations are given in brackets whereas the remaining values denote instantaneous correlations. Lagged correlations given left (right) of the instantaneous values means that the time series of the first column lags (leads) the time series of the n-th column by one year*.Correlations significantly different from zero (at the 95%-confidence level based on a two-sided *Students-t*-test) are indicated as bold numbers.

	PC1[h]	PC2[h]	PC1[u]	PC2[u]	AO	SAT
PC1[h]	**1.00**	0.00	−0.18	(**0.53**) 0.27	(**0.37**) **0.35**	(**0.52**) 0.36
PC2[h]	0.00	**1.00**	**0.58**,	−0.06	**−0.54**	0.26
PC1[u]	−0.18	**0.58**	**1.00**	0.00	**−0.64**	−0.01
PC2[u]	0.27 (**0.53**)	−0.06	0.00	**1.00**	0.24	**0.37**

* For example, the correlation coefficient between PC1[h] and SAT in the preceding year is $r = 0.52$.

to the above mentioned redistribution of mass. Moreover, there is a significant, positive temporal correlation between their corresponding expansion series (PC2[h] and PC1[u], see Fig. 4.12) of $r = 0.58$ (see Tab. 4.2). In the above section, an out of phase relationship between ice thickness anomalies at single grid points in the Beaufort Sea and in the East Siberian Sea (Fig. 4.8) was suggested but failed the proof of a statistically significant correlation. Such an out of phase relation would coincide with the patterns of E2[h] and E1[u] and with the explanation given above. However, this relation could be masked by thickness variations associated with E1[h]. If these variations are subtracted from the original annual mean anomalies, the suggested out of phase behaviour at both locations emerges as a significantly negative correlation of $r = -0.61$. The most probable atmospheric candidate responsible for cyclonic or anticyclonic changes of the ice motion is the Arctic Oscillation, because it represents changes of Arctic SLP [*Thompson and Wallace*, 1998; *Skeie*, 2000, their Figs. 1 respectively] which coincides with variations of the cyclonicity of the surface wind field. That is, a high AO phase is associated with lower than normal SLP over the central Arctic and forces an anomalous cyclonic circulation of the surface winds and, hence, of the ice pack. Such a circulation anomaly means a reduction of the strength of the Beaufort Gyre and, therefore, a reduced advection of ice from the Canadian Archipelago and the Beaufort Sea region to the Chukchi and East Siberian Seas. But it is not only this physical interpretation which give rise to this hypothesis, there are also comparatively strong temporal correlations between the AO index (Fig. 4.12) and the expansion time series PC2[h] ($r = -0.54$) and PC1[u] ($r = -0.64$).

b) SVD Analysis of Ice Thickness and Atmospheric Forcing

So far, the dominant modes of ice thickness variability have been identified and were related to the atmospheric forcing by physical reasoning and correlation analyses. Moreover, the shape of the second mode of ice thickness variability is restricted to being orthogonal to E1[h] and, therefore, does not necessarily represent a typical response to atmospheric forcing variability. Another, more objective, method of finding coupled modes of variability is the Singular Value Decomposition (SVD). The aim of this method is finding, from two data fields, pairs of spatial patterns that explain as much as possible of the mean-squared temporal covariance between the two fields (see Chapter 2). To identify the dominant modes of covariability between ice thickness variations and the atmospheric forcing of the model the SVD analysis was applied to the field of ice thickness anomalies and the fields of SAT and SLP (as a proxy of the wind forcing). The spatial patterns of the first modes of the SVD analyses between h and SAT (S1[SAT,h]) and h and SLP (S1[SLP,h]) are depicted in Fig. 4.13. The lagged cross-correlation functions of their corresponding expansion time series are depicted in Fig. 4.15.

The dominant mode of covariability between h and SAT anomalies (S1[SAT,h]) explains 51% of total squared covariance. The corresponding expansion time series share about 46% of their temporal variability ($r = 0.68$, see Fig. 4.15). Ice thickness variations associated with S1[SAT,h] are nearly identical to those of the first EOF of h. This is obvious by comparing their spatial patterns (Fig. 4.13a for S1[SAT,h] and Fig. 4.10a for E1[h]) but is also documented by a spatial correlation coefficient between their corresponding patterns of $r = 0.92$ and a temporal correlation between their corresponding expansion time series of $r = 0.98$. The associated SAT anomalies are characterised, as stated above, by positive anomalies over the entire ice pack with maximum values centred over the East

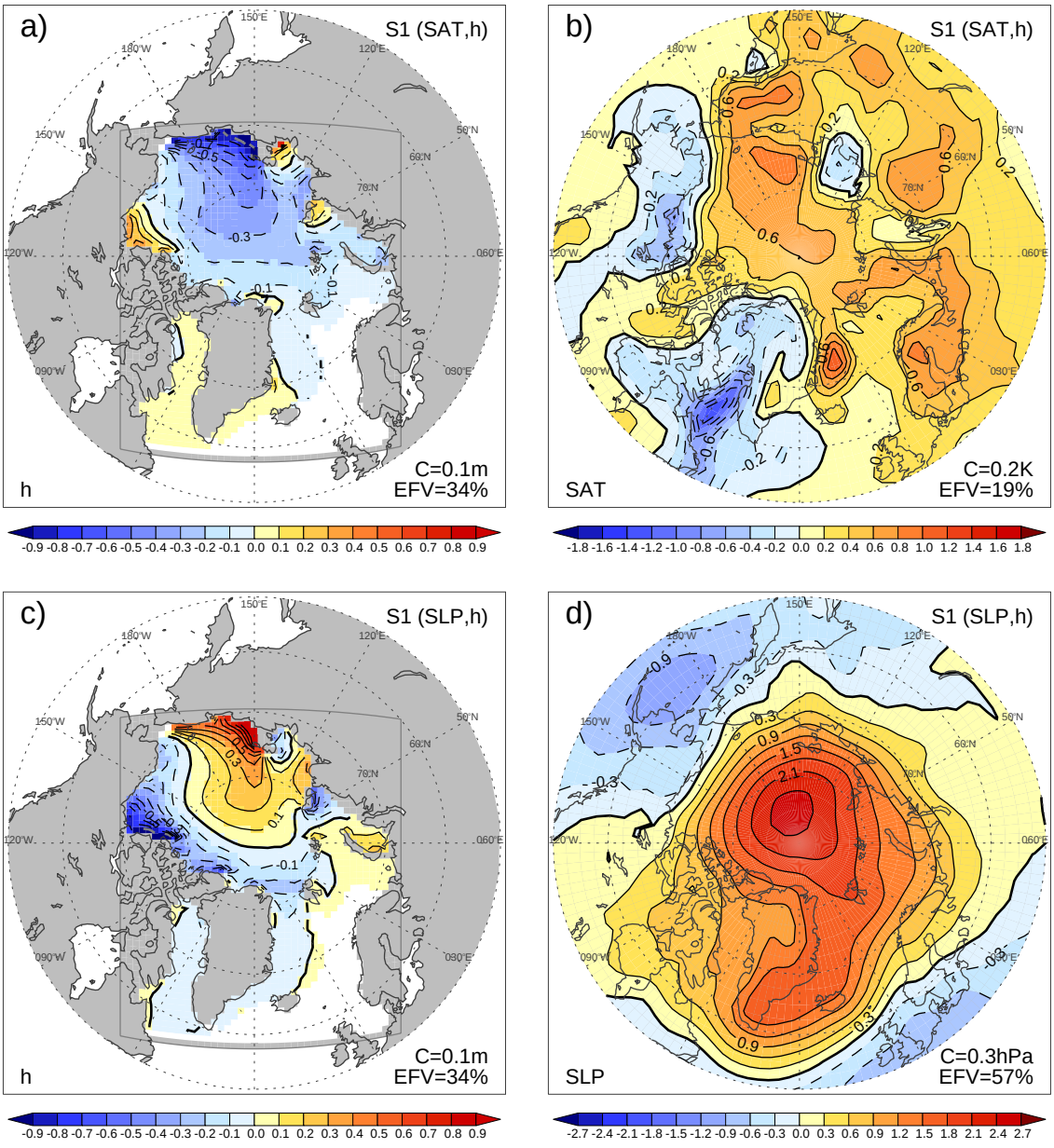

Figure 4.13: First modes of SVD analyses between ice thickness and the atmospheric forcing parameters SAT and SLP. Top) First mode of the SVD analysis between SAT and ice thickness (S1[SAT,h]) with a Squared Covariance Fraction (SCF) of 51% and a temporal correlation between the corresponding expansion time series of $r = 0.68$. Shown are the Singular Vectors of ice thickness (a) and SAT (b). Bottom) First mode of the SVD analysis between SLP and ice thickness (S1[SLP,h]) with a SCF of 89% and a temporal correlation between the corresponding expansion time series of $r = 0.72$. Shown are the SVs of ice thickness (c) and SLP (d). The analyses are based on annual mean data for the period 1951–1999. In the above analyses data on different geographical grids were used. However, the same analysis applied to SAT and SLP data interpolated to the model grid revealed essentially the same results.

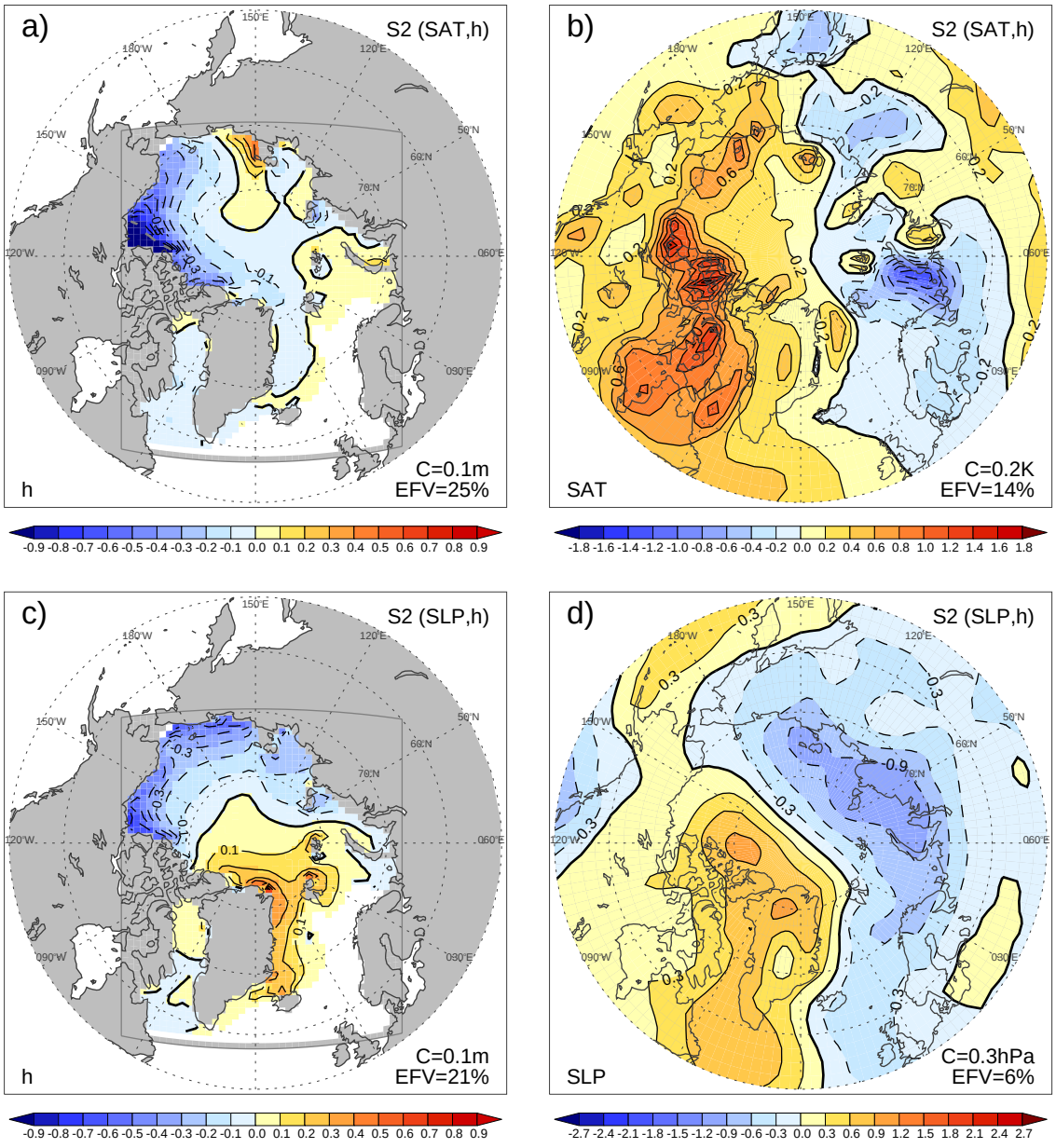

Figure 4.14: As in Fig. 4.14 but for the second modes. The SCFs for S2[SAT,h] and S2[SLP,h] are 29% and 7% respectively. The temporal correlations between the expansion time series are with these modes are $r = 1.0$ for S2[SAT,h] and $r = 1.0$ for S2[SLP,h].

Siberian Sea and, further upstream, over the eastern Siberian continent.

Dominant patterns of covariability between ice thickness and SLP are depicted in Figs. 4.13c and 4.13d for ice thickness and SLP anomalies respectively. The explained covariance fraction between both data sets is 89% and the temporal correlation between the corresponding time series is $r = 0.72$. As for the S1[SAT,h] the ice thickness anomaly pattern of S1[SLP,h] reflects one of the dominant EOF pattern of ice thickness. In particular,

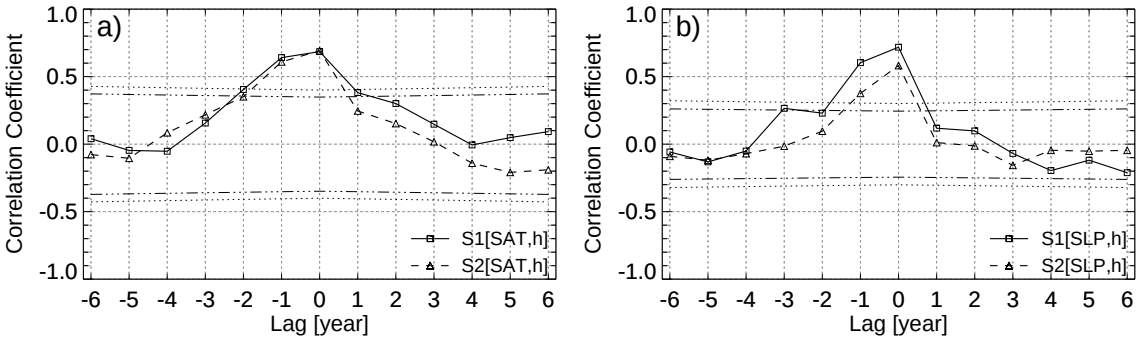

Figure 4.15: Cross-correlation analysis of the expansion coefficients of the SVD analyses of Fig. 4.13 and Fig. 4.13 respectively. Shown are the lagged cross-correlation functions between the expansion coefficients of the first two modes of a) SVD(SAT,h) and b) SVD(SLP,h). The cross-correlation functions of the first modes is represented by the solid lines with squares whereas the dashed lines with triangles show those for the second modes. The expansion time series of the atmospheric parameters (SAT or SLP respectively) leads the sea ice time series for negative lags. 95%-confidence levels, at which correlation coefficients are significantly different from zero, are denoted by the dotted (dash-dotted) lines for the cross-correlations of the first (second) modes. Serial correlation as well as different samples sizes for various lags were taken into account for the estimation of the confidence levels.

it is very similar to E2[h] (Fig. 4.10c) with a spatial correlation coefficient of $r = 0.85$ and a temporal correlation between their corresponding time series of $r = 0.76$. The associated SLP anomaly pattern reflects the first EOF of extra-tropical northern hemispheric SLP anomalies, that is, the AO pattern [*Thompson and Wallace*, 1998, their Fig. 1] (note that Fig. 4.10d represents SLP anomalies associated with a negative AO phase). Thus, the SLP pattern of S1[SLP,h] confirms the hypothesis that the dipole type anomalies of E2[h] can be attributed to the Artic Oscillation which was previously drawn from the analysis of E2[h] and E1[u] only.

The second modes of the SVD analyses are shown in Fig. 4.14. Overall, they explain less of the squared covariance fractions (29% for S2[SAT,h] and only 7% of S2[SLP,h]) than their corresponding first modes but show also some interesting features which clarify the contributions of the atmospheric forcing to the modes of ice thickness variability. S2[SAT,h] show in general the signatures of the Arctic Oscillation which was previously identified as S1[SLP,h]. That is, the ice thickness pattern of S2[SAT,h] (Fig. 4.14a) is rather similar to that of S1[SLP,h] (Fig. 4.14c) and their corresponding expansion time series are very close to each other ($r = 0.99$). Moreover, the SAT pattern of S2[SAT,h] shows anomalies which are typical for the AO [compare with Fig. 1 of *Thompson and Wallace*, 1998]. Its associated expansion time series show significant correlations with the time series of E2[h] ($r = 0.67$), E1[u] ($r = 0.53$), AO ($r = -0.53$), and, accordingly, with the expansion time series of the SLP pattern of S1[SLP,h] ($r = 0.54$). The second mode of ice thickness-SLP covariability points towards a contribution to E1[h] and E2[u]. The ice thickness pattern of S2[SLP,h] shows some similarity to E1[h] with opposite anomalies between the Pacific and Atlantic sides of the Arctic. Its expansion time series shares about 53% of its variance with that of E1[h] ($r = 0.73$) and about 22% with that of E2[u] ($r = 0.47$). The SLP pattern of S2[SLP,h] is very close to the second EOF the SLP

over the northern high latitudes [*Thompson and Wallace*, 1998; *Skeie*, 2000, their Figs. 1 respectively] and represents a forcing of ice drift anomalies as shown by the second EOF of simulated ice drift (Fig. 4.10b). However, there are only significant correlations of the associated time series of that SLP pattern with the PC2[u]. As mentioned before, such SLP anomalies affect the strength of the TPDS (which is shown by E2[u]) and, thus, the export of ice through Fram Strait. Accordingly, the SLP pattern of S2[SLP,h] is very similar to the SLP pattern regressed onto the normalised time series of the ice export through Fram Strait (Fig. 4.23a) and its temporal evolution explains about 64% of the variability of this export time series.

The direction of coupling between two geophysical processes can be statistically analysed by considering the shape of lagged cross-correlation functions [e.g. *Frankignoul*, 1995]. Obviously, from the nature of the experimental design of this study, there are no doubts about the leading role of the forcing quantities. However, there is, at least theoretically, the possibility of a feedback of ice thickness variations onto the forcing fields as suggested by *Gerdes* [pers. communication]. However, as shown by the lagged cross-correlation functions between the expansion time series of both leading SVD modes (Fig. 4.15), there is only a one-way coupling between atmospheric forcing and simulated sea ice thickness variations. That is, apart from the instantaneous correlations, there are also significant temporal correlations if the atmospheric parameters lead the sea ice but not vice versa.

4.3.5 Conclusions

The interannual variability of simulated ice thickness over the last five decades was investigated. Because there are essentially no observational data allowing an investigation of interannual ice thickness variability over a broader spatial and temporal scale the results of the above analyses cannot directly be compared to measurements. However, a comparison with short interannual ice thickness time series of the Beaufort Sea and Fram Strait, as well as with submarine observations from north of Greenland [*Wadhams*, 1990] lead to enhanced confidence in the model results. From the analysis of annual mean time series of the simulated ice thickness it can be concluded that:

- Largest ice thickness variability occurs in the East Siberian Sea as well as in the Beaufort Sea and north of the Canadian Archipelago. On average, year to year variations in these regions are of the order of $1\,m$ but individual annual anomalies can be up to $2\,m$ in magnitude.

- Besides the ice edges, the minimum variability of ice thickness is found around the North Pole with standard deviations of the annual mean time series of about $0.3\,m$.

From EOF analysis of detrended annual mean ice thickness anomalies two dominant modes of variability were identified and related to dynamical and thermodynamical processes by correlation statistics as well as by SVD analyses. Moreover, both dominant modes of ice thickness variability were related to the dominant modes of ice drift variability. As a result, it was found that the first ice thickness mode is a dynamic-thermodynamic mode because it is related to both thermal forcing and ice drift variability. The second mode, on the other hand, is primarily a dynamic-only mode which is strongly related the Arctic Oscillation. In particular, it was found that:

- The first mode of ice thickness variability roughly represents an overall thickening or thinning of the Arctic ice pack with largest amplitudes in the east Siberian Sea.
- The causes of the first mode are in-phase variations of SAT and the TPDS, with the latter emerging as the second EOF of ice drift variability. That is, positive SAT variations, which are most pronounced in the East Siberian Sea, are associated with offshore anomalies of ice drift.
- The anomalous SLP pattern associated to the second mode of ice drift variability also explains more than half of the variability of the ice export through Fram Strait.
- The second mode of ice thickness variability emerges as an uneven dipole with opposite anomalies in the eastern and western Arctic. In contrast to the first mode it represents a redistribution of mass within the Arctic rather than affecting changes of the total volume.
- Associated to the second mode of ice thickness is the first mode of ice drift variability which shows cyclonic or anticyclonic anomalies in the over the entire Arctic Ocean.
- Both, the second mode of ice thickness and the first mode of ice drift are strongly related the Arctic Oscillation

Lagged correlation analyses revealed that the atmospheric modes lead the sea ice, but no evidence was found pointing to an impact of ice thickness anomalies onto the atmosphere.

4.3.6 Discussion

Although most of the above presented results cannot be validated with observations they can be compared with various other modelling studies of different complexity. Since longer-term integrations of sea ice models forced with realistic atmospheric data were performed, it emerged that the ice cover of the Arctic ocean exhibits considerable interannual variability and, thus, the classical picture of the thickness distribution of Arctic ice pack (Fig. 3.3) should rather be considered as a snapshot. Earlier studies [*Häkkinen*, 1993; *Flato*, 1995] have already shown that substantial ice thickness variations occur in the Beaufort and East Siberian Seas. Beyond the present study, these findings are confirmed by the model studies of, e.g., *Arfeuille et al.* [2000], *Zhang et al.* [2000], or *Polyakov and Johnson* [2000].

Information about interannual variability is crucial for the estimation of long-term trends. The larger the variability time-scale is the longer the observed time series has to be in order to assess of significant long-term trends. North of Greenland and the Canadian Archipelago, in the southern Beaufort Sea, and in the East Siberian Sea the interannual variations of ice thickness are at least as large as half of the mean seasonal variations. From the spatial pattern of simulated ice thickness variability (Fig. 4.9) it can thus be suggested that the region around the North Pole would be most suitable for the assessment of long-term changes of the ice pack.

From statistical analyses of the simulation data it was concluded that there are out of phase variations between the Canadian (western) and the Siberian (eastern) Arctic which are primarily due to cyclonic or anticyclonic anomalies of ice advection. That is, primarily changes of the strength of the Beaufort Gyre lead to reduced or enhanced transports of

sea ice from the western to the eastern Arctic. Such cyclonic or anticyclonic regimes were previously identified by *Proshutinsky and Johnson* [1997]. *Johnson et al.* [1999] found a relation of these circulation anomalies to SLP changes associated with the AO, but they did not found much temporal correlation. *Zhang et al.* [2000] report concurring thickness anomalies between the eastern and western Arctic which corresponds in sign and timing to those shown in the present study. From a detailed analysis of east-to-west advection they relate these ice thickness anomalies to changes of the ice drift pattern. Furthermore, from a comparison of the cyclonic and anticyclonic periods with pressure indices they suggest a relation to the AO and NAO. In the present study, filtering due to EOF representation yields a close relation of both ice drift and ice thickness modes to the AO. Although SAT anomalies associated with the AO contribute also to the second mode of ice thickness variability, the agreement of ice thickness anomalies with those found from wind-driven sea ice simulations [WIND, *Arfeuille et al.*, 2000] leads to the statement that this mode is primarily dynamically forced. At a first glance, the uneven dipolar pattern basically represents a redistribution of ice within the Arctic region. However, *Zhang et al.* [2000] found also overall volume changes associated with this mode which are due to the nonlinearity of the ice-albedo feedback. That is, during the period of cyclonic drift anomalies [that is the period 1989–96 in *Zhang et al.*, 2000] less ice is apparent in the eastern Arctic whereas the ice thickness is enhanced in the western part. During summer, the enhanced melting in the eastern Arctic due to a reduced albedo (by early breakup of thin ice) dominates the reduced melting in the regions where the ice thickness is enhanced and, thus, leads to an overall reduction of ice volume.

The dominant mode of ice thickness variability found from the present study describes an efficient pattern for changes of the total sea ice volume because in-phase variations of SAT anomalies and changes of the TPDS were identified as its causes. That is, reduced net growth by positive SAT anomalies is accompanied by divergence at the Siberian coasts due to an enhanced TPDS which in turn also leads to a stronger ice export. Furthermore, due to the ice-albedo feedback, an early opening of the ice pack due to divergence also leads to enhanced melting. Accordingly, the first mode of ice thickness explains much (63%) of the variability of the total sea ice volume. Moreover, the regression pattern of ice thickness anomalies onto the total sea ice volume (not shown) is very similar to the pattern of the first mode with largest amplitudes in the East Siberian Sea. A similar regression pattern was also found by *Goosse et al.* [2000] from a CGCM simulation including a dynamic-thermodynamic sea ice model. *Arfeuille et al.* [2000] also identified the East Siberian Sea as the region where ice thickness anomalies show the strongest correspondence to changes of the total sea ice volume. The importance of the first mode for ice volume changes is further emphasised by the similarity to the pattern of long-term trend derived from the present simulation (Fig. 5.5a) and also to that derived from observations [*Rothrock et al.*, 1999b]. Therefore, the East Siberian Sea emerges as a key region of the Arctic ice pack for indicating changes of the overall volume.

4.4 Variability of Sea Ice Transports into the North Atlantic

4.4.1 Introduction

At high latitudes the density stratification of the oceans is very sensitive to the freshwater budget. This is because at near freezing temperatures the saline expansion coefficient of sea water is much larger than its thermal counterpart. Therefore, the introduction of small amounts of freshwater can therefore prevent convective overturning even in the case of substantial surface cooling [*Aagaard and Carmack*, 1989]. Moreover, it is the deep water formation which drives the thermohaline part of the global ocean circulation. Thus, variations of the freshwater input at high latitudes can lead to changes in the thermohaline circulation and, furthermore, owing to the nonlinearity of the system, can lead to transitions between different equilibrium states of the oceanic circulation [e.g. *Marotzke and Willebrand*, 1991; *Rahmstorf*, 1995]. Because the oceanic circulation accomplishes nearly half of the total meridional heat transport [e.g. *Peixoto and Oort*, 1992] it has profound climatic effects. *Manabe and Stouffer* [1995] found from a sensitivity study with a coupled ocean-atmosphere model that a surface freshwater flux of $1\,Sv$ released over the high latitudes over a period of 10 years leads to an abrupt reduction of convective activity and of the thermohaline circulation associated with a pronounced cooling of the northern North Atlantic region. However, such amounts of freshwater flux anomalies can only result from massive iceberg calvings and melting of glaciers rather than from enhanced sea ice exports from the Arctic which are, on average, of the order of $0.1\,Sv$ [*Aagaard and Carmack*, 1989; *Vinje et al.*, 1998]. However, variations of the sea ice volume export of about one fourth of its mean over a period of 5–10 years can lead to changes of the meridional overturning cell and the associated heat transport of about 10–20% [*Mauritzen and Häkkinen*, 1997; *Häkkinen*, 1999].

Although there is, to some extent, a consensus about the mean sea ice flux through Fram Strait, much less is known about its variability. As a salient example, the occurrence of the "Great Salinity Anomaly" (GSA) [*Dickson et al.*, 1988] of the 1970s of the northern North Atlantic (Fig. 4.1) was presumably triggered by a pronounced sea ice export anomaly in the late 1960s. Based on their fresh water budget estimations, *Aagaard and Carmack* [1989] supposed that excessive sea ice volume exports into the GIN Seas in 1968 might have been the source of the GSA. Later on, their suggestion was confirmed by the modelling study of *Häkkinen* [1993]. From a 7-year integration of a sea ice model over the period 1986–1992 *Harder et al.* [1998] estimated that the standard deviation of the annual mean exports through Fram Strait amounts to 21% of its mean value and that individual annual means differ up to a factor of two. *Vinje et al.* [1998] found from observational based estimates of this export that within the period 1990–1996 the maximum export was about 130% larger than its corresponding minimum and 65% larger than the overall mean.

Beyond numerical modelling [e.g. *Häkkinen*, 1993; *Hilmer et al.*, 1998; *Arfeuille et al.*, 2000], the long-term evolution of the ice export through Fram Strait is also estimated from statistical models [*Vinje and Finnekåsa*, 1986; *Dickson et al.*, 2000]. These are commonly based on linear regressions between well observed atmospheric quantities, such as SLP gradients across the Fram Strait region, and measured sea ice export components, such as ice thickness and ice drift. However, due to the mostly short time periods used for deriving those relations, they strongly rely upon the stationarity of the applied statistical properties. Numerical models, on the other hand, are usually quite complex and need

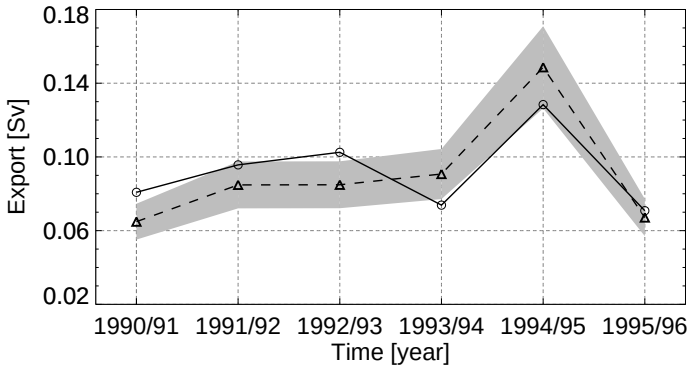

Figure 4.16: Comparison of simulated (solid line with open circles) with observed [*Vinje et al.*, 1998] (dashed line with triangles) ice exports (Sv) through Fram Strait. Shown are winter centred (August–July) annual means. The shaded area indicates the maximum error of the observations which is given as 15% of the observational values [*Vinje et al.*, 1998].

a comparatively larger amount of computer costs. However, they do not suffer from the above listed disadvantages of the statistical approaches. Moreover, they can additionally shed some light on processes which eventual remotely affect the ice export.

The aim of the following section is the analysis of the interannual variability of simulated sea ice exports based on a 49-yr data set. First, the models ability to reproduce the available observations is investigated. Second, temporal characteristics of long-term export time series are presented and some important anomalies are discussed in more detail. In the latter part of the section, the impact of both interannual forcing quantities, that is surface winds and SAT, on the interannual variability of sea ice exports will be assessed.

Parts of the following results have been previously published by *Hilmer et al.* [1998] using a shorter integration of the same model with slightly different forcing data sets. In contrast to the present study *Hilmer et al.* [1998] used an oceanic forcing which was derived from a coupled ice-ocean model of *Hibler and Zhang* [1994] not including the Baffin Bay region. Moreover, the prescribed annual cycles of cloud coverage and precipitation rate were spatially constant in *Hilmer et al.* [1998]. Overall, due to the above listed changes, the present integration performs better in simulating a realistic ice edge in the GIN Seas region and a more realistic annual mean sea ice drift in the Baffin Bay/Labrador Sea region. However, apart from small differences, all results of *Hilmer et al.* [1998] are confirmed.

4.4.2 Observational Estimates

Before discussing the interannual variability of the simulated sea ice exports, the model results have to compared, as far as possible, to observational time series. Unfortunately, observational estimates of sea ice volume exports are only available for Fram Strait over the period 1990-96 [*Vinje et al.*, 1998]. Since the late 1980s ULSs have been moored in the East Greenland ice drift stream to obtain measurements of the ice draft. But it is only since August 1990 that annual time series have been obtained regularly from this region [*Vinje et al.*, 1998]. To relate the measured ice drafts to ice thicknesses *Vinje et al.* [1998] used a conversion factor of 1.136 which was derived from nearly 400 drillings in the Fram Strait region.

To calculate the IVF (Eq. 3.1) the cross-strait profile of both, ice thickness and SDS have to be known. Because the footprint of the ULSs is only some meters and because usually only 1–2 moorings were simultaneously present in Fram Strait, *Vinje et al.* [1998] used a statistically matched cross stream thickness profile for their calculations. This was derived from a 7 month period of four simultaneously operating ULSs. Moreover, cross-strait drift speed profiles were derived from a regression model relating SLP gradients in Fram Strait to a combined set of drifting buoy data and Synthetic Aperture Radar (SAR) derived ice drift observations. The resulting annual mean IVF time series is shown in Fig. 4.16 together with the simulation results for the same period.

As already mentioned in Section 3.6 the mean values of both data sets does not differ significantly. The bias amounts to only 2% (0.002 Sv) relative to the observational average. However, using the same ice thickness data but ice drift estimates derived from passive microwave imagery *Kwok and Rothrock* [1999] revealed a 20% smaller average than *Vinje et al.* [1998]. The more important quantity for comparing interannual variability is the RMSD between model and observations which amounts to roughly 17% (0.002 Sv) of the observational mean value. This difference is only slightly larger than the annual error of about 15% which is given for the observations [*Vinje et al.*, 1998]. The most remarkable agreement between both data sets is the large positive anomaly in 1994/95 which is roughly twice as large as the minimum values at the beginning and ending of the time series.

The comparison of simulated ice volume transports through Fram Strait with observational estimates for a time period of only 6 years cannot be considered as a validation of the model. However, the fair agreement of interannual anomalies and especially the successfully simulation of the large positive anomaly in 1995 points towards the ability of the sea ice model to reproduce major interannual variations of sea ice export, as far as they can attributed to the atmospheric forcing of winds and air temperatures.

4.4.3 Temporal Characteristics

The 49-yr annual mean time series of simulated IVF through the four major passages of the Arctic/North Atlantic region are shown in Fig. 4.17. As already discussed in Sec. 3.6, it is obvious from the time series that by far the largest sea ice export occurs at Fram Strait. In the other passages (Denmark Strait, Barents Sea, and Davis Strait) the transports are an order of magnitude smaller. All time series exhibit large interannual variations about their long-term averages (see Tab. 3.2) with annual anomalies differing by up to a factor of two. Taking the annual mean values into account, the largest relative standard deviations are those for the exports through Barents Sea and Davis Strait with relative magnitudes of roughly 40% (standard deviation relative to the long-term average). The annual mean exports through Fram Strait and Denmark Strait exhibit, on average, variations of about 20%. However, having a closer look onto the time series of the Barents Sea export it appears that the large standard deviation can mainly be attributed to 3 large anomalies in the 1960s which are about twice the long-term average in magnitude. Therefore, and because the annual mean values do not correspond to a normal distribution, the classical standard deviation cannot be considered as an appropriate measure of the interannual variability of the Barents Sea export. In Davis Strait deviations from the long-term mean are rather small in magnitude but they occur as decadal-scale anomalies. Accordingly, the spectral analysis (Fig. 4.18a) of the annual means of this transport reveals a dominant time scale of about 15 years. On the eastern side of Greenland, a shorter time scale with

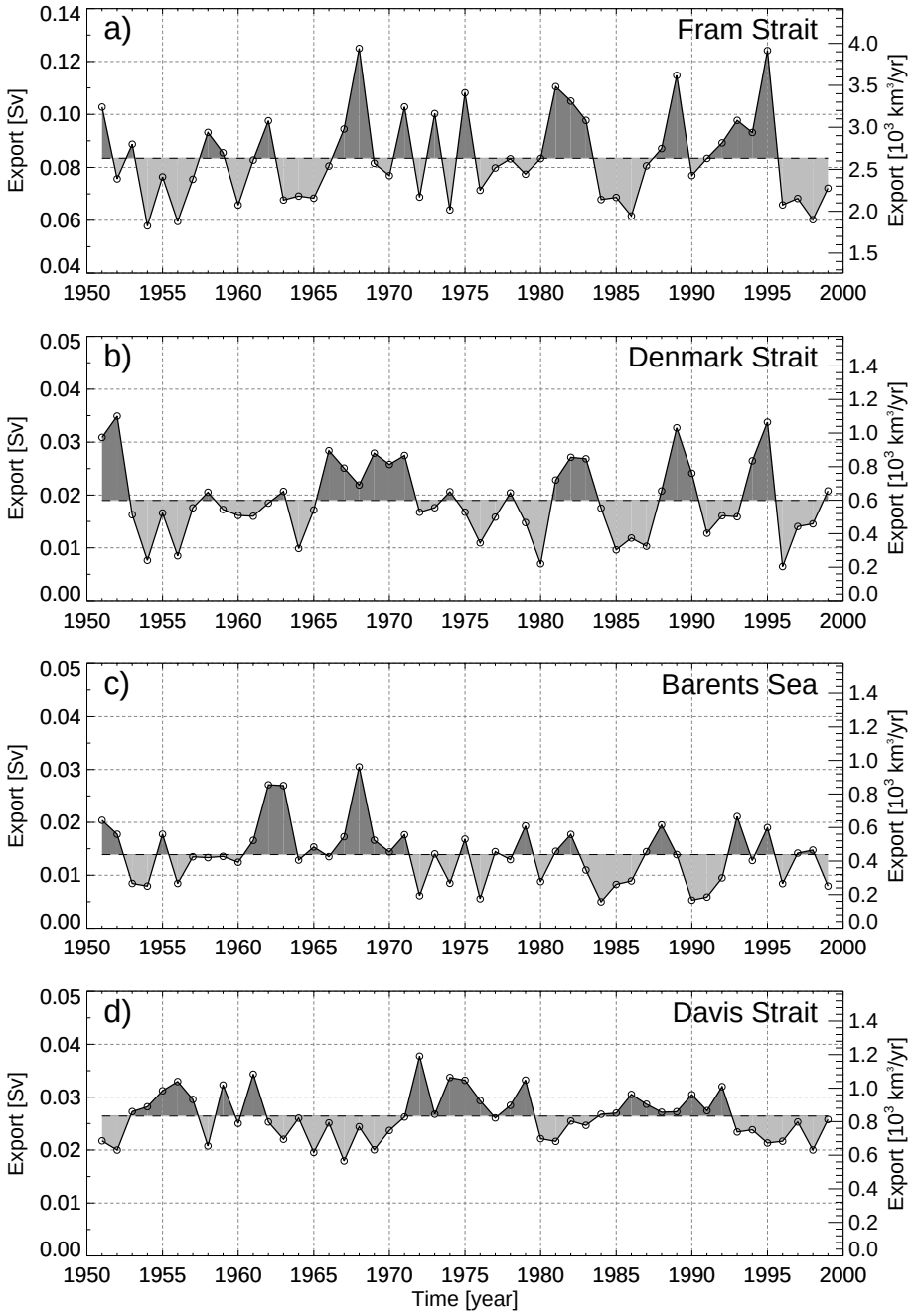

Figure 4.17: Annual mean time series of simulated sea ice transports (Sv and km^3/yr) through a) Fram Strait, b) Denmark Strait, and c) Barents Sea for the period 1951–1999. Note the different scale in the first panel.

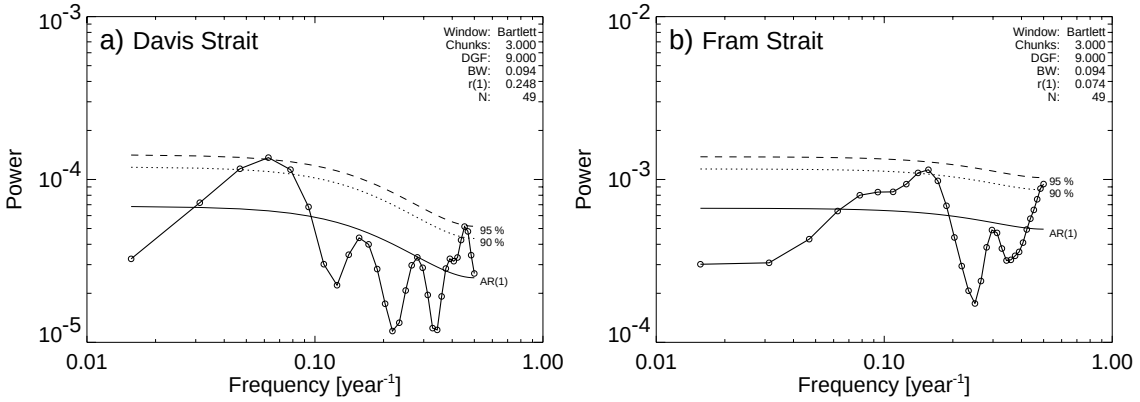

Figure 4.18: Power spectra of annual mean sea ice exports through a) Davis Strait and b) Fram Strait. The estimated spectra (solid line with bullets) are shown along with a first-order autoregressive process (solid line). Additionally shown are the 90% (dotted line)- and the 95% (dashed line)-confidence levels at which the local null-hypothesis of 'red noise' can be rejected. The spectra were estimated by taking the Fourier transform of the auto-covariance function.

dominant periods of 6–7 years governs the annual anomalies of the ice volume export through Fram Strait (Fig. 4.18b) and Denmark Strait (not shown).

The ice volume export through Fram Strait exhibits several outstanding positive anomalies exceeding the magnitude of one standard deviation (in 1968, 1975, 1981, 1982, 1989, and 1995). The two largest anomalies, occurring in 1968 and 1995, show magnitudes of about $3900\,km^3/yr$ and will be discussed in more detail later in this section. Some of the anomalies of the Fram Strait export are accompanied by simultaneous export anomalies at Denmark Strait (e.g. in 1982, 1989, 1995). Overall, the correlation between both time series is $r = 0.57$. On average, about 23% of the ice transport through Fram Strait passes through Denmark Strait. Depending on the drift speed within the East Greenland drift stream this portion varies from highest values of 42% in 1952 to lowest values of 7% in 1996. For comparison, *Aagaard and Carmack* [1989] estimated that 20% of the Fram Strait export passes through Denmark Strait whereas other numerical studies [*Mauritzen and Häkkinen*, 1997; *Arfeuille et al.*, 2000] yield a portion of about 40%. The ice export through Barents Sea, primarily representing a transport near the eastern coast of Spitsbergen (see Fig. 3.7), amounts on average to roughly 16% of the Fram Strait export. As mentioned earlier, there are three outstanding anomalies in the 1960s with a peak in 1968 accounting for 36% of the Fram Strait average. At least the fact that there is indeed a significant southward transport of sea ice east of Spitsbergen can be verified by analysing passive microwave data of sea ice area flux as was done by *Martin and Augstein* [2000]. In their study the southward ice area flux east of Spitsbergen amounts for the winter 1992/93 to about one fourth of that through Fram Strait [*Martin and Augstein*, 2000, their Figure 11].

4.4.4 Ice Export and Great Salinity Anomalies

Aagaard and Carmack [1989] were the first who brought the GSA of the 1960s into context with excessive sea ice export out of the Arctic. The time series of annual ice export through Fram Strait (Fig. 4.17a) supports their suggestion because it reveals a pronounced positive

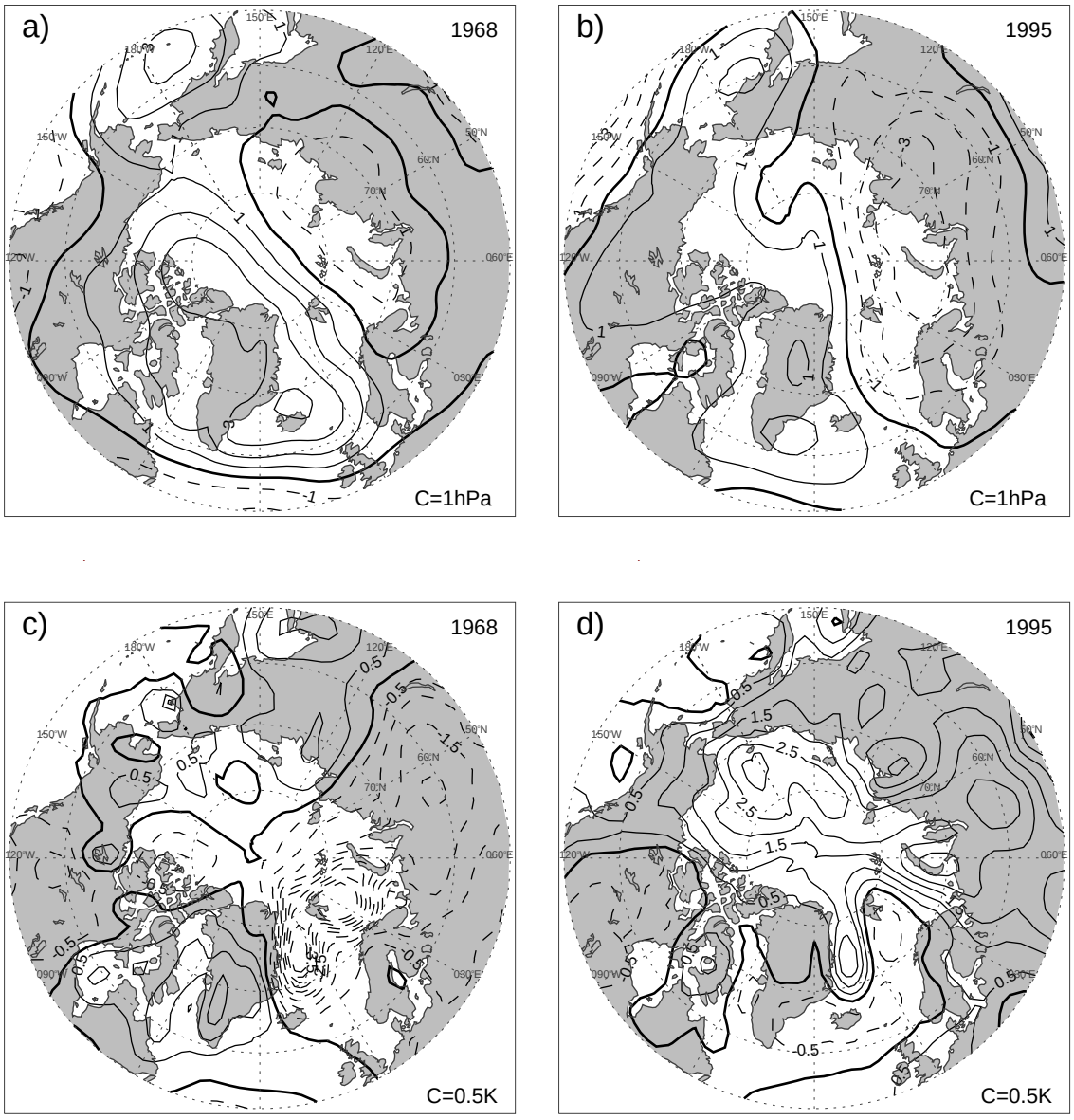

Figure 4.19: Atmospheric conditions for the years of largest sea ice export 1968 and 1995. a) and b) show the annual mean anomalies of SLP (hPa), whereas c) and d) show those for SAT (K). The anomalies where calculated by subtracting the long-term mean over the period 1951–1999 from the individual annual averages.

anomaly in 1968 — the year when the GSA was formed in the waters north of Iceland [*Dickson et al.*, 1988]. However, the simulation reveals, in agreement with observations (Fig. 4.16), another large anomaly in 1995, at a time when no significant low salinities in this area were reported. Furthermore, both simulated ice volume anomalies are nearly equal in magnitude with annual exports of $3900\,km^3/yr$ ($0.124\,Sv$). The export excesses in

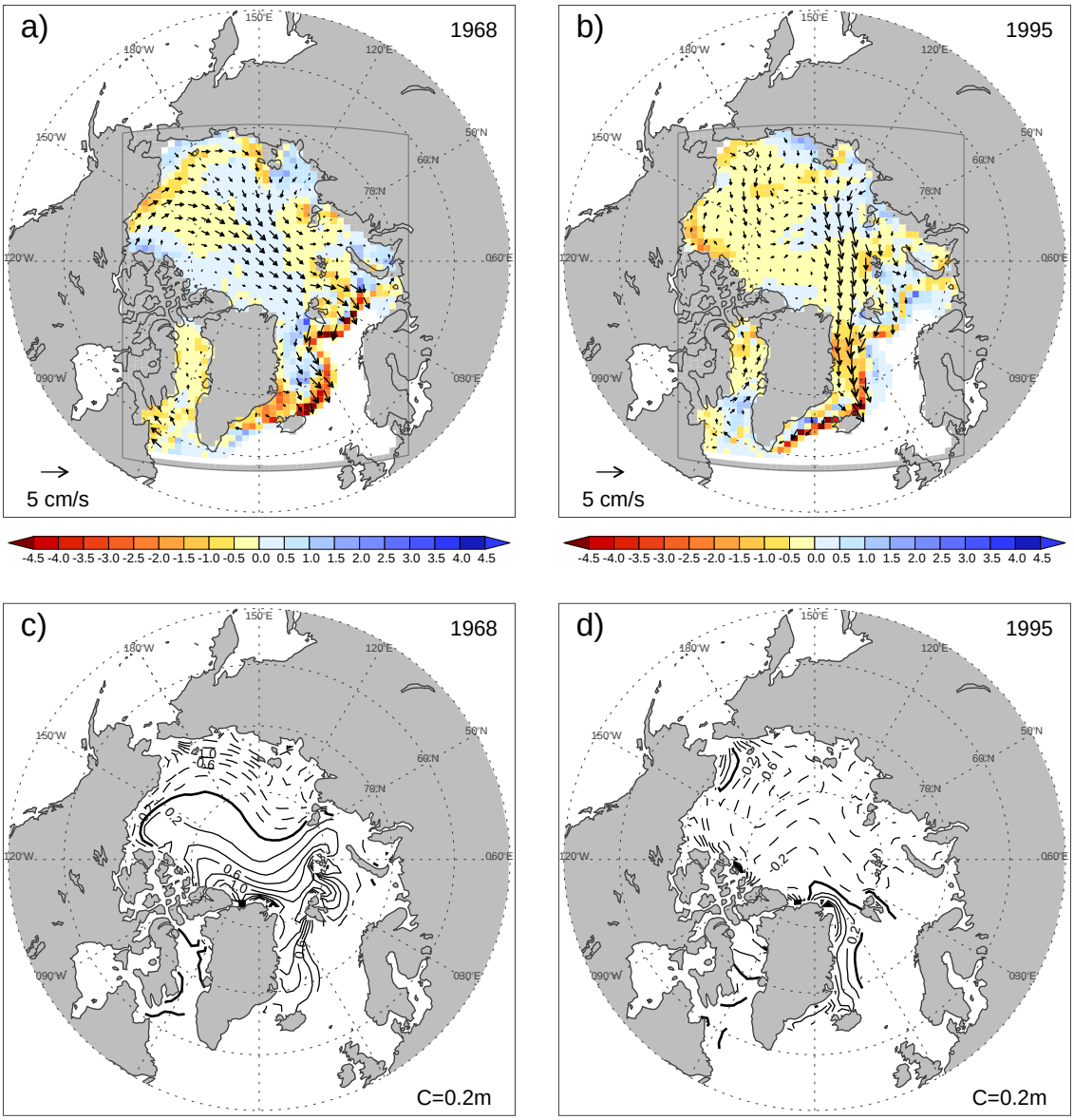

Figure 4.20: Sea ice conditions for the years of largest sea ice exports 1968 and 1995. a) and b) show the annual mean anomalies of the net freezing rate in m/yr (shaded) together with anomalous ice motion vectors (arrows), whereas c) and d) show anomalous ice thickness patterns (m). The anomalies where calculated by subtracting the long-term mean over the period 1951–1999 from the individual annual averages.

these years correspond to about half the long-term average and the associated freshwater excesses amounts to $1040\,km^3/yr$. To elaborate possible differences, both outstanding export anomalies will in the following be discussed in more detail, especially focusing on their impact on the freshwater input into the GIN Seas.

According to the simulation results, for the freshwater input into the GIN Seas it is not sufficient to analyse the IVF through Fram Strait only. Moreover, the flux through the Barents Sea (Fig. 4.17c) has additionally to be considered because it can add significant amounts of sea ice to these waters. Adding both exports together, the annual ice volume discharges from the Arctic amount to $0.155\,Sv$ in 1968 and to $0.143\,Sv$ in 1995. The annual IVF anomalies in these years are $1830\,km^3/yr$ in 1968 and $1440\,km^3/yr$ in 1995 and correspond to an annual freshwater excess of $1470\,km^3/yr$ and $1150\,km^3/yr$ for 1968 and 1995, respectively. Expecting some additional export of liquid freshwater within the surface layers of the East Greenland Current coinciding with large sea ice export anomalies, the freshwater excess in 1968 roughly agrees with the amount of $2000\,km^3/yr$ which was estimated by *Aagaard and Carmack* [1989] to be necessary for initiating the GSA. Moreover, a freshwater input has to be focused on a rather small regional scale to significantly change the salinity of the upper oceanic layers. This was the case in 1968, because only a small amount of the exported sea ice has left the GIN Seas through Denmark Strait further south. Thus, to consider the freshwater input into the GIN Seas the ice volume export through Denmark Strait (Fig. 4.17b) has to be subtracted from the exports through Fram Strait and Barents Sea. These considerations suggest that the freshwater input from melting sea ice into the GIN Seas area amounted to $1390\,km^3/yr$ in 1968 whereas it was only $780\,km^3/yr$ in 1995 due to a large export through Denmark Strait at this time. Similar magnitudes of freshwater input as in 1995 we also simulated in 1962 ($700\,km^3/yr$), 1975 ($750\,km^3/yr$), 1981 ($600\,km^3/yr$), and 1993 ($620\,km^3/yr$). Therefore, it is not surprising that for the 1990s no pronounced low salinity anomaly was reported.

The anomalous atmospheric conditions at the time of both large ice export anomalies are depicted in Fig. 4.19. The comparison of both years reveals a rather similar anomaly pattern of SLP but quite different departures of SAT from its long-term average. Whereas in 1968 roughly half of the ice pack experienced colder than normal conditions, most pronounced in the GIN Seas and in the Barents and Kara Seas (Fig. 4.19c), anomalous warm air temperatures over the entire Arctic region were dominant in 1995 (Fig. 4.19d). The anomalous SLP patterns are both characterised by a lower than normal pressure zone in the eastern part of the Arctic and higher than normal values on the western side and over Greenland. However, the anomalous SLP field in 1995 (Fig. 4.19b) is rotated clockwise by about 45° with respect to that in 1968 (Fig. 4.19a).

The wind field associated with the anomalous SLP pattern in 1968 led to an anomalously strengthened TPDS directed from the Beaufort towards the Barents Sea (Fig. 4.20a). As a consequence, thicker than normal ice was advected from the region north of the Greenland and the Canadian Archipelago to the area upstream of Fram Strait. This resulted in a pronounced positive anomaly of cross-strait averaged annual mean ice thickness in Fram Strait (Fig. 4.21a) whereas the cross-strait averaged SDS was only slightly enhanced at this time (Fig. 4.21b). Furthermore, due to this anomalous drift direction more than normal ice was exported through the Barents Sea (Fig. 4.17c). In general, the ice pack in the Laptev, the East Siberian, the Chukchi, and in the southern Beaufort Seas was thinner than average, whereas it was thicker than normal in the remaining areas. This increase in the latter regions was partly caused by the wind forcing in the previous year. As noted by *Walsh and Chapman* [1990] the SLP field in the year preceding the GSA was favourable to initiate a large IVF anomaly by advecting thicker than normal ice to Fram Strait. The anomalous SLP field in 1967 was characterised by a deep low between the North Pole

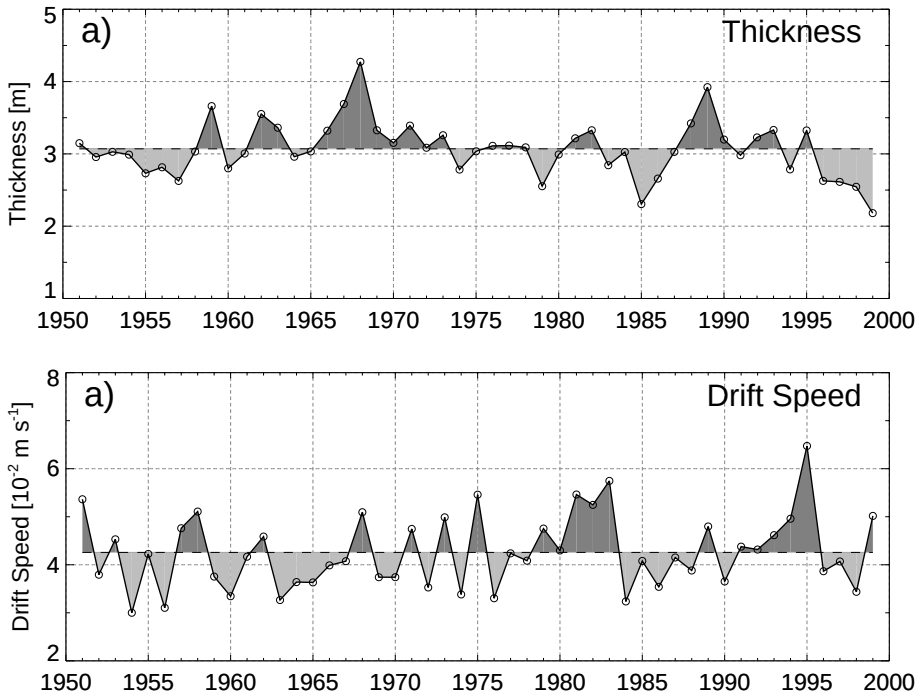

Figure 4.21: Annual mean time series of ice export components at Fram Strait. Shown are the cross-strait averaged annual mean time series of a) ice thickness (m), b) southward drift speed ($10^{-2}\,m/s$)

and Severnaya Zemlya (not shown) leading to a wind forcing which advected ice from the eastern part of the Arctic to the Beaufort Sea as well as from the ice buildup region north of Greenland to the region between the North Pole and Fram Strait. In fact, for 1967 the simulation yields ice thickness anomalies north of Fram Strait with magnitudes of about 0.4 to 0.6 m (not shown). Essentially the same thickness changes resulted from the WIND simulation (not shown), thus indicating that changes of the wind field only were sufficient to produce these ice thickness anomalies at the entrance region to Fram Strait. On the other hand, the main effect of SAT anomalies was obviously the reduction of the melt rates in the northern Greenland Sea and northern Barents Sea (see net freezing rate anomalies in Fig. 4.20a) due to colder than normal air temperatures.

The components of the IVF, ice thickness and SDS, exhibit in 1995 roughly opposite anomalies compared to 1968. That is, the SDS is largest in 1995 whereas the ice thickness in Fram Strait is nearly normal. The reason is that lower than normal SLPs centred over the Barents and Kara Seas (Fig. 4.19b) led to an enhanced TPDS which was this time directed from the Laptev Sea to Fram Strait (Fig. 4.20b). This resulted in an increased southward ice drift speed in Fram Strait and also within the entire East Greenland ice stream and, thus, in a positive anomaly of IVF through Fram and Denmark Straits. Due to this enhanced transport the ice thickness south of Fram Strait increased despite positive SAT anomalies in this area with magnitudes of about 2°C. In the other parts of the Arctic the ice pack was thinner than normal due to increased air temperatures. It is noteworthy, that even at SAT anomalies of 1.5° to 2.5°C in the Laptev and East Siberian Seas the net freezing rates in these regions are enhanced. These net freezing anomalies can be explained

by stronger re-freezing during autumn (not shown) because the ice thicknesses in these areas were anomalously low as a consequence of the large export, which primarily occured during early winter and summer. Similar to the situation in 1968, the SLP field in the year preceding the export anomaly of 1995 was also characterised by a strong anomalous low (not shown). However, this time the low was centred between the North Pole and the Canadian Archipelago leading also to enhanced advection of ice against the Canadian Archipelago and to a transport from the ice buildup north of Greenland to the Fram Strait region.

4.4.5 Atmospheric Forcing of Ice Export Anomalies

The ice volume export is defined as the product of SDS and ice thickness in Fram Strait integrated over the width of the passage (Eq. 3.1). To asses the contributions of either ice thickness or SDS to ice volume export anomalies the IVF and its contributors can be decomposed into mean values and anomalies as was done by *Arfeuille et al.* [2000]:

$$IVF = \int_S [\ (\overline{h\,u}_\perp) + (h\,u_\perp)'\ ]\,dx\ . \tag{4.1}$$

By further applying Reynolds averaging to its components h and $u_\perp$ the ice volume export anomalies $IVF' = IVF - \overline{IVF}$ can be written as:

$$\begin{aligned} IVF' \;=\; \int_S (h\,u_\perp)'\,dx \;=\; \int_S [\;\; & \overline{h}\,u'_\perp \;+\; h'\,\overline{u}_\perp \;+\; h'\,u'_\perp \;-\; \overline{h'\,u'_\perp} \;\;] \,dx \\ & \text{(I)} \;+\; \text{(II)} \;+\; \text{(III)} \;-\; \text{(IV)} \qquad . \end{aligned} \tag{4.2}$$

There are three major and one minor (term IV) terms in Eq. 4.2. The latter describes the negative cross-covariance between SDS and ice thickness anomalies and amounts to only $-2.6 \cdot 10^{-4}\,Sv$ $(-8\,km^3/yr)$ which is roughly 0.3% of the long-term averaged ice export. The three major terms of Eq. 4.2 are shown in Fig. 4.22 together with the ice export anomalies. Term III accounts for the actual joint variability of both SDS and ice thickness and contributes only little to specific export anomalies. Moreover, with a correlation coefficient of $r = 0.28$ between the anomaly time series and that of term III it also shows no temporal correspondence. The first two terms of Eq. 4.2 account for variations of SDS and ice thickness separately and contribute significantly to specific anomalies. As previously discussed, the large export anomaly of 1968 can mainly be attributed to an anomalously large ice thickness in Fram Strait. In fact, term II explains 67% of the export anomaly at this time whereas term I only amounts to 29%. Roughly the opposite holds true for the second major anomaly which occured in 1995. This time, SDS variations (term I) explain 91% of IVF$'$ whereas ice thickness variations (term II) contributed only 13% to this anomaly. From Fig. 4.22 it is obvious that several other large ice export anomalies can be addressed to either term I or term II. In the years 1954, 1956, 1963-65, 1975 and 1981-82 export anomalies are mainly caused by anomalous ice drift speeds in Fram Strait. Ice thickness variations, on the other hand, were primarily responsible for the export anomalies in 1985 and 1989. In general it can be deduced that most of the larger export anomalies in Fram Strait are due to anomalous drift speeds. This is also supported by the larger temporal correspondence between ice export anomalies and term I ($r = 0.83$) compared to that with term II ($r = 0.64$). On average, however, the terms I–IV have to balance.

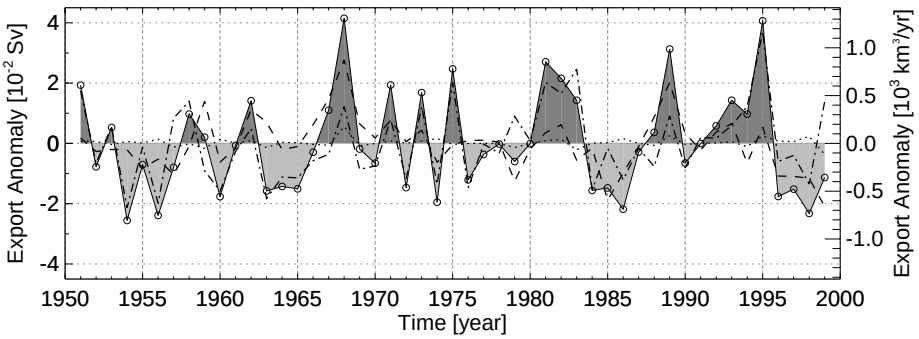

Figure 4.22: Decomposition of Fram Strait ice export anomalies. Shown are the time series of ice export anomalies (Sv) (solid line with grey shadings) together with its decomposition (according to Eq. 4.2) into term I (Sv) (dash-dotted line), term II (Sv) (dashed line), and term III (Sv) (dotted line). The residual term of the decomposition, term IV, is negligible small ($-2.6 \cdot 10^{-4} Sv$ or $-8\, km^3/yr$) and not shown.

The latter result points toward a dominance of the wind field in forcing anomalies of IVF through Fram Strait. As was pointed out in the discussion of the two large export events, even anomalies of ice thickness in Fram Strait can be attributed to the wind forcing. To confirm these statements, the IVF of the WIND simulation was subject to the same decomposition analysis as described above. First of all, the long-term averages of the IVF through Fram of both simulation differ only within 8% and the annual mean time series are correlated with $r = 0.98$. Moreover, the anomalies of IVF of the WIND simulation agree nearly perfectly in magnitude with those shown in Fig. 4.22. Slight differences occur in the magnitudes of the large export events in 1968 and 1995. In the case of the WIND simulation the 1968 export event is somewhat smaller by roughly $200\, km^3/yr$ whereas the 1995 anomaly is slightly larger by about the same amount. The terms I and II of Eq. 4.2 show similar correlation with the export anomalies ($r = 0.89$ for term I and $r = 0.62$ for term II) as those shown above. Furthermore, 58% of IVF anomaly in 1968 can be explained by ice thickness variations (term II) and 39% by the effect of anomalous SDS. This partitioning is nearly the same as in the simulation with interannual variability of both, the wind field and surface air temperatures. The same holds for the partitioning of the 1995 anomaly of the WIND simulation with 19% and 80% explained by the terms II and I respectively. Roughly similar results, at least regarding the partitioning of the larger export anomalies, were obtained by *Arfeuille et al.* [2000] who analysed a wind-driven sea ice model integration. Note, that ice exports resulting from the TEMP simulation (not shown) exhibit only very small anomalies which are entirely due to thermally induced ice thickness variations.

From the analyses above it can be concluded that major anomalies of the ice export through Fram Strait are depending on variations of both, the SDS and ice thickness in Fram Strait. It was also shown that both quantities primarily respond to changes of the wind field. In other words, interannual variations of the thermal forcing of the sea ice via SAT do not significantly affect the variability of IVF through Fram Strait on these time scales. This conclusion is further supported by considering regression patterns of SLP and SAT anomalies associated with ice volume exports (Fig. 4.23a,b). The typical SLP anomaly field associated with large ice exports through Fram Strait is characterised by an anomalous

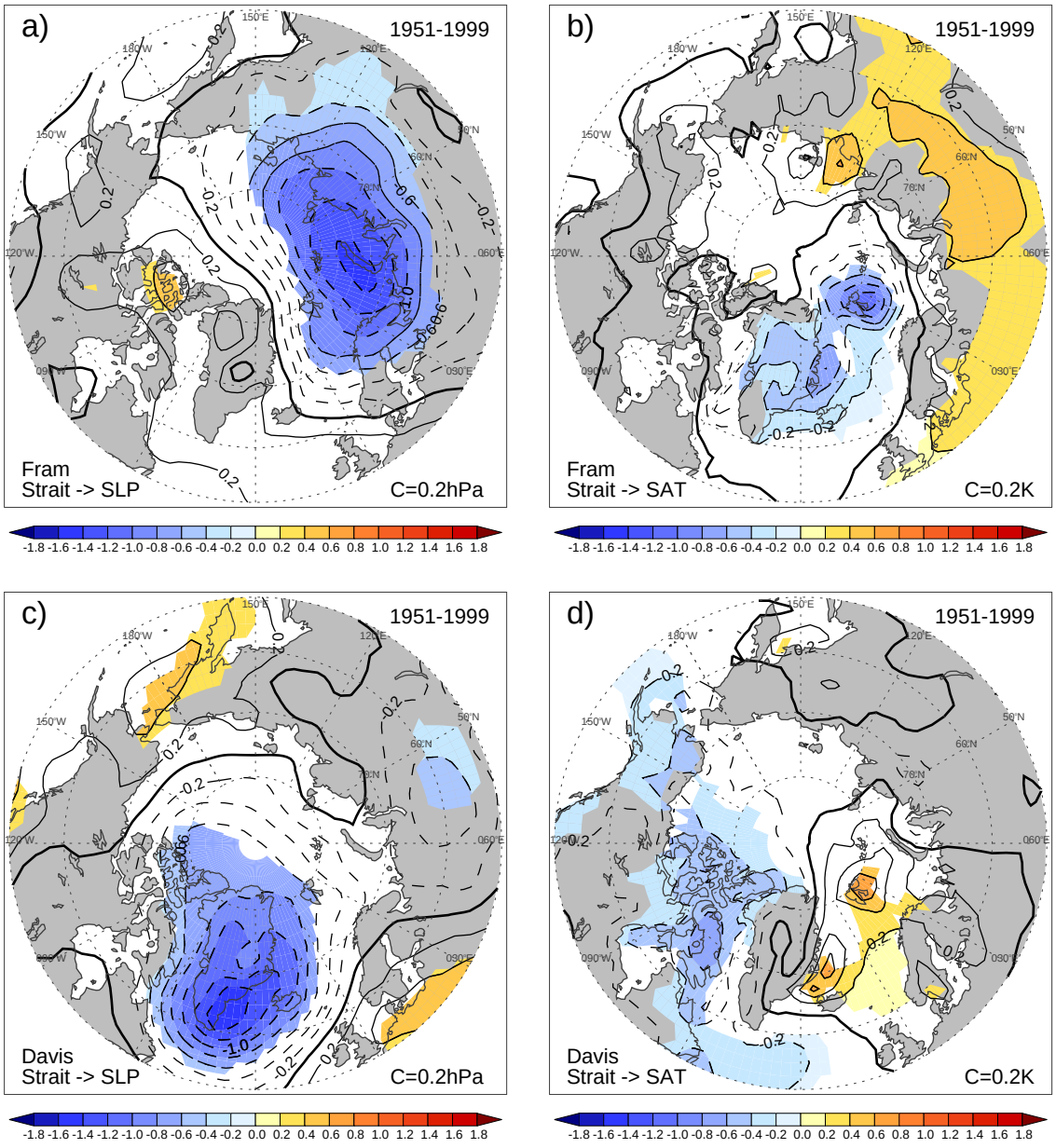

Figure 4.23: SLP anomalies (hPa) associated with ice volume exports through a) Davis Strait and b) Fram Strait. Anomalous annual mean SLP fields were regressed onto the normalised annual mean export time series. Statistically significant slope parameters (95%-confidence level) are coloured. The slope parameters were tested against the null hypothesis 'being zero' and the alternative hypotheses 'lower than zero' or 'larger than zero' using a two-sided *Students* t-test. Linear trends were removed prior to the analyses.

low over the eastern Arctic with its centre over Nowaya Zemlya and higher than normal pressures over the Canadian Archipelago (Fig. 4.23a). This pattern produces wind field anomalies capable of both, enhancing the SDS in Fram Strait an advecting thicker ice to its entrance region. Such ice drift changes emerge as the second EOF of ice drift variability

(Fig. 4.10b) which shows a temporal correlation with the Fram Strait export of $r = 0.77$ (as shown in the previous section). The SAT anomaly pattern associated with larger than normal IVF through Fram Strait (Fig. 4.23b) exhibits no significant anomalies over the main part of the Arctic ice pack. It can rather be interpreted as the typical SAT response pattern to wind field anomalies arising from the anomalous SLP associated to the ice export time series. That is, the negative SAT anomalies over Greenland and the GIN Seas can be explained by enhanced northerly winds advecting colder than normal air temperatures into these regions. The same holds true for the positive anomalies over Siberia which are presumably caused by anomalous westerly winds associated with the SLP pattern shown in Fig. 4.23a. Therefore, the associated SAT pattern shows no anomalies which are capable of causing significant thermodynamic changes of the ice thickness, which in turn could affect the ice export through Fram Strait. For comparison, similar regression patterns are shown for the time series of IVF through Davis Strait (Fig. 4.23c,d). Overall, the above drawn conclusions regarding the export through Fram Strait are also valid for that through Davis Strait. Again, the anomalous SLP pattern exhibits gradients favourable to force enhanced northerly winds over the Baffin Bay and anomalously southerly winds on the eastern side of Greenland. The SAT pattern associated with enhanced IVF through Davis Strait also shows the typical response to anomalies of the wind field with colder than normal temperatures over the Canadian Archipelago, the Baffin Island, and the Labrador Sea and positive anomalies in the GIN Seas region.

4.4.6 Conclusion

The interannual variability of simulated sea ice exports over the period 1951–99 is investigated. As for the ice thickness variability, only a small dataset of observational estimates is available for the comparison with the model results. However, the observations available for the ice export through Fram Strait over the period 1990-96, contain a pronounced example of interannual variability which is successfully reproduced by the model. By comparing with the simulated time series, this anomaly is considered in a longer-term context, and the associated anomalies of the freshwater input into the oceanic surface layers are related to the Great Salinity Anomaly of the northern North Atlantic. Finally, the relative contributions of ice thickness and ice drift speed anomalies to pronounced volume export event are identified and subsequently related to the atmospheric forcing. In particular, following conclusion can be drawn:

- The ice volume export through Fram Strait, which is by far the most important freshwater flux within the northern hemisphere, varies on average by about 20% about its long-term average.

- Within the last five decades, the largest positive anomalies of this export occured in 1968 and 1995 with roughly the same magnitude of $1300\,km^3/yr$ (49%) exceeding the overall mean.

- Differences between both anomalies emerge concerning their causes as well as their impacts on the freshwater input into the GIN Seas. The Anomaly of 1968 was primarily due to enhanced ice thicknesses in Fram Strait whereas that of 1995 was caused by increased southward drift speeds.

- According to different ice exports through the Barents Sea and through Denmark Strait, the anomalous freshwater input into the GIN Seas amounted in 1968 to roughly $1400\,km^3/yr$ whereas in 1995 it was only $800\,km^3/yr$. Similar freshwater flux anomalies as those in 1995 occured also in 1962, 1975, 1981, and 1993.

- A decomposition analysis of the ice volume export through Fram Strait revealed that most of its positive anomalies are caused by excessive southward drift speeds rather than to increased ice thicknesses. Furthermore, both ice thickness and ice drift speed anomalies can be explained to a large degree by interannual variability of the wind field only.

- The anomalous SLP pattern associated with enhanced ice exports through Fram Strait is characterised by an anomalous low centred over the Barents and Kara Seas and higher than normal pressures over Greenland and the Canadian Archipelago. However, the anomalous low dominates in magnitude and is most significant.

4.4.7 Discussion

With about $2100\,km^3/yr$ freshwater discharge, the sea ice export through Fram Strait is the second largest freshwater flux on earth, and by far the largest one of the Northern Hemisphere. The present study has shown that the magnitude of the ice volume export through Fram Strait varies, on average, by about 20% around its long-term mean value. Numerical studies with ocean models [e.g. *Marotzke and Willebrand*, 1991; *Rahmstorf*, 1994; *Mauritzen and Häkkinen*, 1997; *Häkkinen*, 1999] have shown that rather moderate changes of the freshwater input into the northern North Atlantic can lead to variations of the thermohaline circulation. For example, *Mauritzen and Häkkinen* [1997] and *Häkkinen* [1999] found from sensitivity studies with coupled sea ice-ocean models that variations of the Fram Strait ice export by about $800\,km^3/yr$ over 5–10 years lead to changes of the strength of Atlantic meridional overturning cell by about 10–20% with similar changes of the meridional heat transport. From the present study it follows that such variations of the sea ice export are likely to occur. However, various ocean models differ in their sensitivity to freshwater perturbations which, besides individual model parameters, depends on the duration and location of the freshwater input in sensitivity experiments [*Rahmstorf*, 2000].

The most remarkable example of the impact of sea ice exports onto the North Atlantic ocean was the occurrence of the GSA of the 1970s. Whereas *Dickson et al.* [1988] reported the occurrence of the low salinity signal and its subsequent circulation within the subpolar gyre it were *Aagaard and Carmack* [1989] who suggested excessive sea ice exports out of the Arctic as its possible cause. From the analysis of SLP fields over the Arctic Ocean *Walsh and Chapman* [1990] showed that the wind fields of 1967 and 1968 were indeed favourable for the creation of a large anomaly of the sea ice export through Fram Strait. However, only the modelling efforts of *Häkkinen* [1993] confirmed these suggestions by simulating a large ice export anomaly in 1968. From observations during the 1990s [*Vinje et al.*, 1998] another large anomaly of sea ice export was found but no pronounced salinity anomalies were reported. The study of *Hilmer et al.* [1998] and the present study offer the possibility of comparing the two large ice export anomalies. It was found, that both anomalies were equal in magnitude but that differences regarding their formation and their associated freshwater input into the GIN Seas occured. Whereas the 68' anomaly was due to enhanced ice thickness anomalies in Fram Strait (as suggested by *Walsh and Chapman*

[1990]) the 95' anomaly was caused by larger southward ice drift speeds. Therefore, in 1995 a large amount of sea ice was simultaneously exported further southward through Denmark Strait, whereas in 1968 most of the ice melted with the GIN Seas. As a results, the 68' anomaly stands out as the most important anomaly of freshwater input into the GIN Seas by melting sea ice. This agrees with the findings of *Häkkinen* [1999] who stated that a large portion of sea ice exported from the Arctic accumulated in the Greenland Sea and did not exit through Denmark Strait until late fall 1968 and early of the following winter. The timing of this freshwater pulse, from October 1968 to March 1969, has a strong effect on oceanic convection further downstream because in late fall–early winter the new deep water is formed through densification by thermal fluxes [*Häkkinen*, 1999]. Furthermore she stated that this deep mixing process can be disrupted by excessive freshwater input from sea ice melt which in turn leads to a further freshening because the local precipitation is accumulating at the surface.

From salinity sections taken in the North Atlantic during the 1970s a circulation of the GSA around the subpolar gyre was deduced (Fig. 4.1) [*Dickson et al.*, 1988]. Moreover, low salinities in the GIN Seas in 1981/82 were interpreted as the return of the GSA [*Dickson et al.*, 1988]. From the present model results, however, this return is questioned because pronounced positive sea ice export anomalies occurred during this time. This suggests that the 'return of the GSA' rather may have been the formation of a new low salinity signal due to enhanced sea ice melt.

In order to detect the relative impact of ice thickness and sea ice drift to anomalies of the sea ice volume export a decomposition of the export anomalies following *Arfeuille et al.* [2000] was performed. As a result it was found that most of the large ice export anomalies are caused by stronger than normal southward drift speeds in Fram Strait and that only two anomalies (in 1968, 1989) were due to excessive ice thickness. Although SAT variations affect the long-term average [*Harder et al.*, 1998] of the ice export, from a comparison with the decomposition applied to the WIND simulation and that performed by *Arfeuille et al.* [2000] it follows that SAT variations are not important for the interannual variability of ice export nor are they important for the relative contributions of ice thickness and ice drift to pronounced export anomalies. That is, even larger ice thickness anomalies at Fram Strait can be attributed to changes of the wind field as was suggested by *Walsh and Chapman* [1990]. Therefore, the variability of the Fram Strait ice export, and especially some of its major anomalies, cannot entirely (only 69%) be explained by local winds but rather depend on larger scale circulation anomalies. This is important when considering parameterised ice export time series [e.g. *G. Alekseev*, in *Dickson et al.*, 2000] which are based on SLP gradient time series describing the local geostrophic winds in Fram Strait. The typical SLP anomaly pattern associated with larger than normal ice export covers large parts of the Arctic with pronounced negative anomalies over the Barents and Kara Seas. Similar patterns were also found by other studies [*Häkkinen and Geiger*, 2000; *Goosse et al.*, 2000]. *Delworth et al.* [1997] found also a similar pattern but from regression analysis of SLP anomalies onto SST variations in Denmark Strait derived from a coupled ocean-atmosphere model. From composite analyses *Skeie* [2000] found a very similar pattern to be important for the sensible heat loss of the Nordic Seas as well as for Eurasian SAT variations. According to the most dominant mode of SLP variability in the Arctic, that is the Arctic Oscillation, he calls this pattern the 'Barents Oscillation'. Summarising, due to its effects on the export of sea ice out of the Arctic, this pattern seems to be very important for the oceanic conditions of the GIN Seas and the northern North Atlantic.

With its centres of action located over the Barents/Kara Seas and over Greenland and the Canadian Archipelago this pattern does not resemble the NAO pattern. However, recent studies [*Kwok and Rothrock*, 1999; *Dickson et al.*, 2000] suggest a relation between the NAO and sea ice exports through Fram Strait. Therefore, the following section is aimed to clarify this seeming discrepancy.

4.5 The North Atlantic Oscillation and Sea Ice Exports

4.5.1 Introduction

The dominant mode of atmospheric interannual variability over the North Atlantic region is the North Atlantic Oscillation (NAO). The NAO is a large scale alternation of atmospheric mass with simultaneous strengthening and weakening of the Icelandic low and the Azores high [*Hurrell*, 1995, their Fig. 1b]. During high NAO winters the SLP over Iceland is below average whereas it is larger than normal over the Azores. This pattern coincides with stronger than normal westerlies over Europe, anomalous southerly flow over the eastern United States and enhanced northerly winds over the western coast of Greenland and the Labrador Sea. The opposite holds for the negative phase of the NAO. The difference of normalised SLPs between its two major cells commonly serves as an index of this oscillation. *Hurrell* [1995] defined the NAO index as the difference between normalised pressures at Lisbon, Portugal and Stykkisholmur, Iceland. A recent description as well as a detailed overview of the NAO is given, e.g., by *Jung* [2000]. In the recent past the NAO was brought into context with various climate parameters of the Arctic Ocean [*Dickson et al.*, 2000, and references therein]. Among these is a possible correlation of the NAO with sea ice exports out of the Arctic Ocean. Such a linkage would be very attractive for the construction of so-called climate feedback loops for the Atlantic region, like suggested by *Wohlleben and Weaver* [1995], because the IVF could serve as a link between atmospheric NAO variability and fluctuations of oceanic properties. Recent studies indeed report on a high correlation between the wintertime NAO index and sea ice fluxes through Fram Strait. From the analysis of satellite based estimates of the ice area flux through Fram Strait *Kwok and Rothrock* [1999] report a high positive correlation with the NAO index ($r = 0.66$) for the period 1978–1996. For the 5-yr period of ice thickness observations in Fram Strait (1990–1995) they report a correlation coefficient of $r = 0.56$ between the NAO and ice volume exports. *Dickson et al.* [2000] found a slightly higher correlation ($r = 0.77$) when analysing the time series of parameterised ice volume flux through Fram Strait [*G. Alekseev*, in *Dickson et al.*, 2000] for the period 1976–1996. These results support the conclusion of *CLIVAR* [1998] stating that the NAO appears to exert a significant control on the ice and freshwater exports from the Arctic to the North Atlantic.

The facts that roughly 70% of the ice motion variations can be explained by surface winds [*Thorndike and Colony*, 1982] and that ice motion variations dominate the IVF variability (see Fig. 4.22 and Eq. 4.2) can be considered as confirming this hypothesis. On the other hand, the anomalous SLP pattern associated with large ice exports through Fram Strait (Fig. 4.23a) does not resemble the typical NAO related SLP anomaly pattern (NAO pattern) [e.g. *Hurrell*, 1995; *Dickson et al.*, 2000, their Figs. 1b and 1a respectively]. With its northern centre of action located between Iceland and the southeastern coast of Greenland the NAO pattern shows nearly no meridional gradient in the vicinity of Fram Strait. However, such a gradient would be necessary to force southerly wind anomalies in this region which would contribute to the variability of the ice volume flux out of the Arctic. This deficiency is elucidated by the comparison of the anomalous ice drift patterns associated with both the IVF through Fram Strait (Fig. 4.24a) and the NAO index (Fig. 4.24c). Whereas there are large southerly anomalies of the ice drift in the Fram Strait region and an enhanced TPDS associated to positive IVF anomalies only a minor increase of the East Greenland Drift Stream can be accounted for NAO variations.

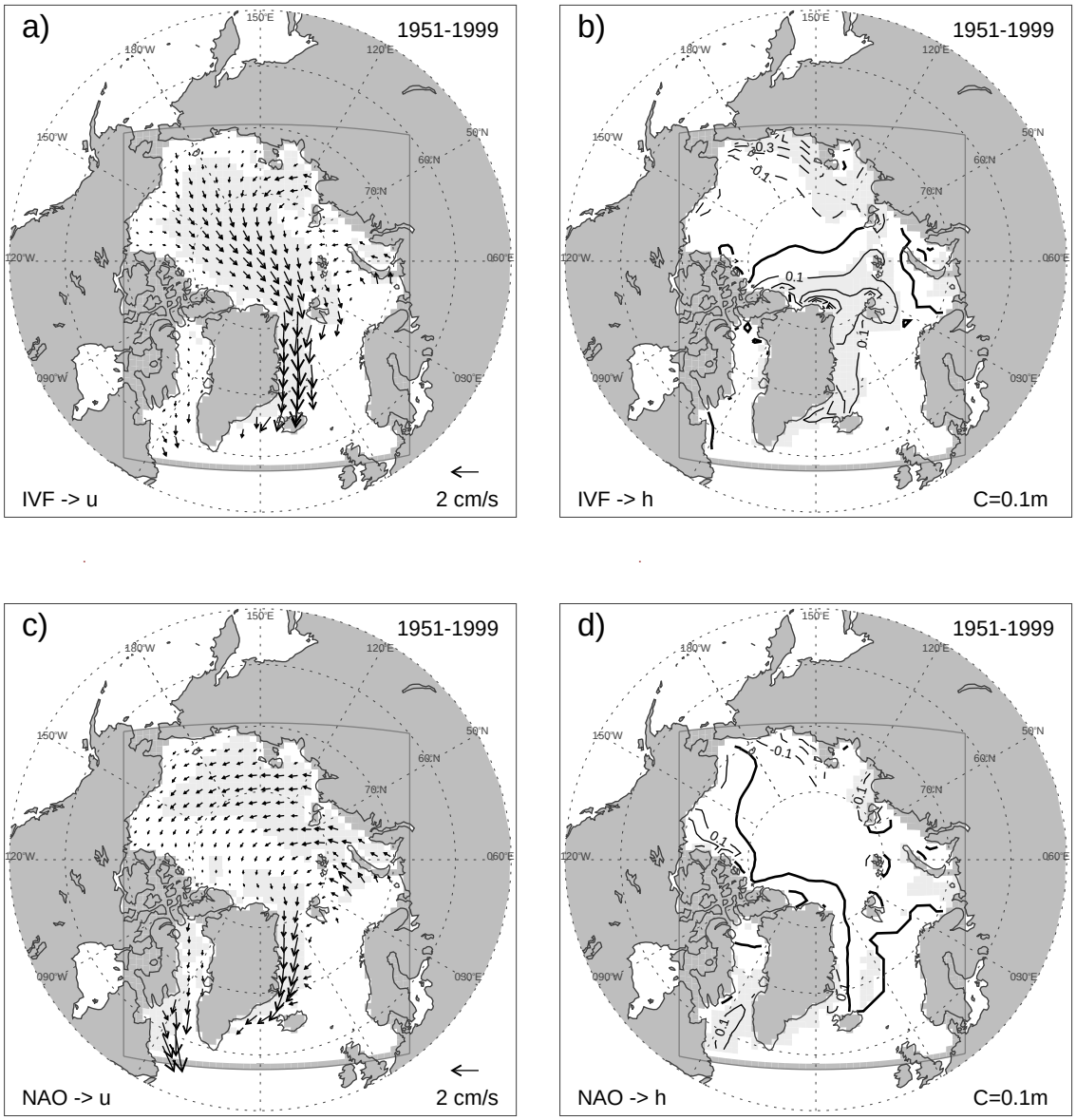

Figure 4.24: Comparison of wintertime (DJFM) anomaly fields of ice drift (left panel in cm/s) and ice thickness (right panel in m) associated with the IVF through Fram Strait (upper panel) and with the NAO index (lower panel) for the period 1951–1999. In b) and c) anomalous ice thickness fields were regressed onto the normalised index time series (IVF and NAO index respectively). Statistically significant slope parameters (95%-confidence level) are grey shaded. Contour interval is 0.1 m. The associated regression pattern of ice drift show vectors consisting of the slope parameters of the regressions of both ice drift components onto the normalised index time series (IVF and NAO index respectively). Grey shadings mark vectors consisting of at least one slope parameter being statistically significant at the 95%-confidence level. Slope parameters were tested against the null hypothesis 'being zero' and the alternative hypotheses 'lower than zero' or 'larger than zero' using a two-sided *Students t*-test.

Moreover, there are nearly no enhancements of southerly ice drift vectors in the region upstream Fram Strait associated with the NAO. Roughly the same holds for ice thickness variations (Fig. 4.24b,d), which are negligibly small in the pattern associated with the NAO index. As a consequence of these considerations the correlations between ice fluxes and the NAO found by *Kwok and Rothrock* [1999] and *Dickson et al.* [2000] seem astonishing.

There are some indications that the NAO exerts a significant control on ice fluxes through Fram Strait. But there are also arguments questioning such a link. Summarising, from the present knowledge it is not clear whether or not the NAO contributes to the variability of ice fluxes out of the Arctic. Providing an answer to this question is the aim of the following section. First, the link between IVF and NAO will be analysed using observational SLP data together with the output of the present sea ice model integration. Furthermore, using data from a Coupled General Circulation Model (CGCM) the possible link will be investigated in a longer-term context.

The results presented in this section are based on fruitful collaboration with Dr. Thomas Jung and have been already published or submitted for publication, respectively, by *Hilmer and Jung* [2000], *Jung et al.* [2000], and *Jung and Hilmer* [2000]. However, the following section can be considered as an update of some of the published results, because the above cited publications applied sea ice data from the integration of *Hilmer et al.* [1998] covering only the period 1958–1997. As already described in the introduction of Section 4.4, the presented sea ice model integration has, besides the increased length of the simulation period, some advantages compared to that of *Hilmer et al.* [1998].

4.5.2 Data Description

In addition to observational data and the output from the present sea ice simulation a possible link between the NAO and IVF through Fram Strait will be analysed using data from the coupled atmosphere-ocean-sea ice general circulation model ECHAM4/OPYC3 [*Roeckner et al.*, 1996]. It consists of the atmospheric model component ECHAM4 and the oceanic model component OPYC3 which includes a dynamic-thermodynamic sea ice model. ECHAM4 is the fourth generation of a hierarchy of models that was developed at the MPI Hamburg, Germany, from the former ECMWF model [*Roeckner et al.*, 1996, 1999]. The horizontal resolution of ECHAM4 is T42 which corresponds to a latitude-longitude grid spacing of about 2.8° by 2.8°. The vertical coordinate is represented by 19 hybrid layers. The oceanic part, OPYC3, is a 3-component ocean general circulation model including an isopycnal interior ocean with embedded mixed layer as well as a dynamic-thermodynamic sea ice model with a viscous-plastic rheology [*Oberhuber*, 1993]. The spatial resolution of OPYC3 is the same as for ECHAM4 outside the tropics. For the coupled system, an annual mean flux correction scheme applied to heat and freshwater fluxes has been applied. In the present study, data from both a 300-yr control integration under present-day climate conditions and from a 240-yr scenario run of this CGCM are used. The latter integration is from a transient experiment under increased greenhouse gas concentrations for the period 1860–2099. The prescribed anthropogenic greenhouse gas forcing is based on observations for the period 1860–1990 and on the IPCC scenario IS92a [*Houghton*, 1996] for the period thereafter. Effects of ozone and sulfate aerosols are not taken into account. More details of these integrations are given by *Ulbrich and Christoph* [1999] and *Christoph et al.* [2000].

The NAO index time series for the period 1951–1999 is derived from the NCEP/NCAR

SLP data set applying the common methodology of *Rogers* [1984]. That is, the NAO index is defined as the difference between normalised SLP of the Azores high and the Icelandic low. Normalising the pressure data means that time time series of anomalous SLP is divided by its standard deviation. The correlation coefficient of this time series with the NAO index derived from station data *Jung* [2000] is $r = 0.99$ for this period. The same method was applied to the ECHAM4/OPYC3 data. Here, after the definition of *Christoph et al.* [2000], the difference of simulated SLP data over the regions $10°$-$15°W$ and $40°$-$42.5°N$ representing the Azores high and $17.5°$-$20°W$ and $65°$-$67.5°N$ representing the Icelandic low is used. These regions exhibits in this CGCM the strongest tele-connectivity [*Christoph et al.*, 2000] and represent the centres of action of the first EOF of North Atlantic SLP anomalies.

Because both the NAO and the IVF through Fram Strait exhibit largest variability in the winter season (see Fig. 3.2 of *Jung* [2000] and Fig. 3.17 of the present study), averages over the months December, January, February, and March (DJFM) will be used throughout the following section.

4.5.3 The Link between the NAO and Sea Ice Exports

The 49-yr time series of winter-averaged (DJFM) sea ice quantities in Fram Strait are shown in Fig. 4.25 together with the NAO index. Compared to their annual mean counterparts (Fig. 4.17a, Figs. 4.21a and b) the winter averaged time series of IVF, SDS and h explain roughly at least half of the variability (60%, 48%, and 64% respectively) of their corresponding annual mean time series. Moreover, as was derived for the annual means, it is mainly SDS and to a lesser degree h that contributes to IVF variability (Tab. 4.3). For comparison with the study of *Kwok and Rothrock* [1999] the sea ice area flux was derived from the model data. This quantity accounts for the width of the ice stream times the drift speed in Fram Strait (it is described by Eq. 3.1 if ice thickness h is exchanged with ice concentration A). Fig. 4.25a reveals that there is a very good agreement between the simulated and the observed area flux ($r = 0.88$). On one hand, this agreement can be considered as a support for the model, but on the other hand it raises an interesting question about the link between the NAO and the ice export through Fram Strait. The facts that *Kwok and Rothrock* [1999] found a high correlation between the NAO and their

Table 4.3: Linear correlations for winter averages (DJFM) of the observed NAO index, the ice volume flux through Fram Strait (IVF) and cross-strait averages of ice thickness (h) and southward drift speed (SDS) in Fram Strait. Correlations coefficients are given for three different periods (1951–1977/1978–1999/1951–1999). Correlations significantly different from zero (at the 95%-confidence level based on a two-sided *Students-t*-test) are indicated as bold numbers.

	IVF	SDS	h
NAO	-0.01/**0.67**/**0.34**	0.02/**0.74**/**0.43**	-0.18/0.19/-0.10
SDS	**0.89**/**0.91**/**0.90**	**1.00**/**1.00**/**1.00**	0.19/0.35/0.22
h	**0.59**/**0.69**/**0.60**	0.19/0.35/0.22	**1.00**/**1.00**/**1.00**

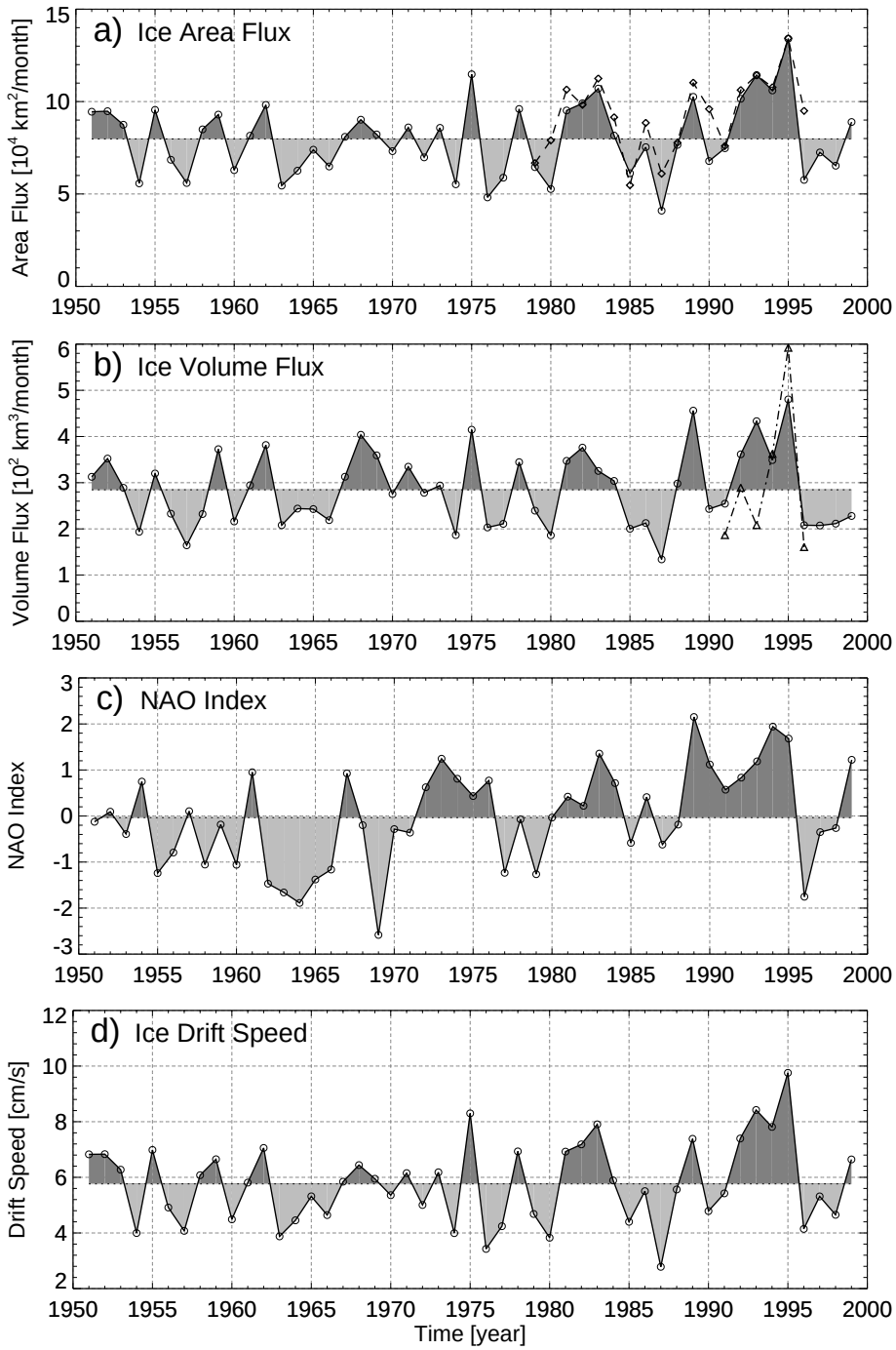

Figure 4.25: Time series of observed and simulated sea ice quantities in Fram Strait and NAO index for the winter season (DJFM). Shown are: a) modelled (solid) and satellite derived (dashed) [*Kwok and Rothrock*, 1999] (dashed) ice area flux ($km^2/month$); b) modelled (solid) and observed (dash-dotted) [*Vinje et al.*, 1998] ice volume flux ($km^3/month$); c) NAO index; d) modelled cross-strait averaged southward drift speed (cm/s); e) modelled cross-strait averaged ice thickness (m). Dotted lines represent long-term averages for the period 1951–1999.

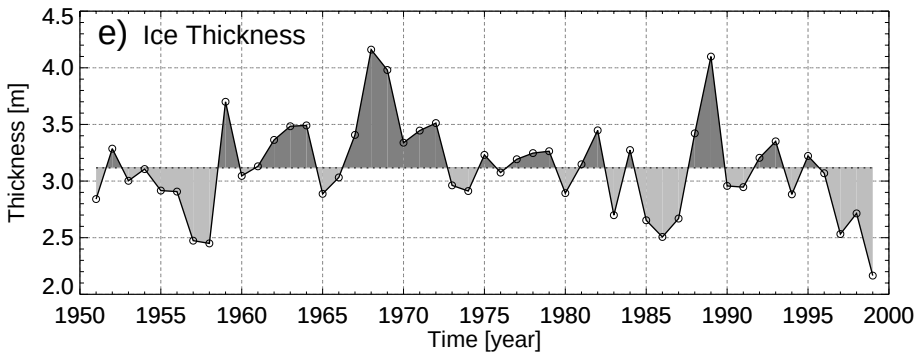

Figure 4.25: (continued)

ice area flux through Fram Strait and that the sea ice model resembles their observations seem contradictory to the fact that the NAO explains only 12% of the variance of IVF over the simulation period 1951–1999 ($r = 0.34$; see Tab 4.3). Partitioning the time series into one part roughly matching the time interval investigated by *Kwok and Rothrock* [1999] and one part representing the time before, this discrepancy can be explained. Whereas during 1978–1999 (P2 hereafter) the NAO explains, in agreement with *Kwok and Rothrock* [1999], about 50% of the IVF variability the correlation was nearly zero during the period 1951–1977 (P1 hereafter) (Tab. 4.3, Fig. 4.26). The correlation analysis shown in Tab. 4.3 reveals that primarily changes in the correlation between the NAO and SDS are responsible for these difference.

To further investigate the time dependence of the link between the NAO and IVF through Fram Strait a running cross-correlation analysis using a window length of 19 years was carried out. That is, the linear correlation coefficients of 33 overlapping chunks were calculated and plotted as a time series (Fig. 4.27). This analysis reveals that indeed in the second half of the 1970s there was a marked transition from no correlation to high correlation between both time series. At the end of the cross-correlation time series, roughly matching the time interval considered by the observational studies [*Kwok and Rothrock*, 1999; *Dickson et al.*, 2000], the NAO explains roughly 50% of the IVF variability. Moreover, a wavelet co-spectra analysis of *Jung* [2000] (also shown in *Hilmer and Jung* [2000]) revealed that in-phase variability between the two time series increased markedly after the late 1970s. Due to the nature of both methods to smooth in the time domain, it is not possible to exactly define a single year as the transition. However, for reasons of comparability, the separation into P1 and P2 as described above will be maintained throughout the remainder of this section.

To investigate possible reasons for the change of the link between the NAO and sea ice exports out of the Arctic, the SLP anomaly pattern associated with both the IVF and the NAO index will be considered. Fig. 4.28c shows the typical SLP anomaly pattern associated with enhanced winter-averaged ice volume exports through Fram Strait (Fram Pattern hereafter). Overall, this pattern is very similar to that obtained for the annual mean time series (Fig. 4.23a) with an anomalous low centred over the Barents Sea, but with stronger magnitudes. The anomalous zonal pressure gradient on the western side of this anomalous low, evident along a line from the North Pole to the East Greenland Sea, is responsible for an enhanced wind forcing of the TPDS as well as for increased northerly

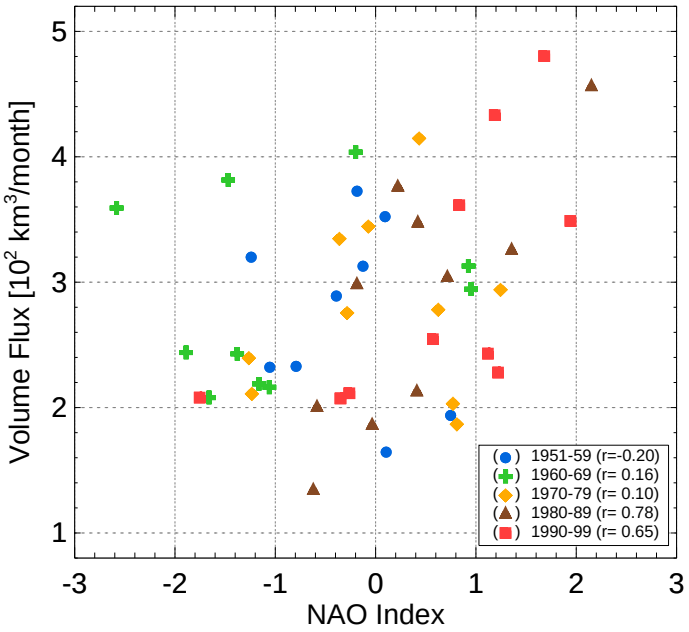

Figure 4.26: Modelled ice volume flux through Fram Strait versus observed NAO index during winter season (DJFM). The legend shows the different symbols used for data of each decade as well as the corresponding correlation coefficients for these periods. Note that the correlation coefficients were not tested for significance due to the small sample size for each period.

winds in Fram Strait. Note, that the regression pattern associated with the total ice export (the sum of the exports through Fram Strait and Barents Sea) given by [*Hilmer et al.*, 1998, their Fig. 5] is also very similar to the Fram Pattern given in Fig. 4.28c. During P1 the anomalous SLP pattern associated with the NAO index (Fig. 4.28a) exhibits the well known dipole structure [e.g. *Hurrell*, 1995] with its northern centre of action located over the south-eastern coast of Greenland. In comparison to the Fram Pattern there are nearly no zonal pressure gradients evident in Fram Strait or in the region upstream of Fram Strait which could affect the ice volume export by anomalous meridional winds. This lack of NAO related wind forcing of ice export anomalies explains the missing correlation in the period 1951–1977. During P2 interannual NAO variability intensified over the Norwegian and Barents Sea region as well as over the Iberian Peninsula (Fig. 4.28b). Compared to P1 the pattern of NAO related interannual SLP variability has shifted eastward during the last two decades as can clearly be seen from their difference pattern (Fig. 4.28d). As a consequence of this eastward shift, during P2 there are NAO related anomalous zonal pressure gradients in the Fram Strait region which are able to affect the variability of IVF through Fram Strait by forcing the sea ice with anomalous northerly winds.

The different impacts of NAO related wind field anomalies onto sea ice drift during P1 and P2 are well documented by the ice drift regression patterns shown by Fig. 4.29. During P1 the pattern of anomalous sea ice drift associated to the NAO is characterised by a cyclonic circulation with its centre north of Fram Strait (Fig. 4.29a) leading to significant anomalous offshore ice drift in the Laptev Sea region, anomalous inflow of sea ice in the Barents Sea, and enhanced southward ice drift in the Davis Strait/Baffin Bay region. In Fram Strait and in the region upstream of Fram Strait there are nearly no drift anomalies,

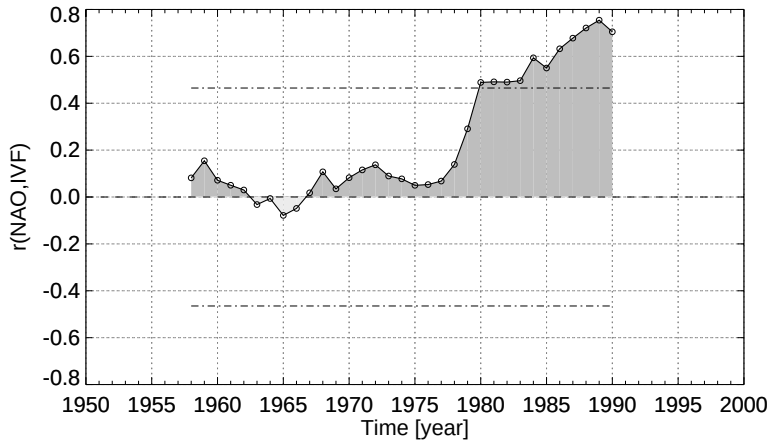

Figure 4.27: Running cross-correlation function (19-yr running window) between wintertime (DJFM) NAO index and simulated ice volume export through Fram Strait. The 95%-confidence levels (dashed) indicate correlation coefficients which are significantly different from zero. For the derivation of these levels a two-sided *Student's-t*-test was applied taking into account the lag-1-autocorrelations of both entire time series as well as the window-length of 19 years.

explaining the missing correlations between NAO and SDS as well as between NAO and IVF through Fram Strait (Tab. 4.3). As a consequence of the eastward shift of NAO related SLP anomalies during P2 there are pronounced southward ice drift anomalies in the entire East Greenland Drift Stream and in the region upstream of Fram Strait (Fig. 4.29b). Also as a result of the shift, NAO related ice drift anomalies in the Davis Strait/Baffin Bay region nearly disappeared. The only features of these pattern which are evident during both periods are the enhanced offshore drift in the Laptev Sea as well as the enhanced southward ice drift anomalies in the Labrador Sea region (see also Fig. 4.24). From Figs. 4.28a and b and from Figs. 4.29a and b it can be deduced that the eastward displacement of NAO related SLP variability should also have an impact on the correlation between NAO and the ice volume export through Denmark Strait and Davis Strait. In fact, the time-dependence of the link between the NAO and IVF through Denmark Strait ($r = -0.01$ during P1 and $r = 0.70$ during P2) is similar to those for the IVF through Fram Strait. In contrast, the correlation between the NAO and ice volume exports through Davis Strait was higher during P1 ($r = 0.61$) as compared to P2 ($r = 0.00$).

The eastward shift of the pattern of interannual NAO variability was deduced from regression analyses which are based on the NAO index which is, by definition, fixed in its position. Thus, one might speculate that longitudinal changes of North Atlantic SLP variability are not well captured by the classical NAO index. This doubt can be dissipated by considering the EOF analysis of winter-averaged SLP anomalies which has been carried out by *Jung* [2000] for the periods P1 and P2 separately (note that P1 and P2 of *Jung* [2000] are slightly different from the definitions of the present study; P1 covers the period 1958–1977 whereas P2 covers 1978–1997). As a result of this analysis *Jung* [2000] found roughly the same eastward shift of North Atlantic SLP variability when comparing the EOFs of P1 and P2. Moreover, this analysis [*Jung*, 2000, their Fig. 6.4] (also shown in [*Jung et al.*, 2000, their Fig. 1]) revealed that the first EOF for both P1 and P2, which are very similar to the patterns shown in Fig. 4.28a and b, explain more than half of the

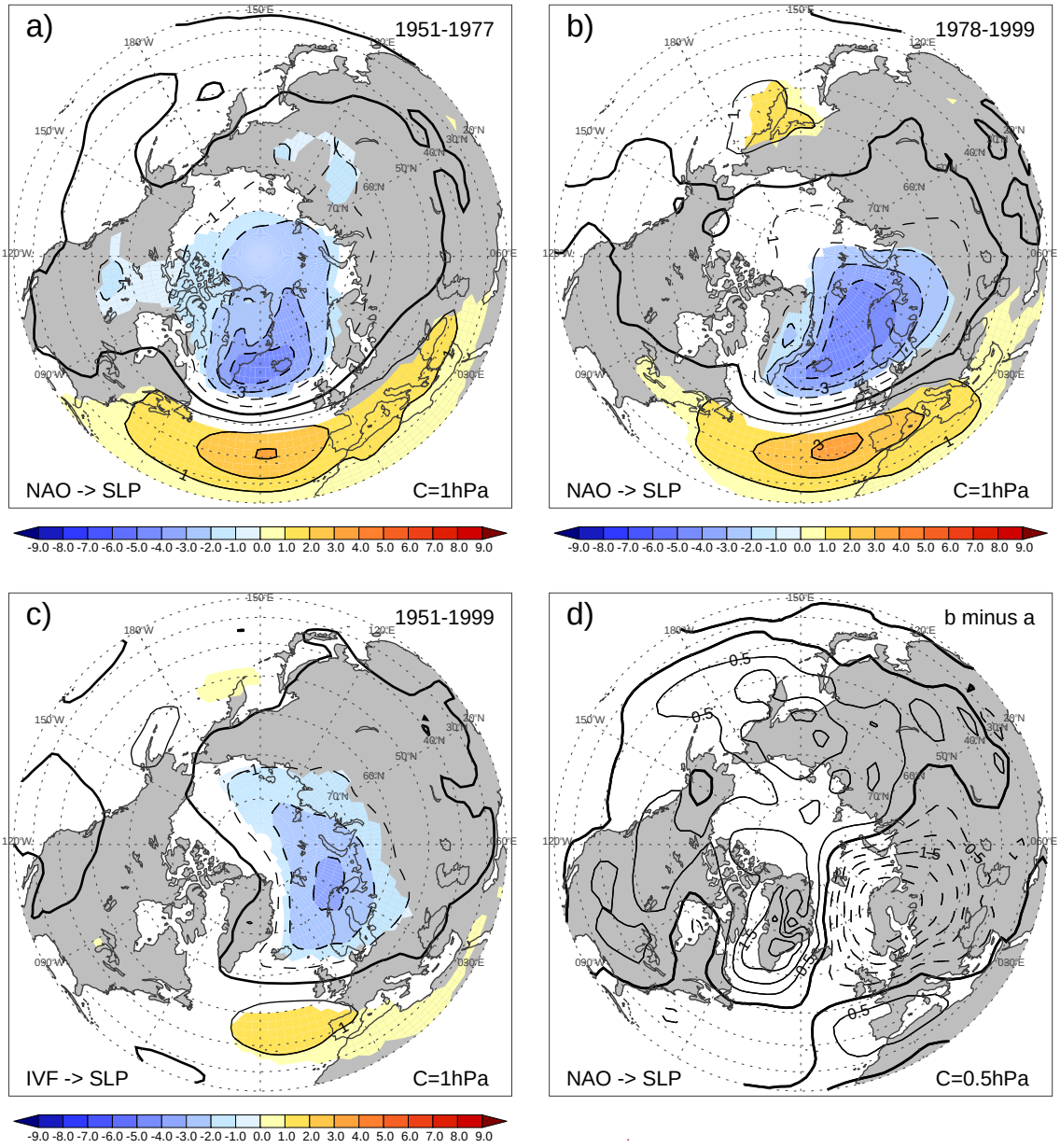

Figure 4.28: SLP anomalies (hPa) associated with the wintertime (DJFM) NAO index during a) 1951–1977 (P1) and b) 1978–1999 (P2), and c) with the time series of modelled ice volume export through Fram Strait (DJFM) over the entire period 1951–1999. Anomalous SLP fields were regressed onto the normalised time series. Statistically significant slope parameters (95%-confidence level; see Fig. 4.24 for details of the test) are coloured. Contour interval is 1 hPa. d) Difference of the NAO-related anomalous fields of SLP, b)-a), between the periods 1978–1999 and 1951–1977. Contour interval is 0.5 hPa. Linear trends were removed prior to the analyses. The standard deviations of the detrended NAO indices for the periods P1 and P2 are nearly equal.

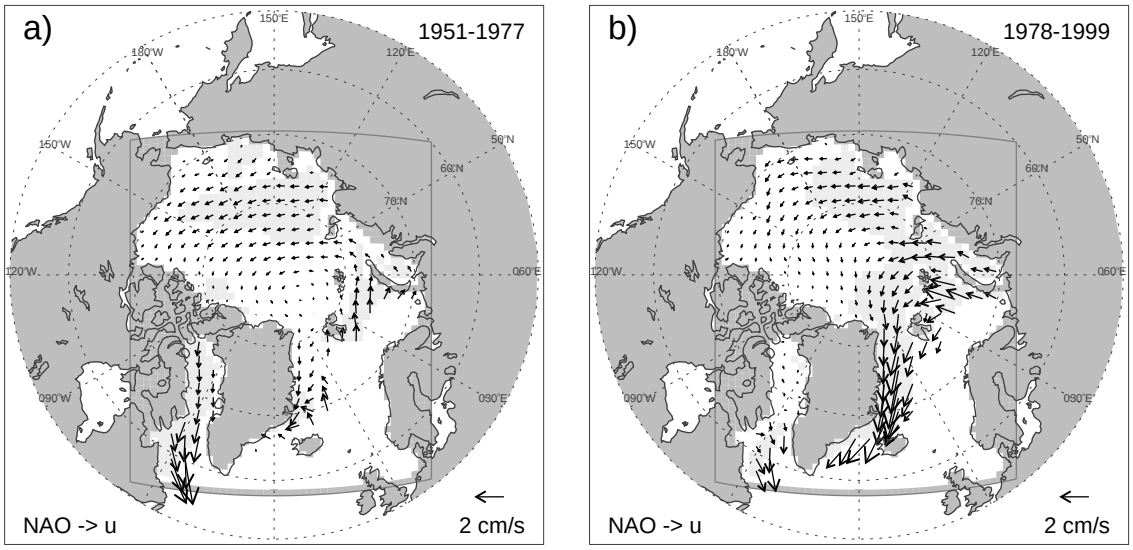

Figure 4.29: Impact of the NAO onto sea ice drift anomalies for the periods 1951–1977 and 1978–1999. Shown are associated regression patterns of sea ice drift anomalies (cm/s) based on the normalised NAO index for the periods a) 1951–1977 and b) 1978–1999. Significant (95%-confidence level) values are grey shaded. For details of the derivation of the associated regression patterns see Fig. 4.24.

total SLP variance (63% for P1 and 56% for P2) during the winter season.

The timing of the shift of interannual NAO variability and the associated change of the link between the NAO and ice fluxes came in parallel with major changes of observational practices. The mid to end 1970s were the beginning of the era of routinely satellite based observations which came along with the removal of most of the Ocean Weather Ships from

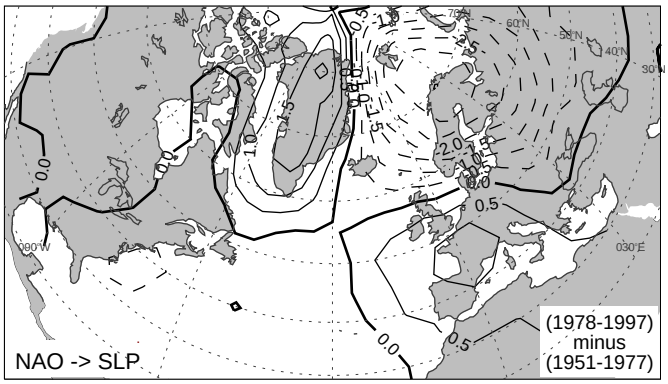

Figure 4.30: The eastward shift of the NAO's centres of interannual variability from an independent data set. Shown is the difference of NAO-related SLP anomaly fields for the periods 1951–1977 and 1978-1999 as in Fig. 4.28d but using the SLP data set from *Trenberth and Paolino* [1980] instead of that from the NCEP/NCAR reanalysis. Contour interval is 0.5 hPa.

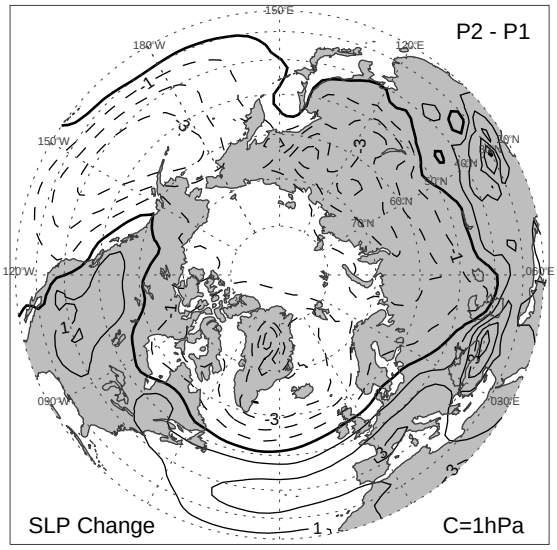

Figure 4.31: Interdecadal change of Northern Hemisphere SLP during wintertime. Shown is the difference between wintertime (DJFM) SLP averages for the periods 1978–1999 and 1951–1977 (P2 minus P1).

the North Atlantic. Also at this time, the IABP began to establish a nearly persistent array of automatic data boys in the Arctic Ocean which routinely report their location, surface atmospheric pressure and temperature [e.g. *Thorndike and Colony*, 1982; *Rigor et al.*, 2000]. All these listed activities affected the data basis used by the data assimilation system of the NCEP/NCAR reanalysis projects [*Kalnay et al.*, 1996]. Because the above findings are based on the SLP data set of the NCEP/NCAR reanalyses it is natural to ask whether the shift of interannual NAO variability around the mid to the end 1970s is solely an artefact of changes of observational practices in the Arctic/North Atlantic region. To answer this question an updated version of the *Trenberth and Paolino* [1980] SLP data set was used to repeat the regression analysis shown in Figs. 4.28a,b,d. The difference of the NAO index based SLP regression patterns between the periods P1 and P2 (as in Fig. 4.28d) is shown in Fig. 4.30 (note that P2 extends only to 1997 instead of 1999). Obviously, this analysis shows the same eastward displacement of the NAO's interannual centres of action. Therefore, and due to the fact that the data set of *Trenberth and Paolino* [1980] is purely based on direct SLP observations, our confidence in the above findings is enhanced. Moreover, the regions of largest changes are located over Greenland, Scandinavia, and southwestern Europe, i.e. over relatively well-sampled areas.

The last five decades were also characterised by longterm SLP changes in the Arctic/North Atlantic region [e.g. *Walsh et al.*, 1996; *Serreze et al.*, 2000] which were excluded from the previous regression analyses. Fig. 4.31 shows the difference between epoch-averaged SLP for P2 and P1 for wintertime. From P1 to P2 the pressure decreased roughly everywhere north of the 50° latitudinal circle with largest magnitudes of more than $3\,hPa$ over Iceland and over the Aleutian Islands, whereas south of this circle the SLP increased with magnitudes up to $3\,hPa$ in the North Atlantic region. In general, the interdecadal SLP change in the North Atlantic regions roughly resembles the classical

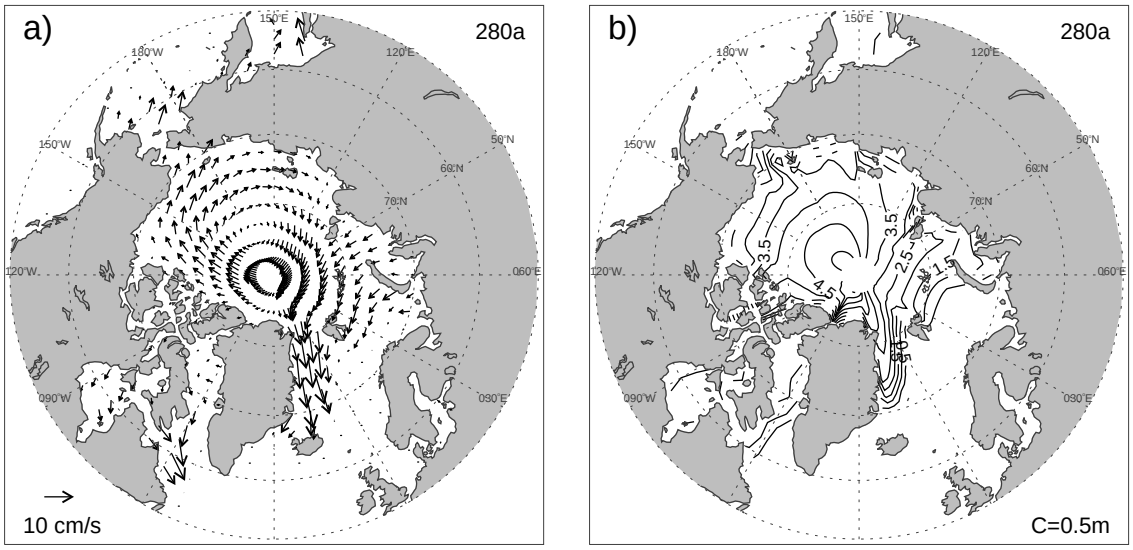

Figure 4.32: Long-term winter-averages (DJFM) of sea ice quantities of a 280-yr control integration of the ECHAM4/OPYC3 model. Shown are averages of a) the ice drift (cm/s) and b) the ice thickness (m). Note that for clarity in a) only every third vector in zonal direction is drawn.

NAO pattern and comes along with an increase of the NAO index. However, nearly no zonal SLP gradient in the Fram Strait region is accompanied with this trend. Therefore, in contrast to the eastward shift of NAO related interannual variability from P1 to P2, the longterm change of Northern Hemisphere SLP cannot have directly affected the southward drift speed in Fram Strait. In other words, the increase of the correlation between NAO and Fram Strait ice exports during the last five decades have to be attributed to the eastward displacement of the NAO pattern rather than to the intensification of the NAO itself (unless there would be evidence that the shift of the NAO pattern is physically related to the interdecadal SLP change).

4.5.4 CGCM Depictions of the Link

In the previous part evidence was presented that the link between the NAO and IVF through Fram Strait underwent secular changes during the last five decades which were explained by an eastward displacement of the NAO pattern. To decide which of the regimes–either control of IVF by the NAO or not—is more typical for the present-day climate, it is necessary to consider the link on a longer-term basis. Because observational time series of ice volume exports are much to short and because realistic hind-cast integrations with the sea ice model (KSIM hereafter) extending the present simulation period by some decades are impossible[1], data of a CGCM including a sea ice component are analysed. In particular, data of the ECHAM4/OPYC3 CGCM [*Roeckner et al.*, 1996,

[1]The quality of the sea ice model simulations depends, besides the physics and numerics implemented in the model, strongly on the quality of the forcing data [*Fischer and Lemke*, 1994]. Prior to 1950 the reliability of possible forcing fields for near surface wind and temperature decreases considerably due to the small number of direct observations especially over the Arctic domain.

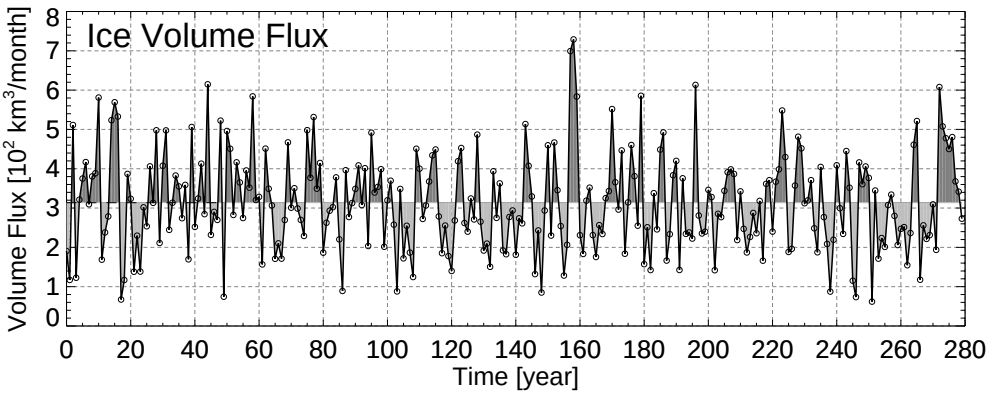

Figure 4.33: Wintertime (DJFM) sea ice volume flux ($km^3/month$) through Fram Strait from a 280-yr control integration of the ECHAM4/OPYC3 model.

1999] are used, because this coupled model contains a dynamic-thermodynamic sea ice component.

Fig. 4.32 shows the winter-averaged fields of sea ice drift and ice thickness derived from 280-years of the control simulation of ECHAM4/OPYC3. Overall, the drift field of the CGCM (Fig. 4.32a) shows much of the general features which are known from observations. It exhibits an anticyclonic gyre and a Trans Polar Drift Stream as well as southward ice motion on both sides of Greenland. However, the anticyclonic gyre is, compared to the observed Beaufort Gyre (see Fig. 3.2), shifted more towards the North Pole. The winter-averaged ice thickness field shows reasonable magnitudes as well as a realistic ice edge (compare to Fig. 3.6a). The spatial structure of the ice thickness field, however, is different from the observations and also different from the pattern simulated by KSIM. Presumably due to structure of the model grid used by the CGCM there is an ice buildup zone around the North Pole instead of north of Greenland and the Canadian Archipelago, as shown by the observations. Due to this structure comparatively small changes of the direction of the TPDS can lead to large changes of the ice thickness entering Fram Strait and, hence, to large anomalies of the ice volume export through this passage (by contribution of term II of Eq. 4.2). Therefore, the correlation of ice thickness with IVF is larger in the CGCM ($r = 0.67$) as compared to the results of KSIM ($r = 0.6$, see Tab. 4.3). On the other hand, the correlation of SDS with IVF is somewhat smaller in the CGCM ($r = 0.84$) than in KSIM ($r = 0.9$, see Tab. 4.3).

The ice volume flux through Fram Strait as simulated by the CGCM is depicted in Fig. 4.33. First of all, the mean winter-averaged export is very similar to that obtained from KSIM (Fig. 4.25b), but there are larger deviations from this average. A comparison of the volume transports as well as their components SDS and h between the CGCM and KSIM is given in Tab. 4.4. Whereas the long-term averages of IVF are rather similar in both simulations, there are some differences SDS and h. The CGCM simulates larger mean drift speeds in Fram Strait and lesser ice thicknesses. However, the mean values depend on the choice of the section S of Eq. 3.1 which is not identical in both simulations due to different model grids. The interannual variability of the sea ice quantities in Fram Strait is more pronounced in the CGCM integration than in KSIM, even if relative magnitudes (normalised to the average) are considered. For the CGCM the standard deviation of

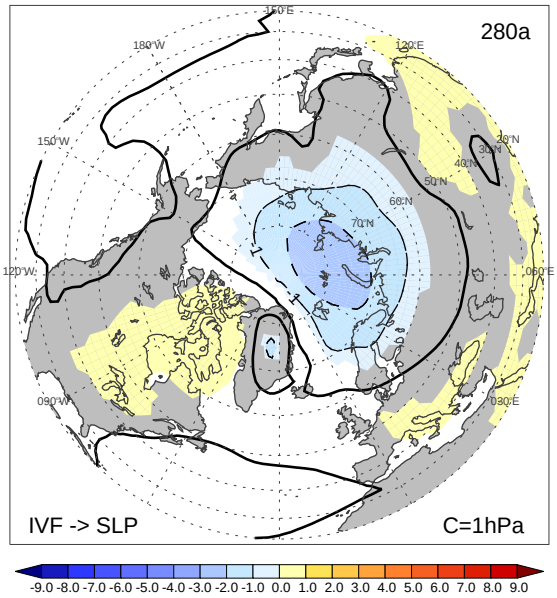

Figure 4.34: Same as in Fig. 4.28c, but for the 280-yr control integration of the ECHAM4/OPYC3 model.

IVF amounts to roughly 40% of its mean value whereas the percentage for the KSIM integration is about 29%.

Besides these—rather small—differences there is an agreement between both simulations which is most important for the analysis of the link between the NAO and ice exports through Fram Strait. The anomalous SLP pattern associated with anomalies of the ice export through Fram Strait is shown in Fig. 4.34. It exhibits nearly the same anomalous low centred over the Barents and Kara Seas as shown in the 'Fram Pattern' derived from the IVF time series of KSIM (Fig. 4.28c). The NAO pattern of the control integration of ECHAM4/OPYC3 closely resembles the common pattern obtained from observations as shown by *Ulbrich and Christoph* [1999] (their Fig. 1) and *Christoph et al.* [2000] (their Fig.4a). Its centres are located northwest of Portugal and over Iceland (see data section

Table 4.4: Comparison of mean value and variability for winter averaged sea ice properties in Fram Strait between ECHAM4/OPYC3 and KSIM.

	ECHAM4/OPYC3			KSIM		
	IVF	SDS	h	IVF	SDS	h
	(Sv)	(cm/s)	(m)	(Sv)	(cm/s)	(m)
Mean	0.121	7.05	2.25	0.110	5.77	3.12
Stdev	0.048	2.23	0.53	0.032	1.47	0.41

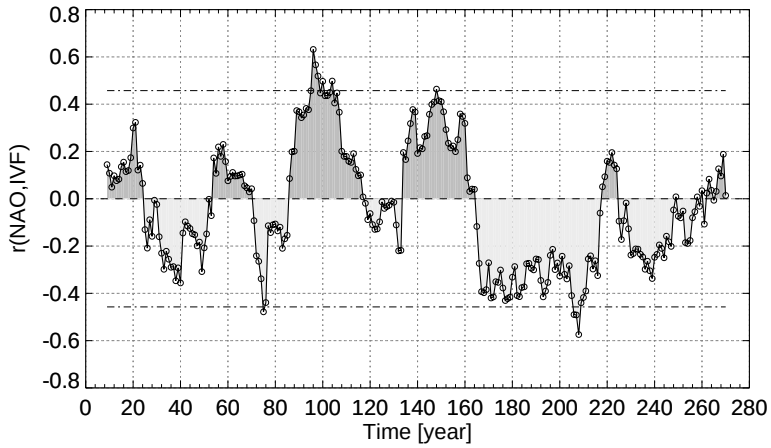

Figure 4.35: Same as in Fig. 4.27, but for the cross-correlation function (19-yr running window) between simulated wintertime (DJFM) NAO index and ice volume export through Fram Strait from a 280-yr control integration of the ECHAM4/OPYC3 model.

above for detailed description).

As for the observations during P1 the NAO pattern of the CGCM simulation shows no correspondence with the SLP pattern associated to large sea ice exports through Fram Strait. As the observed NAO pattern for P1 (Fig. 4.28a) there is no zonal pressure gradient near Fram Strait which could locally force the ice export by anomalous northerly winds. Moreover, there are also no SLP gradients upstream of Fram Strait[2] capable to enhance the TPDS which could subsequently affect the ice fluxes through Fram Strait. From these physically based considerations, no linear relationship between the interannual variability of the modelled NAO and the simulated IVF through Fram Strait can be expected. In fact, the correlation analysis between the 280-yr long time series of the NAO index and IVF through Fram Strait reveals a correlation coefficient of $r = 0.0$. As for the correlation analysis between observed NAO and the results of KSIM during P1 (Tab. 4.3), there is also no linear dependence of both ice thickness and southward drift speed in Fram Strait on the NAO index ($r = 0.0$ for SDS and NAO; $r = -0.1$ for h and NAO) over the entire simulation period. Moreover, as revealed by a cross-spectral analysis [*Jung*, 2000] (also shown in *Jung and Hilmer* [2000]), there are no noteworthy phase-relationships or time-scale dependencies between the CGCM's NAO index and IVF.

To investigate a possible time-dependence of the link a running cross-correlation analysis between the NAO index and IVF using a window-length of 19 years, similar to that shown for the KSIM results (Fig. 4.27), was performed. Fig. 4.35 shows periods of both positive and negative correlations of the length of some decades. But only a few of the values exceed the limits of 95%-confidence and only one chunk exhibits a correlation coefficient about $r = 0.6$. Whereas in Fig. 4.27 11 subsequent chunks exhibit correlations exceeding the confidence limits with largest values of roughly $r = 0.75$, in the analysis of the CGCM results there are only 4 subsequent chunks showing significant correlations. Overall, out of the 262 values shown in Fig. 4.35 there are only 8 correlation coefficients

[2]This is only poorly visible in the figures of *Ulbrich and Christoph* [1999] and *Christoph et al.* [2000]. The reader is referred to the polar stereographic projection of the CGCM's NAO pattern which is shown by *Jung and Hilmer* [2000].

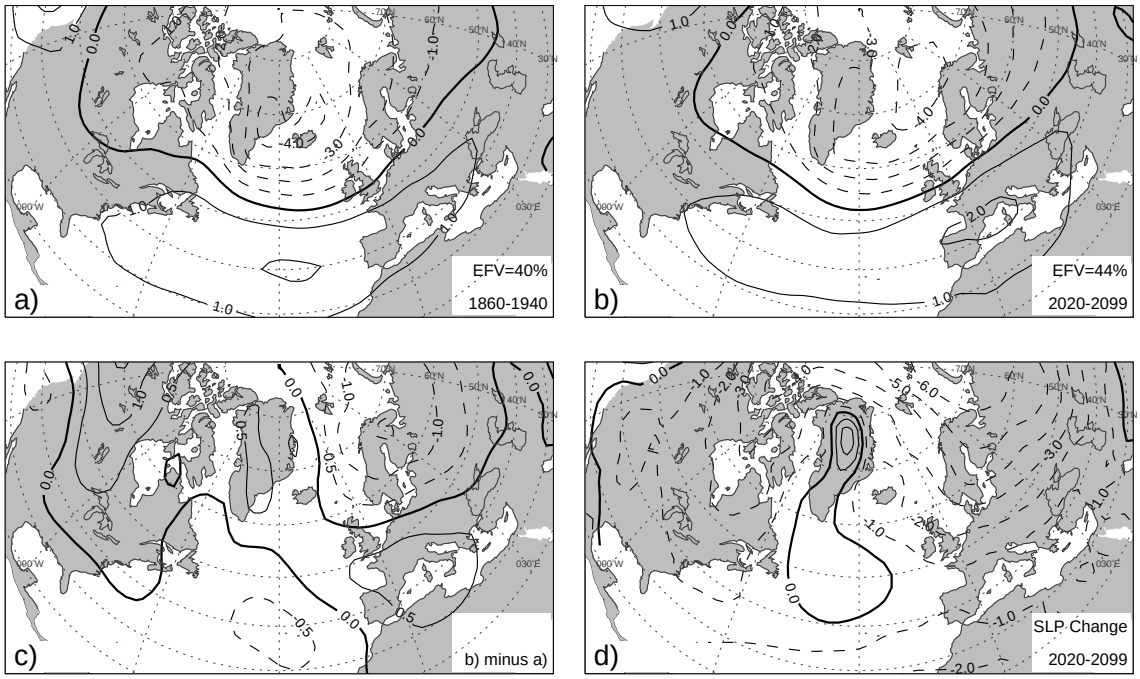

Figure 4.36: The eastward shift of the NAO's centres of interannual variability as simulated by the ECHAM4/OPYC3 model under increasing greenhouse gas concentration forcing along with the linear trend of SLP during the period of increased greenhouse gas concentrations. Shown are the leading EOFs of wintertime (DJFM) SLP anomalies (hPa) for the periods a) 1860–1940 and b) 2020–2099 as well as c) the difference of both patterns (b minus a). Linear trends were removed prior to the EOF analyses. d) Shows the linear change of wintertime SLP during the period 2020–2099. The contour interval is 1 hPa in a), b), and d) whereas it is 0.5 hPa in c). EFV denotes the percentage of explained field variance. The first EOFs are well separated by from their corresponding subsequent modes after the criterion of *North et al.* [1982].

significant at the 95%-confidence level. Note, that at this level (5%-significance) it is expected that on average $262 * 0.05/2 = 6.6$ excursions above the confidence limits occur just by chance. In summary, in the control integration of ECHAM4/OPYC3 there is no strong evidence for a link between the NAO and IVF through Fram Strait.

From a scenario integration of ECHAM4/OPYC3 with increasing greenhouse gas concentrations *Ulbrich and Christoph* [1999] report a northeastward shift of the northern centre of the NAO. From EOF analyses of subsequent 10-yr chunks of simulated SLP data *Ulbrich and Christoph* [1999] found that around the year 2020, when the greenhouse gas forcing exceeded $3\,W/m^2$, the northern cell of the NAO has shifted from its former position above the eastern coast of Greenland to a position within the Norwegian Sea. This shift of NAO variability found from the CGCM integration roughly resembles our findings from the observational SLP data (Fig. 4.28a,b,d). However, *Ulbrich and Christoph* [1999] do not separate between long-term and interannual variability as was done above. Using detrended SLP data of the 240-yr scenario integration of ECHAM4/OPYC3, the first EOFs of two 80-yr periods which represent the time intervals of weakest and strongest greenhouse gas forcing respectively, show the eastward shift of interannual NAO variability only (Fig. 4.36a–c). The period of weakest anthropogenic forcing (1860–1940) (Fig. 4.36a)

reveals an NAO pattern rather similar to that observed during P1 (1951–1977) with an anomalous low between Iceland and the eastern coast of Greenland and an anomalous high over the Azores region. In the 80-yr period after 2020, the dominant mode of interannual SLP variability (Fig. 4.36b) shows a northern centre located over the Norwegian Sea and a southern centre which has slightly weakened in the west and strengthened in the east. The difference between both patterns (Fig. 4.36c) shows an eastward shift of interannual variability which is very similar to that found from observations (Fig. 4.28d). Therefore, it is likely that in the scenario integration of ECHAM4/OPYC3 the increasing greenhouse gas forcing is accompanied by an increasing covariability between NAO and ice exports through Fram Strait on interannual time scales[3].

In the scenario integration of ECHAM4/OPYC3 the increasing greenhouse gas forcing was accompanied by decreasing SLPs over the northern North Atlantic region (Fig. 4.28d). In contrast to the observations where the longterm change of SLP resembles the spatial structures of the NAO, the decreasing trend of SLP is most pronounced over the Barents and Kara Seas region. From the anomalous pressure gradients apparent in this trend pattern one could speculate, that the longterm change of SLP could also lead positive trends of the wind forcing of the IVF through Fram Strait. Therefore, in the scenario integration of ECHAM4/OPYC3 there could be a link between the NAO and sea ice exports out of the Arctic on both interannual to decadal time scales which would be in contrast to the missing link in the control climate of this CGCM.

4.5.5 Conclusions

The possible link between the NAO and the sea ice volume flux through Fram Strait, as suggested by *Kwok and Rothrock* [1999] and *Dickson et al.* [2000], was investigated. Thereby, the focus was on the winter season (DJFM) when the variability of both the NAO and IVF is most pronounced (see *Jung* [2000] for NAO seasonality and Fig. 3.17 for that of IVF). For the simulation period 1951–1999 the following conclusions can be drawn:

- Over the entire simulation period from 1951–99 the NAO explains only 12% of the IVF variability.
- The simulated ice area flux agrees well with that derived from satellite observations for the period 1978–96 ($r = 0.88$). Furthermore, according to the observational results [*Kwok and Rothrock*, 1999; *Dickson et al.*, 2000], during roughly the last two decades (1978–99) the NAO explains about 45% ($r = 0.67$) of the IVF variability, which is primarily based on the NAO influence on the southward drift speed in Fram Strait.
- During the previous decades, that is the period 1951–77, there is no link between the NAO and Fram Strait ice exports ($r = -0.01$).
- Roughly the same time-dependence of the link between the NAO and the Fram Strait export was found for the export through Denmark Strait. The reverse holds true for the export through Davis Strait with higher correlations during 1951–77 and no relation to the NAO thereafter.

[3]We have to confine to suggestions about the IVF in the scenario integration because sea ice data of this simulation were not available.

- The change in the link between NAO and IVF from the periods 1951–77 to 1978–99 is explained by an eastward shift of the centres of interannual NAO variability. As a consequence of this shift, meridional wind anomalies associated with the NAO increased during the latter period and, thus, established a link between the two processes.

- The eastward shift of the NAO's interannual centres came along with a gradual increase of the strength of the NAO.

In order to investigate whether a link between NAO and IVF is unusual in a longer-term context, both the NAO and IVF from a century-scale integration of CGCM (ECHAM4/ OPYC3) are analysed. The analysis of the link between both processes under present-day climate and under increased greenhouse gas forcing revealed the following conclusions:

- The main characteristics of the Fram Strait ice export as simulated by ECHAM4/ OPYC3 are very similar to that of KSIM (this study). That is, the contributions of the anomalies of southward drift speed and ice thickness in Fram Strait to the ice export anomalies are close to those found from KSIM. Most importantly, the anomalous SLP field associated to large ice export anomalies is, as for KSIM, characterised by an anomalous low over the Barents and Kara Seas.

- Under present-day climate conditions the CGCM simulates a NAO with its centres of action close to those observed for the period 1951–77.

- According to the SLP patterns associated with the NAO and IVF there is no significant link between both processes over the 280-yr control simulation of ECHAM4/ OPYC3.

- As found by *Ulbrich and Christoph* [1999], the centres of the simulated NAO shifted eastward under increased greenhouse gas concentrations ($\geq 3\,Wm^{-2}$) which occured in the scenario integration after the year 2020. Considering interannual variability only, this shift is similar to that found from the observations.

4.5.6 Discussion

The influence of the NAO on sea ice exports from the Arctic into the North Atlantic is an attractive mechanism of connecting atmospheric variability with the ocean [e.g. *Wohlleben and Weaver*, 1995]. The NAO is known to affect the North Atlantic Ocean by a variety of processes [e.g. *Dickson et al.*, 2000], for example, by influencing the turbulent fluxes of momentum and heat at the ocean-atmosphere interface due to changes of the surface winds and associated SAT advections or by changing the P-E budget due to increased cyclonic activity. A control by the NAO, at least partly, of the freshwater fluxes into the North Atlantic due to sea ice exports from the Arctic would be an additional mechanism.

The link between the NAO and sea ice exports through Fram Strait has been discussed in several studies. For instance, *Tremblay et al.* [1997] proposed a negative connection between those processes from a comparison of the phase of the NAO with simulated ice drift patterns for the years 1968 and 1984. However, they stated that a direct link between the NAO and ice export remains to be demonstrated. In a more recent study, *Arfeuille et al.* [2000] argued from a comparison of 40-yr long time series of the NAO index

and simulated ice exports that in-phase variability between both processes occured after the mid-1970s and that best agreement was in 1989. As noted in the introduction, the observationally based sea ice flux time series of *Kwok and Rothrock* [1999] and *Alekseev* [in *Dickson et al.*, 2000] show a rather strong correlation with the NAO index for the last two decades. However, *Dickson et al.* [2000] concluded that conditions favourable for enhanced sea ice fluxes can occur during both extrema of the NAO because at the time of the GSA (1968), which most probably was caused by excessive ice exports, the NAO was at its negative phase. Overall, the above listed findings form a rather confuse picture of the link between the NAO and ice volume exports through Fram Strait which is clarified by the results of the present study. We present a consistent and simple explanation which is based on both statistical analysis and physical reasoning: In past decades, prior to the mid 1970s, there was no correlation between the NAO and Fram Strait export because of missing meridional wind anomalies in the Fram Strait region associated to the NAO. After the mid-1970s, however, those meridional wind anomalies have been present leading to a positive and rather large correlation during the last two decades. In summary, during the recent two decades the SLP pattern associated with the NAO has become more similar to the 'Fram Pattern'. Therefore, the statement of *CLIVAR* [1998] that the NAO appears to exert a significant control on the ice exports from the Arctic has to be restricted to the time after the mid-1970s.

The eastward shift of the NAO centres and, therefore, the shift of the NAO related wind field anomalies did not only affected the sea ice exports. As shown by *Jung* [2000] and *Jung et al.* [2000], there have also been temporal changes of the NAO impact on turbulent heat fluxes and near-surface air temperatures of the North Atlantic region. That is, the impact of the NAO on those quantities was prior to (after) the mid 1970s more pronounced in the western (eastern) parts of the North Atlantic region than during the period thereafter (before). For example, in the Labrador Sea and east of Newfoundland anomalies of the turbulent heat fluxes explained by the NAO decreased by a factor of two from the period before the mid-1970s to the period thereafter [*Jung et al.*, 2000].

Ulbrich and Christoph [1999] show that the spatial pattern of interannual NAO variability was unchanged during the course the ECHAM4/OPYC3 control integration and roughly resembles the observed pattern for the period prior to the mid-1970s. This corresponds to our findings, that during the control integration of ECHAM4/OPYC3 a significant link between the NAO and sea ice export through Fram Strait is missing. Moreover, from regression analysis of North Atlantic SLP data it was shown [*Jung and Hilmer*, 2000] that from the beginning of the 20th century to the mid-1970s no eastward shift of the NAO's interannual centres occured and, thus, there was also no possibility for the NAO to influence the sea ice exports through Fram Strait. Therefore, it can be concluded that a link between both processes is rather unusual under present-day climate conditions.

The recent eastward shift of the NAO's centres of interannual variability came along with a secular increase of the overall strength of the NAO. Roughly the same is apparent in the scenario integration of ECHAM4/OPYC3 under increasing greenhouse gas forcing. Whereas *Ulbrich and Christoph* [1999] found that the longterm trend of the NAO projects onto a more easterly position, this study has shown that, furthermore, also its centres of interannual variability have shifted eastward (after subtracting the long-term trend). These findings point towards the possibility that an eastward displacement of the NAO's centres of interannual variability, and, therefore, the higher correlation between the NAO and sea ice exports through Fram Strait, may be associated with an overall increase of the

NAO due to increased greenhouse gas climate conditions.

However, this suggestion is only based on the analysis of one climate model projection of a future climate change. Whereas a couple of climate models predict a decrease of Arctic SLP under increased greenhouse gas concentrations [e.g. *Ulbrich and Christoph*, 1999; *Shindell et al.*, 1999; *Fyfe et al.*, 1999] the behaviour of the NAO in a warmer climate is still an open question. *Fyfe et al.* [1999], for instance, conclude that the NAO may not be a particularly sensitive indicator of climate warming. So far, regional SLP changes have not been the focus of the bulk of studies dealing with climate model projections of a future climate change [e.g. *Houghton*, 1996]. However, with regard to the results presented above and because of the large sensitivity of the oceanic thermohaline circulation to freshwater intrusions at high latitudes, they should receive enhanced attention in future modelling studies.

Chapter 5

Long-term Changes

5.1 Introduction

Climate model projections of a future climate change due to increased greenhouse gas concentrations show maximum annual mean warming near the surface in the high northern latitudes [*Houghton*, 1996]. This warming is aligned with a retreat of sea ice [e.g. *Weatherly and Arblaster*, 2000]. Sensitivity experiments with a dynamic-thermodynamic sea ice model [*Fischer and Lemke*, 1994] have revealed that the sea ice cover is most strongly affected by SAT and the surface wind field. Hence it can be expected that, beside interannual variations, long-term changes of these forcing quantities leave their imprint on the sea ice cover. A comprehensive collection of observational evidences for environmental changes, including atmospheric as well as sea ice changes, in the Arctic was recently published by *Serreze et al.* [2000].

From observations there is evidence of long-term changes of the Northern Hemisphere SAT and wind field. The SAT has risen by about half a degree within the 20th century [e.g. *Chapman and Walsh*, 1993; *Jones*, 1994; *Houghton*, 1996] with largest magnitudes over the Siberian and Alaskan regions. Although data from the central Arctic are sparse there is also evidence. By combining all Russian NP drifting station records from 1961–1990, *Martin et al.* [1997] find statistically significant increases in air temperature during May and June of $0.89\,K$ and $0.43\,K$ respectively. By combining these data with measurements from automatic data buoys and land stations *Rigor et al.* [2000] show that warming over the Arctic ice pack occured in all but the summer season. Moreover, there is observational evidence for a lengthening of the melt season during summer [*Smith*, 1998; *Rigor et al.*, 2000]. Proxy records of the Arctic temperature [*J. Overpeck*, in *Serreze et al.*, 2000] show that the temperatures of the last half of the 20th century were unprecedented within the 400 year record. Consistent to the observed temperature trends are changes of the northern high latitudes circulation. Changes of the wind field in the Arctic towards a more cyclonic circulation are reported by *Walsh et al.* [1996], who describe a decrease of central Arctic SLP over the last two decades being most pronounced since the late 1980s. Moreover, both the NAO and the AO experienced positive trends since about 1970 [e.g. *Hurrell*, 1995; *Thompson and Wallace*, 1998] which are associated with a deepening of the high northern latitudes SLP. Accordingly, cyclonic activity in the extra-tropical Northern Hemisphere has increased [*Maslanik et al.*, 1996; *Serreze et al.*, 1997, 2000].

According to these atmospheric changes, a long-term decrease of the Arctic ice extent is reported by an increasing number of observational studies. *Chapman and Walsh* [1993],

who analysed a combined data set consisting of both ice charts and satellite observations for the period 1953–1990, found significant negative trends of the Arctic ice extent of $-3.6\%/dec$ during summer. From satellite observations only *Johanessen et al.* [1995] report a decrease of sea ice extent of $-2.5\%/dec$ for the period 1978–87 and $-4.3\%/dec$ during 1987–94. In recent papers *Parkinson et al.* [1999] and *Gloersen et al.* [1999] report a statistically negative trend of $-2.8\%/dec$ in Arctic sea ice extent and sea ice area derived from an 18-years satellite based dataset over the period 1978–96. From a comparison of those trends with interannual ice extent variations from control simulations of CGCMs *Vinnikov et al.* [1999] found that the observed reductions of Arctic ice extent are most probably not due to natural variability but rather represent a response of the Arctic to climate warming. Moreover, *Johanessen et al.* [1999] found from satellite retrievals a reduction of the winter (November–March) multiyear ice area of $-7\%/dec$, thus indicating a change of the nature of the perennial ice pack. Much less is known about long-term changes of the sea ice thickness due to sparse data coverage. However, recently *Rothrock et al.* [1999b] presented indication of a thinning of the Arctic ice cover. From a comparison of sea ice draft data acquired on submarine cruises during 1958–1976 and 1993–1997 they found a decrease of the mean ice draft by about $1.3\,m$ in most of the deep water portions of the Arctic.

However, for estimating long-term changes of large scale sea ice quantities observations suffer from the relatively shortness of the available time series (ice concentration) and partly from a small spatial coverage (ice thickness). The following chapter is aimed to describe the long-term changes of simulated sea ice with special focus on the ice thickness and their integrated quantity, the total sea ice volume. Moreover, the effects of both the thermal and dynamical forcing on those long-term changes will be investigated. Parts of the following results have already been published by *Hilmer and Lemke* [2000], but were confined to the period 1961–1998 only.

5.2 Long-Term Changes in Atmosphere and Sea Ice

During the last 50 years the atmospheric parameters SAT and SLP experienced not only interannual changes, as discussed in the previous chapter, but also show long-term trends which have affected the Arctic sea ice cover. Although there are several studies investigating the interannual and long-term changes of northern high-latitude SAT and SLP [e.g. *Chapman and Walsh*, 1993; *Walsh et al.*, 1996; *Rigor et al.*, 2000; *Serreze et al.*, 2000] in the following the trends of SAT and SLP will be investigated from the data set which is explicitly used to force the model.

Fig. 5.1a shows the time series of area averaged SAT derived from the NCEP/NCAR data set. In general the SAT of the extra-tropical Northern Hemisphere (ENH, 50°N to 90°N) has increased by $0.063\,K/dec$ over the period 1951–1999. For the SAT averaged over the model domain (MD) the long-term trend is $0.099\,K/dec$ and corresponds to a warming of roughly $0.5\,K$ from 1951 to 1999. However, from the annual mean time series it is evident that a warming is primarily apparent after the early 1960s. From the mid-1950s to the early 1960s there is a decrease in both the ENH and the MD averages of SAT. From longer records it is known [e.g. *Jones*, 1994; *Serreze et al.*, 2000] that the SATs have risen from 1900 to 1940 followed by a cooling from 1940 to the early 1960s. However, after 1995 the temperatures over the model domain were entirely at least 0.5°C above

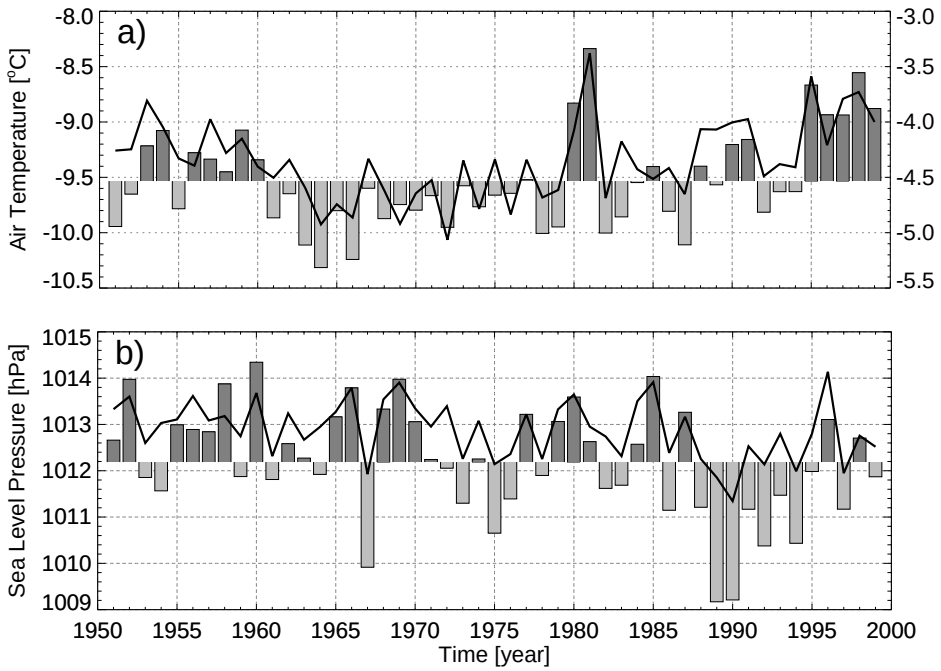

Figure 5.1: Annual mean time series of area averaged a) SAT ($^{\circ}C$) and b) SLP (hPa). Shown are time series averaged over both the model domain (shaded bars) and the extra-tropical Northern Hemisphere (NH) from 50°N–90°N (solid). Note that in a) the right ordinate denotes the scale for the NH averages. The SAT and SLP data are derived from the NCEP/NCAR reanalysis project and the spatial averages were calculated as area weighted spatial means.

the long-term average of -9.5°C. The largest annual mean temperature over the last 50 years occured in 1981 and corresponds, for the MD time series, to an anomaly of 1°C. The ENH time series exhibits an anomaly of about 1°C during this year which corresponds to about three times the standard deviation (see Fig. 4.11 for the normalised time series). The record minimum temperature occured in 1964 with an annual mean of about 0.8°C below the overall mean. Regionally (Fig. 5.2a), positive trends are apparent all over the Arctic ice pack as well as over large parts of the Eurasian continent and over northern Canada. Strongest magnitudes of at least 0.4°C/*dec* occur over the Fram Strait region and the Greenland Sea, the Canadian Archipelago and the southern Beaufort Sea, and over the Chukchi and Laptev Seas. Cooling, on the other hand, primarily occured over the western North Atlantic and eastern Canada. This pattern of NCEP/NCAR derived SAT trends roughly agrees with those derived from direct observations as shown by *Chapman and Walsh* [1993] and *Serreze et al.* [2000] except for the Arctic Ocean which was not included into those analyses. *Rigor et al.* [2000] showed from the International Arctic Buoy Programme/Polar Exchange at the Sea Surface (IABP/POLES) dataset, which is based on measurements from land stations, automatic data buoys, and North Pole drifting stations, that during 1979–97 a warming of about 1°C/*dec* occured in the eastern Arctic, primarily in the area north of the Laptev and East Siberian Seas. The western Arctic shows no trend in this dataset or even a slight cooling in a small portion of the Canadian Beaufort Sea. Because the SAT cannot exceed 0°C if sea ice is present, summer trends of SAT are suppressed over the perennial ice pack. However, a warming of the high-latitude

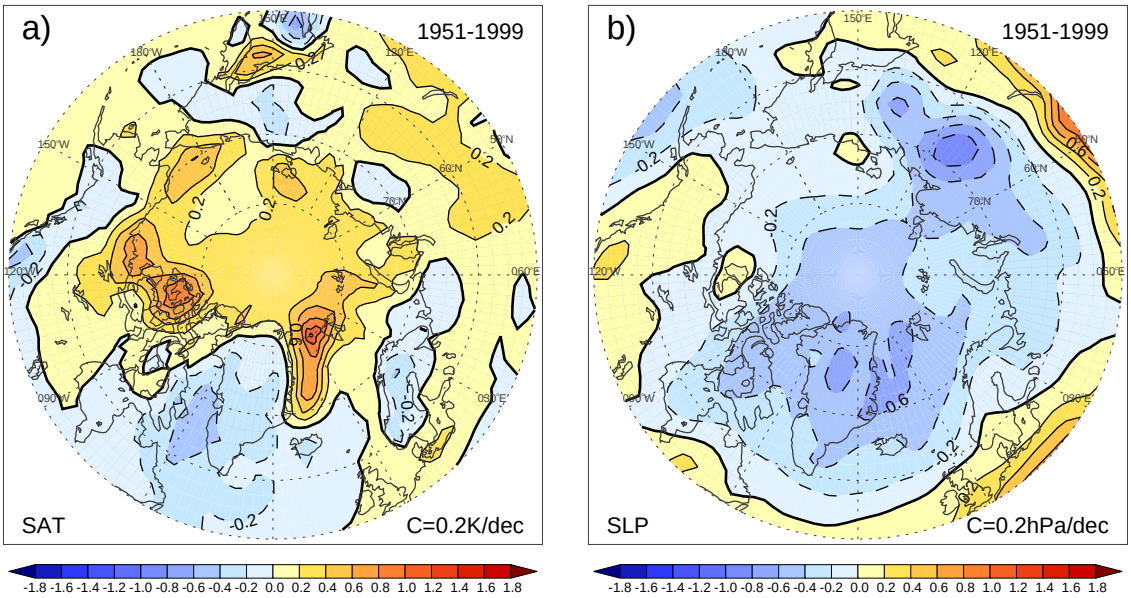

Figure 5.2: Linear trends of annual averaged a) SAT (K/dec) and b) SLP (hPa/dec) for the extra-tropical Northern Hemisphere from 1951–1999. The slopes of the linear regressions of the annual mean ice time series for each grid point are shown. The SAT and SLP data are derived from the NCEP/NCAR reanalysis project.

atmosphere during summertime appears as an increase of the length of the melt season, that is the number of days with surface air temperatures near or above the melting point of sea ice. From the IABP/POLES dataset *Rigor et al.* [2000] found a lengthening of the melt season by $0.9\,days/dec$. For comparison, the mean length of the melt season averaged over the Arctic Ocean is about 70 days with 58 days at the North Pole and about 100 days at the margin of the Arctic Ocean [*Rigor et al.*, 2000]. From both passive microwave data and NCEP/NCAR reanalysis SATs *Smith* [1998] found an increase of the length of the melt season of about $5.3\,days/dec$ over the period 1979–96 which is much larger than the estimate from the IABP/POLES data.

Changes of the SLP can be considered as a proxy for changes of the wind field. That is, if the SLP increases (decreases) the circulation of the near surface wind field becomes more anticyclonic (cyclonic). Over the last five decades the SLP of the ENH (Fig. 5.1b) experienced an overall decrease of about $-0.21\,hPa/dec$. From the spatial distribution of the trends (Fig. 5.2b) it follows that this decrease is more confined to the area north of about 60°N. Accordingly, the trend of SLP averaged over the model domain is stronger than for the ENH averages and amounts to $-0.37\,hPa/dec$. In general, the trend pattern shows a decrease at the northern latitudes and an increase at the mid-latitudes. During wintertime this spatial distribution of trends implies an increase of the AO and of the NAO (see Fig. 4.31) which is shown by, e.g., *Serreze et al.* [2000]. Accordingly, strongest decreases with magnitudes of more than $-0.4\,hPa/dec$ occur over the East Greenland Sea and the central Arctic but also over the Siberian continent. Considering the annual mean SLP time series (Fig. 5.1b) it is evident that the negative SLP trends are primarily due to pronounced negative anomalies since the late 1980s occurring mainly over the central Arctic Ocean [see also *Walsh et al.*, 1996] as can be deduced from the difference between

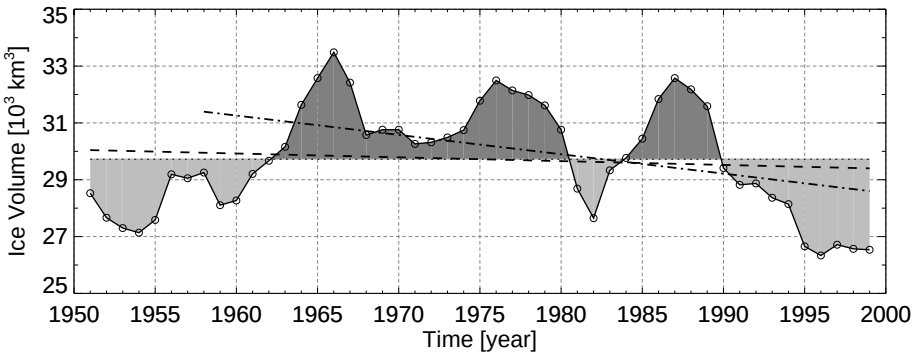

Figure 5.3: Temporal evolution of total Arctic sea ice volume (km^3). Shown are the annual mean time series (solid) together with the linear regressions for both the entire simulation period (dashed) and the period 1958–1999 (dash-dotted).

the ENH and MD averages. Other pronounced minima occured in 1975 and 1967. *Serreze et al.* [1997] show that Northern Hemisphere extra-tropical cyclone activity has increased north of 60°N since the mid 1960s for both the cold and warm seasons. From 6-hourly fields from the NCEP/NCAR reanalysis *Serreze et al.* [2000] show that both cyclone counts and intensity north of 60°N exhibit in all seasons significant upwards trends besides strong interannual variability. From the downward trends of Arctic SLP it can thus be concluded that the poleward heat transport has increased [*Serreze et al.*, 2000] and the wind forcing of sea ice has become more cyclonic [*Walsh et al.*, 1996].

The temporal evolution of the simulated total sea ice volume (SIV) is shown Fig. 5.3. As was previously indicated by individual time series of ice thickness (Fig. 4.8) there is a pronounced variability around the long-term average. The standard deviation of the annual means of the total ice volume amounts to $1.93 \cdot 10^3\, km^3$ which corresponds to roughly 6% of its long-term average and to about 1/8 of the amplitude of its seasonal cycle (Fig. 3.10b). In general the ice volume time series corresponds to the inverse of the SAT anomalies. That is, from the beginning of the simulation period to the mid 1960s the ice volume increased whereas a downward trend is apparent thereafter. Overall, SAT (MD averaged) variations explain roughly 40% of the ice volume variance ($r = -0.63$ for SAT leading the ice volume by one year; $r = -0.58$ for instantaneous correlation). Two years after the SAT minimum (see Fig. 5.1) the largest annual mean volume was simulated in 1966 exceeding the long-term average by about 13%. Moreover, two additional local maxima are apparent in 1976 and 1987 with magnitudes exceeding the overall mean by 9% and 10%, respectively. Local minima, on the other hand, occured in 1954 and 1982 with annual mean anomalies of −9% and −7% respectively. The record minimum occured in 1996 with an annual mean of $26.3 \cdot 10^3\, km^3$ (−11%). Compared to the record maximum the ice volume of 1996 was 21% lower than that of 1966, a difference which is half as large as the amplitude of the mean seasonal cycle. Moreover, all annual means of the second half of the 1990s were lower than any value of the period before. Note that also the SAT exhibits pronounced positive anomalies during 1995–1999. The spectral analysis of the variability of the ice volume reveals enhanced power at periods of 10–12 years. *Hilmer and Lemke* [2000], who analysed ice volume anomalies from 1961–1998 only, found a highly significant peak of the spectral power at this period. However, the spectral analysis of the time series

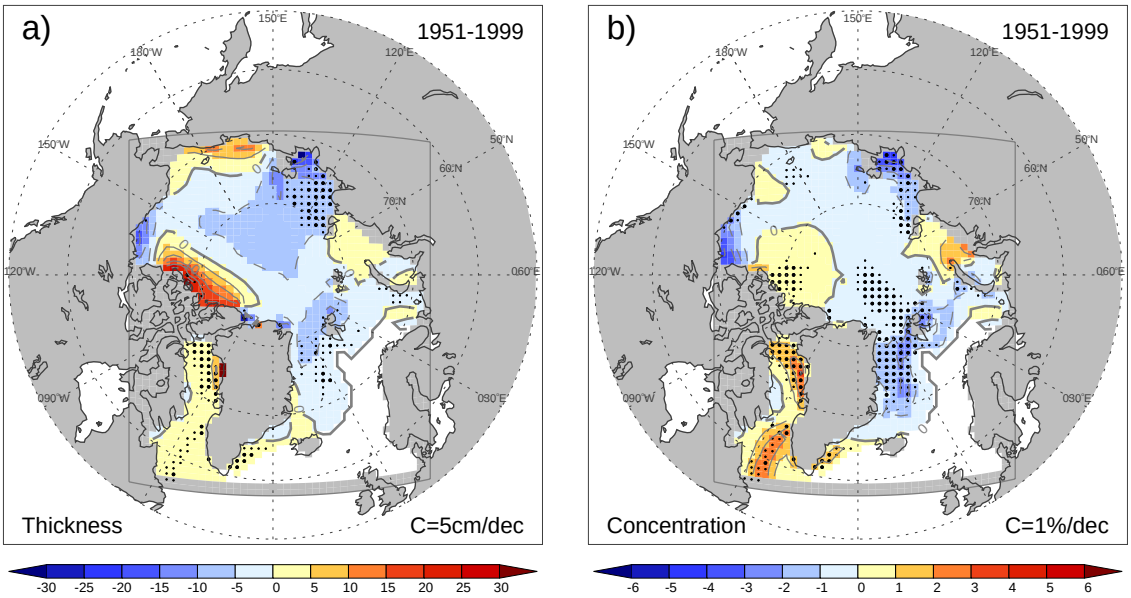

Figure 5.4: Long-term trends of simulated Arctic sea ice thickness and concentration from 1951 to 1999. The slopes of the linear regressions of a) annual mean ice thicknesses (cm/dec) and b) annual mean ice concentration ($\%/dec$) for each grid point are shown. The significance of the trends was tested against the null-hypothesis 'no negative trend' or 'no positive trend', respectively, using a two-sided Mann-Kendall test. To avoid a liberal test due to serial correlation the time series were pre-whitened prior to the test as suggested by [*von Storch and Zwiers*, 1999]. Statistically significant trends at the 90%-(95%-)confidence level are indicated by small (large) dots.

from 1951–1999 reveals that this peak has broadened but is still significantly different from the 'red noise' null-hypothesis. Superimposed on this interannual and decadal variability there is, according to the long-term evolution of the SAT, a negative trend of the SIV of $-0.13 \cdot 10^3\, km^3/dec$ which corresponds to $-0.45\%/dec$ relative to the overall mean. However, due to the pronounced decadal variations this trend is not statistically significant at confidence levels of 90% or above.

Regionally, long-term changes of the total ice volume are expressed by trends of local ice thicknesses as shown by Fig. 5.4a. In general, the trend pattern roughly reflects the inverse of that of the SATs (Fig. 5.2a) with negative values over the central Arctic and positive trends over the Baffin Bay/Labrador Sea region. The largest negative trends are apparent in the region extending from the Laptev Sea towards the Pole, in the southern Beaufort Sea, and in the region around Fram Strait. In the Beaufort and the Laptev Seas those trends have magnitudes of up to $-15\, cm/dec$. However, there are also considerable upward trends within the central Arctic ice pack although the SATs in those regions have risen. That is, the region north of the Canadian Archipelago as well as the Chukchi and East Siberian Seas exhibit increasing ice thicknesses at rates of more than $10\, cm/dec$. Moreover, the ice cover of the Kara Sea also exhibits positive trends but with only small magnitudes. A two-sided *Mann-Kendall* test reveals that only the trends in the Laptev Sea, the East Greenland Sea, and the Baffin Bay/Labrador Sea are statistically significant at least at the 90%-confidence level. The statistical significance of trend depends, besides the length of the sample, on the signal-to-noise ratio between the trend and higher frequency

fluctuations of the time series considered. Therefore, in the regions without significance either the magnitude of the trend is too small or the interannual 'noise' of the simulated ice thicknesses is too large. The latter is responsible for the lack of significance in the Beaufort and East Siberian Seas, and in the region north of the Canadian Archipelago (see Fig. 4.9).

Fig. 5.4b shows the long-term changes of ice concentration. In general, the trend pattern of SIC is very similar to that of ice thickness because SIC changes depend, besides the freezing or melting rates, also on the actual thickness of the ice floes (Eq. 2.4). However, SIC variations cannot be directly linked to ice thickness changes. As long as the ice thickness is sufficiently large, enhanced melting (or reduced freezing) due to warmer air temperatures manifests itself in changes of ice thickness but not necessarily in changes of SIC. This can be seen from the seasonal evolution of ice concentration within the central ice pack. There, the SICs fall significantly below 100% only during summer and early autumn when the ice thicknesses are at a minimum (see, e.g., Fig. 3.6 or *Gloersen et al.* [1992]). Note, that the long-term trends of ice thickness are substantially smaller than the amplitude of the seasonal cycle. Moreover, during summer the positive ice-albedo feedback tends to enhance SIC anomalies. Therefore, it can be expected that the trends of the annual mean SICs within the central ice pack primarily reflect changes of the summer conditions. Accordingly, the magnitudes of the long-term trends of the SIC are smallest within the central ice pack and largest at the ice margins. According to the ice thickness trends strongest decreases of SIC are apparent in the southern Beaufort, the Laptev, and in the Greenland Seas with reductions of roughly $-3\%/dec$. Pronounced upward trends of about the same magnitude are simulated in the Baffin Bay/Labrador Sea region and in the Kara Sea. As for the ice thickness, the positive trends in the Kara Sea and in the region north of the Canadian Archipelago are in contrast to rising SATs in these areas. The opposing trends east and west of Greenland are consistent with the long-term trend of the first EOF mode of wintertime SIC (Fig. 4.6a) as described by *Slonosky et al.* [1997] and *Deser et al.* [2000]. Statistically significant trends occur roughly in the same regions as those of ice thickness. However, due to different patterns of interannual variability, SIC trends in the region extending from Fram Strait to the Pole and north of the Canadian Archipelago are also significant.

In summary, the Arctic ice cover experienced an overall slight thinning over the entire simulation period which is most pronounced in the eastern portions of the ice pack. However, from the time series of both SAT and SIV it can be concluded that the thinning primarily occured since the mid 1960s.

5.3 On the Recent Decrease of Arctic Sea Ice

So far, long-term changes over the entire simulation period were considered. From the time series of simulated SIV it is evident, however, that a long-term thinning of the Arctic ice pack started in the mid 1960s which coincides with a general warming of the northern high latitudes. From 1966, when the record maximum of ice volume occured, to 1999 the ice volume decreased by $-1.43 \cdot 10^3\, km^3/dec$ which corresponds to $-4.80\%/dec$ relative to the overall mean. However, for comparison with observational estimates [*Rothrock et al.*, 1999b] in the following the thinning of the Arctic ice cover will be considered for the period 1958–1999. Although the first 9 years of this time interval represent a

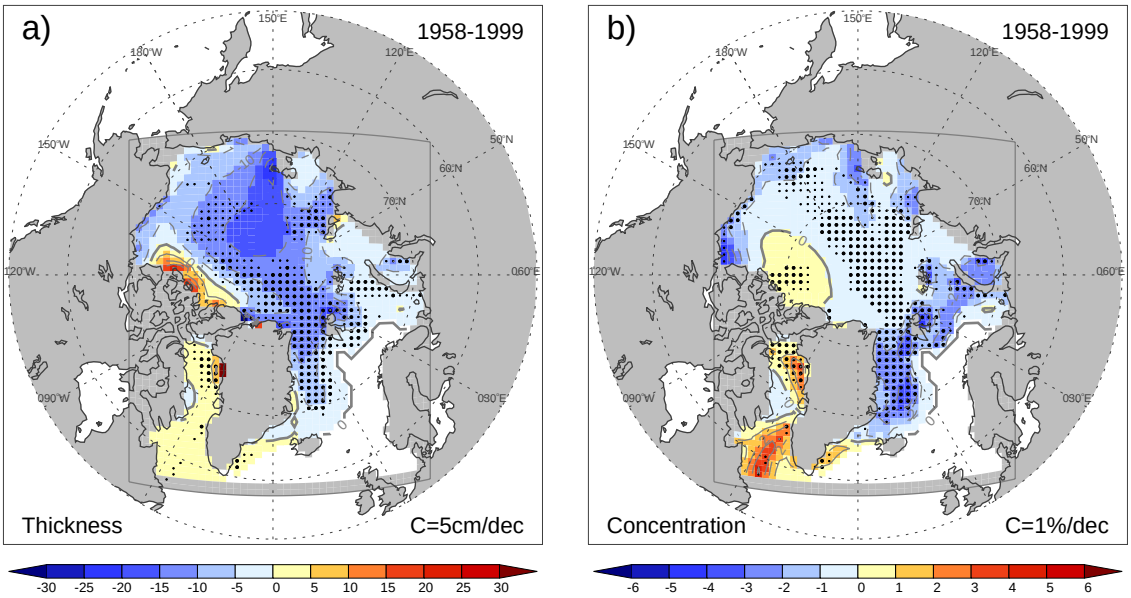

Figure 5.5: As in Fig. 5.4 but for the period 1958–1999.

period of strong increase of sea ice volume, the overall downward trend from 1958 to 1999 is roughly 5 times larger in magnitude than that for the entire simulation period. It amounts to $-0.68 \cdot 10^3\, km^3/dec$ or $-2.27\%/dec$ relative to the overall mean respectively (dash-dotted line in Fig. 5.3). A two-sided *Mann-Kendall* test reveals that this negative trend is significantly different from zero at the 99%-confidence level. Applying the test to the 'pre-whitened'[1] volume time series reveals a significance of the trend still at the 95%-confidence level. The procedure of pre-whitening is suggested by *von Storch and Zwiers* [1999] to avoid a too liberal test due to serial correlation.

The trend patterns of ice thickness and ice concentration for the period 1958–99 are shown in Fig. 5.5. In comparison to the trends for the entire period (Fig. 5.4) from 1958 onwards nearly the entire Arctic ocean exhibits downward trends for both ice thickness and concentration. In the region north of the Canadian Archipelago trends are still positive although with smaller magnitudes than for the entire period. Strongest thinning is apparent in the eastern Arctic north of the Laptev and East Siberian Seas with magnitudes between -15 and $-20\, cm/dec$ (Fig. 5.5a). Due to large interannual variability, the trends in this area are statistically significant at a few grid points only. However, in comparison to the entire period a much larger fraction of the ice pack exhibits significant trends. This is, additional to regions which already showed significant trends for the entire period, the region north of Greenland, the Barents Sea, and the region extending from Fram Strait via the North Pole to the northern Beaufort and Chukchi Seas. In the latter region the negative trends are between -10 and $-15\, cm/dec$. Besides the smaller magnitudes, the trend pattern of the simulated ice thickness roughly agrees with the findings of *Rothrock et al.* [1999b] with largest thinning in the eastern Arctic north of the Laptev Sea, mod-

[1] To remove the effect of autocorrelation, *von Storch and Zwiers* [1999] suggest to apply the test to a filtered time series $\mathbf{y}_t = \mathbf{x}_t - \hat{\alpha}\mathbf{x}_{t-1}$, where $\hat{\alpha}$ denotes the lag-1 autocorrelation, instead of applying to the original time series $\mathbf{x}_t$. This process is named 'pre-whitening'.

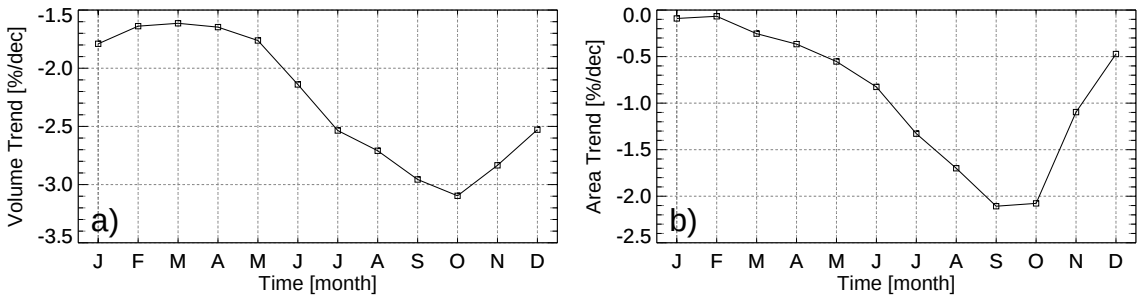

Figure 5.6: Annual cycle of the long-term trends ($\%/dec$) of a) sea ice volume and b) sea ice area for the period 1958–1999. The slopes of the linear regressions of the monthly mean time series relative to the overall mean values were calculated.

erate negative trends in the region between the North Pole and Fram Strait, and minor decreases in the central Beaufort and Chukchi Seas.

The pattern of SIC trends (Fig. 5.5b) is very similar to that for the entire period with small magnitudes within the central ice pack, opposing but larger trends east and west of Greenland, and slight positive trends north of the Canadian Archipelago. Having in mind the larger magnitudes of the ice thickness trends for the recent time interval, the rather small differences of SIC trends between both periods emphasise the above mentioned statement that SIC changes cannot directly be linked to changes of ice thickness. The downward SIC trends in the Greenland and Barents Seas and the upward trends in the Baffin Bay/Labrador Sea are also more pronounced during the period 1958–99. In general, opposing anomalies of SIC east and west of Greenland are associated with SAT advections due to the NAO (see Section 4.2). Moreover, the opposing trends in these regions are consistent with an increase in the strength of the NAO (Fig. 4.31) [see also *Slonosky et al.*, 1997; *Parkinson et al.*, 1999; *Deser et al.*, 2000] which also starts in the 1960s [e.g. *Hurrell*, 1995; *Jung*, 2000].

Within the seasonal cycle strongest decreases of both ice volume and ice area occur during summer and early autumn (Fig. 5.6a,b). This is, at least for the ice area, consistent with the findings from observational data [*Chapman and Walsh*, 1993; *Parkinson et al.*, 1999; *Serreze et al.*, 2000]. At a first view, this seasonal evolution seems contradictory to the annual cycle of SAT trends exhibiting largest warming in winter and spring (Fig. 5.7a) [see also *Jones*, 1994; *Serreze et al.*, 2000]. However, as stated above, during summer the temperature over sea ice cannot exceed the melting point which explains the small SAT-trends during those months. This is clearly seen from the seasonal trends of the SAT averaged over the mean ice cover only (Fig. 5.7b). Here, warming is strongest during spring and autumn but nearly no trend is apparent during the melting period. As noted earlier, a warming trend during the summer period appears as a lengthening of the melting season as was found by *Smith* [1998] and *Rigor et al.* [2000]. The physical explanation for the enhanced decreases of ice thickness and ice concentration during summertime is twofold. First, sea ice growth (and melt) depends on the heat conduction through the ice slab which in turn depends on the inverse of its thickness (Eq. 2.3). Thus, thin ice is more sensible to variations of the thermal forcing than thick ice [see also *Fischer and Lemke*, 1994; *Lemke et al.*, 2000]. Second, the ice-albedo feedback, which is most effective during early summer, further enhances the sensitivity of the ice cover to thermal perturbations.

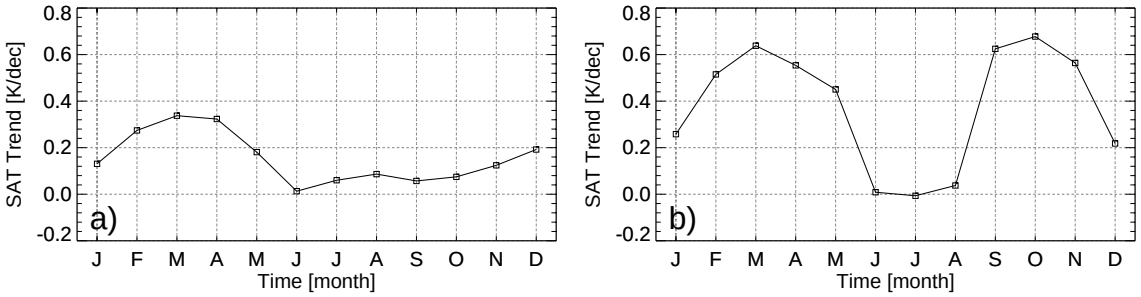

Figure 5.7: Annual cycle of the long-term trends (K/dec) of area averaged SAT for the period 1958–1999. The trends area shown for a) the extra-tropical Northern Hemisphere (50°N–90°N) and b) the model area which has, on average, an ice coverage of at least 15%. The slopes of the linear regressions of the monthly mean time series were calculated.

5.4 Dynamic versus Thermodynamic Effects

The total sea ice volume can be affected by both the wind and the air temperature forcing. The effects of SAT variations are rather obvious. During the freezing period, SAT changes influence the local ice thicknesses, and thus the total ice volume, by altering the energy balance at the surface of the sea ice and subsequently, by heat conduction through the ice, the basal freezing. During summer, the thermal forcing primarily leads to changes of the surface melting rate. Changes of the wind can influence the total ice volume primarily in three ways. First, changing winds can alter the export of ice into regions where it melts. Second, the wind speed influences the energy balance at the ice surface by changing the strength of the turbulent heat fluxes and, thus, the freezing (melting) rate. The third effect of wind field changes is altering the local ice thicknesses by advection and, thus, changing the local freezing rates due to changed heat conduction through the ice. Moreover, during summer a divergent ice drift can lead to a breakup of the ice pack and, thus, to enhanced absorption of solar radiation due to the reduced albedo of the surface (ice-albedo feedback).

In the following, by analysing the idealised simulations WIND and TEMP, the effects of the interannual and long-term variations of both the wind and temperature forcing on the thinning of the Arctic ice cover will be investigated. Fig. 5.8 shows the ice volume time series of both the TEMP (SIV_T) and the WIND (SIV_W) integrations. First of all, the SIV_T time series is very similar to that of the standard simulation (SIV). It exhibits roughly the same local minima and maxima as that of the SIV (Fig. 5.3) as, e.g., the record maximum in 1966 as well as two local maxima around 1976 and 1987. With an instantaneous correlation of $r = 0.91$ the ice volume of the TEMP run and that of the standard simulation share about 83% of their variance. As expected, the correlation of SIV_T with the SAT time series is, with $r = 0.71$, larger as that for SIV. Therefore, the trends of SIV_T are also much more pronounced. For the entire simulation period the ice volume of the TEMP simulation decreases by $-0.33 \cdot 10^3\, km^3/dec$ which corresponds to $-1.06\%/dec$ relative to its overall mean. For the period from 1958 to 1999 the trend amounts to $-0.86 \cdot 10^3\, km^3/dec$ ($-2.27\%/dec$).

The total volume of the WIND simulation, on the other hand, exhibits a positive trend which amounts to $0.23 \cdot 10^3\, km^3/dec$ ($0.70\%/dec$) and $0.18 \cdot 10^3\, km^3/dec$ ($0.54\%/dec$) for the periods 1951–1999 and 1958–1999 respectively. However, during the last 15 years of

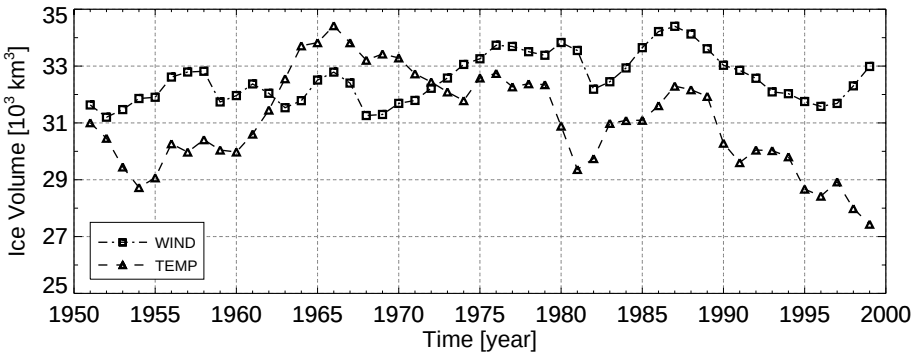

Figure 5.8: Temporal evolution of total Arctic sea ice volume (km^3) of the idealised simulations TEMP (dashed with triangles) and WIND (dash-dotted with squares).

this simulation the ice volume also decreases. This decrease can partly be explained by large ice exports through Fram Strait during this period (Fig. 4.17). Moreover, other large export events, like those in 1968 and 1981, are clearly visible as local minima of the SIV_W time series. As expected, there is no relation (no significant correlation) of the SIV_W to the SAT. However, the ice volume time series of the WIND simulation shares about 30% of its variance ($r = 0.55$) with that of the standard run. Interestingly, the superposition of SIV anomalies of the WIND and the TEMP integrations (${SIV_W}' + {SIV_T}'$) are almost equal to the volume anomalies of the standard run (SIV'). The correlation coefficient between ${SIV_W}' + {SIV_T}'$ and SIV' is $r = 0.995$ and the RMS difference between those both time series amounts to $0.22 \cdot 10^3\, km^3$. Thus, nonlinear interactions between anomalous wind and temperature forcing are of minor importance for the total ice volume. Such effects can, e.g., lead to enhanced melting if a breakup of the ice pack due to anomalous wind-driven divergence is accompanied by advection of anomalously warm air.

Summarising, from the analysis of the total sea ice volume time series it can be concluded that the overall thinning of the Arctic ice pack due to increased air temperatures is somewhat damped by the effects of the wind forcing. On the other hand, the strong decrease during the last 15 years can be explained by the superposition of negative trends in both, the TEMP and the WIND integration.

The trend pattern of ice thickness of the TEMP simulation (Fig. 5.9a) represents almost exactly the inverse of that for the SAT trends. It exhibits a thinning of sea ice in all regions of the Arctic and positive trends only in the Baffin Bay/Labrador Sea region where SAT trends are negative. Due to small interannual variability of the ice thicknesses of the TEMP run, the trends larger than $5\, cm/dec$ in magnitude are significant for all grid points. However, in contrast to the SAT trends, the largest thinning occurs in the East Siberian Sea with trends between -15 and $-20\, cm/dec$. There, thinning is enhanced due to the ice-albedo feedback because during summer the ice thicknesses are rather small. This is not the case in the Fram Strait region, where SAT trends are largest, because the ice is still rather thick during summer due to advection from the interior of the Arctic ice pack (Fig. 3.13). About the same holds true for the region north of the Canadian Archipelago where the SAT trends exhibit a secondary maximum.

The ice thickness trends of the WIND simulation show a very different pattern (Fig. 5.9b). Here, thinning occurs in the central Arctic, in the region north of the Laptev and East

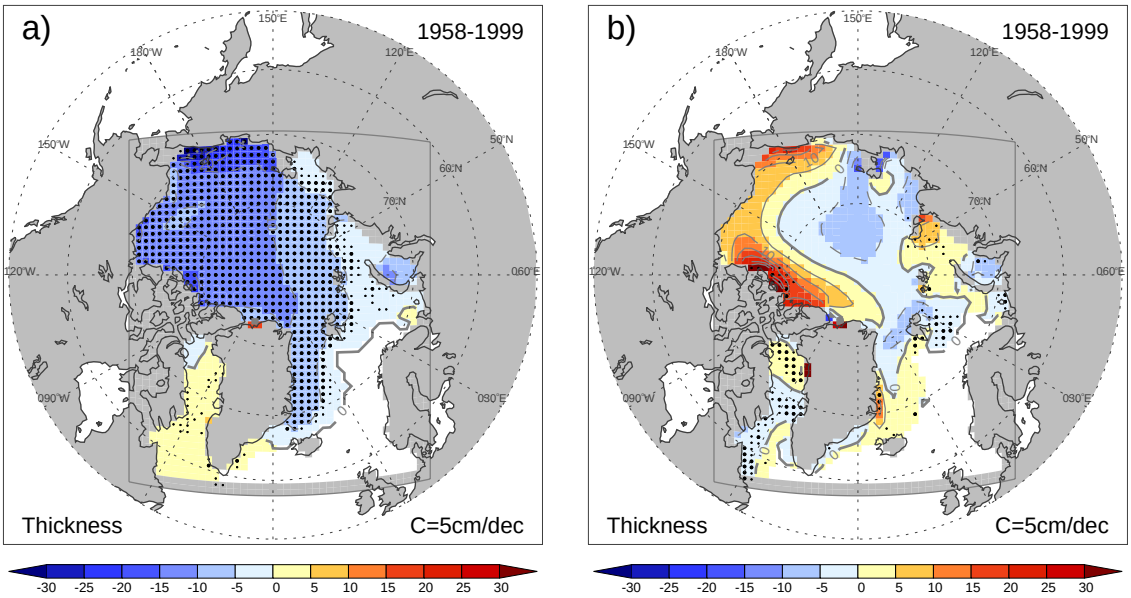

Figure 5.9: Long-term trends of simulated Arctic sea ice thickness (cm/dec) of the idealised simulations a) TEMP and b) WIND from 1958 to 1999. For the symbols see Fig. 5.4.

Siberian Seas, and around Fram Strait. However, the magnitudes of the downward trends are smaller than those found for the TEMP integration. On the other hand, there are pronounced increases north of Greenland and the Canadian Archipelago and in the Beaufort, Chukchi, and East Siberian Seas. Due to large interannual variability only a few grid points exhibit significant trends. The trend pattern of the WIND simulation can primarily be explained by the long-term changes of sea ice drift (Fig. 5.10a). Due to an overall decrease of Arctic SLP the sea ice drift has become more cyclonic as was suggested, e.g., by *Walsh et al.* [1996] and *Serreze et al.* [2000]. The anomalous cyclonic drift is associated with divergence in the Laptev Sea and north of the Laptev Sea as well as north of Fram Strait and, thus, with reduced ice thicknesses in these areas. On the other hand, anomalous convergence occurs in the regions showing an upward trend. Compared to the mean motion of sea ice (Fig. 3.7) the trend of the ice drift imply a weakening of the Beaufort Gyre and the TPDS. However, a deepening of the Arctic SLP associated with a reduced anticyclonic circulation of the ice cover does not necessarily implies a increase of the Arctic ice volume. This is best illustrated by the decrease of SIV_W from 1988–1995, a period with the lowest annual mean pressures over the model domain. During this time, the centre of anomalous low, and so the centre of the anomalous cyclonic gyre, was located between the North Pole and the Laptev Sea (Fig. 5.10b). As a result, the TPDS was not much reduced but the ice drift from the region north of the Canadian Archipelago to the area north of Fram Strait was enhanced. Therefore, thick ice from the Canadian side of the Arctic was advected to Fram Strait and was subsequently exported southward into the melting regions of the North Atlantic. Similar conditions also prevailed in 1967 and 1968 (Figs. 4.19a and 4.20a). In summary, for sea ice volume changes the location of anomalous pressure systems is more important than their magnitude.

By comparing the ice thickness trend pattern of both idealised simulation with that

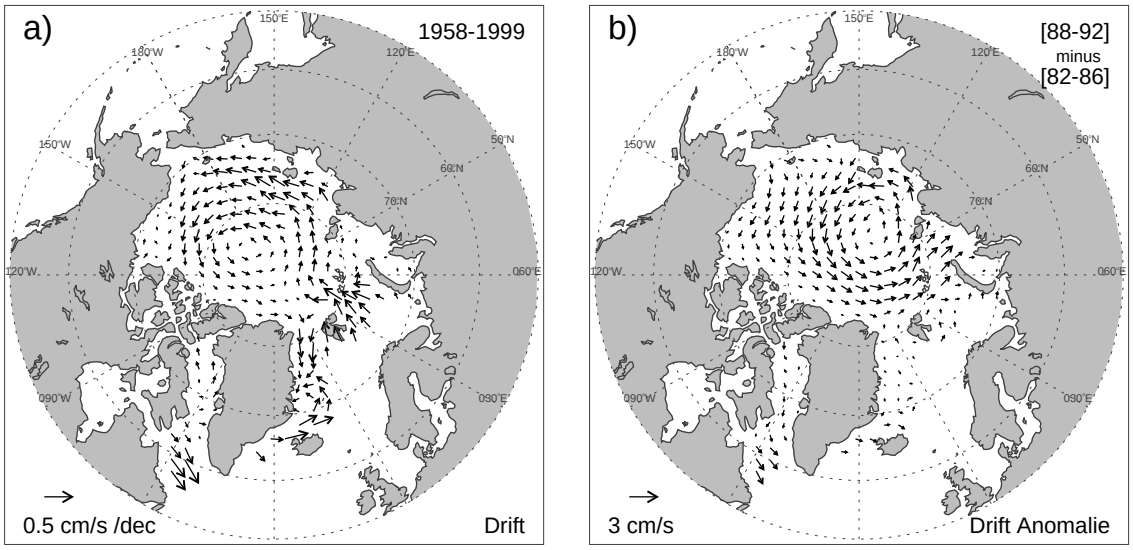

Figure 5.10: a) Long-term trends of simulated Arctic sea ice drift ($cm/(s \cdot dec)$) for the period 1958–1999. Vectors consisting of the slopes of the linear regressions of the u- and v-component time series of annual mean sea ice drift for each grid point are shown. b) Differences of the ice drift patterns (cm/s) between the periods 1988–92 and 1982–86 corresponding to periods of decreasing and increasing total sea ice volume of the simulation WIND (Fig. 5.8).

of the standard run it can be concluded that the overall thinning of the Arctic ice pack is primarily due to rising air temperatures. However, due to long-term changes of the wind forcing this thinning is damped in the East Siberian, Chukchi, and Beaufort Seas or even has become a thickening north of the Canadian Archipelago. On the other hand, the thermally induced decreases of ice thickness in the central Arctic and in the region around Fram Strait are enhanced by dynamic effects.

5.5 Conclusions

Long-term changes of main properties of the simulated Arctic ice cover for the last half of the past century were investigated. The total sea ice volume of the Arctic exhibits pronounced decadal-scale variability superimposed on a slight linear decrease of $-0.45\%/dec$ over the entire simulation period. However, according to the long-term evolution of the Northern Hemisphere SATs since the mid 1960s, the Arctic has lost about 16% of its volume at a rate of about $-5\%/dec$. From 1995 onwards the total sea ice volume shows magnitudes which are lower than any other during the preceeding period. From trend analyses over the last 40 years the following conclusions can be drawn:

- The ice thickness as well as the ice concentration decreased in most parts of the Arctic but show an increase north of the Canadian Archipelago and in the Baffin Bay/Labrador Sea region.
- The pattern of ice thickness trend agrees with that found from observational estimates, with largest thinning in the eastern Arctic, moderate decreases in the region

upstream of Fram Strait and only slight negative trends in the central Beaufort and Chukchi Seas.

- The largest magnitudes of the thinning occurring in the eastern Arctic correspond to a linear decrease of annual mean ice thickness of about $80\,cm$ over the last 40 years.
- During the annual cycle the negative trends of both ice thickness and ice concentration are most pronounce at the beginning of the freezing period in September and October.

Additional trend analyses of idealised simulations with prescribed interannual variability of either winds or temperatures only were used to assess the thermal and dynamical contributions to the thinning of the Arctic. The comparison of the results of the idealised simulations with those of the standard case revealed the following:

- The effects of long-term changes of the Arctic wind field damp the long-term decrease of the total sea ice volume which would be stronger by thermal forcing only. However, during the the last 15 years they lead to an enhanced decrease of SIV.
- Overall, the long-term deepening of Arctic SLP leads to a more cyclonic circulation of the ice pack, which regionally increase the ice thickness in the East Siberian and Chukchi Seas as well as in the Canadian Arctic. On the other hand, in the Central Arctic north of the Laptev Sea as well as in the Fram Strait region the long-term circulation changes enhance the thermally induced thinning of the ice pack.
- For variations of the total ice volume, the location of the anomalous pressure systems, and, therefore, the circulation anomalies, are more important than their magnitudes. That is, the more eastern the location of the SLP deepenings are, the more the total ice volume is reduced by enhanced export via the TPDS. On the other hand, the more western their position is the more is the TPDS reduced and the total volume is increased.

In summary, it can be stated that because of the rise of surface air temperatures during the last decades the Arctic sea ice has decreased. However, for the spatial pattern of the trends dynamic effects of the wind field are important and can even reverse the trends which would result from thermal forcing only.

5.6 Discussion

The previous investigation has shown that, in response to long-term trends of the forcing data, the sea ice volume of the Arctic has decreased over the last few decades. According to the temporal evolution of the extra-tropical Northern Hemisphere SAT a pronounced downward trend of SIV is apparent from the 1960s onward and corresponds to a loss of 16% of volume. Although the magnitude of the loss can presently not be exactly determined, there is a broad agreement between observational and other modelling studies that the sea ice volume of the Arctic has decreased. From observational data *Rothrock et al.* [1999b] estimated a much larger loss by about 40% between the 1960s and 1990s. On the other hand, *Weatherly and Arblaster* [2000] found a loss of about 5% over this period

from hind-cast simulations with a global coupled atmosphere-ice-ocean model including a sophisticated dynamic-thermodynamic sea ice component. From a hind-cast simulation of a coupled sea ice-mixed layer-ocean model *Zhang et al.* [2000] report an overall decrease of sea ice volume of 6% for the period 1979–1996. From satellite observations only trends of the areal ice coverage can be deduced, although there are efforts under way to also retrieve the ice thickness [*S. Laxon*, pers. comm.]. However, the areal coverage of multiyear ice derived from the satellite data indicate a loss of thicker, perennial sea ice of $7\%/dec$ over the last two decades [*Johanessen et al.*, 1999]. This is much larger than the decrease of the overall ice extent of $-2.8\%/dec$ [e.g. *Parkinson et al.*, 1999]. This difference agrees with the findings of the present analysis which shows a larger decrease of ice thickness in the central Arctic than in ice concentration. Over the period of 1966–99, when the SIV shows a trend of $-4.8\%/dec$, the simulated sea ice area (Fig. 4.2) decreased by only $-1.44\%/dec$. Roughly the same was found *Weatherly and Arblaster* [2000] who also obtained a smaller trend for simulated ice area than for ice volume. From sensitivity studies with a dynamic-thermodynamic sea ice model similar to that used in the present study *Lemke et al.* [2000] found a typical change of Arctic sea ice volume of $1.8\%/(W\,m^{-2})$ to perturbations of the downwelling longwave radiative forcing whereas the sensitivity of the ice extent was only $0.3\%/(W\,m^{-2})$. This difference can be explained by the 'land-locking' of sea ice in the Arctic. Therefore, from trends of the Arctic ice extent, which are well observed during the last two decades, no direct informations about a thinning of the Arctic sea ice can be gained.

The only source for direct estimates of the Arctic ice thickness are presently submarine based measurements of ice draft (see Sec. 3.4). Primarily two studies [*Wadhams*, 1990; *Rothrock et al.*, 1999b] analysing these ice draft data reported a thinning of the Arctic ice pack. However, without long time series of it is difficult to distinguish long-term trends from interannual variability. For example, *Wadhams* [1990] report a reduction of ice thickness north of Greenland by about 15% from 1976 to 1987, based on a comparison of submarine data from those both years. However, as was shown in Sec. 4.3, this decrease was only part of pronounced interannual fluctuations and was followed by the record maximum ice thickness in this area only three years later. From the model results, the ice thickness north of Greenland and the Canadian Archipelago only slightly decreased over the last 50 years or even increased in the region north of Ellesmere Island. In contrast, in the study of *Rothrock et al.* [1999b] a much larger number of submarine measurements were analysed allowing the detection of regional changes of the ice thickness. However, this study is primarily a comparison of two climatologies because data from the 1990s (1993–1997) were compared to data from 1960s and 1970s (1958–1978). This comparison resulted in ice draft changes of -1.5 to $-2.0\,m$ in the Eastern Arctic, -1.0 to $-1.5\,m$ between the North Pole and the Beaufort Sea, and -0.5 to $-1.0\,m$ in the central Beaufort and Chukchi Seas. These differences are much larger than the linear trends derived from the model data for the period 1958–1999 (Fig. 5.5) which show changes of about -0.6 to $-0.8\,m$ over this period in the eastern Arctic. A comparison of the two sets of model data for the same years[2] reveals changes of -0.9 to $-1.2\,m$ (not shown) which are larger than those derived from the linear trends. Moreover, if only summer data are analysed, as done by *Rothrock et al.* [1999b], changes in the eastern Arctic are further enhanced and amount to -1.2 to $-1.5\,m$ (not shown). The latter is due to enhanced trends of ice thickness and

[2]For their comparison *Rothrock et al.* [1999b] used submarine data from the years 1958, 1960, 1962, 1970, and 1978 as well as from 1993, 1996, and 1997 [*Y. Yu*, pers. comm.].

ice concentration during summertime (Fig. 5.6). Therefore, the study of *Rothrock et al.* [1999b] can undoubtly be considered as an observational evidence of a thinning of the Arctic ice cover. However, their conclusion that the observed ice draft changes correspond to a 40% loss of Arctic ice volume seems to be exaggerated.

The submarine data analysed by *Rothrock et al.* [1999b] furthermore show a continuation of the thinning during 1990s. Indeed, as shown by the simulated sea ice volume time series (Fig. 5.3) during the 1990s there is still a downward trend leading to record low values in the years after 1995. Overall, from the comparison with the idealised simulations, it was concluded that the overall decrease and especially the decrease during th 1990s can primarily be attributed to the warming of the high northern latitudes. In particular, the ice volume of the idealised simulation with prescribed variability of SAT forcing only shows a downward trend from the mid 1960s onward as well as an enhanced decrease during the 1990s. This cannot be explained by enhanced ice exports which exhibit, besides small interannual variability, only a slight decrease (not shown). In the standard simulation the ice export (Fig. 4.17) shows nearly no trend over the entire simulation period but some larger positive anomalies during the late 1980s and early 1990s. Note, that the ice export through Fram Strait of the WIND simulation is very close to that of the standard run. Furthermore, as shown in Sec. 4.2 anomalous winds were primarily important for the evolution of the pronounced summer openings in the eastern Arctic in 1990 and 1995, as was also argued by *Polyakov and Johnson* [2000]. Therefore, from the late 1980s to the early 1990 the WIND simulation exhibits also downward trends, although over the entire period there is an increase of the ice volume. Roughly the same conclusions were drawn by *Zhang et al.* [2000] from a coupled sea ice-ocean simulation over the period 1979–96 primarily forced with IABP derived geostrophic winds and IABP/POLES air temperatures. They also found from a sensitivity study without interannual variability of SAT an increase of sea ice volume before 1987, a peak of ice volume in 1987, and a decrease thereafter which closely corresponds to the temporal evolution of SIV_W (Fig. 5.8). The overall loss of volume by 6% of their standard simulation (interannual variability of winds and SAT) was explained by almost equal contributions of enhanced melt during summertime and increased ice outflow. Furthermore, the simulation of *Zhang et al.* [2000] yields enhanced decrease of ice volume during the period 1987–96 which also agrees with the findings of the present study. From these considerations it can be concluded that the overall thinning of Arctic sea ice is primarily due to reduced net growth but that the enhanced decrease after the late 1980s is attributable to wind driven effects also.

As was shown above, forcing a sea ice model with interannual varying SAT and winds is sufficient to explain much of the observed interannual and long-term evolution of the Arctic ice cover. However, other environmental effects were not taken into account, or were at least prescribed as climatological values. Especially the underestimation of the trends of sea ice extent and ice area by the model compared to the satellite observations, even when considered over the time interval, point towards a probable lack of other interannual varying forcing quantities. The first candidate could be the cloud coverage, which must have been increased during the last decades because the number of cyclones entering the Arctic has significantly increased since the 1960s in all seasons but autumn [*Serreze et al.*, 2000]. During spring and summertime an increased cloud coverage would lead to less melting because downwelling shortwave radiation, which dominates the energy balance at the ice surface during this time, would be reduced. On the other hand, during wintertime an increased cloud coverage and, therefore, increased humidity of the atmosphere would

reduce the outgoing longwave radiation and, thus, lead to reduced freezing. Another candidate most likely affecting the ice cover is a warming of the Arctic Ocean by oceanic processes. As noted by *Dickson et al.* [2000] there was increased oceanic heat transport into the Barents and the adjacent Seas associated with an increase of the NAO. Moreover, an increased import of Atlantic Water through the West Spitsbergen Current from the mid 1960s to the mid 1990s was deduced from a 1°–2°C increase of the $50\,m$–$500\,m$ water temperatures in the region west of Spitsbergen (9°E–11°E). From SCICEX data there is evidence that the Atlantic-derived sublayer of the Eurasian Basin had also warmed by 1°–2°C as compared to data from the 1940s to the 1970s. According to these changes *Steele and Boyd* [1998] report a retreat of the cold halocline layer during the 1990s in this region which usually acts to insulate the sea ice from the warm Atlantic water below. From a simple model calculation *Steele and Boyd* [1998] concluded an increased heat flux from the deep Atlantic Water towards the surface which lead to a reduction of winter ice growth. The latter was confirmed by a model study of *Zhang et al.* [1998]. From a coupled sea ice-ocean model integration over the period 1979–96 they found a significant increase in the temperature and salinity over a large area of the upper Arctic Ocean which is due to enhanced Atlantic Water inflow primarily via the Barents Sea. Due to a reduced insulating strength of the halocline layer the oceanic heat flux from the deeper ocean to the mixed layer and the cover ice cover. However, *Zhang et al.* [1998] concluded that the increase of the SAT forcing (from IABP) plays a more prominent role in the simulated decrease in ice thickness than the oceanic effect.

The present study has shown that the sea ice volume of the Arctic has decreased primarily in response to a warming of the high northern latitudes. Considering the proxy record of Arctic temperatures [*J. Overpeck*, in *Serreze et al.*, 2000], which show the 20th century as the warmest period within 400 years, and having in mind the rather strong relation of ice volume to SAT it can be suggested that, accordingly, the present sea ice volume is lowest within the last few centuries. Due to an increase in greenhouse gas concentrations CGCMs predict a further decrease of the Arctic ice pack due to increasing temperatures. In particular, the ensemble of scenario integrations *Weatherly and Arblaster* [2000], including the radiative effects of a series of greenhouse gases as well as the reflecting effect of sulfate aerosols, predict a warming of the global temperature between 1.8° and 2.0°C until the year 2080 depending on the prescribed scenario. Associated with this warming is a further thinning of the Arctic ice pack by about $0.5\,m$ until the end of the 21th century.

Chapter 6

Final Discussion

In this study the variability of the Arctic sea ice cover was investigated by analysing hindcast experiments of a state-of-the-art dynamic-thermodynamic sea ice model for the past 50 years. As interannual forcing of the model were used realistic fields of near surface winds and air temperatures derived from the NCEP/NCAR reanalysis projects. Because other atmospheric and oceanic quantities, which may be important for sea ice variations, were prescribed as climatologies, the simulations presented in this study can also be considered as sensitivity experiments. However, it was found that the sea ice model integration under such a configuration was not only able to reproduce the mean quantities of the Arctic ice cover (this was already shown by previous studies) but also observed features of its interannual variability. In the following, the major findings of this study are summarised and discussed with respect to their broader importance.

The simulations revealed that due to both temperature and winds the total sea ice volume of the Arctic exhibit considerable decadal-scale variations. Locally, these fluctuations manifest themselves as interannual ice thickness variations which are largest at the Canadian and Siberian coasts. These variations are primarily due to the combined effects of dynamics and thermodynamics but, at some occasions, also due to purely dynamic forcing of circulation anomalies associated with the Arctic Oscillation (AO). Beside the ice edge at the Atlantic side of the Arctic, where the mean ice thickness is generally small and so its standard deviation, it is the central Arctic Ocean which exhibits a local minimum of interannual ice thickness variability within the perennial ice pack. Hence, this region would be suitable for detecting significant long-term changes.

The sea ice export out of the Arctic, primarily passing Fram Strait, turned out to be highly variable and to be solely associated with variations of the wind field as long as interannual time scales are considered. Moreover, two different types of ice export anomalies were identified. The first type, which was responsible for the initiation of the Great Salinity Anomaly of the northern North Atlantic, is due to ice thickness changes which strongly depend on the overall wind field of the Arctic. The second and more frequent type is due to anomalies of the drift speed of ice which are associated with more local changes of meridional winds in the Fram Strait region. A coherence with the North Atlantic Oscillation (NAO) was only found during the last two decades because of an eastward shift of the NAO's centres of interannual variability.

The simulation reveals a long-term downward trend of the simulated ice volume of the Arctic. This trend is primarily due to an increase of SAT but is accelerated since the mid-1980s. This acceleration was found to be due to a wind-driven decrease, whereas

over the entire simulation period the winds tends to damp the overall thinning caused by rising air temperatures. Interestingly, the general trend of the ice drift towards a reduced anticyclonic circulation leads to a decrease of the thermal sensitivity of the ice cover because of an increase of its thickness in the melting regions. However, during the last 15 years cyclonic anomalies were strongest in the eastern Arctic and led to reduced ice thicknesses in the melting regions and, therefore, to enhanced thermal sensitivity. Moreover, they also led to a strengthened outflow of ice into the North Atlantic. In general, ice thickness variations in the East Siberian Sea were found to be an indicator of overall sea ice volume changes.

The simulation results strongly emphasise the need for basin-wide ice thickness observations. Although there have been ongoing efforts in the release of previously classified submarine observations, the current database is not sufficient to make reliable statements about the interannual variability of ice thickness. Unfortunately, the region of most interest for large scale changes of the Arctic ice cover, the East Siberian Sea, is excluded from the area where submarine data are released (the so-called Gore Box). Although the simulation results support the spatial pattern of ice thickness changes derived from observations, they also highlight possible problems in estimating the correct amplitudes of sea ice trends. That is, due to pronounced interannual-to-decadal changes of Arctic sea ice volume, ice thickness changes based on a comparison of data from different periods cannot separate long-term trends from natural variability. On the other hand, the results of sea ice models have to be compared with ice thickness observations. In the near future, however, ice thickness data from the CryoSat mission will make such a comparison possible and will allow, after some years of collecting data, the direct estimation of trends. So far, sea ice model results as presented in this study provide an estimate of the magnitude of longer-term changes on the background of interannual and decadal-scale variability.

Moreover, the results of this study are also important for global climate modelling. Historically, sea ice processes have been treated rather crudely in global models. Even in the 1995-assessment of the IPCC, only 6 out of 16 coupled climate models discussed have included ice dynamics, and only 3 of them used a scheme which solves the momentum balance for sea ice [*Houghton*, 1996]. The remaining 10 models used thermodynamic-only parameterisations of the sea ice cover. *Fischer and Lemke* [1994] have shown, that dynamic-thermodynamic sea ice models are less sensitive to climate perturbations. Moreover, the results of the Sea Ice Model Intercomparison Project (SIMIP) [*Kreyscher et al.*, 1997; *Lemke et al.*, 1997; *Kreyscher et al.*, 2000] give a guideline for the implementation of sea ice dynamics schemes for the use in global coupled climate models. Furthermore, this study has shown that there are considerable effects of ice dynamics on both the interannual variability and the long-term trends of the sea ice cover.

Furthermore, the variability of the ice volume export from the Arctic into the North Atlantic Ocean, which is important for variations of the thermohaline circulation of the oceans, depends on the proper treatment of sea ice dynamics. These findings further stress the need for including ice dynamics into climate model simulations. Moreover, the accuracy of simulating the atmospheric circulation is important for sea ice processes. As was shown in this study, the effects of decreasing sea level pressures in the Arctic on sea ice volume changes may depend on rather small longitudinal displacements. The same was found for the coupling of atmospheric variability due to the NAO to variations of the sea ice volume flux into the North Atlantic.

Finally, it can be stated that this study has revealed some insight into the variability of

the Arctic ice pack. However, the above presented results have to be validated with forthcoming observations and compared with results from other models of different complexity. In particular, it is suggested to extend the Sea Ice Model Intercomparison Project in order to include the evaluation of the effects of different rheologies schemes implemented in sea ice models on the long-term behaviour of the simulated ice pack.

Bibliography

Aagaard, K. and E. C. Carmack, 1989: The role of sea ice and other fresh water in the Arctic circulation. *J. Geophys. Res.*, *94*(C10), pp. 14,485–14,498

Agnew, T. A., H. Le, and T. Hirose, 1997: Estimation of large-scale sea-ice motion from SSM/I 85.5 GHz imagery. *Ann. Glaciology*, *25*, pp. 305–311

Arfeuille, G., L. A. Mysak, and L.-B. Tremblay, 2000: Simulation of the interannual variability of the wind-driven Arctic sea ice cover during 1958–1998. *Climate Dyn.*, *16*, pp. 107–121

Barnett, T. P., K. Hasselmann, M. Chelliah, T. Delworth, G. Hegerl, P. Jones, E. Rasmusson, E. Roeckner, C. Ropelewski, B. Santer, and S. Tett, 1999: Detection and attribution of recent climate change: a status report. *Bull. Amer. Meteor. Soc.*, *80*(12), pp. 2631–2659

Bourke, R. H. and R. P. Garret, 1987: Sea ice thickness distribution in the Arctic Ocean. *Cold Reg. Sci. Technol.*,*13*, pp. 259–180

Bourke, R. H. and A. S. McLaren, 1992: Contour mapping of Arctic basin ice draft and roughness parameters. *J. Geophys. Res.*, *97*(C11), pp. 17,715–17,728

Bretherton, C. S., C. Smith, and J. M. Wallace, 1992: An intercomparison of methods for finding coupled patterns in climate data. *J. Climate*, *5*, pp. 541–560

Cavalieri, D. J., P. Gloersen, C. L. Parkinson, J. C. Comiso, and H. J. Zwally, 1997: Observed hemispheric asymmetry in global sea ice changes. *Science*, *278*, pp. 1104–1106

Cavalieri, D. J., C. L. Parkinson, P. Gloersen, J. C. Comiso, and H. J. Zwally, 1999: Deriving long-term time series of sea ice cover from satellite passive-microwave multisensor data sets. *J. Geophys. Res.*, *104*(C7), pp. 15,803–15,814

Chapman, W. L. and J. E. Walsh, 1993: Recent variations of sea ice and air temperature in high latitudes. *Bull. Amer. Meteor. Soc.*, *74*(1), pp. 33–47

Christoph, M., U. Ulbrich, J. M. Oberhuber, and E. Roeckner, 2000: The role of ocean dynamics for low-frequency fluctuations of the NAO in a coupled ocean-atmosphere GCM. *J. Climate*, *13*(0), pp. 2536–2549

CLIVAR, 1998: CLIVAR Initial Implementation Plan. WMO/TD No. 869. World Climate Research Program Report No. 103

Colony, R., I. Appel, and I. Rigor, 1992: Surface air temperature observations in the arctic basin. *Applied Physics Laboratory Technical Memorandum, APL-UW TM 01-92*

Colony, R. and A. S. Thorndike, 1984: An estimate of the mean field of Arctic sea ice motion. *J. Geophys. Res.*, *89*(C6), pp. 10,623–10,629

Comiso, J. C., 1995: SSM/I concentrations using the Bootstrap algorithm. NASA RP 1380

Comiso, J. C., D. J. Cavalieri, C. L. Parkinson, and P. Gloersen, 1997: Passive microwave algorithms for sea ice concentration: A comparison of two techniques. *Remote Sens. Environ.*, *60*, pp. 357–384

Cullather, R. I., D. H. Bromwich, and M. C. Serreze, 2000: The atmospheric hydrological cycle over the Arctic Basin from reanalyses. part i: Comparison with observations and previous studies. *J. Climate*, *13*, pp. 923–937

Delworth, T. L., S. Manabe, and R. J. Stouffer, 1997: Multidecadal climate variability in the Greenland Sea and surrounding regions: a coupled model simulation. *Geophys. Res. Lett.*, *24*(3), pp. 257–260

Deser, C., 2000: On the teleconnectivity of the "Arctic Oscillation". *Geophys. Res. Lett.*, *27*(6), pp. 779–782

Deser, C. and M. L. Blackmon, 1993: Surface climate variations over the North Atlantic Ocean during winter: 1900–1989. *J. Climate*, *6*, pp. 1743–1753

Deser, C., J. E. Walsh, and M. S. Timlin, 2000: Arctic sea ice variability in the context of recent atmospheric circulation trends. *J. Climate*, *13*, pp. 617–633

Dickson, R. R., J. Meincke, S. A. Malmberg, and A. J. Lee, 1988: The "Great Salinity Anomaly" in the northern North Atlantic 1968–1982. *Progr. Oceanogr.*, *20*, pp. 103–151

Dickson, R. R., T. J. Osborn, J. W. Hurrell, J. Meincke, J. Blindheim, B. Adlandsvik, T. Vinje, G. Alekseev, and W. Maslowski, 2000: The Arctic response to the North Atlantic Oscillation. *J. Climate*, *13*, pp. 2671–2696

Dietrich, G., W. Kalle, W. Krauss, and G. Siedler, 1975: *General Oceanography*. John Wiley and Sons, second ed.

Fischer, H. and P. Lemke, 1994: On the required accuracy of atmospheric forcing fields for driving dynamic-thermodynamic sea ice models. In: *The Polar Oceans and their role in shaping the global environment*, Geophys. Monogr. Ser., vol. 85, AGU, Washington D. C., pp. 373–381

Flato, G. M., 1995: Spatial and temporal variability of Arctic ice thickness. *Ann. Glaciology*, *21*, pp. 323–329

Frankignoul, C., 1995: Climate spectra and stochastic climate models. In: H. von Storch and A. Navarra, eidtors, *Analysis of climate variability: Applications of statistical techniques*, Springer Verlag, pp. 139–157

Fyfe, J. C., G. J. Boer, and G. M. Flato, 1999: The Arctic and Antarctic oscillations and their projected changes under global warming. *Geophys. Res. Lett.*, *26*(11), pp. 1601–1604

Gibson, P., J. K.and Kallberg, S. Uppala, A. Hernandez, A. Nomura, and E. Serrano, 1997: Ecmwf re-analysis, project report series: 1. era description. *Europe an Centre for Medium-Range Weather Forecasting, Reading UK*, p. 72

Gloersen, P., W. J. Campbell, D. J. Cavalieri, J. C. Comiso, C. L. Parkinson, and H. J. Zwally, 1992: Arctic and antarctic sea ice, 1978-1987: Satellite passive microwave observations and analysis. NASA Special Publication 511

Gloersen, P., C. L. Parkinson, D. J. Cavalieri, J. C. Comiso, and H. J. Zwally, 1999: Spatial distribution of trends and seasonality in the hemispheric sea ice covers: 1978–1996. *J. Geophys. Res.*, *104*(C9), pp. 20,827–20,835

Goosse, H., E. Deleersnijder, T. Fichefet, and M. H. England, 1999: Sensitivity of a global coupled ocean-sea ice model to the parameterization of vertical mixing. *J. Geophys. Res.*, *104*(C6), pp. 13,681–13,695

Goosse, H., F. M. Selten, R. J. Haarsma, and J. D. Opsteegh, 2000: Decadal variability in high northern latitudes as simulated by an intermediate-complexity climate model. submitted to *Ann. Glaciology*

Gudkovich, Z. M., 1961: Relation of the ice drift in the Arctic Basin to ice conditions in Soviet Arctic seas (in Russian). *Tr. Okeanogr. Kom. Akad. Nauk SSSR, 11*, 14–21

Guttridge, L., 1988: *Icebound: the Jeanette expedition's quest for the North Pole*. New York: Paragon House. First published New York, 1987

Häkkinen, S., 1993: An Arctic source for the Great Salinity Anomaly: A simulation of the Arctic ice-ocean system for 1955–1975. *J. Geophys. Res.*, *98*(C9), pp. 16,379–16,410

Häkkinen, S., 1999: A simulation of thermohaline effects of a Great Salinity Anomaly. *J. Climate*, *12*, pp. 1781–1795

Häkkinen, S. and C. A. Geiger, 2000: Simulated low-frequency modes of circulation in the Arctic Ocean. *J. Geophys. Res.*, *105*(C3), pp. 6549–6564

Harder, M., 1994: Erweiterung eines dynamisch-thermodynamischen meereismodells zur erfassung deformierten eises. *Ber. Fachbereich Phys. 50*, Alfred-Wegener-Inst. für Polar- und Meeresforschung, Bremerhaven, Germany

Harder, M., 1996: Dynamik, rauhigkeit und alter des meereises in der arktis — numerische untersuchungen mit einem grösskaligen modell. *Ber. Polarforschung 203*, Alfred-Wegener-Inst. für Polar- und Meeresforschung, Bremerhaven, Germany

Harder, M., 1997: Roughness, age and drift trajectories of sea ice in large-scale simulations and their use in model verifications. *Ann. Glaciology*, *25*, pp. 237–240

Harder, M., H. Lemke, and M. Hilmer, 1998: Simulation of sea ice transport through Fram Strait: Natural variability and sensitivity to forcing. *J. Geophys. Res.*, *103*(C3), pp. 5595–5606

Hibler, W. D., 1979: A dynamic-thermodynamic sea ice model. *J. Phys. Oceanogr.*, *9*(4), pp. 815–846

Hibler, W. D., 1980: Modeling a variable thickness sea ice cover. *Mon. Wea. Rev*, *108*, pp. 1943–1973

Hibler, W. D., 1984: The role of sea ice dynamics in modeling co_2 increases. In: *Climate processes and climate sensitivity*, Geophys. Monogr. Ser., vol. 29, edited by J. E. Hansen and T. Takahashi, AGU, Washington, USA, pp. 238–253

Hibler, W. D. and J. Zhang, 1994: On the effect of circulation on Arctic ice-margin variations. In: *The Polar Oceans and their role in shaping the global environment*, Geophys. Monogr. Ser., vol. 85, AGU, Washington D. C., pp. 383–397

Hilmer, M., 1997: Numerische Untersuchungen des Einflusses atmosphärischer Antriebsfelder in Simulationen der Grenzfläche Atmosphäre-Eis-Ozean in der Arktis. Master thesis, Inst. für Meereskunde, Kiel, Germany, 71 pp.

Hilmer, M., M. Harder, and P. Lemke, 1998: Sea ice transport: A highly variable link between Arctic and North Atlantic. *Geophys. Res. Lett.*, *25*(17), pp. 3359–3362

Hilmer, M. and T. Jung, 2000: Evidence for a recent change in the link between the North Atlantic Oscillation and Arctic sea ice export. *Geophys. Res. Lett.*, *27*(7), pp. 989–992

Hilmer, M. and P. Lemke, 2000: On the decrease of Arctic sea ice volume. *Geophys. Res. Lett.*, *27*(22), pp. 3751–3754

Houghton, J. T. e., ed., 1996: *Climate Change 1995: The Science of Climate Change*. Cambridge Univ. Press

Hurrell, J. W., 1995: Decadal trends in the North Atlantic Oscillation: regional temperatures and precipitation. *Science*, *269*, pp. 676–679

Jin, G., J. F. Lynch, R. Pawlowicz, P. Wadhams, and P. Worcester, 1993: Effects of sea ice cover on acoustic ray travel times, with applications to the Greenland Sea Tomography Experiment. *J. Acoust. Soc. Am.*, *94*(12), pp. 1044–1056

Johanessen, O. M., M. Miles, and E. Bjørgo, 1995: The Arctic's shrinking sea ice. *Nature*, *376*, pp. 126–127

Johanessen, O. M., E. V. Shalina, and M. W. Miles, 1999: Satellite evidence for an Arctic sea ice cover in transformation. *Science*, *286*, pp. 1937–1939

Johnson, M. A., A. Y. Proshutinsky, and I. V. Plyakov, 1999: Atmospheric patterns forcing two regimes of Arctic circulation: A return to anticlyclonic conditions? *Geophys. Res. Lett.*, *26*(11), pp. 1621–1624

Jones, P. D., 1994: Hemispheric surface air temperature variations: a reanalysis and an update to 1993. *J. Climate*, *7*, pp. 1794–1802

Jung, T., 2000: The North Atlantic Oscillation: variability and interactions with the North Atlantic Ocean and Arctic sea ice. Berichte aus dem Institut für Meereskunde Kiel No. 315, Institut für Meereskunde an der Universität Kiel, Kiel, Germany, ISSN 0341-8561

Jung, T. and M. Hilmer, 2000: On the link between the North Atlantic Oscillation and Arctic sea ice export through Fram Strait. *submitted to J. Climate*

Jung, T., M. Hilmer, S. Kleppek, E. Ruprecht, S. K. Gulev, and O. Zolina, 2000: Recent shift of interannual NAO variability: Impacts on North Atlantic climate. *submitted to Geophys. Res. Lett.*

Kalnay, E., M. Kanamitsu, R. Kistler, W. Collins, D. Deaven, L. Gandin, M. Iredell, S. Saha, G. White, J. Woollen, Y. Zhu, M. Chelliah, W. Ebisuzaki, W. Higgins, J. Janowiak, K. C. Mo, C. Ropelewski, J. Wang, A. Leetmaa, R. Reynolds, R. Jenne, and D. Joseph, 1996: The NCEP/NCAR 40-year reanalysis project. *Bull. Amer. Meteor. Soc.*, *77*(3), pp. 437–470

Koerner, R. M., 1973: The mass balance of the sea ice of the Arctic Ocean. *J. Glaciol.*, *12*, pp. 173–185

König-Langlo, G. and E. Augstein, 1994: Parameterization of the downward longwave radiation at the earth's surface in polar regions. *Metorol. Zeitschrift*, *N. F. 3*(H. 6), pp. 343–347

Kreyscher, M., 1998: Dynamics of Arctic sea ice — validation of different rheology schemes for the use in climate models. Berichte zur Polarforschung 291, ISSN 0176-5027, Alfred-Wegener-Institut, Bremerhaven

Kreyscher, M., M. Harder, and P. Lemke, 1997: First results of the Sea Ice Model Intercomparison Project SIMIP. *Ann. Glaciology*, *25*, pp. 8–11

Kreyscher, M., M. Harder, P. Lemke, and G. M. Flato, 2000: Results of the Sea Ice Model Intercomparison Project: Evaluation of sea ice rheology schemes for use in climate simulations. *J. Geophys. Res.*, *105*(C5), pp. 11,299–11,320

Kwok, R. and D. A. Rothrock, 1999: Variability of Fram Srait ice flux and North Atlantic Oscillation. *J. Geophys. Res.*, *104*(C3), pp. 5177–15,189

Kwok, R., A. Schweiger, D. A. Rothrock, S. Pang, and C. Kottmeier, 1998: Sea ice motionfrom satellite passive microwave data assessed with ERS and buoy motion. *J. Geophys. Res.*, *103*(C4), pp. 8191–8214

Laevastu, T., 1960: Factors affecting the temperature of the surface layer of the sea. *Comment. Phys. Mat.*, *25*, pp. 1

Lemke, P., 1987: A coupled one-dimensional sea ice-ocean model. *J. Geophys. Res.*, *92*(C12), pp. 13,164–13,172

Lemke, P., M. Harder, and M. Hilmer, 2000: The response of Arctic sea ice to global change. *Clim. Change*, *46*, pp. 277–287

Lemke, P., W. D. Hibler, G. Flato, M. Harder, and M. Kreyscher, 1997: On the improvement of sea-ice models for climate simulations: the sea ice model intercomparison project. *Ann. Glaciology*, *25*, pp. 183–187

Lemke, P., E. W. Trinkl, and K. Hasselmann, 1980: Stochastic dynamic analysis of polar sea ice variability. *J. Phys. Oceanogr.*, *10*, pp. 2100–2120

LeSchack, L. A., 1980: Arctic ocean sea ice statistics derived from the upward looking sonar data recorded during five nuclear submarine cruises. technical report (for Office of Naval Research), LeSchack Assoc., Long Key, Fla.,

Manabe, S. and R. J. Stouffer, 1995: Simulation of abrupt climate change induced by freshwater input to the North Atlantic Ocean. *Nature*, *378*, pp. 165–167

Marotzke, J. and J. Willebrand, 1991: Multiple equilibria of the Global Thermohaline Circulation. *J. Phys. Oceanogr.*, *21*, pp. 1372–1385

Martin, S. and E. Munoz, 1997: Properties of the Arctic 2-meter air temperature fields for 1979 to the present derived from a new gridded data set. *J. Climate*, *10*, pp. 1428–1440

Martin, S., E. Munoz, and R. Dreucker, 1997: Recent observations of a Spring-Summer warming over the Arctic Ocean. *Geophys. Res. Lett.*, *24*(10), pp. 1259–1262

Martin, T. and E. Augstein, 2000: Large-scale drift of Arctic sea ice retrieved from passive microwave satellite data. *Geophys. Res. Lett.*, *105*(C4), pp. 8775–8788

Maslanik, J. A., M. C. Serreze, and T. Agnew, 1999: On the record reduction in 1998 western Arctic sea-ice cover. *Geophys. Res. Lett.*, *26*(13), pp. 1905–1908

Maslanik, J. A., M. C. Serreze, and R. G. Barry, 1996: Recent decreases in Arctic summer ice cover and linkages to atmospheric circulation anomalies. *Geophys. Res. Lett.*, *23*(13), pp. 3359–3362

Mauritzen, C. and S. Häkkinen, 1997: Influence of sea ice on the thermohaline circulation in the Arctic-North Atlantic Ocean. *Geophys. Res. Lett.*, *24*(24), pp. 3257–3260

McLaren, A. S., 1989: The under-ice thickness distribution of the arctic basin as recorded in 1958 and 1970. *J. Geophys. Res.*, *94*, pp. 4971–4983

McLaren, A. S., R. G. Barry, and R. H. Bourke, 1990: Could Arctic ice be thinning? *Nature*, *345*, pp. 762–762

McLaren, A. S., J. E. Walsh, R. H. Bourke, R. L. Weaver, and W. Wittmann, 1992: Variability in sea-ice thickness over the North Pole from 1977 to 1990. *Nature*, *358*, pp. 224–226

McPhee, M. G., 1979: The effect of the oceanic boundary layer on the mean drift of pack ice: Application of a simple model. *J. Phys. Oceanogr.*, *9*, pp. 388–400

Melling, H. and D. A. Riedel, 1996: Development of seasonal pack ice in the beaufort sea during the winter 1991–19992l a view from below. *J. Geophys. Res.*, *101*(C5), pp. 11,975–11,991

Mesinger, F. and A. Arakawa, 1976: Numerical methods used in atmospheric models. GARP Publ. Ser No. 17, Geneva, 64 pp.

Milliman, J. D. and R. H. Meade, 1983: World-wide delivery of river sediment to the oceans. *J. Geol.*, *91*, pp. 1–21

Mysak, L. A. and D. K. Manak, 1988: Arctic sea-ice extent and anomalies, 1953–1984. *Atmos. Ocean*, *27*, pp. 376–405

Mysak, L. A., D. K. Manak, and R. F. Marsden, 1990: Sea-ice anomalies observed in the Greenland and Labrador seas during 1901–1984 and their relation to an interdecadal Arctic climate cycle. *Climate Dyn.*, *5*, pp. 111–133

Mysak, L. A. and S. A. Venegas, 1998: Decadal climate oscillations in the Arctic: A new feedback loop for atmosphere-ice-ocean interactions. *Geophys. Res. Lett.*, *25*(19), pp. 3607–3610

North, G. R., T. L. Bell, and R. F. Cahalan, 1982: Samplin errors in the estimation of Empirical Orthogonal Functions. *Mon. Wea. Rev*, *110*, pp. 699–706

Oberhuber, J. M., 1993: Simulation of the Atlanticcirculation with a coupled sea ice-mixed layer-isopycnal general circulation model. part i: Model desciption. *J. Phys. Oceanogr.*, *22*, pp. 808–829

Owens, W. B. and P. Lemke, 1990: Sensitivity studies with a sea ice-mixed layer-pycnocline model in the Weddell Sea. *J. Geophys. Res.*, *95*(C6), pp. 9527–9538

Parkinson, C. L. and D. J. Cavalieri, 1989: Arctic sea ice 1973–1987: seasonal, regional, and interannual variability. *J. Geophys. Res.*, *94*(C10), pp. 14,499–14,523

Parkinson, C. L., D. J. Cavalieri, P. Gloersen, H. J. Zwally, and J. C. Comiso, 1999: Spatial distribution of trends and seasonality in the hemispheric sea ice covers: 1978–1996. *J. Geophys. Res.*, *104*(C9), pp. 20,827–20,835

Parkinson, C. L., J. C. Comiso, H. J. Zwally, D. J. Cavalieri, P. Gloersen, and W. J. Campbell, 1987: Arctic sea ice, 1973–1976: satellite passive-microwave observations. *NASA SP–489*, p. 296

Parkinson, C. L. and W. M. Washington, 1979: A large-scale numerical model of sea ice. *J. Geophys. Res.*, *84*(C1), pp. 311–337

Peixoto, J. P. and A. H. Oort, 1992: *Physics of climate*. American Institut of Physics, New York. ISBN 0 88318 711 6

Perovich, D. A., G. A. Maykut, and T. Grenfell, 1986: Optical properties of ice and snow in polar regions. I: Observations. *Proceedings of the International Society for Optical Engineering, Ocean Optics VIII*, *637*, pp. 232–241

Pfirman, S., R. Colony, D. Nürnberg, H. Eicken, and I. Rigor, 1997: Reconstructing the origin and trajectory of drifting Arctic sea ice. *J. Geophys. Res.*, *102*(C6), pp. 12,575–12,586

Pollard, R. T. and S. Pu, 1985: Structure and circulation of the upper Atlantic Ocean northeast of the Azores. *Progr. Oceanogr.*, *14*, pp. 443–462

Polyakov, I. V. and M. A. Johnson, 2000: Arctic decadal and interdecadal variability. submitted to *Geophys. Res. Lett.*

Proshutinsky, A. Y. and M. A. Johnson, 1997: Two circulation regimes of the wind-driven Arctic Ocean. *J. Geophys. Res.*, *102*(C6), pp. 12,493–12,514

Rahmstorf, S., 1994: Rapid climate transitions in a coupled ocean-atmosphere model. *Nature*, *372*, pp. 82–85

Rahmstorf, S., 1995: Bifurcations of the Atlantic thermohaline circulation in response to changes in the hydrological cycle. *Nature*, *378*, pp. 145–149

Rahmstorf, S., 2000: The thermohaline ocean circulation: a system with dangerous thresholds? *Climatic Change*, *46*, pp. 247–256

Rigor, I. G., R. L. Colony, and S. Martin, 2000: Variations in surface air temperature observations in the Arctic, 1979–97. *J. Climate*, *13*, pp. 896–914

Roeckner, E., L. Bengtsson, J. Feichter, and H. Lelieveld, J. Rhode, 1996: Transient climate change simulations with a coupled atmosphere-ocean GCM including tropospheric sulfur cycle. *J. Climate*, *12*, pp. 3003–3032

Roeckner, E., J. M. Oberhuber, A. Bacher, M. Christoph, and I. Kirchner, 1999: ENSO variability and atmospheric response in a global coupled atmosphere-ocean GCM. *Climate Dyn.*, *12*, pp. 737–754

Rogers, J. C., 1984: The association between the North Atlantic Oscillation and the Southern Oscillation in the Northern Hemisphere. *Mon. Wea. Rev*, *112*, pp. 1999–2015

Rothrock, D. A., W. Maslowski, D. Chayes, G. Flato, J. Grebmeier, R. Jackson, R. Sambrotto, W. Smethie, W. Sternberger, J. Swift, J. Tarduno, and A. Thorndike, 1999a: Arctic ocean science from submarines—a report based on the SCICEX 2000 workshop. Applied Physics Laboratory, University of Washington, Seattle

Rothrock, D. A., Y. YU, and G. A. Maykut, 1999b: Thinning of Arctic sea-ice cover. *Geophys. Res. Lett.*, *26*(23), pp. 3469–3472

Semtner, A. J., 1976: A model for the thermodynamic growth of sea ice in numerical investigations of climate. *J. Phys. Oceanogr.*, *6*, pp. 379–389

Serreze, M. C., F. Carse, R. G. Barry, and J. C. Rogers, 1997: Icelandic Low cyclone activity: climatological features, linkages with the NAO, and relationships with recent changes in the Northern Hemisphere circulation. *J. Climate*, *10*, pp. 453–464

Serreze, M. C. and C. M. Hurst, 2000: Representation of mean Arctic precipitation from NCEP-NCAR and ERA reanalyses. *J. Climate*, *13*, pp. 182–201

Serreze, M. C., J. A. Maslanik, J. R. Key, R. F. Kokaly, and D. A. Robinson, 1995: Diagnosis of the record minimum in Arctic sea ice area during 1990 and associated snow cover extremes. *Geophys. Res. Lett.*, *22*(16), pp. 2183–2186

Serreze, M. C., J. E. Walsh, F. S. Chapin, T. Osterkamp, M. Dyurgerov, V. Romanovsky, W. C. Oechel, J. Morison, T. Zhang, and R. G. Barry, 2000: Observational evidence of recent change in the northern high-latitude environment. *Clim. Change*, *46*, pp. 159–207

Shindell, D. T., R. L. Miller, G. A. Schmidt, and L. Pandolfo, 1999: Simulation of recent northern winter climate trends by greenhouse-gas forcing. *Nature*, *399*, pp. 452–455

Shuchman, R. A., E. G. Josberger, C. A. Russel, K. W. Fischer, O. M. Johanessen, and P. Gloersen, 1998: Greenland Sea Odden sea ice feature: Intra-annual and interannual variability. *J. Geophys. Res.*, *103*(C6), pp. 12,709–12,724

Skeie, P., 2000: Meridional flow variability over the Nordic seas in the Arctic Oscillation framework. *Geophys. Res. Lett.*, *27*(16), pp. 2569–2572

Slonosky, V. C., L. A. Mysak, and J. Derome, 1997: Linking Arctic sea ice and atmospheric circulation anomalies on interannual and decadal time scales. *Atmos. Ocean*, *35*, pp. 333–366

Smith, D. M., 1998: Recent increase in the length of the melt season of perennial Arctic sea ice. *Geophys. Res. Lett.*, *25*(5), pp. 655–658

Steele, M. and T. Boyd, 1998: Retreat of the cold halocline layer in the Arctic Ocean. *J. Geophys. Res.*, *103*(C5), pp. 10,419–10,435

Steele, M. and G. M. Flato, 1999: Sea ice growth, melt, and modeling: a survey. In: The Arctic Ocean Freshwater Budget, a NATO ARW volume

Steele, M., J. Zhang, D. Rothrock, and H. Stern, 1997: The force balance of sea ice in a numerical model of the Arctic Ocean. *J. Geophys. Res.*, *102*(C9), pp. 21,061–21,079

Steffen, K., J. Key, D. J. Cavalieri, J. Comiso, P. Gloersen, K. St. Germain, and I. Rubinstein, 1992: The estimation of geophysical parameters using passive microwave algorithms. In: Microwave Remote Sensing of Sea Ice, Geophysical Monograph 68, AGU, Washington, USA

Thompson, D. W. J. and J. M. Wallace, 1998: The Arctic Oscillation signature in the wintertime geopotential height and temperature fields. *Geophys. Res. Lett.*, *25*(9), pp. 1297–1300

Thorndike, A. S. and R. Colony, 1982: Sea ice motion in response to geostrophic winds. *J. Geophys. Res.*, *87*(C8), pp. 5845–5852

Tremblay, L.-B. and L. A. Mysak, 1998: On the origin and evolution of sea-ice anomalies in the Beaufort-Chukchi sea. *Climate Dyn.*, *14*, pp. 451–460

Tremblay, L.-B., L. A. Mysak, and A. S. Dyke, 1997: Evidence from driftwood records for century-to-millenial scale variations of the high latitude atmospheric circulation during Holocene. *Geophys. Res. Lett.*, *24*(16), pp. 2027–2030

Trenberth, K. E. and D. A. Paolino, 1980: The Northern Hemisphere sea-level-pressure data set: Trends, errors and discontinuities. *Mon. Wea. Rev*, *108*, pp. 855–872

Ulbrich, U. and M. Christoph, 1999: A shift of the NAO and increasing storm track activity over Europe due to anthropogenic greenhouse gas forcing. *Climate Dyn.*, *115*, pp. 551–559

Vaughan, R., 1994: *The Arctic. A History.* Alan Sutton Publishing Inc, Dover. ISBN 0 7509 0177 2

Venegas, A. A., L. A. Mysak, and D. N. Straub, 1997: Atmosphere-ocean coupled variability in the South Atlantic. *J. Climate*, *10*, pp. 2904–2920

Vinje, T. and Ø. Finnekåsa, 1986: The ice transport through the Fram Strait. *Norsk Polarinst. Skr.*, *186*, pp. 37–39

Vinje, T., N. Nordlund, and A. Kvambekk, 1998: Monitoring ice thickness in Fram Strait. *J. Geophys. Res.*, *103*(C5), pp. 10,437–10,450

Vinnikov, K. Y., A. Robock, R. J. Stouffer, J. E. Walsh, C. L. Parkinson, D. J. Cavalieri, J. F. B. Mitchell, D. Garrett, and V. F. Zakharov, 1999: Global warming and northern hemisphere sea ice extent. *Science*, *286*, pp. 1934–1937

von Storch, H., 1995: Spatial patterns: EOFs and CCA. In: H. von Storch and A. Navarra, eidtors, *Analysis of climate variability: Applications of statistical techniques*, Springer Verlag, pp. 227–257

von Storch, H. and F. W. Zwiers, 1999: *Statistical Analysis in Climate Research.* Cambridge University Press. ISBN 0-521-45071-3

Voss, R. and U. Mikolajewicz, 2001: Long-term climate changes due to increased CO_2 concentration in the coupled atmosphere-ocean general circulation model ECHAM3/LSG. *Climate Dyn.*, *17*, pp. 45–60

Wadhams, P., 1990: Evidence for thinning of the Arctic ice cover north of Greenland. *Nature*, *345*, pp. 795–797

Wadhams, P., 1997: Ice thickness in the Arctic ocean: The statistical reliability of experimental data. *J. Geophys. Res.*, *102*(C13), pp. 27,951–27,959

Walsh, J. E., 1991: The Arctic as a bellwether. *Nature*, *352*, pp. 19–19

Walsh, J. E. and W. L. Chapman, 1990: Arctic contribution to upper-ocean variability in the North Atlantic. *J. Climate*, *3*, pp. 1462–1473

Walsh, J. E. and W. L. Chapman, 1998: Arctic cloud-radiation-temperature associations in observational data and atmospheric reanalyses. *J. Climate*, *11*, pp. 3030–3045

Walsh, J. E., W. L. Chapman, and T. L. Shy, 1996: Recent decrease of sea level pressure in the central Arctic. *J. Climate*, *9*, pp. 480–486

Walsh, J. E., W. D. Hibler, and B. Ross, 1985: Numerical simulation of northern hemisphere sea ice variability, 1951–1980. *J. Geophys. Res.*, *90*(C3), pp. 4847–4865

Walsh, J. E. and C. M. Johnson, 1979a: An analysis of Arctic sea ice fluctuations, 1953–77. *J. Phys. Oceanogr.*, *9*, pp. 580–591

Walsh, J. E. and C. M. Johnson, 1979b: Interannual atmospheric variability and associated fluctuations in Arctic sea ice extent. *J. Geophys. Res.*, *84*(C11), pp. 6915–6928

Weatherly, J. W. and J. M. Arblaster, 2000: Sea ice and climate in 20th and 21th century simulations with a global atmosphere-ocean-ice model. *J. Climate*, in press

Weeks, W. F., 1998: Growth conditions and the structure and properties of sea ice. In: Physics of Ice-Covered Seas, Helsinki University Printing House, Helsinki, Finland

Windmüller, M., 1997: Untersuchung von atmosphärischen reanalysedaten im weddellmeer und anwendung auf ein dynamisch-thermodynamisches meereismodell. Master thesis, Inst. für Meereskunde, Kiel, Germany, 67 pp.

Wingham, D. J., 1999: The first of the European Space Agency's opportunity missions: CryoSat. *Earth Observation Quarterly, 63*, ESA

Wohlleben, T. M. H. and A. J. Weaver, 1995: Interdecadal climate variability in the subpolar North Atlantic. *Climate Dyn.*, *11*, pp. 459–467

Yi, D., L. A. Mysak, and S. A. Venegas, 1999: Decadal-to-interdecadal fluctuations of Arctic sea-ice cover and the atmospheric circulation during 1954–1994. *Atmosphere-Ocean*, *37*(4), pp. 389–415

Zhang, J. and W. D. Hibler, 1997: On an efficient numerical method for modeling sea ice dynamics. *J. Geophys. Res.*, *102*(C4), pp. 8691–8702

Zhang, J., D. Rothrock, and M. Steele, 1998: Warming of the Arctic Ocean by a strengthened Atlantic inflow: Model results. *Geophys. Res. Lett.*, *25*(10), pp. 1745–1748

Zhang, J., D. Rothrock, and M. Steele, 2000: Recent changes in Arctic sea ice: the interplay between ice dynamics and thermodynamics. *J. Climate*, *13*, pp. 3099–3114

Zillmann, J. W., 1972: A study of some aspects of the radiation and heat budgets of the Southern Hemisphere oceans. In: Meteorology study, **26**, Bureau of Meteorology, Dept. of the Interior, Canberra, Australia, 526 pp.

List of Figures

List of Tables

List of Abbreviations

CGCM ...	Coupled General Circulation Model
DMSP	Defense Meteorological Satellite Program
ECMWF .	European Centre for Medium-Range Weather Forecasts
EGC	East Greenland Current
EOF	Empirical Orthogonal Function
ENH	Extratropical Northern Hemisphere
ERA	ECMWF Re-Analysis Project
ESMR	Electrically Scanning Microwave Radiometer
ESA	European Space Agency
GIN	Greenland/Iceland/Norwegian
GSA	Great Salinity Anomaly
GSFC	Goddard Space Flight Center
IABP	International Arctic Buoy Programme
IVF	Ice Volume Flux
KSIM	Kiel Sea Ice Model
MD	Model Domain
NAO	North Atlantic Oscillation
NCAR	National Centre for Atmospheric Research
NCEP	National Centre for Environmental Prediction
NSIDC ...	National Snow and Ice Data Center
PC	Principal Component
POLES ...	Polar Exchange at the Sea Surfac
RMSD	Root Mean Square Difference
RMSE	Root Mean Square Error
SAR	Synthetic Aperture Radar
SAT	Surface Air Temperature
SIC	Sea Ice Concentration
SIV	Sea Ice Volume
SLP	Sea Level Pressure
SCICEX ..	Scientific Ice Expeditions
SMMR ...	Scanning Multichannel Microwave Radiometer
SSM/I	Special Sensor Microwave/Imager
SVD	Singular Value Decomposition
TEMP	Simulation excluding interannual variability of wind forcing
TPDS	Transpolar Drift Stream
ULS	Upward Looking Sonar
WIND	Simulation excluding interannual variability of SAT forcing

Aknowledgements

I am very grateful to Prof. Dr. Peter Lemke for supervising this thesis, and for his guidance and his comments during the evolution of this work.

Many thanks to Dr. Thomas Jung for endless hours devoted to the exchange of ideas and for fruitful collaborations during five years of sharing one office. I am grateful for receiving advice as a good friend.

I thank Prof. Dr. Eberhard Ruprecht for valuable discussions and for helpful comments and suggestions on earlier versions of the manuscript. Thanks also to all my colleagues of the Department of Meteorology for a friendly and stimulating working atmosphere and for their scientific and technical support.

Special thanks to my wife Svea for an enormous amount of support, patience and encouragement during the difficult periods of this work as well as for maintaining a warm and relaxing atmosphere at home. I would also like to thank my parents for always supporting the choices I have made and believing that I could accomplish what I have set out to do.

Thanks go to Drs. R. Gerdes and C. Köberle from the AWI Bremerhaven for kindly providing the oceanic forcing data. The NCEP/NCAR reanalysis data were provided through the NOAA Climate Diagnostics Center and the ERA-15 were made available by the Deutsches Klimarechenzentrum Hamburg. Data from the control run of the ECHAM4/OPYC3 model were provided by Drs. E. Roeckner, M. Esch, and J.M. Oberhuber and the SLP data from the scenario run of ECHAM4/OPYC3 were provided by Dr. U. Ulbrich.

The German Science Foundation provided financial support in the framework of the Sonderforschungsbereich 460 “Dynamics of Thermohaline Circulation Variability”.